Investigation of ultra-thin Gallium compound layers fabricated by liquid metal chemistry for hybridintegrated photonics

Panteha Pedram

To cite this version:

Panteha Pedram. Investigation of ultra-thin Gallium compound layers fabricated by liquid metal chemistry for hybridintegrated photonics. Other. Ecole Centrale de Lyon; RMIT University (Melbourne), 2023. English. NNT : 2023ECDL0033 . tel-04477708

HAL Id: tel-04477708
https://theses.hal.science/tel-04477708
Submitted on 26 Feb 2024

N° d’ordre NNT : **2023ECDL0033**

THESE de DOCTORAT DE L’ECOLE CENTRALE DE LYON

Membre de l’Université de Lyon

En cotutelle internationale avec Royal Melbourne
Institute of Technology (RMIT)

Ecole Doctorale N° 160
Electronique, Electrotechnique et Automatique

Spécialité de doctorat : Electronique, micro et nano-électronique, optique et laser

Soutenue publiquement le 15/09/2023, par :

Panteha PEDRAM

Investigation of ultra-thin Gallium compound layers fabricated by liquid metal chemistry for hybrid integrated photonics

Devant le jury composé de :

Dr. BESLAND	Marie-Paule	Directrice de Recherches	Institut des matériaux de Nantes	Rapporteure
Pr. VEAL	Tim	Professeur des Universités	Université de Liverpool	Rapporteur
Pr. BROQUIN	Jean-Emmanuel	Professeur des Universités	Grenoble INP	Président du jury
Pr. MONAT	Christelle	Professeure des Universités	École Centrale de Lyon	Directrice de thèse
Dr. CUEFF	Sébastien	Chargé de recherche	CNRS INL	Directeur de thèse
Dr. DAENEKE	Torben	Professeur associé	Royal Melbourne Institute of Technology	Directeur de thèse
Pr. JOURNET	Catherine	Professeure des Universités	Université Claude Bernard Lyon 1	Invitée
Pr. MITCHELL	Arnan	Professeur	Royal Melbourne Institute of Technology	Invité
Dr. BOES	Andy	Professeur associé	Université de Adélaide	Invité

Acknowledgments

I would like to seize this opportunity to express my profound gratitude to all the individuals who accompanied me throughout my PhD journey.

Firstly, I would like to thank my supervisor, Christelle Monat. Her knowledge and seasoned guidance have been invaluable during my PhD. Her comprehensive and persistent feedback on my work has notably improved my research, making it more professional.I extend my gratitude to Sebastien Cueff , my patient supervisor who was alongside me at each stage of my work. His calm demeanor and kind guidance helped me overcome the obstacles I faced.I also appreciate my supervisor at RMIT, Torben Daeneke. Though we never had the opportunity to meet in person, his remote guidance and knowledge significantly enhanced the chemistry aspects of my project.A big thank you to Andy Boes for providing the first set of waveguides, enabling me to gain invaluable experience and improve my work with his meticulous corrections and comments.

I would like to acknowledge the ECLAUSion, CoFUND directed by Christian Grillet and Arnan Mitchell and ALPhFA project that financially supported by PhD project both in France and Australia and given me the opportunity to present my work in conferences and research events.I want to extend a heartfelt thank you to Ali Zavabeti, who played a critical role in my PhD journey. Despite the significant time difference between France and Australia, he dedicated considerable time to teaching me fabrication methods from afar and was always available to assist me and answer my questions.

Thank you to all the members of my jury for reading and evaluating the quality of my research. I am grateful to the two reviewers, Dr. Marie-Paule Besland, and Prof. Tim Veal, who carefully responded in writing to my manuscript. Your comments and remarks were carefully read, taken into account and aided in the enhancement of my research. I also thank Dr. Jean-Emmanuel Broquin and Dr. Catherine Journet for their questions and comments that clarified some points of my thesis and promoted a stimulating scientific discussion.

I am grateful for the kind individuals from INL who assisted me with experiments and taught me essential techniques. My thanks go out to Aziz Benamrouche, Claude Botella , Solène Brottet, Yann Chevolot , Pierre Crémillieu, Brice Devif , Jules Galipaud ,Thomas Gehin , Anne

Lamirand , Radoslaw Mazurczyk , Isabel Nabeth , Régis Orobtchouk, Benjamin Fornacciari, Céline Chevalier, Christian Sessal , Ségolene Callard and all the members of the i-Lum team.

I would also like to extend my gratitude to Arrigo Calzolari and Amine Slassi for the DFT calculations, as well as Bernard Pelissier and Badreddine Smiri for their assistance with Raman measurements.

Special thanks to my wonderful colleagues who became my best friends and helped create some of the most memorable moments of these past three and a half years. I appreciate Ana for always bringing intriguing topics to our lunchtime discussions ;), which often extended our breaks to two or even three hours. I am grateful to Greta for cultivating a lively atmosphere in our fourth-floor office.Harris, thank you for sharing your delicious food and proving that even an annoying person can be quite endearing. I'm profoundly grateful to Marko, my colleague in crime, for his unfaltering support and for elevating my understanding of what being a teammate truly means..I want to thank Paule for her generous kindness and relentless support. A big thanks to Antonin for being there during the ups and downs of my PhD journey. Oleh, thank you for teaching me the power of resilience.Jesus, thank you for your warm personality and kindness. Gaukhar, your energy and joy are infectious; I will never forget your amazing cakes. I am thankful to Ali for his supportive presence in my work, his endless kindness, and for being there during the challenging moments. Our 10 am coffee breaks were the fuel that kept me going. Koukou, my office mate and teammate, I appreciate your companionship throughout our shared ECLAUSion journey.

I'd also like to extend my gratitude to everyone who participated in my PhD journey at RMIT: Nitu, Chung, and Patjaree.

A big thank you to both the previous and the new generation of my office mates at INL: Pierre, Remi, Jeremy, Jordan, Tom, Capucine, Tam, Adam, Marina, and Shirin.

I want to acknowledge my closest friends - Samira, Jorjet, Faeze, Amir, Raha, Gui, Coco, and Piotrek. You are the chosen family who stood by me throughout this journey.

To Ali and Shayesteh, my parents, the best family one could wish for, thank you for giving me the courage to persevere through the most challenging moments of this journey. Even though we live far apart, you're always close in my heart, and I know I can always count on you. I owe you all the success I've achieved in my life.I would also like to thank my second family for their kindness and support: Laure, Philippe, Mathilde, Victor, and Pierre.

Finally, and most importantly, I would like to acknowledge my best friend, best colleague, partner in crime, and beloved fiancé, Clément. Without you, I could not have completed this PhD. You were the motivation behind my work, the one who turned my failures into success and my tears into smiles. Your unwavering support, especially during the final months of my PhD, and your patience with my complaints during writing were invaluable. You helped me scientifically, aiding me to overcome my weaknesses. Thank you for your patience and for listening to all my words. I am so fortunate to have you in my life.

Table of contents

Chapter 4: Integrated Optics 104

List of Figures

List of Tables

Glossary

2D	Two Dimensional
2PA	Two-Photon Absorption
3PA	Three-Photon Absorption
AOI	Angle Of Incidence
AFM	Atomic Force Microscopy
BP	Black Phosphorous
BSE	Back Scattered Electron
CCD	Charge-Coupled Device
CVD	Chemical Vapour Deposition
Cv	Covalent
Cs	Cesium
CMOS	Complementary Metal-Oxide-Semiconductor
DFT	Density Functional Theory
DFG	Difference Frequency Generation
DOS	Density Of States
DKS	Dissipative Kerr Soliton
EGaIn	Eutectic Gallium–Indium
IoT	Internet of Things
FET	Field Effect Transistor
FWM	Four Wave Mixing
Ga	Gallium
Ga_2O_3	Gallium Oxide
GaLMM	Auger Lines of Gallium
GaN	Gallium Nitride
GaNOI	Gallium Nitride -on-insulator
GaO_xN_y	Gallium OxyNitride
LED	Light-Emitting Diode
LMC	Liquid Metal Chemistry
LPCVD	Low pressure chemical vapor deposition
Hg	Mercury
HRTEM	High Resolution Transmission electron microscopy

ICP	Inductively Coupled Plasma
IR	Infrared
Me	Metal
MBE	Molecular beam epitaxy
MMI	Multi-Mode Interference
MoS_2	Molybdenum Disulfide
MIR	Mid-Infrared
MUT	Material Under Study
MRR	Micro ring Resonator
MZI	Mach-Zehnder Interferometers
TE	Transverse Electric
TM	Transverse Magnetic
NIR	Near Infrared
NLO	Non-Linear Optics
NPL	Nonlinear Photoluminescence
NPs	Nanoparticles
PDMS	Polydimethylsiloxane
PPT	Pump Probe Technique
PR	Photo Resist
PSPD	Position Sensitive Photo Detector
Rb	Rubidium
SiO_2	Silicon Dioxide
SiGe	Silicon Germanium
SiN	Silicon Nitride
Si_3N_4	Silicon Nitride
SA	Saturable Absorption
SAED	Selected Area Electron Diffraction
SE	Spectroscopic Ellipsometry
SEM	Scanning Electron Microscopy
SERS	Surface-Enhanced Raman Scattering
SFG	Sum-Frequency Generation
SHG	Second Harmonic Generation
SPM	Self-Phase Modulation
SPM	Scanning Probe Microscope
STM	Scanning Tunneling Microscope

TA	Transient Absorption
TEM	Transmission electron microscopy and Gap
TMDs	Transition Metal Dichalcogenides
TO	Thermo–Optic
TPF	Two-Photon Fluorescence
UV	Ultra Violet
UHV	Ultra-High Vacuum
WG	Waveguide
XPS	X-Ray Photoelectron Spectroscopy
XPS	X-ray Photoelectron Spectroscopy
MUT	Material Under Test
vdW	van der Waals
XRD	X-ray Diffraction
ZS	Z Scan

Introduction

In today's digital age, the demand for internet connectivity is growing at an unprecedented rate[1]. As more devices become connected and data-intensive applications such as video streaming, cloud computing, and Internet of things (IoT) gains prominence, traditional communication systems face challenges in meeting the ever-increasing bandwidth requirements[2]. Conventional optical transceivers, although effective, are often bulky, costly and energy consuming, limiting their widespread implementation. It is imperative to seek out innovative technologies that can address this demand for high-speed data transmission while overcoming the limitations of traditional solutions. In the span of the past two decades, the landscape of photonic technology has undergone a dramatic transformation, with silicon photonics emerging as a mature technological platform. By integrating various optical components on a silicon substrate, it can provide advanced functionality while harnessing the advantages of silicon's well-established manufacturing processes. With its ability to transfer optical data at very high speeds, across a wide bandwidth, with its power efficiency and scalability, silicon photonics has created an effective and compact technology for telecommunications, data centers, and sensing systems[3][4]. Nowadays, multiple optical functions can be integrated onto a single chip, resulting in the availability of optical systems including electro-optic modulators, Silicon germanium (SiGe) photodetectors, and low-loss silicon waveguides (**Figure 0-1**).

However, silicon encounters intrinsic limitations regarding light emission or nonlinear functions, calling for the use of complementary materials. Light emission enables high-speed data transmission, optical sensing, and imaging through efficient generation and control of light. It plays a vital role in technologies like lasers, light sources, and optical communication, offering faster and more secure communication compared to traditional electronic systems. Nonlinear functions, on the other hand, provide advanced signal processing capabilities such as frequency and wavelength conversion, signal amplification, and all-optical switching. These functionalities could be useful for tasks like signal modulation, regeneration, and complex optical processing in telecommunications, optical computing, and signal processing. Advancements in nonlinear devices hold exciting potential for the field of information processing. While it's still early days, their ability to manipulate light signals offers a promising alternative to the energy-intensive, sizeable electronic routers commonly used in telecommunications. As data flows across the internet continue to grow at an unprecedented rate, there's an increasing urgency to explore and develop innovative technologies. Nonlinear, all-optical devices might not replace opto-electronic routers completely, but they are poised to play a significant, complementary role in this technological evolution.

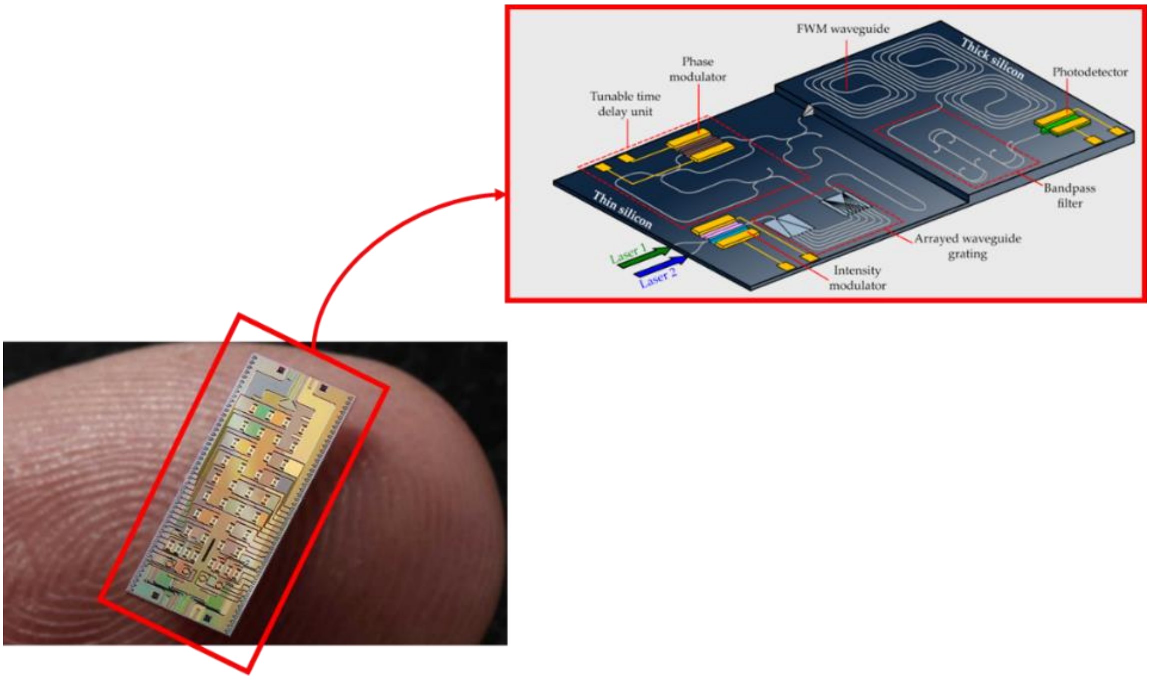

Figure 0-1. A schematic representation of a silicon photonic integrated circuit [5][6]

The heterogeneous integration of III-V materials onto silicon has offered one route to overcome these limitations, enabling, for instance, the realization of efficient A light-emitting diode (LEDs) or laser devices[7][8]. Concurrently, several material candidates are being investigated for their nonlinear properties with the aim to integrate them onto the mature silicon photonic platform[9]. The nonlinear optical response of materials has sustained the realization of all-optical devices like switches and amplifiers, capable of controlling light signals with other light signals. Optical mechanisms offer several advantages over their optoelectronic counterparts, including potentially higher speeds. In addition, they enable innovative functions such as wavelength conversion, frequency comb generation, and supercontinuum pulse creation.

However, despite the high application potential of nonlinear optics for all-optical information processing, no clear nonlinear material candidate has clearly emerged to complement silicon photonics. Wide bandgap semiconductors have been probed, but their integration with silicon photonics is not straightforward. Despite some high advances on glass materials, such as Silicon nitride (SiN) and Silicon dioxide (SiO_2), the latter suffer from relatively weak nonlinearity, hindering the realization of compact devices. Hence, scientists continue to search for materials with strong nonlinearities even at a reduced scale, which could be readily integrated with silicon photonics. This material should possess a high nonlinear coefficient, wide transparency window, and compatibility with silicon photonics platforms.

Enter two-dimensional (2D) materials, a promising contender in the quest for the ideal nonlinear material. Since the ground-breaking isolation of graphene, a monolayer of carbon, in 2004, researchers have explored and successfully isolated a variety of other materials in their 2D form.These 2D materials, compatible with planar photonic devices through post-processing techniques, bring new properties to the table that can potentially complement silicon photonics. Since then, numerous 2D materials have been explored, exhibiting many unique electronic, optical, and mechanical properties. Therefore, our research endeavors began with the aim of identifying new 2D materials that have the potential to complement silicon photonics for applications at around 1,55um wavelength. Among the candidates, gallium oxide (Ga_2O_3) and gallium nitride (GaN) have gained significant attention due to their impressive optoelectronic properties and promising applications in electronics, photonics, and bio sensing. However, it is worth noting that the existing research primarily focuses on the properties of Ga_2O_3 and GaN in bulk or thick layers, leaving a significant knowledge gap regarding their behavior in the 2D or ultrathin dimensions. Recognizing this gap, our research aims to address this limitation by conducting an in-depth analysis specifically on the properties of ultrathin Ga_2O_3 and GaN. Through this investigation, we aim to shed light on the unique properties of these materials in the 2D realm, paving the way for their potential applications in this dimension.

My PhD study has focused on these intriguing materials, encompassing their synthesis, characterization, and eventual integration into photonic devices. My PhD research project was centred on three main focal points, guiding my work towards meaningful outcomes:

- The synthesis of ultrathin Ga_2O_3 and GaN through an inventive method known as liquid metal chemistry
- the structural and optical characterization of these ultrathin Ga-based materials
- The integration of these materials into photonic devices.

This project is part of an international cotutelle between Ecole Centrale de Lyon (ECL) and Royal Melbourne Institute of Technology (RMIT) under the umbrella of European Union and Marie Curie framework. The investigative endeavor this project presented unfolded across two state-of-the-art laboratories:

(i) Institute of Nanotechnologies of Lyon (INL) and NANOLYON nanotechnology platform
(ii) RMIT Micro Nano Research Facility (MNRF) and the assistance of RMIT Microscopy and Microanalysis Facility (RMMF).

In the scope of our collaboration with CNR-NANO Istituto Nanoscienze in Modena, Italy, Arrigo Calzolari and Amine Slassi we provided substantial assistance by conducting the integral Density Functional Theory (DFT) calculations pivotal to this research. Ali Zavabeti and Chung Nguyen at RMIT University proficiently carried out the TEM and XPS measurements necessary for our research. Further enriching our research, Jules Galipaud offered technical support by facilitating our use of the XPS equipment housed in the LTDS laboratory at Ecole Centrale de Lyon. Our work was further augmented by Bernard Pelissier and Badreddine Smiri from LTM-CNRS of Grenoble, who performed the Raman measurements. Subsequently, we selected a SiN waveguide as the first device geometry for probing our 2D material, which was fabricated at STMicroelectronics.In pursuit of optical measurements, we utilized the optical setup available at INL, where the expertise of Regis Orobtchouk guided us.

This thesis is further divided into 4 parts. In Chapter 1:, which we call 'State of the Art', we provide a thorough overview of research literature related to 2D materials, particularly emphasizing Ga_2O_3 and GaN, as well as some survey on how 2D materials have been used and combined with integrated optics so far. This chapter explores the ongoing journey to find a method that is affordable, scalable, and efficient in producing high-quality Ga_2O_3 and GaN. Moreover, we are looking for a technique that allows for easy integration of these materials into photonic devices. We also discussed the structure and characteristics of liquid metal as a method for synthesizing these materials. This discussion highlights the importance of finding new techniques to overcome current obstacles that prevent us from fully harnessing the potential of 2D materials and their integration on photonic devices.

Chapter 2: expands upon our exploration by tackling a central issue: large-area, ultra-thin layer fabrication. Here, we introduce an inventive approach in the form of liquid metal chemistry has been recently developed [10][11] at RMIT university and mainly relies on a two-step process: the first step uses the 'liquid metal chemistry' (LMC) method, which is proven effective for synthesizing large-scale ultrathin oxide, the second step involves a microwave plasma-enhanced nitridation reaction [12]. This method has exhibited encouraging outcomes in the scalable synthesis of exceedingly thin layers of Ga_2O_3 and GaN. Next, the chapter delves into intricate details, elaborating on the various characterization methods utilized to investigate the topography, spectroscopy, and optical traits of the synthesized ultra-thin Ga_2O_3 and GaN. The study employs state-of-the-art tools like atomic force microscopy (AFM), Transmission electron microscopy (TEM), X-ray photoelectron spectroscopy (XPS), and Spectroscopic ellipsometry (SE) to study these materials' structural and optical properties in detail.

Chapter 3: presents the experimental results of the Ga-based ultra-thin layers synthesized by the method developed in chapter 2. It also turns our attention to a pivotal element of our research – exploring Gallium OxyNitride (GaO_xN_y) compounds. These intriguing compounds represent an intermediate stage between Ga_2O_3 and GaN. Understanding these intermediate compounds is essential as it sheds light on the transformation process from Ga_2O_3 to GaN. Additionally, this chapter exhibits the results from the characterization methods previously introduced in Chapter 2. It proffers an in-depth examination of the structural and optical attributes of these intermediate compounds and Ga_2O_3 and GaN. We combined sophisticated characterization methods, Raman measurement, and Density functional theory (DFT) calculations to achieve this.

In the final chapter (Chapter 4:), we turn our focus to practical applications. Specifically, we develop an approach to integrate 2D Ga_2O_3 and GaN materials into photonic devices. We exploit here Mach-Zehnder Interferometers (MZIs) and selective patterning to study the optical properties of hybrid SiN waveguides covered with ultra-thin Ga-based compounds. This step is crucial, for it paves the way towards realizing hybrid integrated photonics with these 2D materials. We discuss the integration process in detail, the challenges faced, and the ways to overcome these challenges. The chapter presents how the integration of ultra-thin layers of Ga_2O_3 and GaN into MZI can enhance our understanding of these materials. We undertook precise linear measurements on the MZIs to characterize the properties of Ga_2O_3 and GaN in detail. The initial choice of these materials was driven by our aim to develop nonlinear 2D materials for chip-based devices. However, it's important to acknowledge that in this phase of our research, we focused on their linear properties and have not yet studied their nonlinear characteristics. Nonetheless, this investigation underscores the significant potential of these 2D materials in advancing the field of integrated photonics and paves the way for further studies into their nonlinear properties

Overall, this research provides a comprehensive overview of ultra-thin Ga_2O_3 and GaN, taking the reader from their basic properties and potential applications to their synthesis, characterization, and integration into photonics devices. By addressing the current challenges and proposing innovative solutions, this work makes a significant and original contribution to the ongoing global research on 2D materials. With an ever-increasing interest in these materials, the knowledge generated in this study will have far-reaching implications in the fields of materials science, nanotechnology, and photonics.

Chapter 1: State of the art

The chief aims of this chapter are to furnish a comprehensive overview of the latest advancements in the research field of two-dimensional (2D) materials, with an emphasis on Gallium Oxide (Ga_2O_3) and Gallium Nitride (GaN), both of which have been identified as pertinent candidates for photonic applications. Furthermore, the chapter elucidates recent studies regarding liquid metals, highlighting their capability to expedite the synthesis of 2D materials in a cost-effective manner. Additionally, an in-depth analysis of contemporary techniques for the integration of 2D materials into photonic devices is provided, thereby establishing an informed foundation for subsequent scholarly exploration within the thesis.

1.1 Introduction

For hundreds of years, the basic design of optical systems did not change; they have consisted of bulky and heavy components which required careful alignment and protection against vibration, moisture, and temperature drift. In an effort to make them more compatible with modern technology, integrated optics came into being in the early 1970's (Miller, 1969 [13]; Tien, 1971, 1974 [14][15]; Miller, Marcatili and Li, 1972,1973 [16][17]). [18] The area defined by the name "integrated optics" has expanded gradually. The field of integrated optics has undergone progressive expansion, encompassing the exploration of guided-wave techniques for the fabrication of novel or enhanced optical devices. This development is motivated by the desire to achieve compact and miniaturized devices, with the expectation that reduced size will yield improved reliability, enhanced mechanical and thermal stability, lower power consumption, and more favourable drive voltages in active devices [19] .

In the late 1970s, a combination of factors led to the practical application of integrated optics. In the 1980s, optical fibers largely replaced metallic wires in telecommunications, and several manufacturers began producing optical integrated circuits for use in various applications. In the 1990s, the incorporation of optical fibers into telecommunications and data-transmission networks was extended to the subscriber loop in many systems. This provides an enormous bandwidth for multichannel voice, video, and data signal transmission. In addition, computer networks such as the Internet have provided access to worldwide communications and data banks. As a result, we are developing what some have called the “Information superhighway.” The implementation of this technology has provided the continuing impetus to the development of new integrated optic devices and systems at the beginning of the 21st century. Improved fabrication methods have played a significant role in driving the development of integrated optic devices. With the evolution of microtechnology, which works at micrometer dimensions, it has now advanced to nanotechnology where features are produced at the nanometer scale. This has given rise to the emerging field of Nanophotonics [20].

The inception of research on integrated optics dates back to the 1970s when a series of novel concepts were explored, including the use of thin-film technology for forming optical devices and circuits. This approach was appealing as thin-film technology had already revolutionized electronic devices and circuits. Despite over five decades of research on thin films, investigations into their potential applications persist even in 2023. This fact motivated the present PhD thesis, which seeks to explore a new definition of thin films as applied to integrated optics, namely, the utilization of 2D materials.

Ultra-thin two-dimensional materials, such as graphene and MoS_2, have distinctive properties including high carrier mobility [21] and tunable bandgaps [22]. These properties of 2D materials are crucial for enhancing the performance of electronic devices like high-speed transistors[23], and optoelectronic devices such as photodetectors [24] and LEDs [25]. Many synthetic approaches have been suggested for developing 2D materials. Yet, the synthesis of large-area, ultra-thin 2D materials remains a substantial technological challenge [26][27][28]. With some recent progress, the field of liquid metal chemistry could lead to the creation of new 2D materials and address challenges associated with their integration into various applications and devices. The unique property of certain liquid metals to support the growth of self-limiting surface oxide skins on exposure to air has resulted in the development of various new 2D materials which were previously inaccessible [10][29]. In addition, this technique promises easier integration of 2D materials onto photonic devices compared to traditional “top-down” and “bottom-up” methods. In particular, liquid gallium and gallium-based alloys have attracted significant attention due to their remarkable properties, which can create more opportunities to advance existing synthesis processes [30]. However, the isolation of the surface oxide from liquid metals and processes for transforming these 2D oxide skins into other 2D compounds are still in their infancy. The focus during the development of the synthesis strategies is not only to achieve a few atom-thick 2D nanosheets but also to deposit large-area 2D nanosheets at projected low cost and to explore the possibility of direct transfer to the intended device for applications. This chapter will list possible applications that may be achieved through liquid metal chemistry with a main focus on photonic applications. At the end of the chapter, integrated optics with 2D materials will be discussed, since these materials can advantageously complement silicon photonics and enhance the performance of silicon-based devices. The nonlinear properties of gallium nitride are explored in further detail, motivating the study of this material in the research chapters of this thesis. Overall, this chapter will present a brief epitome of the relevant topics, focusing on the work addressed in this Ph.D. thesis.

1.2 The advent of two dimensional (2D) Materials

Following the discovery of graphene in 2004 by Novoselov et al. [31], a group of materials known as 2D materials have been identified [32]. These materials have a thickness of only a few nanometers or less, which allows charge carriers to move freely in the 2D plane while their motion is restricted in the third direction [33]. Due to their atomic thinness, 2D materials possess unique properties with respect to their structure, optics, and physics, which often differ from their bulk counterparts. As a result, 2D materials have generated significant interest [34]–[40]. They possess a large surface area compared to their volume, which makes them particularly useful for applications where interactions on the surface are crucial [41]. In addition, 2D materials are mechanically flexible and can be bent, folded, or twisted without breaking, making them promising candidates for flexible electronics [42]. Furthermore, despite their thinness, 2D materials are incredibly strong, and some, such as graphene, have a higher tensile strength than steel [43]. On top of this, 2D materials can have unique optical and electrical properties; due to their atomically thin dimensions, such as strong light-matter interactions (compare to their thickness), meaning that even a single layer can strongly absorb or emit light. Moreover, the atomically thin nature of 2D materials gives rise to their photoluminescence properties(such as MoS_2), which refers to their ability to emit light upon absorption of photons[44]. This phenomenon occurs due to quantum confinement effects and the bandgap structure of these materials, resulting in highly efficient and tunable light emission [45]. They can also exhibit a range of electrical properties, from conductors to insulators, semiconductors, and even superconductors [34]. Thanks to these properties, specific 2D materials are suitable for targeted fields of applications and thus, have been exploited for creating photonic, nanoelectronic, and optoelectronic devices [31], [46]–[52]. However, few limitations such as the existence of intrinsic defects, the absence of an electronic band-gap and difficulties in controlling the number of layers during synthesis, have stimulated enormous interest toward the exploration of substitute 2D materials that feature their own diverse and remarkable properties [28], [31], [33], [46].

In recent years, transition metal dichalcogenides (TMDs) have been a prominent area of research due to significant discoveries such as the first MoS_2 field-effect transistor[53] and strong photoluminescence in single-layer MoS_2. TMDs are a type of hexagonal crystal with a monolayer consisting of a transition metal from groups 4-10, represented as "M," sandwiched between two chalcogen atoms, such as sulphur (S), selenium (Se) or tellurium (Te) (represented as “X”), with the stoichiometry of MX_2 [54]. Currently, there are over 40 known TMDs composed of various combinations of chalcogen atoms and transition metals [55]. Interest has also grown in 2D transition metal oxides (i.e. MnO_2, MoO_3, WO_3) [56], [57] and 2D layered hydroxides[57], [58], as well as in 2D nanostructures of group III-VIs (e.g., InSe, GaSe, GaS) [59], group V-VIs (i.e. Bi_2Te_3 and Sb_2Se_3[60], [61], and metal trichalcogenides and trihalides, as shown in **Figure 1-1**.

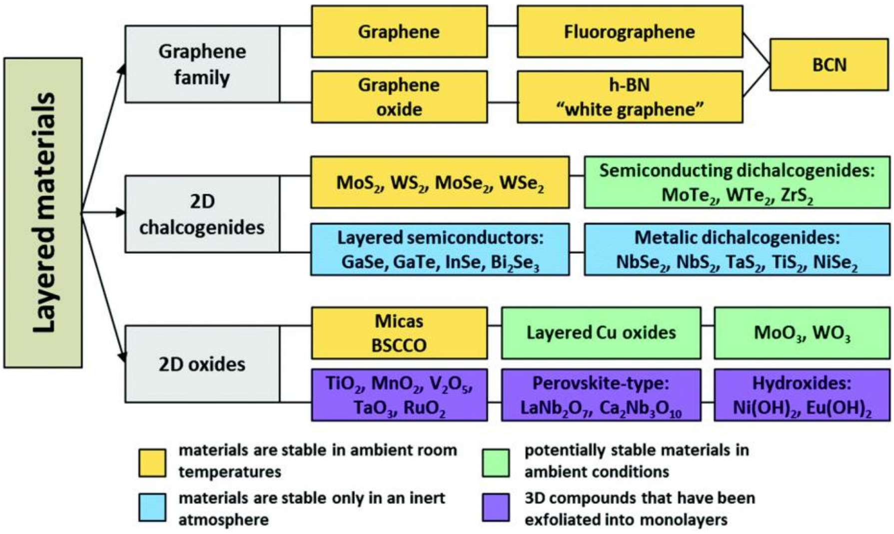

Figure 1-1 Chart illustrating the categorized library of 2D materials. hBN is a hexagonal boron nitride; BCN is 2D nanocomposites containing boron, carbon and nitrogen; BSCCO is bismuth strontium calcium copper oxide [62].

Ultra-thin 2D nanostructures have shown potential as promising materials for a wide range of applications, including electronics, sensing, catalysis, optoelectronics, energy storage, and photonics, as evidenced by various studies [37], [56], [63]. To date, a variety of methodologies have been proposed for synthesizing single- or few-layered 2D materials. These synthesis techniques can be broadly categorized into two fundamental approaches: (1) top-down and (2) bottom-up techniques (as shown in **Figure 1-2**). Top-down techniques involve exfoliating 2D nanostructures by delaminating individual atomic layers from the bulk through methods such as micromechanical cleavage [53], [63], [64], laser ablation [65], [66], ion intercalation [67], or ultrasound exfoliation [68]. In contrast, bottom-up techniques build up 2D materials from molecular precursors through thermal and/or chemical reactions, such as chemical vapour deposition [33], [69], wet chemical synthesis [70], atomic layer deposition [71], or thermolysis [72]. Some bottom-up methods allow 2D structures to be directly deposited onto substrates.

Layered van der Waals compounds are a class of materials that have strong covalent or ionic bonds within the plane of the material, resulting in stable sheets. However, these sheets are weakly bonded to each other through van der Waals forces [73]. Graphite is a well-known example of a layered van der Waals compound, consisting of weakly arranged graphene layers that can be easily separated (**Figure 1-3**) [54].

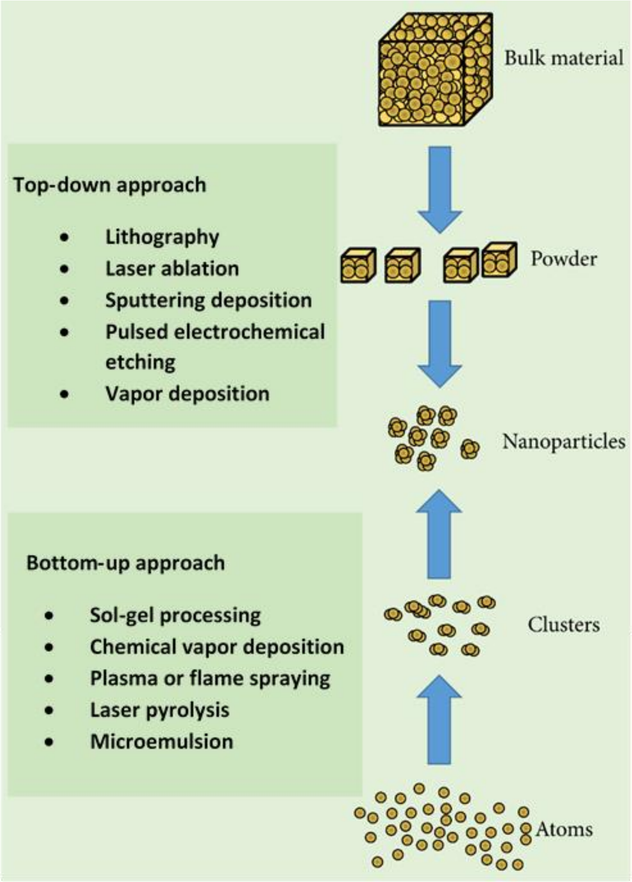

Figure 1-2 Schematic diagram of currently used chemical and physical methods of nanoparticle synthesis[74]. It presents the top-down approach including : lithography [75] ,laser ablation [76] ,sputtering deposition [77] ,pulsed electrochemical etching [78] ,vapor deposition [79] and bottom-up approach including : Sol-gel processing [80], chemical vapor deposition [81] ,plasma or flame spraying [82], laser pyrolysis [83] and microemulsion [84].

In contrast with graphite, non-layered materials have crystals that are connected internally in three dimensions, making it challenging to obtain ultra-thin 2D structures through exfoliation due to the strong bonds between vertical layers and the lack of intrinsic driving force for anisotropic 2D growth [73]. However, in recent years, a few non-layered 2D nanomaterials, including metal oxides(e.g. TiO_2, In_2O_3, SnO_2) and metal chalcogenides(e.g. PbS, ZnSe, ZnS), have been synthesized through wet-chemical synthesis approaches [73], resulting in a limited number of ultra-thin 2D materials for non-layered crystals. These breakthroughs have expanded the available pool of 2D materials, albeit with a relatively small number of non-layered crystals.

Motivated by the potential applications of 2D materials in various fields, researchers are actively exploring ways to produce 2D nanosheets from non-layered materials. The ability to synthesize ultra-thin 2D nanosheets from non-layered materials holds immense promise for a broader range of applications and functionalities.

By unlocking the potential of non-layered materials for 2D growth, researchers aim to overcome the limitations of conventional exfoliation techniques and enable the deposition of few-atom-thick, laterally large 2D materials. To address these challenges, scalable synthesis methods are needed to deposit large-area 2D materials on various substrates, which could fundamentally enrich the future prospects of 2D industries.

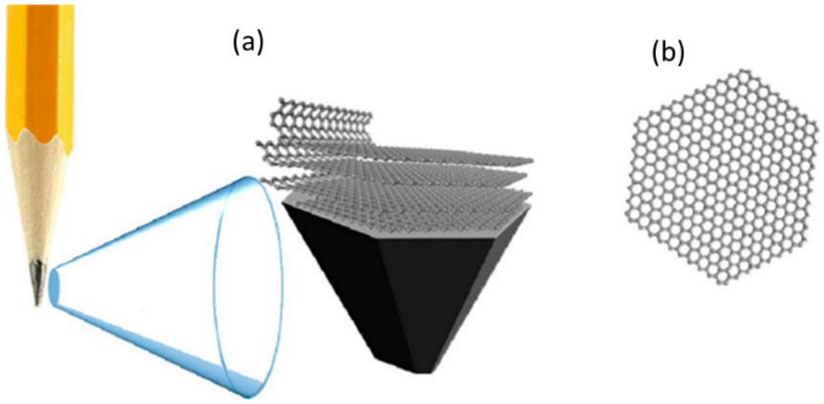

Figure 1-3 (a) weakly bonded graphene layers found in graphite. (b) A layer of graphene peeled away from the graphite found in a common pencil [85].

1.3 Gallium compounds

Gallium, a post-transition metal, and its compounds, especially Ga_2O_3 and GaN, are notable for their distinct electronic and optoelectronic properties. These materials (in bulk form) find applications in power electronics, Ultraviolet (UV) photodetectors, LEDs, and high-electron-mobility transistors. The following sections discuss the optoelectronic properties of gallium and its key compounds, Ga_2O_3 and GaN, which will represent the main focus of my PhD thesis.

1.3.1 Gallium Oxide (Ga_2O_3)

Ga_2O_3 is a semiconductor compound composed of group III and VI elements, and it has five different crystalline structures (α, β, γ, δ, and ε [86]), known as polymorphs. The two most studied structures are α- Ga_2O_3 and β- Ga_2O_3 [87], [88]. The α- Ga_2O_3 has a rhombohedral structure with a space group R3c, while β- Ga_2O_3 has a monoclinic structure with a space group C2/m, and lattice parameters a = 12.214 Å, b = 3.0371 Å, c = 5.798 Å, β = 103.83° [89]. The crystal structure of monoclinic Ga_2O_3 is depicted in **Figure 1-4**[90]. The other two polymorphs, δ- Ga_2O_3 and ε- Ga_2O_3, were first reported by Roy et al. in 1952 [91]. These different polymorphs can be prepared under specific condition [91], [92].

The band-gaps of bulk gallium oxides are wide, ranging from Eg ≈ 4.2 - 4.9 eV[60][87]. Due to its non-toxicity and stability, Ga_2O_3 has the potential to be used in a variety of applications, including electronics [93], photonics [94], sensing [95], resistive switching [96], and bio-inspired technologies [97]. Recently, research on 2D surface oxide films of liquid gallium alloys has been set up to realize economically affordable techniques for synthesizing and extracting high-quality 2D semiconductors [98].

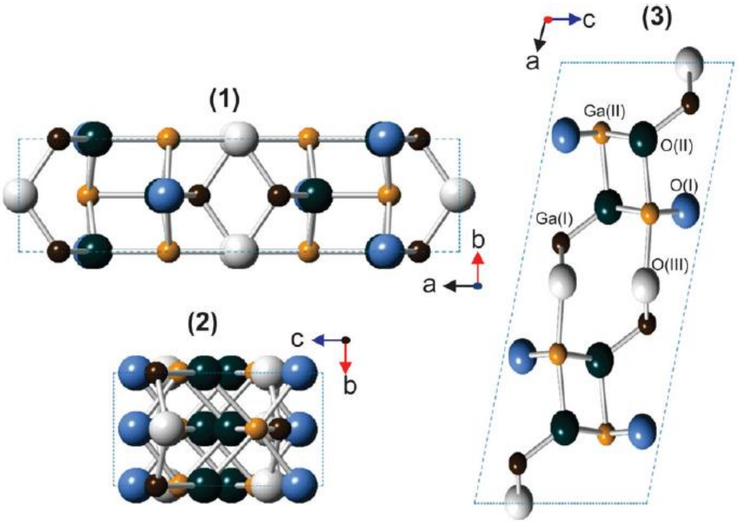

Figure 1-4 Unit cell of Ga_2O_3. It possesses two inequivalent Ga sites: Ga (I), Ga (II) and three inequivalent O-sites: O(I), O(II) and O(III). The Ga (I) sites have tetrahedral coordination, and the Ga (II) sites have octahedral coordination. Depicted is the projection of the unit cell of Ga_2O_3 along the c-(1), a-(2) and b-axis (3) [90].

Until this point in time, researchers have developed various methods in liquid phase for creating Ga_2O_3, which include hydrothermal (with or without surfactant), microwave, and solvothermal techniques [60], [86], [88], [99]–[105]. These methods produce nanorods, nanowires, and nanoplates with different sizes. However, these techniques usually demand lengthy processing times, which could take several days to attain satisfactory yields, and they also face challenges concerning flake size, thickness, and crystallinity, particularly in the case of 2D Ga_2O_3 nanosheets. As a result, producing large, homogeneous layers of 2D nanosheets across a wide area remains a significant obstacle. Reducing the thickness of the Ga_2O_3 material to just a few unit cells and depositing wafer-scale 2D nanosheets would have a substantial impact on this area of research for several reasons.

1.3.2 Gallium Nitride (GaN)

GaN, a third-generation semiconductor, possesses a wide direct band gap of 3.4eV [106]–[110], a high breakdown electric field, and high carrier mobility [111], [112]. GaN also exhibits chemical robustness and possesses piezoelectric and pyroelectric properties. These combined characteristics have led to its utilization in important applications such as optoelectronic quantum wells, various types of field-effect transistors, high-power devices, energy harvesting systems, sensors, and photocatalysts [113]–[117].

GaN is a semiconductor material that is widely used for optoelectronic devices such as LEDs and laser diodes due to its wide direct band-gap. The band-gap allows for the efficient emission of blue and near UV light [118]–[122]. GaN has a wurtzite crystal structure, which consists of covalent bonds in all three dimensions (**Figure 1-5**).

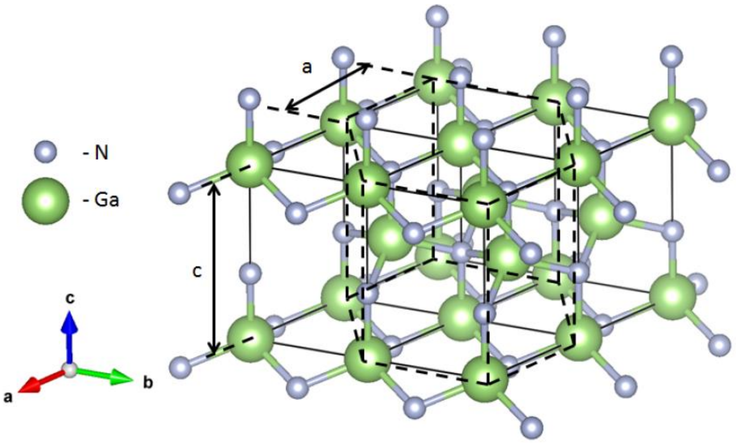

Figure 1-5 Ball and stick model of GaN crystal structure with lattice constants a and c. The green balls represent Ga atoms and grey balls represent N atoms. The hexagonal unit cell is represented by dotted lines [123].

There are different traditional techniques available for depositing thin films of GaN. Among these techniques, the most widely used are based on elemental epitaxial or chemical vapor deposition processes, which have been discussed in previous studies [124]–[130].Although elemental epitaxial methods enable the precise formation of ultra-thin films, they can be expensive. On the other hand, chemical vapor deposition (CVD) methods are less expensive but are not suitable for creating thin films with a thickness of only a few unit cells due to their inherently non-uniform nucleation.

Until recently, there have been no reported methods capable of synthesizing 2D GaN nanosheets that are only a few nanometers thick, which remains a significant technological challenge. Therefore, there is a great deal of interest in creating large-area 2D GaN. Recently, Balushi et al. successfully synthesized 2D GaN using a migration-enhanced encapsulation technique [131], and for the first time confirmed that the atomic layer GaN is a wurtzite structure . However, this technique does not produce 2D GaN films with lateral dimensions that exceed a few hundred nanometers. Additionally, the resulting 2D nanosheets are encapsulated between conductive graphene sheets, which impedes their use in devices. Therefore, a more scalable synthesis method is necessary to obtain large-area 2D GaN and fully explore the capabilities predicted through computational methods for practical applications.

1.4 Liquid metals for the synthesis of 2D materials

1.4.1 Key Attributes of bulk liquid metals

Liquid metals refer to metals and alloys that remain in a liquid state near room temperature, exhibiting both metallic and fluidic properties. Elemental liquid metals such mercury (Hg), gallium (Ga), rubidium (Rb), and cesium (Cs) remain in a liquid phase, along with liquid metal alloys that have even lower melting points. The variety of liquid metals and their corresponding melting points are summarized in **Table 1-1**.

Table 1-1 Melting points and major drawbacks of near-room-temperature liquid metals [132]

Liquid metals	**Ga**	**EGaIn**	**Galinstan**	**Hg**	**Rb**	**Cs**	**Fr**	**NaK-77**
Melting point (°C)	29.8	15.7	10.6	-38.8	39.5	28.4	27	-12.6
Major drawback	-	-	-	toxic	reactive	reactive	reactive	reactive

While mercury has historically been widely used, its toxicity has restricted its commercial use since the 1990s [133]. Gallium and gallium-based alloys have emerged as alternatives, offering remarkable properties for various applications(Stretchable wires[134],Soft electrodes [135] and Antennas [136]) in the past three decades [137].

Among the group of liquid metals, gallium has unique properties that make it attractive for a variety of applications that list in the following. Gallium has a very low melting point (~29.6 °C) compared to other post transition metals, which makes it liquid at room temperature.

This property makes it useful in applications such as soft robotics and flexible electronics. Gallium also has low toxicity and low vapour pressure, making it safer to handle than other metals. Gallium persists in its liquid state from near room temperature to 2400°C [138]. The crystal structure of gallium features covalent dimers of gallium atoms [139] that are organized in an orthorhombic structure with a short bond length of 2.44 Å within the dimers [89]. An interatomic distance of 2.71 to 2.79 Å is observed between the gallium dimers (**Figure 1-6**) [89]. The anisotropic nature of the gallium crystal structure has been harnessed in the development of liquid metal-based microfluidic devices, which can be used in a variety of applications such as drug delivery, chemical analysis, and microreactors. Gallium-based liquid metals have also been utilized in the field of 3D printing, as they can be easily printed and offer a high degree of flexibility and stretchability in the printed structures [29], [140]. Furthermore, the unique properties of gallium-based liquid metals have enabled the development of reconfigurable devices and optics, as well as reversible electrochemical systems for energy storage and conversion [29], [141], [142].

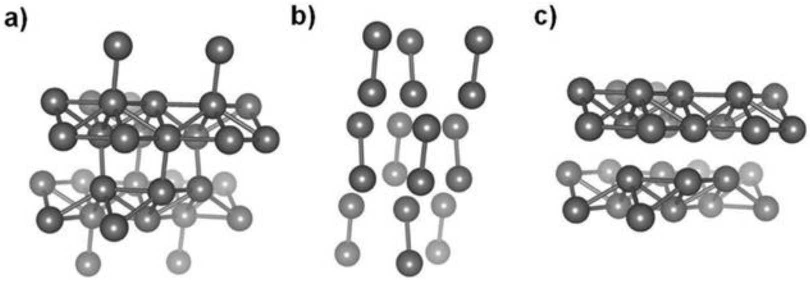

Figure 1-6 (a) Crystal structure of α-Ga (b) crystal structure of a-Ga showing only short bonds d < 2.5 Å, (c) crystal structure of α -Ga showing only the long bonds 2.5 Å<d<3 Å [18], [78].

Gallium has a low bulk viscosity (approximately twice that of water) [143]. In addition, it has essentially no vapor pressure. It can consequently be handled as a liquid in ultra-high vacuum chambers. There is also no danger of inhalation in a laboratory environment or in an application space. It has metallic conductivity that is an order of magnitude lower than copper, but orders of magnitude larger than other liquids such as salt water. Its conductivity in the liquid state is larger than the solid state [144].

An oxide layer forms on the surface of liquid gallium in any oxygen-containing environment [141]. The formation of the oxide layer is a self-limiting reaction, which means that it stops once a certain thickness is reached. This helps to ensure that the oxide layer remains thin and does not interfere with the properties of the liquid gallium. This thin yet robust oxide layer helps preserve the liquid gallium against deformation. Initially, the oxide layer was considered a problem because of its adhesive nature, making gallium difficult to use in fluidic applications

[145]. However, in recent years, the oxide layer has become the subject of interest because it provides opportunities to develop 2D materials (refer to section 1.4.2).

1.4.2 Surface Properties of liquid metal

1.4.2.1 Surface tension

Liquid metals differ from other liquids as they possess metallic bonding within their bulk phase. This bonding is characterized by highly dispersed valence electrons, which determine the electronic properties of molten metals [146], [147]. Upon losing valence electrons, metal ions form without any ordered arrangement, unlike the structured atomic arrangements seen in solid metals. To maintain local charge neutrality, strong coulombic forces exist between the ions and electrons, allowing both to remain fluid. These coulombic forces result in a well-defined boundary on the surface of liquid metals, preventing the formation of isolated particles like free ions or electrons [147], [148]. The surface of liquid metals is generally atomically flat due to their high surface tension, making them ideal for creating ultrathin 2D materials. To enhance the physical and chemical properties of the alloy mixture and explore more materials, one can alloy two or more liquid metal elements synergistically. When producing alloys, the solubility of metal is exponentially dependent on temperature in the dilute solution regime, which depends on various material properties like the atomic diameter, crystal structures, valency, and electronegativity. To produce alloys, these properties should be as similar as possible for the constituent metals [149].

Liquid metals are characterized by their high surface tension, which can be determined by calculating the difference between their heat of evaporation and total pairwise atomic interactions within the bulk or through modeling atomic interactions [150]–[152]. Contact angle measurements between a droplet and a surface can be performed [142], [153] via pendant drop methods [154], [155] and can also be modulated through electrochemical methods [156]. Nevertheless, measuring contact angle of liquid metal droplets with non-reactive surfaces results in underestimation due to oxide layer formation in air [157]. The formation of an oxide layer leads to lower apparent surface tension and higher wetting ability, indicating significant interactions between surface oxides and solid interfaces. This fact presents the possibility of selective transfer of surface oxides onto different substrates and directly to devices.

Surface layering may also occur in liquid alloys, which reduces surface tension and causes the metal with the lower surface tension to dominate the interface. This surface layering is limited to a few atomic diameter on the surface [148], [158] Surface layering occurs on molten alloys as a response to the abrupt termination of the metallic phase and serves to reduce surface tension, causing the metal with the lower surface tension to dominate the interface [159]. Binary alloys like Eutectic Gallium–Indium (EGaIn) exhibit this phenomenon, and in situ sputtering in a vacuum caused the top surface to become significantly indium enriched, even though indium is the minority component [145], [160]. Gallium oxide forms on the surface of EGaIn due to its more favorable Gibbs free energy of oxide formation, suggesting that adding metallic solutes to molten metal can modify interfacial layering and surface oxide composition [10][161].

1.4.2.2 Surface Oxidation

The presence of ambient atmosphere or other oxygen-containing environments leads to the spontaneous formation of surface oxides on liquid metals(**Figure 1-7**(a)) [10], [145], [162]. At low to moderate temperatures, the growth of surface oxides is self-limiting and can be explained by the Cabrera-Mott process [163]. According to the Cabrera-Mott theory, the initial growth kinetics are rapid and result in the formation of a few monolayers of oxide almost immediately upon exposure to molecular oxygen. As electrons from the metallic bulk ionize surface-adsorbed oxygen through a tunneling process, an electric field gradient is created across the oxide layer(**Figure 1-7** (b)) [164]. This electric field, known as the Mott field, drives ion migration into the oxide layer and promotes growth. As the oxide layer becomes thicker, the field strength decreases, leading to the self-termination of the process and a final oxide thickness of a few nanometers. The thickness and oxidation kinetics of the oxide can be controlled by decreasing the oxygen partial pressure or through surface functionalization [165], [166]. Due to the weak interfacial force between the oxide skin and its parent liquid metal, this surface oxide can be easily isolated and utilized for its naturally occurring ultrathin interfacial compounds [167]. Like aluminium, gallium rapidly forms a thin oxide layer on its surface when exposed to ambient oxygen [168]. This oxide layer is thin (~0.7 nm according to X-ray diffraction studies done under vacuum conditions [169], although it is likely thicker under laboratory conditions [170], [171]) and does not grow significantly thicker over time in dry air in the absence of a driving force or physical perturbation [171], [172]. It forms on alloys of gallium as long as the concentration of oxygen is greater than a few ppm [173] and forms almost instantly in air at ambient conditions. Importantly, the oxide skin mechanically stabilizes gallium, enabling the formation of nonequilibrium shapes [145], [174]. Typically, a liquid with low viscosity and high interfacial tension will form into spherical droplets to minimize interfacial tension.

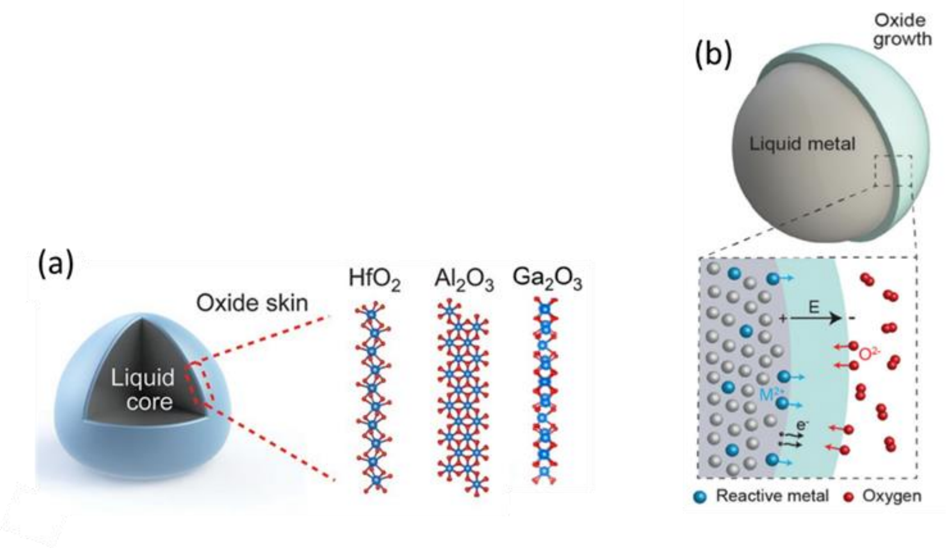

Figure 1-7 (a) A cross-sectional diagram of a liquid metal droplet, with possible crystal structures of thin layers of HfO_2, Al_2O_3,and Ga_2O_3 as indicated [10], [162]. (b) Cabrera–Mott oxidation occurs at the surface of liquid metals in the presence of oxygen. Electrons from the metal tunnel through the growing oxide shell, resulting in a self-generated electric field called the Mott field. This field promotes the diffusion of metal and oxygen ions into the oxide shell, leading to oxide growth. As the oxide becomes thicker, the field strength reduces until ion diffusion ceases [164].

Studies using synchrotron-based techniques have shown that the electron density profile of liquid gallium features a minimum at the interface between the liquid metal and its naturally grown surface oxide, as depicted in **Figure 1-8**. This simple electron density model, proposed by Regan et al. [169], has been utilized to explore the oxidation of liquid gallium surfaces. The model indicates that the liquid/oxide and oxide/vacuum interfaces are atomically flat with a significant loss of electron density at the liquid core and oxide interface. This finding suggests that the interaction between the liquid metal and the surface oxide is weak. Moreover, the absence of a solid crystal structure inhibits cumulative atomic interactions, preventing macroscopic attachment [11], [175]. Therefore, the interfacial 2D oxide skin shows minimal adhesion to the metallic core, providing a unique route for synthesizing and exfoliating various 2D materials[10]. A minimum in the electron density distribution at the interface between the liquid Ga surface and its oxide indicates the absence of covalent bonds. Additionally, the nonpolar nature of liquid metals limits non-covalent interactions. These two factors result in weak attachment of native surface oxides to their molten parent metal [176].

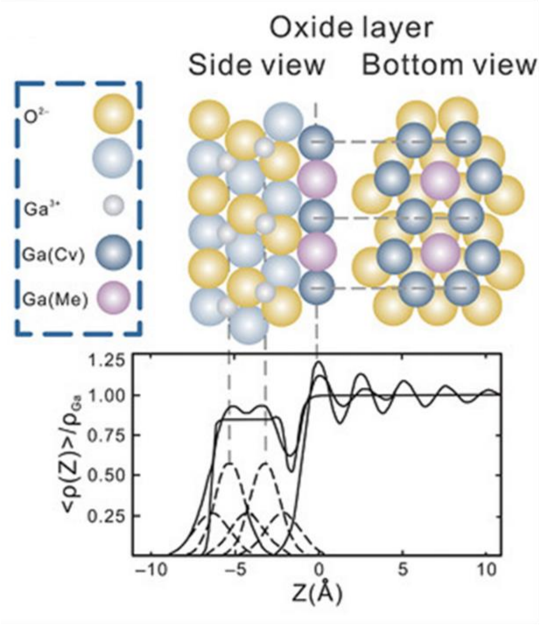

Figure 1-8 Schematic of the surface oxide of Ga, with the electron density profile plotted for the interface. Top: the projected atomic structure of gallium and gallium oxide layer where the atomic diameters for O2- , Ga3+, covalent (Cv) Ga and metal (Me) Ga is 2.64 Å, 1.24 Å , 2.44 Å and 2.50 Å, respectively. Bottom: the thin solid line represents the corresponding electron density profile with its different components; the underlying liquid Ga (large dash line) and the Gaussians representing the Ga3+ (dash-dotted line) and O2- layers(short-dashed line) [176].

1.4.3 2D material synthesis from liquid metals

As discussed in the previous section (1.4.1), the unique properties of liquid metals, such as their solubility, chemical reactivity, and weak interface force, make them an attractive option for the fabrication of 2D metal oxides. The interfacial oxide layers that develop naturally on liquid metals, such as gallium and gallium-based alloys, are considered high-quality 2D films. These skins can be easily delaminated, offering opportunities for the synthesis of various 2D metal oxides [177]. The interfacial oxide skin can be effectively delaminated because of the weak attractive force between the parent liquid metal and the surface oxide skin [10].

There are various liquid metal-based techniques for isolating 2D metal oxides , including printing (touch [10], squeeze [178], [179] or blade print [30], [180]–[184] techniques), liquid phase growth and exfoliation (including sonication [185] and bubbling [10], [186], [187] methods), and surface templated growth of materials on liquid metal surfaces [188], [189].

These methods are fast, substrate-independent, and can produce large-area 2D materials. The resulting 2D materials are ultra-thin (<5nm) with high homogeneity in thickness and are laterally large (centimeter scale), making them ideal alternatives to established epitaxial approaches [190], and mechanical exfoliation [191]. Additionally, the smooth surface of the liquid metal allows for the synthesis of low-defect materials. Liquid metals offer a unique synthesis route for fabricating a wide range of 2D metal oxides and other 2D materials that would otherwise be impossible to synthesize. The video below is showing the different deposition techniques in details (Scan QR code).

Video 1. Different deposition techniques of 2D semiconductors from molten metal (published at [164])

1.4.3.1 Applications of 2D materials synthesized from liquid metals

The use of liquid metal-based techniques to synthesize 2D materials is becoming increasingly popular. By utilizing these new synthesis methods, 2D materials derived from liquid metals can easily access various devices and applications that would be difficult to achieve through conventional means. These materials are ultrathin (<10 nm [178], [179], [187], [192]–[195]), laterally large (centimetre scale [178], [179], [192], [194] compared to some materials produced using conventional methods[30]), and highly mechanically robust [179], [192]. With this technique, materials that were previously difficult to produce in a stable 2D form can now be achieved [178], [179], [187], [192]–[195], including semiconductors, van der Waals heterostructures, transparent conductive oxides, and other 2D metal oxides. These materials have been used in various devices, such as transistors and transistor components [30], [187], photodetectors [195], [196], ITO capacitive touch screens [179], piezoelectric nanogenerators [192], photocatalysts [185], [188], and gas sensors [187], [195], [197]. A summary of their properties is provided in **Table 1-2** [161]. Two-dimensional metal oxides and other 2D materials derived from liquid metals are extremely versatile and are increasingly utilised in a wide array of applications. For example, 2D metal oxides derived from liquid metals have been used for water filtration, the creation of dielectric materials [10], [187] and optoelectronic heterostructures [196], [198]. A 2D SnO-based lateral memristor was recently demonstrated using an adapted touch- printing method involving liquid Sn [199]. A 2D-SnO_2 memtransistor that could be utilised in neuromorphic computing was also recently fabricated via a touch-printing method [200]. Another work reported the isolation of SnOx nanosheets through a bubbling synthesis, which was then utilised for electrocatalytic CO_2 reduction [201].

Eventually, two-dimensional materials, including 2D metal oxides ,have been exploited into a broad range of applications, such as biosensors, drug delivery, bio-imaging, dye-sensitized solar cells, and photodetectors, among others [202]. Additionally, future applications may arise in fields where liquid metals are already used, including the design of tunnel junctions [203]–[205], soft electronics [206]–[209], reverse electrowetting [210][211], and liquid metal based catalysis [146]. In all these applications, the control of the surface oxide atop a liquid metal can be beneficial for tuning reactivity, contact properties, electric resistances, and the fluidic nature of the underlying metal. Furthermore, 2D metal oxides are expected to contribute to the burgeoning fields of van der Waals (vdW) heterostructures, optoelectronics, spintronics as well as the development of future wearable and transparent electronics[212].

Table 1-2 Devices prepared using various liquid metal printing techniques including touch and squeeze printing, air injection, and two-step conversion methods where CVD (ammonolysis or sulphurisation) is used to convert from a 2D metal oxides to other 2D materials (nitrides and sulphides) *e^- mobilities. ^ on/off ratio of ~170 for phototransistors (with a responsivity 0f 6.4 AW-1). † Layer 1: 1nm, layer 2: 4.5nm. [161]

Electronic devices

Device	Material	Synthesis method	Thickness (nm)	Band gap (eV)	Mobilities ($cm^2V^{-1}s^{-1}$)	On/off ratio	Optical transparency (%)	Sheet resistance ($k\Omega^{-1}$)	Ref
Touch screen	Bilayer ITO	Squeeze	1.5	3.9	14	-	99.3	5.4	[212]
FET	In_2S_3	Touch+CVD	3.7	2.3	58	10^4	-	-	[194]
FET+ phototransistor	GaS	Screen print+CVD	1.5 (bilayer)	3.02	0.2	~150	-	-	[30]
Hall device	GaN	Squeeze+CVD	1.3	3.5	21.5	-	-	-	[213]
FET	GaN	Surface-confined nitridation	4.1	-	160	10^6	-	-	[214]

Photodetector devices

Device	Material	Synthesis method	Thickness (nm)	Band gap (eV)	Photodetectivity (Jones)	Response time (μs)	Responsivity (AW^{-1})	Ref
Two-terminal	Bi_2O_3	Touch	0.75	3.5	$1.1x10^{13}$	~70	400	[215]
UV	SnO/In_2O_3	Layered touch	5.5	2.3	$5x10^{9}$	<1000	1047	[196]

Gas sensors

Device	Material	Synthesis method	Thickness (nm)	Band gap (eV)	Gas response factor (%)	Response/recovery time (s)	Ref
Two-terminal	Ga_2S_3	Squeez+CVD	2	2.1	50%(107ppmNO_2)	108/1800	[195]
UV	SnO/In_2O_3	Layered touch	5.5	2.3	$5x10^{9}$	<1000	[195]

Piezoelectric devices

Device	Material	Synthesis method	Thickness (nm)	Band gap (eV)	Motilities ($cm^2V^{-1}s^{-1}$)	Piezoelectric coefficient (pmV^{-1})	Peak output (mV)	Ref
Hall device+piezo-electric nanogenerator	SnS	Touch (anoxic conditions)	0.7	1.4	35	26.1±0.3	~150(0.7% strain)	[192]

1.5 2D materials for integrated Optics

Utilizing semiconductor technology, integrated photonics can condense fiber or free-space optical circuits into on-chip photonic devices, leading to optical systems with reduced energy consumption, size, and cost. This cutting-edge technology has garnered attention for its potential in communication, sensing, imaging, and other fields. Over the past decade, therefore, corresponding optoelectronic devices in integrated photonic systems based on Si, Ge, glass, $LiNbO_3$, and III–V semiconductors (such as GaAs, InP, InGaAs) including Lasers[216]–[218], couplers [219]–[221], waveguides [222]–[225], modulators [226]–[228] and photodetectors [229]–[231] have been systematically explored and continuously optimized. Heterogeneously integrated III-V/ silicon photonics has been successfully commercialized and currently serves as the backbone of communication technology [232]–[235]. As integration technology continues to advance rapidly, the performance of individual basic unit devices is approaching its fundamental limits. This presents a significant challenge in developing novel device architectures and operational mechanisms to enhance the capabilities of device components using the current optoelectronic materials platform. Additionally, the intrinsic limitations of silicon in terms of light emission and nonlinear optical properties necessitate the use of alternative materials with complementary properties. In this regard, two dimensional materials have gained attention in integrated photonics since the discovery of graphene in 2004. These materials offer new properties that can complement silicon photonics to enhance their performance [24], [236], [237], as will be discussed in the section 1.5.2.

1.5.1 Integration strategies of 2D materials in optoelectronic devices

The integration process of 2D materials severely impacts the performance of the resulting optoelectronic devices based on the materials. Therefore, the synthesis of 2D materials and their integration into device applications are closely intertwined processes that are essential for advancing the field of 2D materials and developing high-performance devices. In this context, Jia, Linnan, et al.[238] divided the integration process into two main groups: material synthesis and on-chip transfer. (**Figure 1-9**).

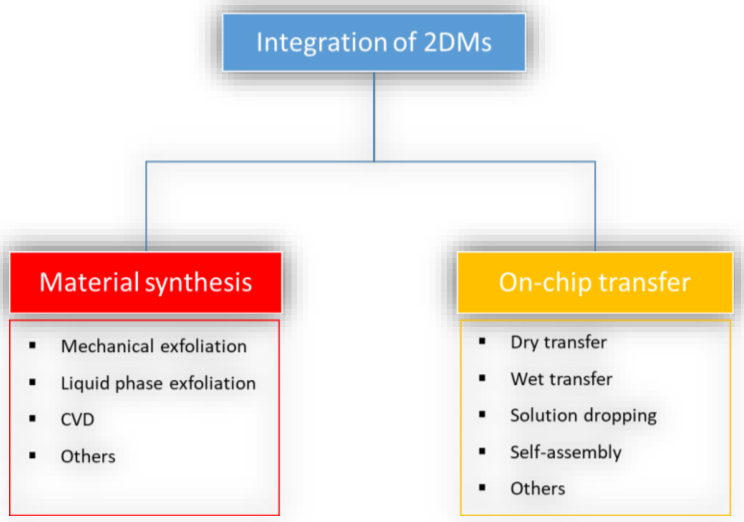

Figure 1-9 Integration fabrication techniques for 2D materials (Reproduced from [238])

Based on the synthesis method for 2D materials, as discussed in Section 1.2, there are several strategies available for transferring these materials onto chip-based devices, each with its own potential advantages and considerations .As shown in **Figure 1-9**, material synthesis includes Mechanical exfoliation, Liquid phase exfoliation, CVD, and Others (e.g., Molecular beam epitaxy (MBE)). Subsequently, for transfer of the fabricated material on the chip, dry transfer, wet transfer, solution dropping, self-assembly, and other techniques (e.g., Polydimethylsiloxane (PDMS) stamp) can be used. A comparison of different transfer techniques is shown in **Table 1-3**[350].

Table 1-3 Comparison of on-chip transfer techniques of 2D materials (CVD, chemical vapor deposition; PDMS, polydimethylsiloxane; PMMA, poly (methyl methacrylate)). (Reproduced from[239])

Technique	sample	Medium	Coating area	Uniformity	Yield	Refs
Dry transfer	Exfoliated flakes	PDMS	Small	High	Low	[240][241]
Semidry transfer	CVD-grown flakes	PDMS/Sacrificial polymer	Moderate	Moderate	Low	[242][243][241]
Wet transfer	CVD-grown films	PMMA	Large	Low	High	[244][245]
Solution dropping	Nanosheet dispersion	-	Large	Low	High	[246][247][248]
Self-assembly	Nanosheet dispersion	-	Large	Moderate	Moderate	[249][250]
Direct growth	-	-	Large	High	Moderate	[251][252]

Achieving large-area coating over complex device structures with high film uniformity is a critical requirement for practical device fabrication. **Table 1-3** outlines several techniques that can achieve large-area coating, with the exception of dry transfer approaches. The latter have limitations due to the relatively small lateral size of exfoliated 2D flakes, which restricts the coating area. The use of wet transfer and solution-dropping methods leads to poor film uniformity due to the occurrence of imperfections like wrinkling, voids, and layer overlap that are introduced during the transfer process. On the other hand, the different fabrication techniques mentioned in **Figure 1-9** have their difficulties for the fabrication of some 2D materials ; hence, developing new fabrication techniques for these 2D materials, wherein integration and synthesis could be readily achieved, would greatly facilitate the development of hybrid 2D material optoelectronics devices.

Liquid metal-based synthesis methods offer an alternative platform to assemble 2D materials as well as integrate them into useful devices. By way of example, a 2D SnO/In_2O_3 vdW heterostructure photodetector was successfully developed through the liquid metal touch printing method. Therefore, the direct integration of 2D materials onto devices offers the possibility of developing novel and high-performance electronic and optoelectronic devices (This will be the subject of Chapter 4:).

1.5.2 Applications of 2D materials in photonics

Emerging integrated photonic applications such as flexible photonics [253]–[255], mid-infrared (MIR) photonics [256][257], terahertz technology [258]–[260], quantum optics [261]–[263], microwave photonics [264]–[266], etc. all highlight the need for new functionalities and tailored material properties, as well as compatibility with nanofabrication processing technologies (**Figure 1-10**).

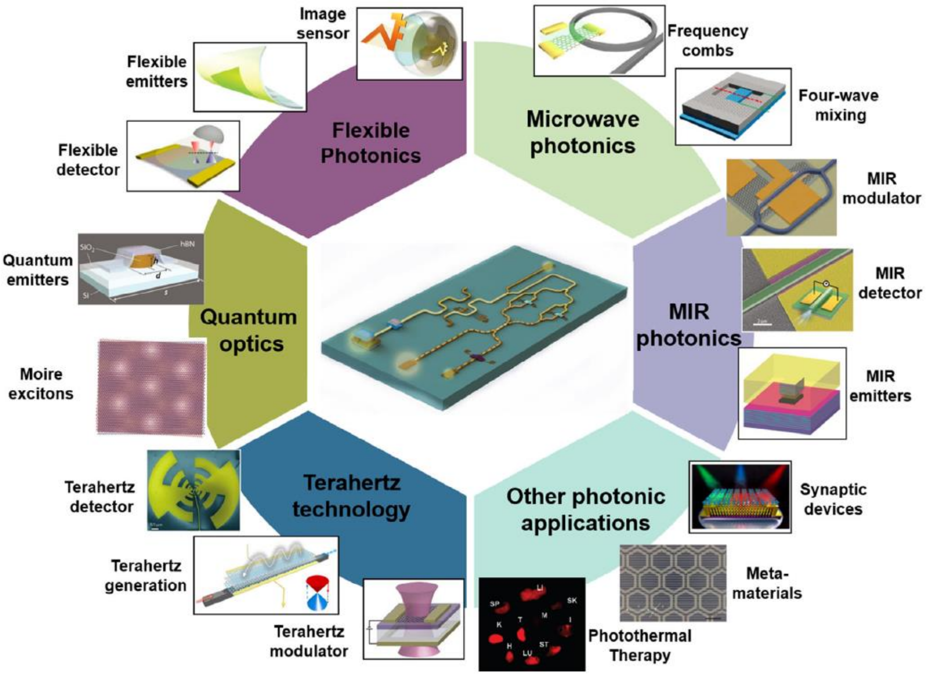

Figure 1-10 Some emerging photonic applications based on 2DMs have been demonstrated, including flexible photonics [flexible emitter, flexible detector, and image sensor], MIR photonics [MIR emitter, MIR modulator, and MIR detector], terahertz technology [terahertz generation, terahertz modulator, and terahertz detector], microwave [frequency combs, and four-wave mixing], quantum optics [quantum emitter and moire exciton], and other photonic applications [synaptic devices, metamaterials, and photothermal therapy][267].

Resorting to the integration of 2D materials on silicon-based photonic devices and circuits can fill many of those needs, and greatly enhance devices performance (e.g., increasing light absorption or emission efficiency [268][269]), provide mechanisms to tune device characteristics (e.g., laser emission wavelength), as well as enable new functionalities (e.g., frequency doubling [270], enhancement four-wave mixing (FWM) or self-phase modulation (SPM) [271][272], or broadband light emission [273]). (

Figure 1-11)

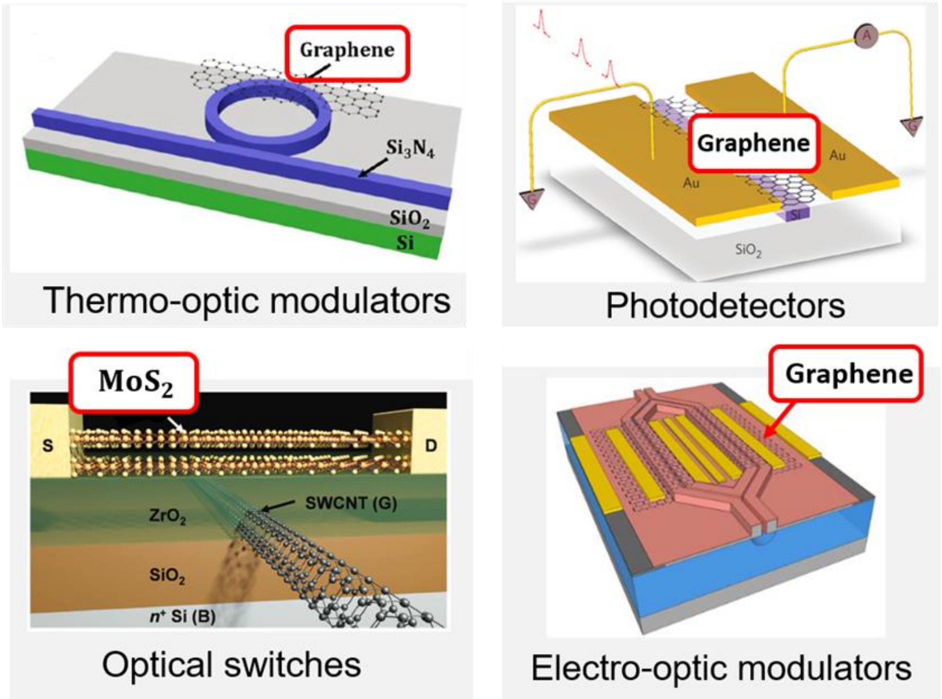
Thermo-optic modulators

Photodetectors

Optical switches

Electro-optic modulators

Figure 1-11 Integration of 2D materials on photonic devices (Reproduced from [274][24][275][276])

Certain 2D materials possess zero or near-zero bandgaps, such as BP, $PtSe_2$, and graphene, and are particularly promising for applications in the mid-infrared (MIR) [277]–[280], such as thermal imaging, infrared homing, and spectroscopic sensing [281]. A wide gamut of MIR devices, such as mode-locked pulses [282], modulators, and photodetectors [283], have already been developed using 2D materials. Additionally, graphene, which has zero bandgap, appears as a prime candidate for supporting terahertz technology, which is essential for noninvasive and nondestructive sensing. Notably, a number of representative devices have been fabricated that demonstrate the generation [284][285], modulation [286] and detection [287] of terahertz signal based on graphene.

Quantum emitters based on 2D materials [288], Moiré excitons in van der Waals' heterojunctions of two dimensional materials [289][290], and gate-tunable frequency combs based on graphene/Si_3N_4 microresonator [291] have been realized, which bring about a new possibility for quantum optics.Furthermore, despite being atomically thin, many 2D materials show large light absorption over a broad wavelength range [292][293], which is partially due to the strong quantum confinement in the direction perpendicular to the 2D plane.

Some 2D materials also exhibit ultra-high carrier mobility at room temperature [294],[295], which can greatly enhance the response time of photodetectors and modulators [236][296], but also enable novel physical phenomena. For example, bilayer graphene with magic-angle super lattices can work as both a superconductor and an insulator at a different angle [297][298].

Last but not least, the strong optical response of two dimensional materials is another advantage [299]–[301], and nonlinear properties of two dimensional materials including ultrafast non-linear absorption [302]–[304], thermo–optic (TO) nonlinearities [305], second-harmonic generation (SHG) [306]–[308], and third-order non-linear optical response [309][310] have been observed, which are important for next-generation nonlinear photonic circuits.

1.5.3 2D materials for integrated nonlinear optics

As already alluded to in the introduction of this thesis, chip-based nonlinear optics could underpin new architectures for all-optical signal processing in future communication networks. In this context, the nonlinear optical (NLO) properties of various 2D materials have been experimentally investigated. These can be orders of magnitude stronger than for conventional bulk materials [311] because of the unique physical properties arising from their unusual electronic band structures. Integrating these materials into a scalable and silicon-compatible platform could provide a pathway towards realizing low-power nonlinear optical devices, such as cavity integrated nonlinear 2D material devices [312]. Hence, rapidly growing interests have been attracted to various NLO properties of 2D materials. We can divide the nonlinear optical process into three main categories. First, coherent optical parametric processes, such as second harmonic generation (SHG), third-harmonic generation (THG) and four- wave mixing (FWM). For example, graphene and graphene oxide generates strong THG and FWM signals, whereas MoS_2 has unique SHG property that reflects its crystal symmetry in mono and few-layered samples. Second, nonlinear dissipative processes, including transient absorption (TA), two-photon absorption (TPA) and saturable absorption (SA) that pump electrons into the excited state[271], [272], [313], [314]. In particular, TA could be used to learn the transient dynamics of excited photo-carriers through a pump-probe based method and reveal ultrafast electron-electron or electron-phonon interactions. Third, incoherent photon up-conversion processes, such as two-photon fluorescence of MoS_2, and nonlinear photoluminescence of graphene. Taking graphene as an example, it possesses several relevant properties for nonlinear optics, including, beside a substantial nonlinear optical response, ultrafast photoexcitation dynamics, and significant thermal and optical threshold damage [315][316]. While graphene has received much attention, its intrinsic linear absorption makes it challenging for practical devices applications[314][313]. Graphene oxide represents a better trade-off with a large nonlinear optical response and a two orders of magnitude lower absorption[271][272]; it has been exploited in hybrid waveguides for enhanced FWM, SPM and parametric amplification. More generally, other 2D materials might be better suited for these nonlinear applications, motivating the development of new 2D materials, as intended in this thesis. Ideally, these materials should present a strong nonlinear optical response and a modest absorption, while being compatible with planar optical devices. Understanding their behavior and performance in this sense is crucial for developing next-generation photonic devices.

1.5.3.1 Gallium nitride: an attractive material for nonlinear optics

Group III-nitrides, specially GaN, owing to its optical properties and wide transmission ranges, are strong candidates for nonlinear optical applications [317]. GaN has a combined transparency range of LiNbO3 and GaAs (365nm to 13.6μm), and therefore this material has a potential of generating wavelengths in either far-Infrared (IR) or near-UV by sum-frequency generation (SFG) or difference frequency generation (DFG) [318]. Additionally, thanks to its non-centrosymmetric crystal structure, GaN possesses both $\chi(3)$ and $\chi(2)$ nonlinearities, which makes it appealing for electrically tuned chip-based photonic applications as well as second-harmonic generation (SHG).

Moreover, GaN possesses a wide transparency window ranging from ultraviolet to mid-infrared due to its large bandgap of 3.4 eV. This property ensures that GaN does not exhibit two-photon absorption (2PA) or three-photon absorption (3PA) at telecommunications wavelengths. Consequently, GaN waveguides hold significant potential for all-optical nonlinear signal processing applications. In addition, the refractive index of GaN at telecom wavelengths is approximately 2.3. The GaN-on-insulator (GaNOI) platform, which offers a high refractive index contrast of around 0.6, is particularly advantageous for all-optical signal processing applications at telecom wavelengths. The nonlinear refractive index of GaN films at telecom wavelengths is $n_2 \approx 10^{-18} m^2 W^{-1}$ [319][320], which is about an order of magnitude larger than that of conventional platforms, such as Si_3N_4 [321][322], AlN[323][324], and $LiNbO_3$[325][326]. These unique properties make GaNOI platform attractive for compact chip-scale nonlinear photonic applications, such as frequency conversion, supercontinuum, and frequency comb generation. SH of thin films of GaN was investigated by J. Miragliotta et al. They showed that for thin films with thickness ranging from 0.74 to 5.3 µm, the SH transmission dependence on incident angle and film thickness permitted a determination of the film orientation and the coherence length [327]. E. Fazio et al.[328], performed eclipsing Z-scan analysis of GaN thin films at 800 nm, in order to escape any two-photon absorption at this wavelength and monitor a pure refractive (Kerr) nonlinearity. They have measured the third- order nonlinearities of GaN 302nm thick films in the near IR spectral region while no absorptive nonlinearity (TPA) was observed. Accordingly, efficient refractive Kerr nonlinearity was recorded $n_2 = -(7.3 \pm 0.4) \times 10^{-14} cm^2 W^{-1}$.

Various strategies can be combined to leverage the nonlinear optical properties of GaN for chip-based photonic devices. Air-suspended GaN waveguides and photonic crystal membranes have been successfully fabricated [329]. Moreover, there has been recent success in reducing propagation loss in GaN waveguides. GaN waveguides with the propagation loss coefficients as low as 0.65dB/cm at 1550nm, 1dB/cm at 1550nm, and 2dB/cm at 700nm have been realized [330]–[332]. High-Q-factor microring resonators (MRR) based on GaN have been demonstrated in [333][319] a quality factor exceeding 5×10^4 in the near-infrared, infrared, and visible wavelength ranges [333], and a quality factor of 1×10^5 at the Telecom wavelength range [319]have been reported. Munk, Dvir, et al. [320] demonstrated a low-loss GaN ridge waveguide, enabling four-wave mixing at telecommunication wavelengths. Comparatively high nonlinear propagation parameters were observed, which confirm the potential of highly nonlinear GaN waveguides for all-optical signal processing applications.

Nonlinear integrated photonics based on III-nitrides is still in its early stages of development due to the challenges associated with defect mitigation and the lack of a native substrate. **Table 1-4** includes results from only a small number of studies that have reported on the measurement of the second and third-order nonlinear optical coefficients in GaN waveguides. These results are presented alongside measurements of nonlinear coefficients in bulk materials. As shown in **Table 1-4**, most of the studies on the GaN nonlinearity are related to the bulk material. Hence, the nonlinear properties of this material in the two dimension remained unknown. Yet, considering the GaN bulk and thin film nonlinear properties, we anticipate having a nonlinear response for lower-dimension films as well. Therefore, among the various 2D materials accessible by the liquid metal chemistry presented in section 1.4, and besides the suitable properties of GaN already discussed in section 1.3.2, this quick overview of GaN for nonlinear optics led me to focus my PhD studies on 2D GaN, which appears as a relevant candidate for both linear and nonlinear photonic applications.

Table 1-4 Nonlinear optical properties of GaN (Reproduced from [334])

Form	Wavelength (nm)	$\chi^{(2)}$,d (pm/V)	n_2 ($10^{-14}cm/W^{-1}$)	a_2 (cm/GW)	γ (m^{-1}/W^{-1})	Technique	Ref
WG	1560	16($\chi^{(2)}$)	-	-	-	SHG	[318]
Bulk	1064	-16.5(d_{33})	-	-	-	SHG	[335]
Bulk	1064	8.2(d_{31})	-	-	-	SHG	[335]
Bulk	1064	8.0(d_{15})	-	-	-	SHG	[335]
WG	1550	-	3.4	-	1.6	FWM	[320]
MRR	1450 to 1650	-	1.4(1550)	-	-	DKS	[317]
WG	1550	-	1.1	-	7.3	FWM	[319]
Bulk	377 to 720	-	-	16(400)	-	PPT	[336]
Bulk	724	-	-	0.9	-	ZS	[337]

WG-waveguide, MRR-microring resonator
SHG-second harmonic generation, FWM-four wave mixing, DKS-dissipative Kerr soliton, PPT-pump probe technique, ZS-Z scan

1.6 Conclusion

The field of 2D materials research has been considered one of the most active and dynamic research areas in nanoscience these last few years, due to its exciting properties suitable for several applications. Despite the potential benefits of 2D nanosheets, there are several challenges to synthesizing them in an ultra-thin, large-area form on desired substrates. These limitations have thus far hindered their widespread use for industrial applications. For this, new synthetic approaches must be explored to empower the scalable deposition of wafer-scale 2D nanosheets while maintaining the features associated with their ultra-thin nature. In this chapter, I introduced the Liquid metal chemistry method, which has shown some potential for synthesizing a wide range of 2D materials, including Ga_2O_3 and GaN, which are at the center of my PhD work. The liquid metal chemistry method has quickly provided large areas, high crystalline quality, and uniform 2D materials. Moreover, with this approach the synthesis of

2D materials and their transfer to device are done within the same step. However, it is still in its infancy, requiring further research while offering significant potential for future discoveries. Moreover, this technique shall provide an easy path for the direct transfer of 2D materials into device applications compared to traditional methods.

In addition, understanding the behavior of integrated 2D materials on the device and their performance is crucial for developing next-generation photonic devices. In this context, different properties of 2D material have been investigated. In the quest to discover new materials with nonlinear properties to complement silicon photonics for all-optical signal applications, we selected gallium oxide and gallium nitride as promising candidates. In particular, bulk and thin-film GaN have already demonstrated relevant nonlinear optical properties, which have been recently exploited in chip-based nonlinear devices. Currently, there is a paucity of research on the nonlinear properties of Ga_2O_3, highlighting a need for further exploration in this area. As such 2D GaN, which is compatible with the liquid metal chemistry, and its Ga_2O_3 precursor, will form the main focus of my PhD thesis. Developing photonic devices with such 2D materials that can be selectively deposited to functionalize an otherwise passive photonic circuit has been the main goal of my PhD work. The first technological challenge to address is the development of a process exploiting the liquid metal chemistry to synthesize high quality Ga_2O_3 and GaN 2D materials that are readily compatible with integrated optics. This will be the subject of chapter 2 and 3, which will subsequently describe the fabrication/ characterization tools and the associated results of the synthesis of such 2D materials. I leave the integration of these 2D materials into chip-based photonic devices to chapter 4. These last efforts demonstrate the compatibility of this new synthesis approach with integrated optics, and although I could not go as far as a nonlinear optical demonstration, my efforts still provide new pathways for photonic applications using hybrid material platforms.

Chapter 2: Fabrication and Characterization Methods of 2D Materials

The focal point of this chapter is to establish a novel synthesis approach for 2D materials, specifically Ga_2O_3 and GaN that embodies the following attributes:

- Generic and cost-effectiveness.
- Favorable for integration with chip-based optical devices.
- Independent of the host substrate.

This chapter unfolds the innovative synthesis technique that was developed during my PhD studies and, more specifically, implemented for Ga_2O_3 and GaN 2D materials. This method was primarily based on the liquid metal chemistry approach that was set up at RMIT before I began my PhD. I will also present the characterization tools we used to assess the structural and optical properties of the resulting 2D materials. Understanding these properties can help us make better materials for various applications.

2.1. Introduction

Among 2D materials, Ga_2O_3 and GaN stand out due to their interesting optoelectronic properties. Indeed, wide-band-gap Ga_2O_3 films have found unique applications in electronics [93], photonics [94], sensing [95] , resistive switching [96], and bio-inspired artificial technologies [97]. Accordingly, the research on 2D surface oxide films of liquid gallium alloys is extensively established to realize economically affordable techniques for synthesizing and extracting high-quality 2D semiconductors [98]. The choice of the synthesis technique profoundly impacts the morphologies and phases of Ga_2O_3 and, therefore, its band structure [338]–[343]. Many different liquid phase methods have been shown for synthesizing Ga_2O_3 based on hydrothermal, microwave, and other solvothermal approaches [86], [88], [99], [100], [102]–[105]. However, such synthesis techniques generally require an extended processing time of up to several days for acceptable synthesis yields.

On the other hand, GaN has become one of the main materials for the fabrication of optoelectronic devices, such as high-efficiency light-emitting diodes [122][121][344], lasers [345][346], photodetectors [347], and solar cells [348], due to its wide bulk bandgap (3.4 eV) [118]. Compared with its bulk counterpart, 2D GaN shows enlarged bandgap, thus allowing electronic components to hold their durability even at a higher voltage [131]. Sanders, Nocona, et al. theoretically demonstrated that light emission from monolayer 2D GaN is blue shifted into the deep ultraviolet range, which is promising for sterilization and water-purification applications [349]. Chen, Yunxu, et al, fabricated a field effect transistor (FET) device on a 2D GaN crystal to probe the intrinsic electronic property of 2D GaN single crystals [214]. However, traditional fabrication techniques, such as mechanical exfoliation, cannot be applied to produce 2D GaN due to its wurtzite structure which features covalent bonds in all three dimensions [350]. Among all the fabrication techniques, CVD and elemental epitaxial methods are the most common methods for the deposition of GaN thin film [124]–[128]. The epitaxial method is yet inherently limited by high cost in order to allow control of the formation of thin films. Therefore, developing a substrate-independent, scalable process for synthesizing highly crystalline 2D GaN nanosheets across large areas would grant access to 2D GaN at a low cost.

Here we introduce a new synthesis technique for 2D Ga_2O_3 and GaN. This chapter will be organized as follows: first, we will present and explain our fabrication process, which nicely expands on the liquid metal chemistry that was recently developed at RMIT. We anticipate that this technique could allow the synthesis of ultra-thin Ga_2O_3 and GaN nanosheets that can be deposited directly onto flat substrates and silicon photonic devices such as optical waveguides. This technology thus paves the way towards the realization of hybrid photonic circuits that locally exploit 2D materials so as to adjust or enhance the optical properties of mature silicon photonic chips.

Next, we will describe the different characterization tools used to study these materials' structural and optical properties, such as atomic force microscopy (AFM), Transmission electron microscopy (TEM), X-ray photoelectron spectroscopy (XPS), and Spectroscopic ellipsometry (SE). Overall, this chapter will provide a comprehensive overview of the different tools and techniques that we used to fabricate and characterize Ga_2O_3 and GaN, specifically. Interestingly, these techniques could be nicely expanded to a wide range of 2D materials achievable with liquid metal chemistry, as well as their oxide derivatives.

2.2 Fabrication of 2D materials

This section introduces our fast and low-cost synthesis approach, developed to produce ultra-thin Ga_2O_3 and GaN which is compatible with the integration of 2D materials onto photonic devices. This technique has been recently developed [10][11] at RMIT university and mainly relies on a two-step process: the first step uses the ‘liquid metal chemistry’ (LMC) method [10][11], which is proven effective for synthesizing large-scale ultrathin oxide and metallic layers with various compositions depending on the liquid metal precursor (**Figure 2-1**(a)) [164], the second step involves a microwave plasma-enhanced nitridation reaction (**Figure 2-1**(b)) [12]. The LMC technique has been widely demonstrated for metals and metal alloys present in liquid form below approximately 350°C, which includes several post-transition elements, group 12 elements, and their alloys [164]. Using this LMC technique, we synthesized here ultrathin Ga_2O_3 nanosheets from the self-limiting oxide layer that forms on the surface of liquid gallium at room temperature in a few seconds. Next, our ultra-thin Ga_2O_3 nanosheets undergo a microwave plasma-assisted nitridation reaction, eventually resulting in ultra-thin GaN layers [12]. These two steps illustrated in Figure **2-1** are explained in further details in the sections 2.2.1 and 2.2.2.

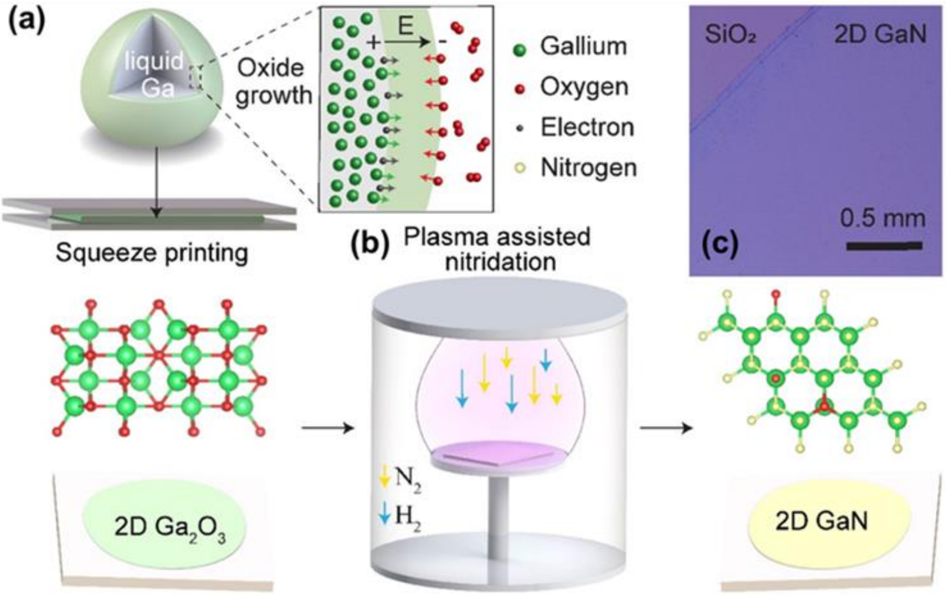

Figure 2-1 Synthesis process of large-area ultrathin GaN nanosheets. (a) Schematic illustration of the Cabrera–Mott oxidation that occurs at the surface of liquid metals in the presence of oxygen followed by the printing technique used to exfoliate 2D oxides from molten metal. The liquid metal droplet is squeezed between two substrates allowing the transfer of the Ga_2O_3 layer. (b) Synthesis process of the ultrathin GaN nanosheet from ultrathin layer of Ga_2O_3 utilizing a microwave-activated nitrogen/hydrogen plasma conducted in a cylindrical cavity plasma reactor. (c) Optical image of the synthesized GaN on SiO_2/Si, confirming the presence of an ultrathin and homogeneous layer reaching several millimeters in lateral size.

2.2.1 2D Ga_2O_3 fabrication using the squeeze printing process

Following the Cabrera–Mott oxidation model depicted in **Figure 2-2**, an ultrathin and self-limiting oxide layer forms on the liquid metal surface once it is exposed to the ambient atmosphere in the presence of oxygen. Electrons from the metal tunnel through the growing oxide shell, resulting in a self-generated electric field called the Mott field [12], [161], [164], [179], [184], [213], [351] This field promotes the diffusion of metal and oxygen ions into the oxide shell, leading to oxide growth. The field strength reduces as the oxide becomes thicker until ion diffusion ceases. This oxide skin is weakly attached to its parent metal, easing exfoliation onto desired substrates through van der Waals adhesion. This indicates no covalent bond between the oxide layer and the base metal. Also, liquid gallium metal is a monoatomic liquid, which is nonpolar by default, which limits the possibility of interactions. Hence, the interaction between the liquid metal and the surface oxide is expected to be minimal. The lack of a stable crystal arrangement hinders the collective atomic bonding of liquid metal across extensive regions, confining any feeble connections to specific areas and preventing significant adhesion. Additionally, due to the liquid state of the parent metal and the absence of covalent bonds between the liquid metal together with the liquid form of the parent metal, there are only minimal interactions between the oxide and the liquid metal.

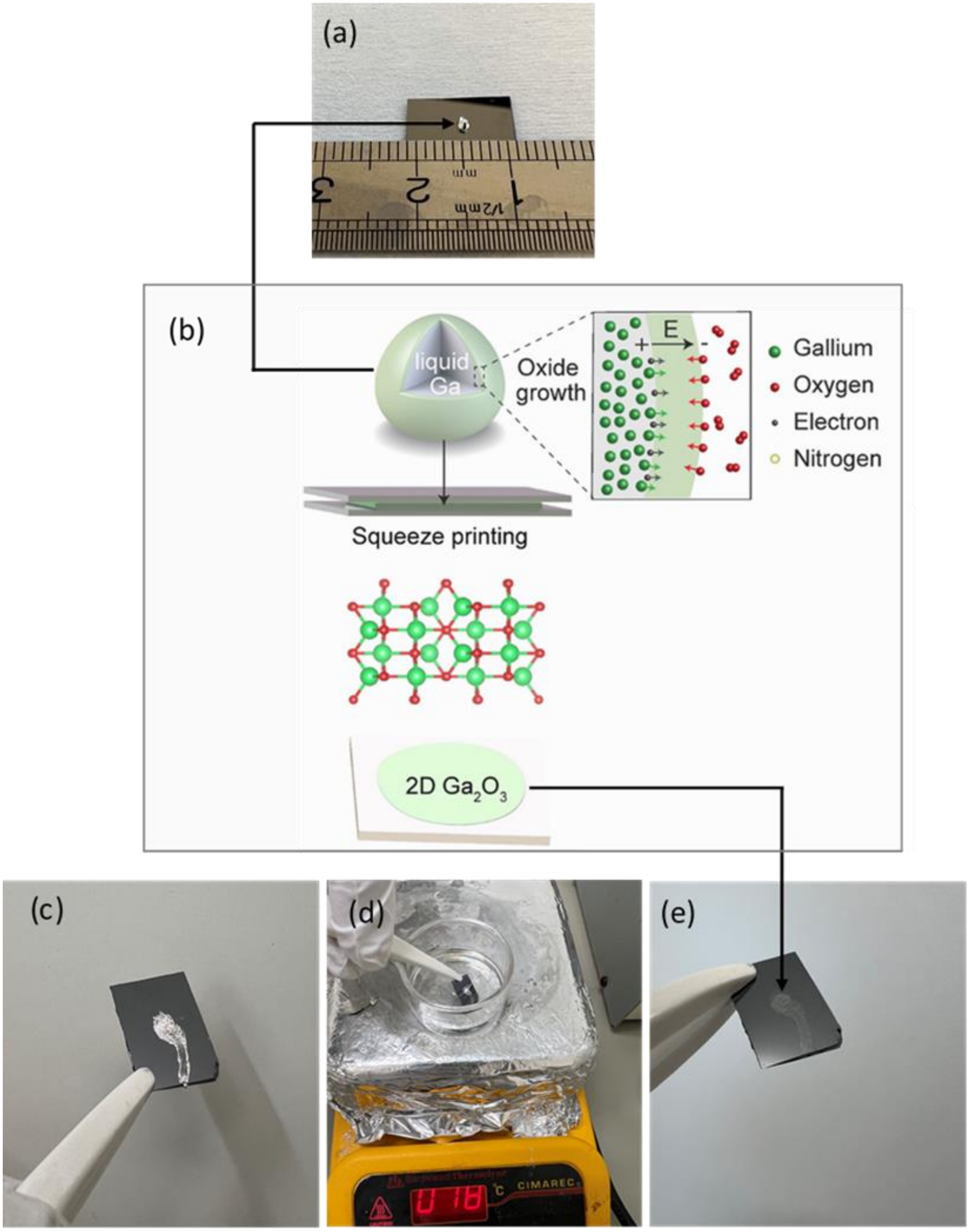

Figure 2-2 Fabrication process of Ga_2O_3 ultra-thin layers (a) Gallium droplets with ~1 mm in diameter (b) Schematic illustration of the Cabrera–Mott oxidation occuring at the surface of liquid metals in the presence of oxygen followed by the printing technique used to exfoliate 2D oxides from molten metal..Mechanical cleaning procedure (c) Squeezed droplet after removing the top substrate (d) washing the sample with hot ethanol to remove the micro droplets (e) washed sample without any residue and with 2D materials attached to the substrate

We started our fabrication with placing a droplet (~1 mm in diameter) of liquid gallium (**Figure 2-2** (a)) (m.p. 29.8 °C) on an atomically flat centimeter scale SiO_2/Si (200 nm SiO_2) substrate (any substrate with low surface roughness is suitable). As shown in **Figure 2-2** (b), a glass slide was firmly pressed onto the droplet, effectively squeezing the droplet into the shape of a thin metal film. Upon removal of the top glass substrate, a large and continuous ultrathin gallium oxide film which reached lateral dimensions exceeding several centimeters remained on the SiO_2/Si wafer and the glass slide (**Figure 2-2**(c)). To remove the remaining liquid metal microdroplets, we used a solvent-assisted mechanical cleaning protocol based on ethanol heated at 78 °C (**Figure 2-2** (d)). The SiO_2/Si wafer with deposited 2D Ga_2O_3 sheet was submerged in hot ethanol for 1 minute. The metal inclusions can be entirely removed by wiping the SiO_2/Si wafer with a polyurethane foam swab while submerged, whereas the Ga_2O_3 sheet remains anchored on the substrate (**Figure 2-2** (e)) [193].

2.2.2 Plasma-assisted nitridation process to convert the 2D Ga_2O_3 to GaN

In our synthesis approach, which was outlined in Section 2.2, a crucial step is the conversion of 2D Ga_2O_3 to GaN through a nitridation process. There are two primary techniques for this conversion: *ammonolysis reaction* and *Plasma-assisted nitridation process*.

The ammonolysis method involves placing Ga_2O_3 sheets inside a quartz tube situated within a horizontal tubular furnace. Urea pellets serve as the source material for generating NH_3 gas. With the samples centrally positioned, the tube is heated to 800°C, and N_2 gas is introduced at a flow rate of 50 sccm as the carrier gas. The entire process lasts for 90 minutes after the system reaches 800°C. At this temperature, the 2D Ga_2O_3 samples undergo a reaction with ammonia vapor, resulting in the formation of 2D GaN films[178].

In contrast, the plasma treatment method for nitridation is quicker and can be conducted at lower temperatures, reducing the risk of damaging the final device. For our research, we employed the Plasma-Enhanced Chemical Vapor Deposition (PECVD) equipment at INL's NANOLYON cleanroom to convert the 2D oxide material into nitride. Our technique primarily utilized the plasma generation capability of the PECVD equipment. In this process, a precursor is combined with a plasma-generating gas mixture and exposed to a high-energy plasma field. The plasma disintegrates the precursor gas into reactive species, which subsequently react with the substrate and 2D oxide material, forming a thin nitride film. As will be demonstrated in Chapter 3, our plasma-assisted nitridation process allows for precise control over the film's properties, including thickness, uniformity, and chemical composition. We will delve into the details of this process in subsequent sections. It is important to note that similar results for the nitridation process can be achieved using alternative equipment, provided it offers control over temperature, gas flow, pressure, and RF power.

2.2.2.1 General presentation of the plasma process and controlled parameters

The process chamber receives the reactant (and dilution) gases through a shower head situated above the sample. This arrangement ensures an even dispersal of the reactant gases across the sample surface. The shower head is subjected to an RF potential to generate a plasma. Energetic electrons in the plasma ionize or dissociate ("crack") reactant gases to generate more chemically reactive radicals. Instead of forming a thin film through deposition, in our case, these radicals actively participate in the conversion of the 2D oxide material into nitride, modifying the material's properties and composition. The energy supplied by the plasma provides the key advantage of a reduced process temperature for PECVD compared to Low pressure chemical vapor deposition (LPCVD) where all of the energy for reaction is supplied thermally. (**Figure 2-3**)

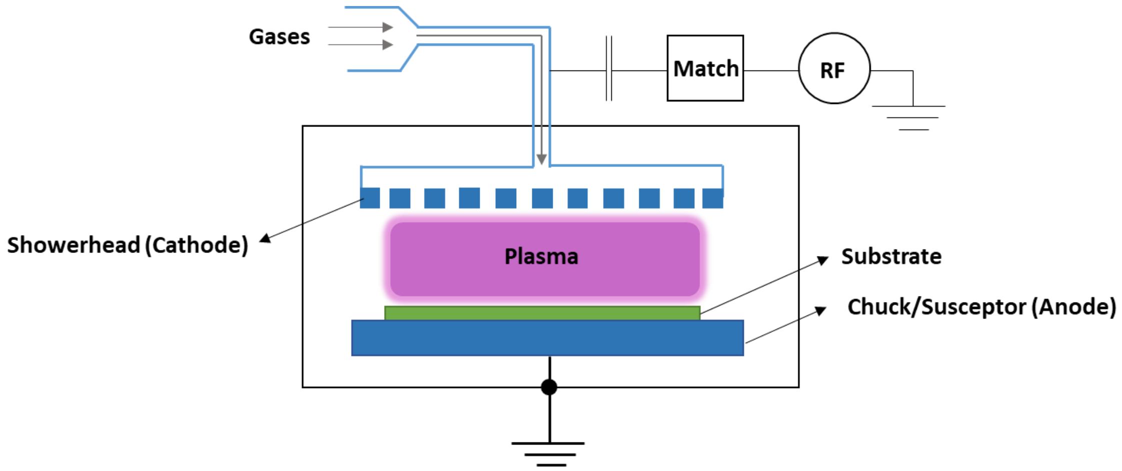

Figure 2-3 Schematic of PECVD operation

Within the PECVD reactor chamber, temperature, pressure, power or gas flow entering the chamber can be adjusted. All these parameters are more or less correlated and will have an impact on the quality of the film obtained, on its growth rate and on the precursor/substrate interactions. We remind these links below.

- **Pressure**

The pressure in the chamber during PECVD processes is of the order of magnitude of one Torr [352] or a hundred milliTorr. These pressure conditions are necessary for the creation of a plasma and its adjustment is a matter of compromise between limiting ion bombardment, avoiding powder formation in the gas phase which can occur in high power/high pressure regimes.

- **RF-Power Density**

The power supplied by the RF generator allows for the decomposition of the precursors in the gas phase. This power is normalized with respect to the surface of the PECVD reactor electrode to define a power density, often given in mW/cm^2. An increase in this power density increases gas phase precursor dissociation and therefore increases the concentration of reactive species and ions in the plasma. Depending on the gas mixture in the chamber as well as pressure, a low power density can lead to an unstable plasma or even to the impossibility of igniting it.

- **Temperature**

Temperature can be limited by the thermal constraints of the device, such as not exceeding 350°C for a substrate integrating Complementary metal-oxide-semiconductor (CMOS) elements with copper interconnections or working below the glass transition for polymers. In our work, where integration with chip-based optical devices is essential, managing temperature during fabrication is crucial. We must ensure temperatures remain within limits to protect both the material and the sensitive optical components like waveguides.

- **Gas flow rate**

Finally, the gas flow rate is adjusted for each gas, whether they are used as a precursor or a dilution gas. The total gas flow rate is typically given in standard centimeter cube per minute (sccm) and has an impact on the deposition rate since it is directly correlated to the amount of species available for deposition. Even more crucial than total gas flow rate is the relative gas flow rates of the different gases in the mixture, which controls the chemistry and the structural properties of the film.

The equipment used over the course of this PhD project is a commercially available PlasmaTherm Vision 310 PECVD (**Figure 2-4**(a)) at INL. It is a capacitively coupled PECVD with a 13.56 MHz radiofrequency generator and a low frequency 100-460 kHz generator which can be used simultaneously. The low-frequency capability was only used for post-deposition cleaning of the chamber. A summary of main characteristics are given in **Table 2-1**. The top electrode seen in **Figure 2-4**(b) is a shower-head electrode from which the gas mixture is injected into the chamber. The bottom electrode can be heated up to 380 °C and can hold substrates up to 12” in diameter. Among the 10 available gas lines, 2 gases are predominantly used for the nitridation process. Gases have purity levels of 99.9999 % to prevent any unwanted species to be incorporated in the film. The concentration and gas flow rate specification for each of these gases is given in **Table 2-1**.

Table 2-1 Plasma Therm Vision 310 PECVD specifications

Electrode dimension	12” – 305 mm
Inter-electrode spacing	22 mm
Temperature range	50 – 380 °C
Maximum Power supply	300W (at 13.56 MHz)
Pressure range	0 – 1000 mTorr
Gas lines (flow rate)	H_2 (15 - 1000 sccm) N_2 (1 - 1000 sccm)

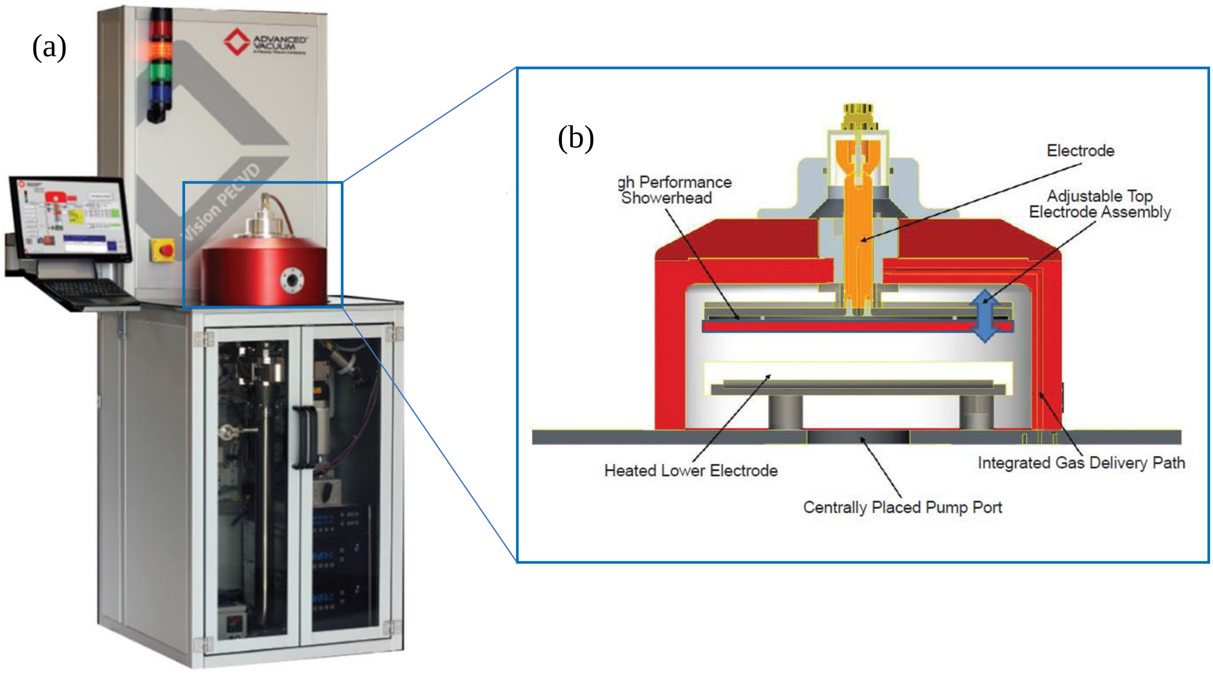

Figure 2-4 (a) Photo of the PlasmaTherm Vision 310 PECVD equipment used (b) Schematic cross-section of the reactor chamber @ PlasmaTherm

2.2.2.2 Nitridation Procedure

We refer to the transformation of oxide sheets to nitride as the "nitridation process", in the rest of this thesis. During this step, gallium oxide sheets (synthesized by squeeze printing (2.2.1)) were converted into gallium nitride using a microwave-activated plasma reaction (**Figure 2-5**(a)). The synthesis was carried out in the PECVD equipment presented above using the parameter settings summarized in **Table 2-2**.

Table 2-2 Plasma parameter used for the full nitridation process to convert Ga_2O_3 into GaN

Temperature	320 °C
Time	10 min
Gas	N2 (99.5%) + H2 (0.5%)
Flow rate	200 sccm/1 sccm
Pressure	1 Torr
Power	150 W

The small amount of H_2 plasma was used to improve the nitridation process by reducing the oxide of the nanosheets. The adoption of plasma reaction assists the transformation of the metal oxides into metal nitrides in the existence of active and high energy nitrogen ions/species at relatively low temperature whereas in other chemical vapor deposition techniques, higher temperature prompts the chemical reaction between the metal oxide and nitrogen source. During the full transformation of Ga_2O_3 to GaN, the samples were exposed to the plasma for 10 minutes. During the nitridation process, active $NH_x^{\bullet}$ (x = 1, 2) radical species are expected to form within the mixed N_2 - H_2 plasma [12][353][354] aside from a variety of $NH_x^{\bullet}$ radicals, atomic and ionic $N^{\bullet}$ and N^+ species are formed. These species are highly reactive and promote the conversion of Ga_2O_3 to GaN at comparatively low temperatures and pressures.As we shall see, the values mentioned above for the plasma treatment allowed us to fully transform the oxide films into nitrides. However, by slightly modifying the process parameters, such as power and time, we were able to achieve an intermediate level between Ga_2O_3 and GaN, as will be explained in chapter 3.

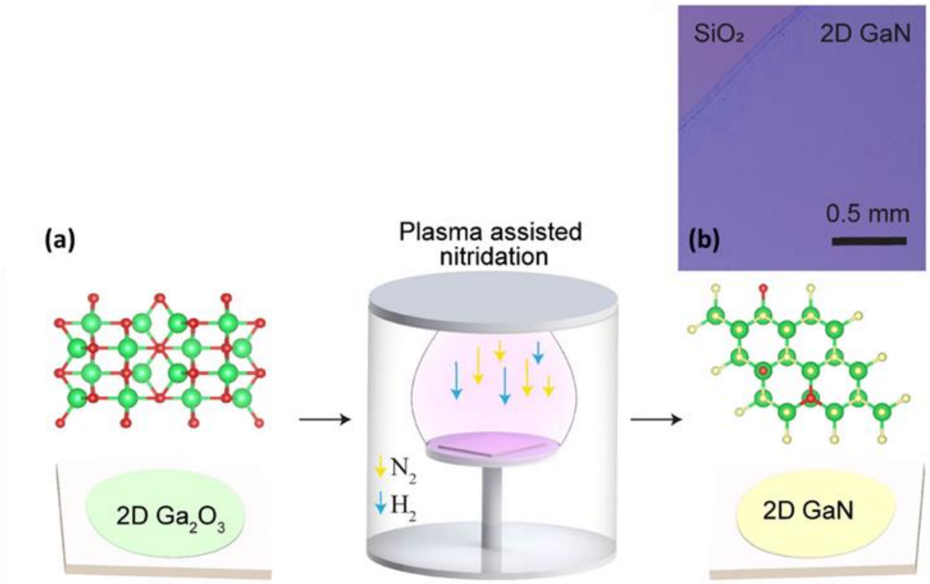

Figure 2-5(a) Synthesis process of the 2D GaN nanosheet from 2D Ga_2O_3 utilizing a microwave-activated nitrogen/hydrogen plasma conducted in a cylindrical cavity plasma reactor. (b)Optical image of the synthesized GaN on SiO_2 confirming the presence of an ultrathin and homogeneous layer reaching hundreds of micrometers in lateral size

2.3 Characterization of the synthesized 2D materials

Characterizing 2D materials such Ga_2O_3 and GaN is critical for understanding their unique properties and potential applications. For example, these materials exhibit size-dependent properties due to the reduced dimensionality, which makes them different from their bulk counterparts. Therefore, the morphology characterization of 2D Ga_2O_3 and GaN is essential for tailoring their properties for specific applications. We thus used in this thesis a combination of characterization equipment that allow us to assess both the morphology, as well as structure and composition of the thin-films, and eventually their optical properties. However, characterization of 2D Ga_2O_3 and GaN pose significant challenges. To overcome these challenges, various tools and techniques have been developed to synthesize and characterize 2D Ga_2O_3 and GaN, and grasp a comprehensive overview of their interdependent properties.

In this section we will describe the different characterization tools used to study these materials' structural and optical properties, such AFM, TEM, XPS, and Spectroscopic Ellipsometry. **Table 2-3** summarizes the different tools and the information they allow us to retrieve.

All of these tools will be extensively used to study the 2D materials synthesized through the 2 step process explained in section 2.2, and the related results will be presented in detail in Chapter 3.

Table 2-3 Characterization Tools and Their Retrieved Information

Characterization Tool	Retrieved Information
AFM	Topography: Film thickness, Homogeneity, Deposition location
TEM	Crystalline structure
XPS	Chemical composition, Bonding configuration
Ellipsometry	Film thickness, Optical properties (index, dispersion)

2.3.1 Topography characterization

The topography of 2D materials plays a crucial role in their physical, chemical, and electronic properties. Therefore, accurately characterizing their topography, including their uniformity and smoothness, is essential for understanding their behaviour and optimizing their performance. Various techniques have been applied to study the topography of 2D materials. Among them, AFM and TEM have been actively used for this project. These topography techniques provide different types of information about the structure of 2D materials, and their combined use can offer a comprehensive understanding of these materials.

2.3.1.1 AFM

The The Scanning Probe Microscope (SPM) revolutionized microscopy by enabling the observation of atoms, earning it the title of the third-generation microscope after optical and electron microscopes. Among SPMs, the Scanning Tunneling Microscope (STM) was the first to image conductive materials through tunneling current. Its limitation with non-conductive materials was overcome by the AFM. AFM can be used to measure almost any sample, regardless of its electrical properties. It is an imaging method with a resolution below one nanometer [355]. It is designed to provide the surface topography of a sample at the nanoscale by measuring the force between a probe and the sample.

The AFM uses a micro-machined cantilever with a sharp tip to measure a sample's surface topography. Central to AFM technology is the feedback loop that maintains a constant force between the cantilever tip and the sample's surface by adjusting the height of the cantilever. This force is dependent on the distance between the atoms at the tip of the cantilever and those on the sample's surface, and can be either attractive or repulsive. The feedback loop thus plays a crucial role in accurately mapping the topography. **Figure 2-6**(a) displays the basic configuration for most AFMs along with a topography of 2D Ga_2O_3 synthesized by liquid metal. The force between the atoms at the sample's surface and those at the cantilever's tip is detected by monitoring the cantilever's deflection. This deflection can be quantified by measuring a beam that is reflected off the backside of the cantilever and onto a Position Sensitive Photo Detector (PSPD). The tube-shaped scanner located under the sample moves the sample in the horizontal (X-Y) and vertical (Z) directions. It scans the sample line by line, and the PSPD signal is used to establish the aforementioned feedback loop, which controls the vertical movement of the scanner as the cantilever moves across the sample surface.

The AFM is versatile and can be applied to characterize conductive, non-conductive, and even some liquid samples with minimal sample preparation, which is an advantage over the extensive preparation required for TEM or SEM. In this context, as shown in **Figure 2-6** (b), AFM was conducted on the ultrathin layer of deposited Ga_2O_3 on the SiO_2 substrate to measure the thickness of the deposited layer (2.5 nm in this example).

In our study, AFM was the primary characterization technique used after each deposition. Our decision to utilize AFM stemmed from two key motivations. First, it enabled us to verify deposition in target areas which were impossible to visualize with optical microscopy. SEM, though a powerful tool, was unable to provide information on specific devices like planarized waveguides due to the fabrication technique that obscures surface features from SEM detection. Thus, AFM was the only technique capable of detecting the deposition area in these cases. Secondly, AFM empowered us to quantify the thickness of the deposited material. This was achieved by calculating the height difference between the substrate and our material. Additionally, AFM facilitated the measurement of the homogeneity scale of the layer, the details of which are elaborated in section 3.2.1 of Chapter 3.

Nevertheless, while AFM was invaluable in our research, it is important to note its limitations. With the Park NX10 AFM that we used, the maximum scan size is constrained to 50x50 µm in the X and Y directions. For our research, it was imperative to determine whether the area of deposition covered the entire device or just partially, and the 50 µm scan size was not sufficiently large to conclusively assess this. A larger scan size would have been invaluable for examining larger areas of the sample, and providing a more comprehensive understanding of the deposition coverage across the device.

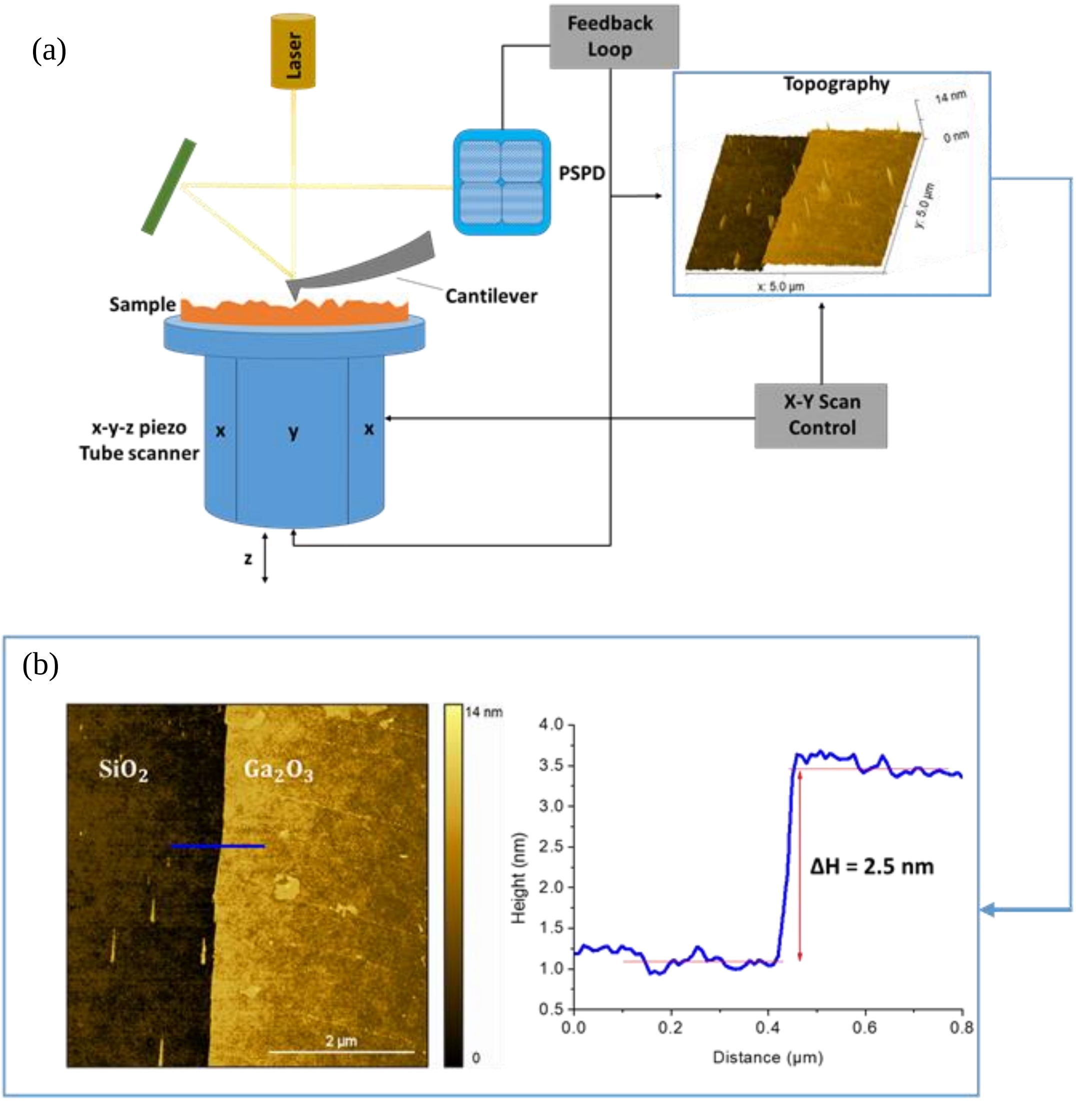

Figure 2-6 (a) Diagram of Conventional AFM's scanning (b) topography of 2D Ga_2O_3 on SiO_2 substrate

2.3.1.2 TEM

Electron microscopy techniques, including TEM is capable of revealing crystal structures at an atomic or nanometer scale [356]. TEM is a high-resolution imaging technique that uses a beam of electrons to interact with a sample, providing images with resolutions as high as a few picometers. This makes TEM a powerful tool for microstructure characterization, allowing the imaging of materials with sub-nanometer precision and providing direct insights into a material system down to the atomic scale. Unlike traditional microscopy techniques that rely on visible light, TEM can reveal the atomic structure and defects of 2D materials, providing crucial information for understanding their behavior and potential applications in various fields.

Compared to other surface analysis techniques like SEM and AFM, TEM enables analyzing internal and small-size microstructures along the cross-section and plan-view. In addition, it has been used to obtain local crystalline and chemical information about grown thin films, showcasing the versatility of the technique.

For nanomaterials, High Resolution Transmission Electron Microscopy (HRTEM) is particularly useful since conventional diffraction experiments like X-Ray diffraction (XRD) and neutron diffraction may not provide sufficient structural information [357][358]. With the emergence of 2D materials, HRTEM and Selected Area Electron Diffraction (SAED) have become essential for understanding their properties and potential applications. HRTEM routinely allows the determination of structure at atomic-resolution and precision in atomic location [359]. In this work both techniques used for characterization of 2D material as HRTEM can reveal defects affecting the properties of 2D materials, while SAED can determine their crystal structure and potential applications. These techniques have played a significant role in advancing 2D materials research, providing insights into their fundamental properties and guiding their applications in various fields.

TEM consists of an electron gun to generate high-energy electron beams, condenser lenses for controlling spot sizes, an objective lens for imaging the sample, intermediate and projector lenses for mode switching between diffraction and imaging, and detectors for collecting secondary signals. This structure can be seen in **Figure 2-7**(a). For the source, an electron gun is used where the electrons are emitted from a solid surface cathode and accelerated by high voltage to form the final high-energy electron beam. The resolution of the microscope is predominantly governed by the acceleration voltage, which in turn influences the wavelength of the electrons. For instance, a microscope with an acceleration voltage of 40 kV typically produces a resolution of 0.56 nm, whereas an acceleration voltage of 500 kV is associated with a resolution of 0.13 nm. Electromagnetic lenses, such as the condenser and 'adjusting' lenses, utilize magnetic force to focus the electron beam. The condenser lenses are used to control the beam diameter and convergence angle and typically consist of two or more lenses. 'Adjusting' lenses include objective, intermediate and projector lenses that are used for magnification control and changing between imaging and diffraction mode, and an aperture between the electromagnetic lenses to limit light scattering and control the beam diffraction. For the specimen, it requires ultra-thin samples (< 100 nm). Finally, when the electrons pass through the lenses, this data is used to create images directly on a fluorescent screen or onto a computer screen using a charge-coupled device (CCD) camera.

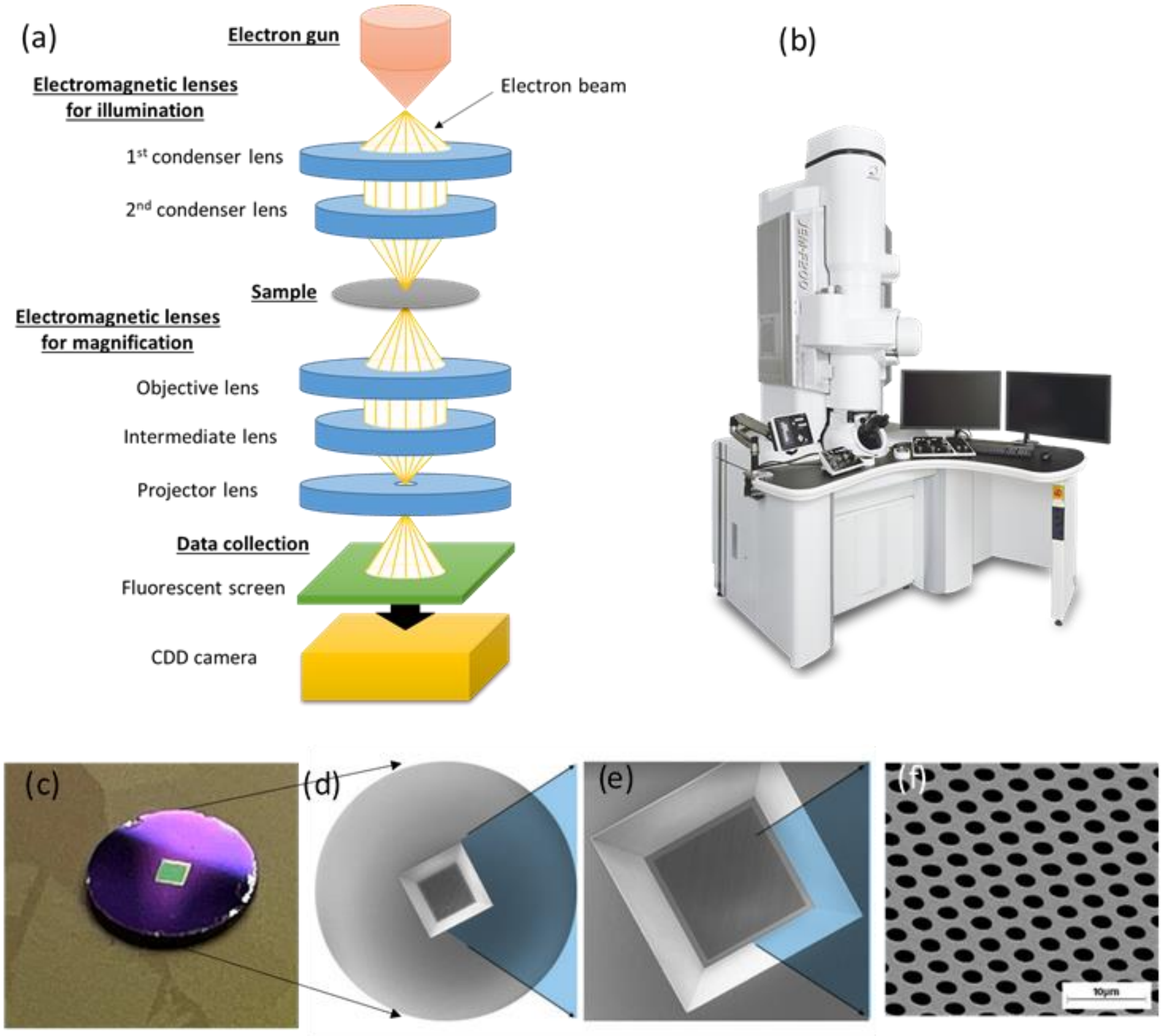

Figure 2-7(a) Simplified schematic of the TEM optical path (b) JEOL JEM-F200 TEM (c) Image of TEM grid (d) Holey 200nm silicon nitride support frame on 3mm frame (e) 0.5 x 0.5mm window with holey silicon nitride membrane imaged from back side (f) image of 2.5µm circular holes (Image d, e and f are taken from [360])

In this project, the high resolution TEM measurements were performed using a JEOL JEM-F200 TEM at RMIT University with acceleration voltages of 200 kV (Figure **2-7** (b)). The Gatan micrograph 3.4. Software Package was used for TEM/HRTEM analysis. Thermally and mechanically robust Si_3N_4 TEM (Ted Pella, 21587-10) membranes were used to develop the TEM samples that were prepared by directly printing the gallium oxide sheet onto the TEM membrane and submitting it to the plasma assisted nitridation process (See result in section 3.2.3 Chapter 3). The platform for this holey Silicon Nitride support film is the low stress 200 nm Silicon Nitride support film on a circular 3mm silicon frame with a 0.5 x 0.5mm membrane. The diameter of the holes is 2.5µm with a pitch of 4.5µm in an array of 100 rows x 100 columns in a hexagonal high density arrangement (Figure **2-7** (c,d,e,f)).The Si_3N_4 TEM grid suits the synthesis process presented in this work (T°<320 °C). The Si_3N_4 TEM grids also feature pores which are completely empty and allow analysis of the suspended flakes through the pore without contribution of the TEM grid.

2.3.2 Spectroscopy characterization

Spectroscopy characterization plays a critical role in understanding the properties and behavior of 2D materials. It can provide valuable information about the electronic and optical properties of 2D materials, including their band structure, carrier mobility, binding energy, chemical composition, and optical index. This project uses XPS and ellipsometry as the primary spectroscopy characterization of our 2D materials. Combining these two methods can provide a comprehensive description of our materials. XPS can give information about the material's surface, elemental composition and chemical state. In contrast, ellipsometry can provide information about the thickness and optical properties of a thin film. Together, these techniques can provide a complete picture of the material's structure, composition, and properties.

2.3.2.1 XPS

X-ray photoelectron spectroscopy (XPS) is now the most commonly used technique for surface analysis, as driven by the increasing importance of surfaces, thin films, and interfaces in various areas of science and technology. XPS has also been an essential tool to characterize 2D materials, providing valuable information on their chemical composition, bonding configuration, and electronic structure. It has been widely used to study the surface chemistry of 2D materials, such as graphene [361][362], transition metal dichalcogenides [363][364], and black phosphorus [365][366]. With its high sensitivity to elemental composition and chemical states, and accuracy in quantitative analysis, XPS has proven to be a valuable technique in advancing the understanding of 2D materials and their potential applications. Additionally, the advent of micro-XPS, which employs a focused X-ray beam (10µm), enables localized information to be obtained. This is particularly useful for studying heterogeneities and specific regions within 2D materials, thereby providing insights into their structural and compositional attributes on a nanoscale and microscale.

2.3.2.1.1 Working principle

The working principle of XPS relies on the photoelectric effect, whereby electrons (called photoelectrons) are ejected from the surface sample placed under Ultra High Vacuum (UHV) conditions and exposed to soft X-rays. The elements present in the sample can be identified from the analysis of the kinetic energies and binding energies of the detected photoelectrons. Additionally, the intensities of specific photoelectrons provide information about the concentration of the related element in the sample. An electron energy analyzer measures the kinetic energy $\mathrm{E_k}$ of the ejected electrons. The original binding energy $\mathrm{E_b}$ experienced by an electron (before being ejected) in the sample can be calculated from $\mathrm{E_k}$ using the simple relationship ($E_k = h\nu - E_b - \phi$ (**Figure 2-8**(a)), where hν is the incident photon energy and ϕ is the work function of the spectrometer. Through analysis of kinetic energies and intensities of the photoelectrons, XPS can identify elemental composition and characterize chemical bonds, making it an invaluable tool for material analysis.

The XPS instrument consists of five essential components: 1) An Ultra-High Vacuum (UHV) system that ensures surface cleanliness and allows for longer photoelectron path lengths, 2) An electron analyzer, which includes a lens system for collecting photoelectrons, an analyzer for filtering electron energies, and a detector for counting electrons, 3) An X-ray source, typically using Al Kα radiation, and employing a monochromators with a quartz crystal, 4) A low-energy electron flood gun for analyzing insulating samples, and 5) An ion gun, used for sample cleaning and depth profiling (Figure **2-8** (b)).In this study, XPS analyses were performed using two different instruments: a Thermo Scientific K-alpha XPS at RMIT University in Melbourne and a PHI 5000 VersaProbe III at LTDS Laboratory in Ecole Centrale de Lyon. The materials, grown on SiO_2/Si substrates, were subjected to XPS analysis with Thermo Scientific K-alpha utilizing a spectrometer furnished with a monochromatic Al K-α source (hv ≈ 1486.7 eV). The Thermo Scientific K-alpha XPS was operated with a pass energy of 50 eV, recording core-level spectra at a 300 µm spot size across 50 scans for each sample. In contrast, the PHI 5000 VersaProbe III offered a more precise 1-micrometer spot size, which was essential for the detection and localized characterization of 2D materials on the device. This precise spot size is particularly relevant for the integrated devices analyzed later in chapter4. Furthermore, both XPS are equipped with a flood gun which inundates the analysis chamber with low energy Ar+ ions and electrons. For this project, we specifically employed a low-energy electron flood gun as a strategy to mitigate the surface charging effect exhibited by the synthesized materials, avoiding the need for an ion gun. This ensured a more accurate representation of the materials' properties.

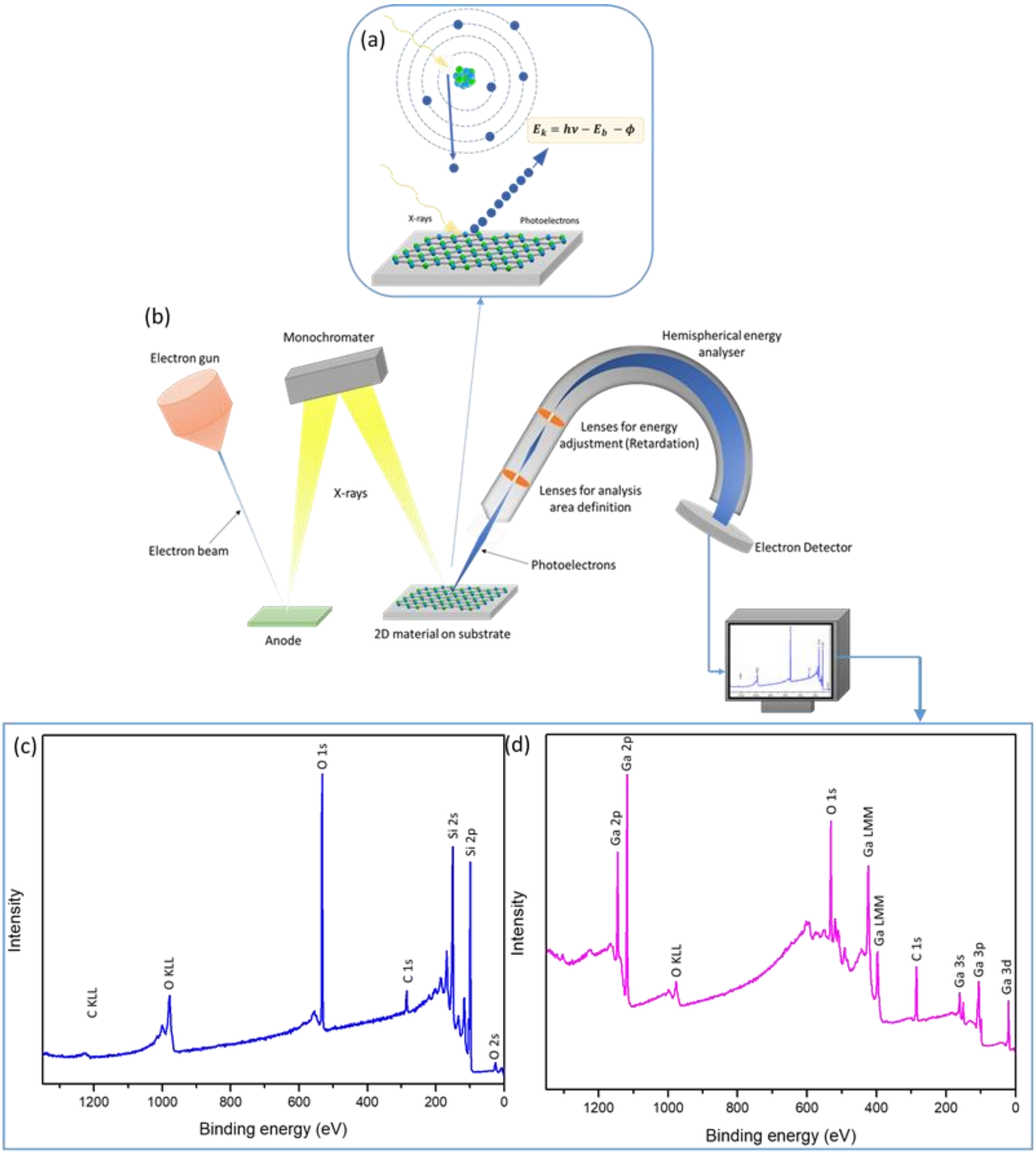

Figure 2-8 (a) Schematic of photoelectric effect (b) Simplified schematic of an XPS equipment (c) Illustrative XPS spectrum of SiO2/Si and (d) of 2D Ga_2O_3 onto SiO2/Si obtained with Thermo Scientific K-alpha

All the samples are adjusted with the C-C bond of carbon at 284.68 eV. As an illustration, Figure **2-8** (c), shows the XPS spectrum of SiO_2/Si measured with Thermo Scientific K-alpha (300 µm spot size) before the deposition of the 2D material, while Figure **2-8** (d) shows the

XPS spectrum of the sample after the deposition of Ga_2O_3 (2.5 nm thickness) by the method described in section 2.2.1. Obviously, by comparison of the two figures we can see that in **Figure 2-8** (d) , the spectra contain the expected photoemission lines of Ga (Ga2p at 1117 eV, Ga3s at 159.5 eV, Ga3p at 109 eV, Ga3d at 18.7 eV and GaLMM Auger) in good agreement with the spectral values for thin film and ultrathin Ga_2O_3 [367][10], which confirms the effectiveness of this characterization technique for 2D materials. Additionally, we employed XPS to quantitatively determine the conversion of Ga_2O_3 to GaN, which will be presented in the results section 3.2.2 of Chapter 3.

2.3.2.2 Ellipsometry

While the above techniques give us some valuable information about the composition, morphology and structure of the ultra-thin films, ellipsometry is a powerful tool for characterizing their optical properties. These are particularly relevant when intending to integrate these 2D materials within optical devices. In recent years, ellipsometry has indeed been applied to measure the optical properties of 2D materials as well [368][369].

Ellipsometry is a commonly used technique to analyze the optical properties of materials, whether in bulk or thin-film format, by using polarized light. The name ‘ellipsometry’ comes from the fact that polarized light often becomes elliptical upon light reflection. In other words, ellipsometry relies on the measurement of light polarization upon its reflection (or transmission) on a sample under oblique incidence. If the surface is covered by a thin film (or a stack of films), the entire stack and substrate influence the change in polarization. Hence, we can infer information about the characteristics such as its thickness and optical index of the films within the stack. Ellipsometry boasts several notable advantages including its high precision and exceptional sensitivity, particularly when dealing with ultrathin films (less than 10 nm). Moreover, it is a non-destructive, non-invasive, non-contact, and rapid measurement technique.In addition to these benefits, Ellipsometry is characterized by its broad application range. It can accurately measure the ratio of two values with high reproducibility and is versatile in its material applicability, including polymers, semiconductors, dielectrics, metals, and alloys. This makes it ideally suited for in-situ applications

Two values, Ψ and Δ, are typically measured by ellipsometry, to characterize the polarization of the light interacting with the sample as a function of wavelength. From these values, several characteristics of the single layer or complex multilayer stack can be retrieved, including the layer thickness(es) within 1 angstrom to several microns, the presence of a native oxide/ roughness at the layer interfaces, the refractive index and extinction coefficient of the different layers, or their anisotropy. Ellipsometry can also indirectly provide material properties such as its composition, crystallinity, microstructure, and film uniformity, which affect the optical properties.

2.3.2.2.1 Working principle of the ellipsometry

When light is reflected or transmitted by a sample at oblique incidence, it is classified as being p- and s-polarized depending on the oscillatory direction of its electric field with respect to the plane of incidence. Each polarized light wave shows a distinct reflection behaviour. This effectively distorts the polarization of randomly polarized light upon reflection.

The (ψ, Δ) measured from ellipsometry are defined from the complex ratio ρ of the amplitude reflection coefficients (r_p and r_s) for p- and s-polarizations [370] [371][372]:

$$\rho \equiv tan\psi \exp(i\Delta) \equiv \frac{r_p}{r_s} \qquad (2\text{-}1)$$

Figure 2-9 depicts the schematic illustration of ellipsometric measurement.

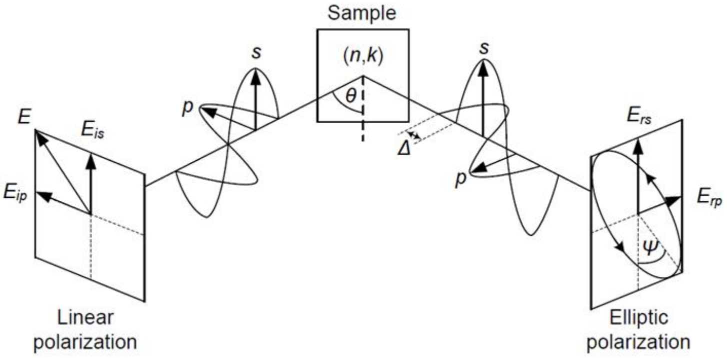

Figure 2-9 Schematics of ellipsometric measurement principle, taken from [444]

2.3.2.2.2 Ellipsometry components

In my PhD studies, the ellipsometric characterization was performed using a HORIBA-Jobin Yvon UVISEL Ellipsometry at INL (setup is shown in the **Figure 2-10**), which is composed of a broadband light source, a polarizer, an analyser, and a monochromator that disperses and redirects the reflected light to two different photo-detectors. The light source is a Xenon lamp, which spans a broad range of wavelengths between 250 and 2100 nm. Once the light passes through the initial polarizer, it becomes linearly polarized before reflecting off the sample at an oblique angle of typically 70°. To determine the polarization state of the reflected beam, an output head consisting of a photoelastic modulator and an analyzing polarizer is employed. Throughout the measurement process, the two polarizers remain fixed, while the photoelastic modulator is used to generate a modulated phase shift in the reflected beam.

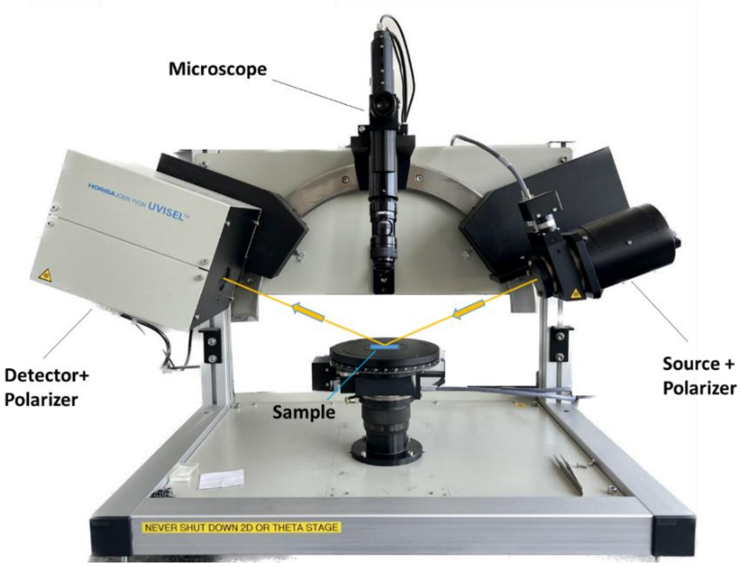

Figure 2-10: HORIBA-Jobin Yvon UVISEL Ellipsometry setup

2.3.2.2.3 Data analysis in ellipsometry

Ellipsometry is an indirect process in the sense that it does not directly measure physical quantities. Besides, in the case of phase modulated ellipsometers, like the one we use, we do not measure the ellipsometric angles ψ and Δ directly. Instead the three measured values are Is, Ic, and Ic', which are functions of ψ and Δ according to $I_s = \sin 2\psi . \sin \Delta$, $I_c = \sin 2\psi \cos \Delta$, and $I_c' = \cos 2\psi$. Information such as the layer thickness and optical dispersion are therefore extracted via a model that represents the sample structure and yields the same polarization change (i.e. Is and Ic) as that measured for light interacting with the sample. Accordingly, the experimental data is fitted using Horiba's DeltaPsi2 software. Once a model has been built to describe the characterized sample, the parameters of this model can be fitted to best match the observables Is and Ic obtained (**Figure 2-11**). A model is typically defined by a "semi-infinite" substrate and a stack of one or several layers defined by their thickness and the material(s) composing them. The materials are then described by their optical properties, generally with fixed n(λ) and k(λ) or as dispersion formulas. The building blocks of ellipsometric models are schematized in Figure **2-11**. In the fitting process, the thickness of the layer and the parameters of the dispersion formula can be obtained. The quality of the fit is measured by $\chi 2$ (equation 2-2) which should be minimized.

$$\chi^2 = \min \sum_{i=1}^{n} \left[\left(\Psi_{\mathrm{theoretical}} - \Psi_{\mathrm{experimental}}\right)^2 + \left(\Delta_{\mathrm{theoretical}} - \Delta_{\mathrm{experimental}}\right)^2 \right] \qquad (2-2)$$

In order to restrict the degrees of freedom of the model, we suppose our materials are isotropic and homogeneous. For materials exhibiting an amorphous to microcrystalline transition, the homogeneity hypothesis may not be valid along the growth direction. This can be accounted for by subdividing the grown layer into several layers in our model which can be fitted independently.

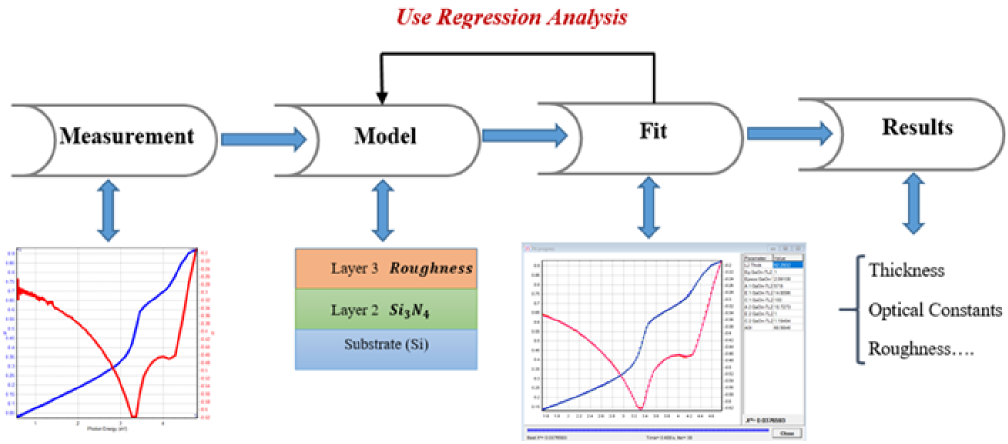

Figure 2-11 Schematic showing the data analysis procedure in ellipsometry

2.3.2.2.4 Dispersion formula for Ga_2O_3 and GaN

Ellipsometry is a versatile tool but it is very sensitive to the choice of the model used for fitting the data. As such, choosing the appropriate dispersion formulas to retrieve the refractive index of our layers is critical. According to the expected nature and chemistry of the fitted material, different dispersion formulas should be used. The dispersion formula is used to calculate the complex dielectric function of the material ε. In this work, for both Ga_2O_3 and GaN, the dispersion of the ultrathin layer was accounted for by a Tauc-Lorentz formula with adjusted parameters.

The Tauc–Lorentz model is a mathematical formula for the frequency dependence of the complex-valued relative permittivity, referred to as the dielectric function. The model has been used to fit the complex refractive index of amorphous semiconductor materials at frequencies greater than their optical band gap. The dispersion relation bears the names of Jan Tauc and Hendrik Lorentz, whose previous works [373] were combined by G. E. Jellison and F. A. Modine to create the model [374][375]. The formula is defined as below:

$$\varepsilon = \varepsilon_1 + \varepsilon_2 \qquad (2-3)$$

$$\varepsilon_1 = \varepsilon_\infty + \frac{2}{\pi}.P.\int_{E_g}^{\infty} \frac{\xi.\varepsilon_2(\xi)}{\xi^2 - E^2}\,d\xi \qquad (2-4)$$

$$\varepsilon_2 = \begin{cases} \dfrac{1}{E} \times \left(\dfrac{A.E_0.C.\left(E - E_g\right)^2}{(E^2 - E_0^2)^2 + C^2.E^2} \right), & E > E_g \qquad (2-5) \\ 0, & E \leq E_g \end{cases}$$

Where:

- E is the photon energy,
- ε is the relative permittivity,
- ε_∞ is the value of the relative permittivity at infinite energy,
- A is a fitting parameter related to the strength of the Lorentzian oscillator,
- C is a fitting parameter related to the broadening of the Lorentzian oscillator,
- E_0 is a fitting parameter related to the resonant frequency of the Lorentzian oscillator,
- E_g is a fitting parameter related to the bandgap of the material,

Solving the integral:

$$\varepsilon_1 = \varepsilon_\infty + \sum \left\{ \frac{A.C.a_{ln}}{2.\pi.\zeta^4.\alpha.E_0}.\ln\left[\frac{E_0^2+E_g^2+\alpha.E_g}{E_0^2+E_g^2-\alpha.E_g}\right] - \frac{A.\alpha_{atan}}{\pi.\zeta^4.E_0}.\left[\pi - arctan\left(\frac{2.E_g+\alpha}{C}\right) + arctan\left(\frac{\alpha-2.E_g}{C}\right)\right] + \frac{4AE_0E_g\left(E^2-\gamma^2\right)}{\pi.\zeta^4.\alpha}\left[arctan\left(\frac{2.E_g+\alpha}{C}\right) + arctan\left(\frac{\alpha-2.E_g}{C}\right)\right] - \frac{AE_0C\left(E^2-E_g^2\right)}{\pi.\zeta^4.E}.ln\left(\frac{|E-E_g|}{E-E_g}\right) + \frac{2AE_0E_gC}{\pi.\zeta^4}.ln\left[\frac{|E-E_g|.(E+E_g)}{\sqrt{(E_0^2+E_g^2)+E_g^2.C^2}}\right] \right\} \qquad (2\text{-}6)$$

Where:

$$a_{ln} = \left(E_g^2 - E_0^2\right)E^2 + E_g^2.C^2 - E_0^2(E_0^2 + 3E_g^2)$$

$$a_{atan} = (E^2 - E_0^2)\,(E_0^2 + E_g^2) + E_g^2.C^2$$

$$\zeta^4 = (E^2 - \gamma^2)^2 + \frac{\alpha^2.C^2}{4}$$

$$\alpha = \sqrt{4.E_0^2 - C^2}$$

$$\gamma = \sqrt{E_0^2 - \frac{C^2}{2}}$$

A Tauc-Lorentz model has been employed to perform a fitting analysis on the experimentally acquired data, facilitating the extraction of the optical properties of the ultrathin film deposited on the substrate. The primary result of the deduced optical properties will be quickly covered in the next section, and there will be a more in-depth look at all the details in Chapter 3.

2.3.2.2.5 Ellipsometry in 2D compounds

We show in this section, as a typical example, the results of ellipsometry conducted on our Ga_2O_3 2D materials deposited on Quartz, and the associated fitting analysis. **.**

Figure 2-12(a) and (b) display the ellipsometry data obtained on the Quartz substrate before and after the deposition of Ga_2O_3 2D material. Comparing these two spectra reveals a distinct signature before and after the deposition, which indicates that the ellipsometry equipment is sufficiently sensitive to detect changes induced by very thin films. This validates that ellipsometry can provide accurate and reliable measurements for 2D materials, which typically have thicknesses on the order of a few nanometers.

Figure **2-12** (a) presents the Is and Ic for both experimental data and fitted data of quartz as a function of wavelength. The data were fitted with a model that includes a single layer of quartz. This layer followed the Classical dispersion formula, and measurements were done at a 55° angle of incidence, which was used as a fitting parameter. After the fitting process, a value of 0.6 was extracted for χ^2, quantifying the difference between the observed data and the values expected based on the model used for fitting. Figure **2-12** (b) shows Is and Ic for experimental data and fitted data of an ultrathin layer of Ga_2O_3 (3nm thickness) deposited on quartz. The measurements were conducted at a 55° angle of incidence, which was also used as one of the fitting parameters. For the fitting, a model was used that included a quartz layer underneath a Ga_2O_3 layer and followed the Tauc-Lorentz dispersion formula. After fitting, values of 2.6 ± 0.72 for Ga_2O_3 thickness and 0.89 for χ^2 were extracted. The fitting results confirm that specific models accounting for the 2D Ga_2O_3 response can reproduce the measured spectra relatively well. Ellipsometry was also extensively used for measuring the effective index of 2D materials before and after the nitridation process, as discussed in Section 3.2.4 of Chapter 3

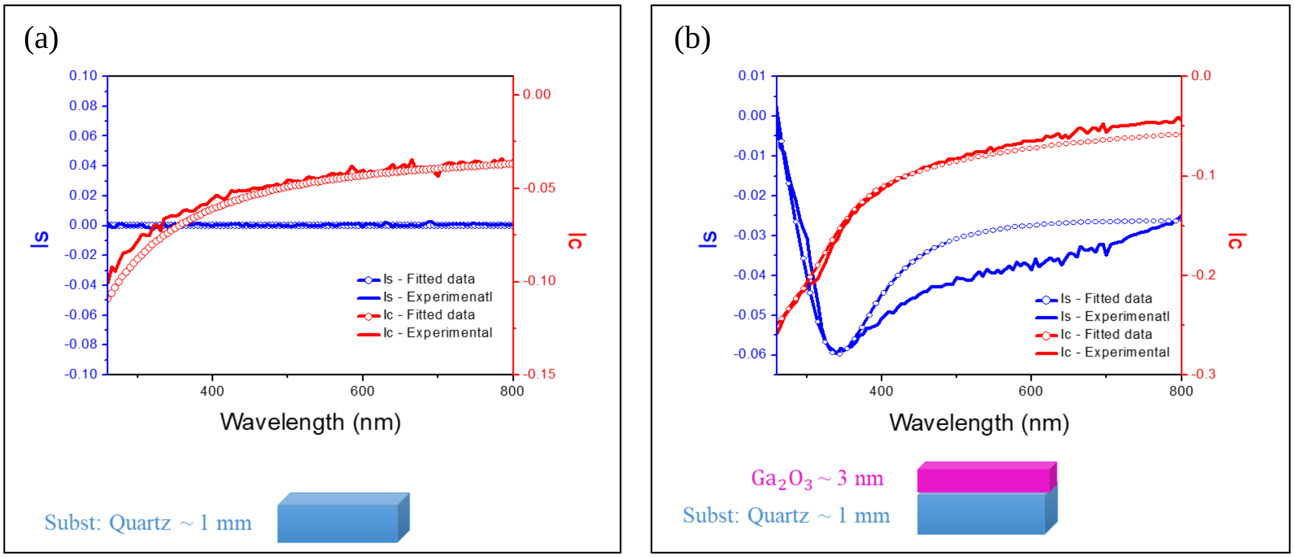

Figure 2-12 Ellipsometry data for quartz substrate before and after deposition of ultrathin Ga_2O_3 layer (a) Experimental and fitted data for a single layer of quartz, showing Is and Ic as functions of wavelength. (b) Experimental and fitted data for an ultrathin layer of Ga_2O_3 (3nm thickness) deposited on quartz, showing Is and Ic as functions of wavelength

2.4 Summary

In this chapter, we presented a process to realize ultrathin Ga_2O_3 and GaN films by liquid metal-based van der Waals squeeze printing technique followed by a plasma-assisted nitridation process. This method was primarily based on the liquid metal chemistry approach that was developed at RMIT a few years ago. During my PhD studies, I mastered it further to provide a better control of the final composition of the 2D material layer between Ga_2O_3 and GaN, as will be shown in chapter 3. Essentially, our approach exploits the oxidation of naturally occurring interfacial oxide of molten gallium to first synthesize ultra-thin Ga_2O_3 layers. A subsequent microwave plasma enhanced nitridation reaction, is then further used to obtain ultrathin 2D GaN sheets. As will be demonstrated in chapter 3, the use of a reactive N_2/H_2 plasma was found to induce the replacement of oxygen atoms with nitrogen. The proposed synthesis method is scalable and fast, providing access to large-area 2D GaN nanosheets. Most specifically, the plasma treatment that allows us to reliably control the composition of the resulting 2D material layer. Alterations to the plasma treatment conditions outlined in this chapter enable precise manipulation of the composition within the Gallium OxyNitride (GaO_xN_y) layer, which acts as an intermediate between GaN and Ga_2O_3 that will be discuss in the next chapter. Most importantly, I will demonstrate in chapter 4 that, as intended for optoelectronic applications, this method lends itself to the integration of the resulting 2D materials within chip-based optical devices.

This chapter also presented the different characterization techniques (XPS, AFM, TEM, and ellipsometry) that we used to characterize the composition, structure and optical properties of the resulting nm-thick, GaN, and Ga_2O_3 ultrathin films. We showed that these characterization tools are adequate to characterize ultra-thin layers of materials, confirming their sensitivity to 2D materials.

The next chapter will present the combined characterization results and discuss the resulting properties of Ga_2O_3, GaN and GaO_xN_y ultra-thin layers that can be achieved in a controlled manner with this approach.

Chapter 3: Characterization Results

The main goals of this chapter are:

- Conducting a thorough characterization of the ultra-thin layers produced through the synthesis process detailed in Chapter 2, utilizing various characterization techniques to examine their composition and structural properties.
- Evaluating the effectiveness of plasma-assisted nitridation as a practical method for converting Ga_2O_3 into GaN.
- Demonstrating the adaptability and potential of the nitridation process by highlighting its capability in synthesizing ultra-thin intermediate GaO_xN_y layers, and assessing their unique characteristics.

3.1 Introduction

In the previous chapters, we delved into the fabrication of ultarthin Ga_2O_3 and GaN using the liquid metal chemistry method. The use of PECVD for transforming Ga_2O_3 to GaN was also discussed, along with the characterization tools employed in the study. In this chapter, we present the results of our characterization techniques introduced in chapter 2; namely AFM, TEM, XPS, Ellipsometry, Raman, and DFT, which confirm the effectiveness of our synthesis method as well as the nitridation process. AFM and TEM were utilized to study the morphology, thickness, and crystalline structure of ultrathin Ga_2O_3 and GaN. XPS provided a comparative analysis of the material composition before and after the nitridation process. Furthermore, we examined the optical properties of ultrathin Ga_2O_3 and GaN through the measurement of their refractive indices by spectroscopic ellipsometry. These results were then compared with those obtained from density functional theory (DFT) calculations conducted by our collaborators at NANO Istituto Nanoscienze(Modena-Italy) . Notably, our collaborators at CEA-LETI-LTM laboratory (Grenoble, France) performed Raman measurements to furnish additional information regarding the structure of the synthesized material.

As we transition to Chapter 3, our focus will shift to exploring GaO_xN_y compounds, which represent an intermediate phase between Ga_2O_3 and GaN, as well as examining our characterization results for these compounds. The presence of intermediate phases in the transformation process between ultrathin Ga_2O_3 and GaN is a significant aspect of this research. Within this chapter, we will scrutinize the various parameters that influence the formation of these intermediate phases during the PECVD process. To analyze the intermediate phases, we will employ the characterization tools introduced in Chapter 3. XPS will be deployed to investigate the elemental composition and chemical states of the intermediate phases. Most importantly, through XPS measurements, we demonstrate that this two-step process allows us to access intermediate GaO_xN_y compounds. Additionally, we will obtain information on the distinct optical properties of the intermediates through ellipsometry measurements. This study significantly broadens our knowledge of GaO_xN_y compounds, which have been relatively under-researched compared to their GaN and Ga_2O_3 counterparts[376].

In conclusion, this chapter offers a thorough analysis of the topography, structure and optical properties of ultrathin Ga_2O_3 (before nitridation), GaN (after nitridation), and their intermediate levels. Our aim is to augment our understanding of ultrathin gallium compounds and to explore the potential applications of these materials across various fields.

3.2 Characterization

The composition and optical properties of these ultra-thin-films are characterized using XPS, AFM, TEM, Ellipsometry and Raman measurements. Finally, the optical indices measured by ellipsometry are compared with theoretical results obtained by density functional theory (DFT).

3.2.1 AFM results for Ga_2O_3 and GaN

In order to explore the uniformity of the synthesized ultrathin GaN sheets, atomic force microscopy (AFM) was conducted on the deposited layer. **Figure 3-1**(a) shows the results from the measurement of Ga_2O_3 before nitridation, it shows a homogenous deposited layer with 3 ± 0.2 thickness. AFM was conducted on the ultrathin layer after the full nitridation process as well (**Figure 3-1** (b)). The GaN was found to have formed a continuous and atomically flat nanosheet, approximately 3 ± 0.2 nm in thickness across an area of a few microns. This thickness was found to be similar to that of the initial Ga_2O_3 layer, showing that the nitridation did not affect the thickness of the film. In general, the ultrathin sheets featured minimal cracks and holes, and relatively homogeneous thickness across large distances, on the order of ~100µm (see **Figure 2-6**(b) in Chapter 2). This length scale is compatible with the typical size of integrated optical devices, as intended for this PhD study.

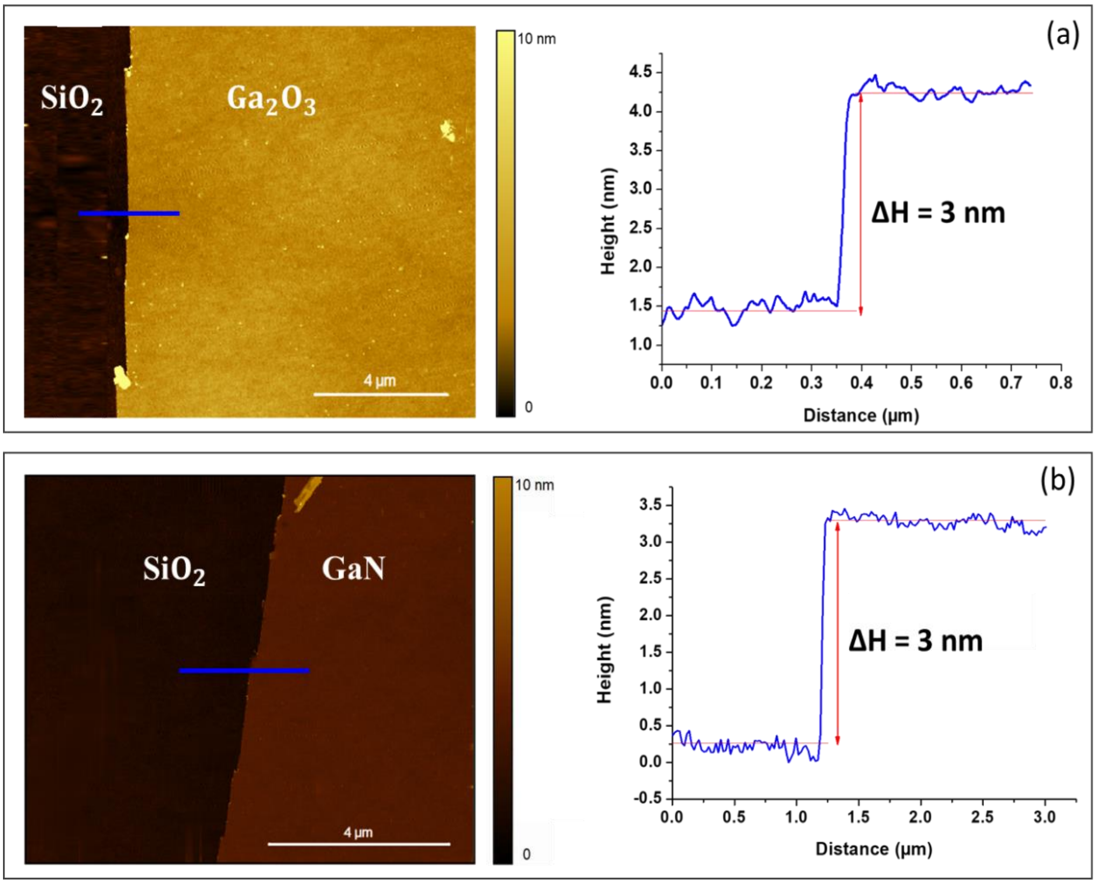

Figure 3-1 Morphology of 2D Ga_2O_3 and GaN. (a) AFM topography image of a Ga_2O_3 sample before nitridation, taken at the edge of a nanosheet; the height profile was measured along the blue line (b) AFM topography image of a GaN sample after nitridation, taken at the edge of a nanosheet; the height profile was measured along the blue line

3.2.2 XPS result for Ga_2O_3 and GaN

To ascertain that a quantitative conversion of Ga_2O_3 to GaN occurred, XPS was utilized and relevant spectra were compared before (**Figure 3-2**(a)) and after nitridation (**Figure 3-2** (b))**.** It is important to note that the full spectra provide an overview of the elemental composition, but the difference between the peaks corresponding to gallium oxide and gallium nitride are not clearly distinguishable in this representation. To gain a deeper understanding of the changes undergone by nitridation process, a detailed examination of the peaks is necessary which is shown in **Figure 3-3**.

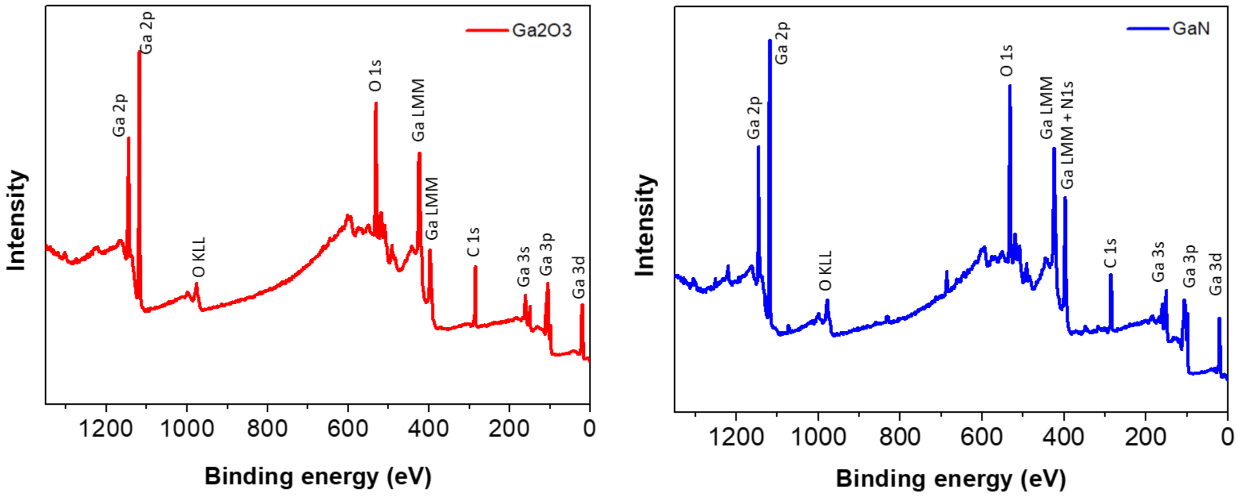

Figure 3-2. XPS spectrum of ultrathin layer of Gallium before and after nitridation (a) Illustrative XPS spectrum of Ga_2O_3 on SiO_2/Si (before nitridation) and (b) Illustrative XPS spectrum of GaN on SiO_2/Si (after nitridation)

In **Figure 3-3**, a comparative analysis of the XPS peaks is conducted to compare the variations in peak before (**Figure 3-3** (a),(b),(c)) and after the nitridation process (**Figure 3-3** (d),(e),(f)), using the plasma parameters indicated in the previous chapter. First of all, **Figure 3-3** (a) and (d) show the XPS spectra of a doublet in the Ga 2p region centered at ~1118.19 eV and ~1144.8 eV corresponding to $2p_{3/2}$ and $2p_{1/2}$, respectively, in good agreement with the spectral values for bulk and ultrathin Ga_2O_3 and GaN [377][10][378]. As anticipated, these signatures do not exhibit significant changes between Ga_2O_3 and GaN, with the two peaks observed at the same positions for both samples. Indeed, the electronic configuration of gallium remains similar in both compounds, with only the anion (oxygen or nitrogen) being replaced during the transformation process. As a result, the Ga 2p doublet peaks serve as a reliable marker for the presence of gallium in both Ga_2O_3 and GaN films, while further analysis is required to differentiate between the two materials and investigate the extent of the conversion. To that aim, we compared next the O1s peak for Ga_2O_3 and GaN (i.e. before and after the nitridation process).In **Figure 3-3** (b) (Ga_2O_3), we can see a double peak for O 1s: the peak at ~530.9 eV can be assigned to the O-Ga-O bonds in gallium oxide, and the O 1s peak at slightly larger binding energy ~532.2eV can be ascribed to the Si-O bonding from the SiO_2 substrate layer underneath [351]. In contrast, after the nitridation process, only one single O 1s peak is detected on **Figure 3-3** (e), centered at ~532.2 eV. The disappearance of the shorter binding energy peak thus confirms the effectiveness of the nitridation process for fully converting Ga_2O_3 into GaN.

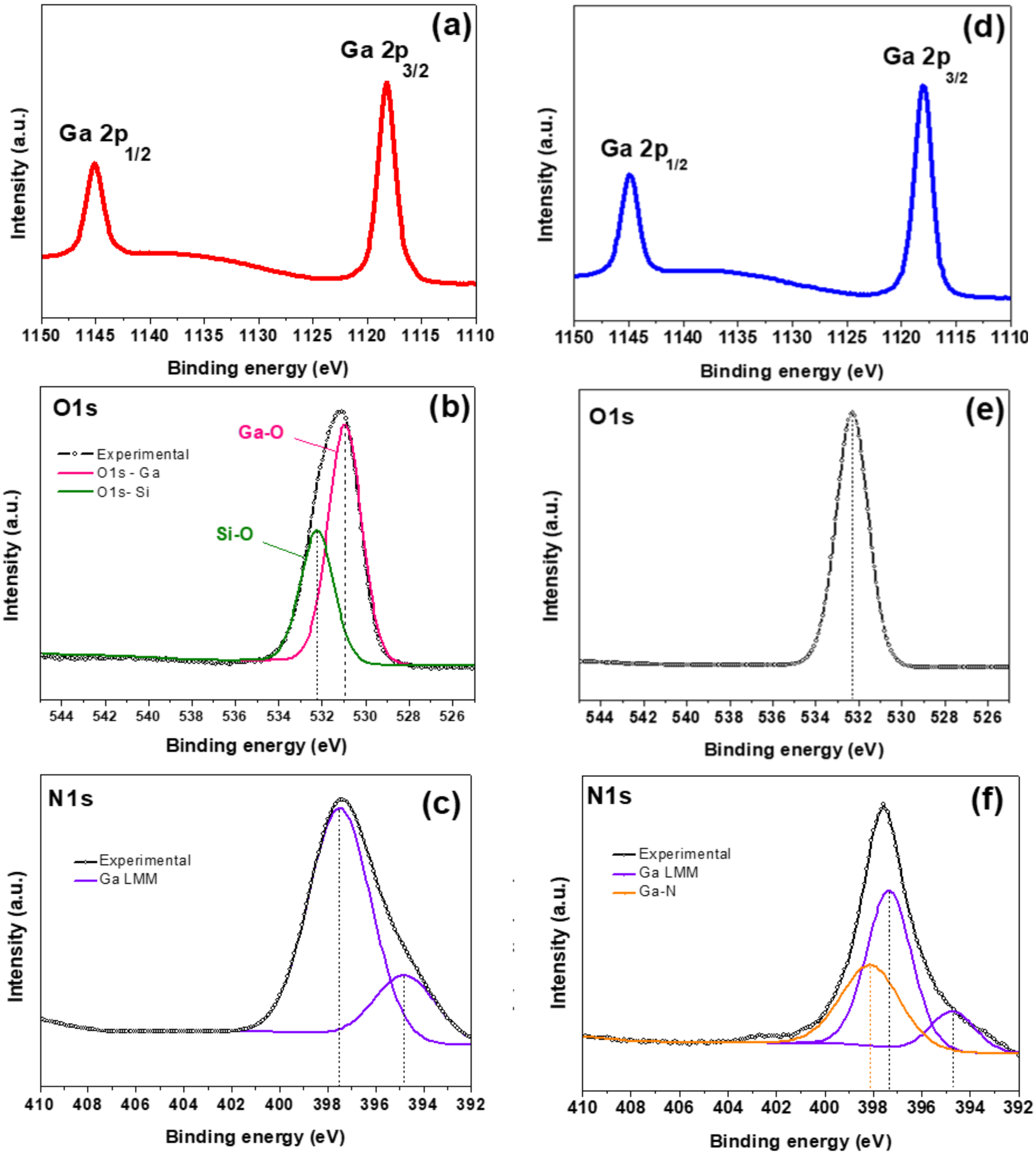

Figure 3-3 Material characterization of ultra-thin Ga_2O_3 (before nitridation (a,b,c)) and ultra-thin GaN (after the nitridation (d,e,f)) on a SiO_2/Si substrate.(a, b, c) XPS results of the ultrathin Ga_2O_3 for the spectral regions of interest, around (a) the Ga 2p peak and (b) the O 1s peak (The black line represents the experimental data, while the colored line shows the fitted data) (c) the N1s peak (d, e, f) XPS result for the the ultra-thin GaN around (d) the Ga 2p peak and (e) the O 1s peak (f) the N1s peak (The black line represents the experimental data, while the colored line shows the fitted data).

Figure 3-3 (c) shows the XPS spectrum of N1s before nitridation, this spectrum shows two pronounced peaks at 394.7 eV and 397.4 eV, corresponding to the Auger lines of gallium (Ga LMM)[379][380]. In contrast, in **Figure 3-3** (f) the XPS spectrum of GaN exhibits a main peak with a slightly larger binding energy centered at 398.1 eV, which is attributed to nitrogen bonded to gallium (Ga - N)[381][380]. This peak signifies the formation of the Ga-N bond, which is not observed in the XPS analysis of Ga_2O_3. It is unfortunately not prominent since it is overlapped with the Ga-LMM peak and is thus not used for quantification.Consequently, it is deduced that the presence of the two peaks at binding energies of 394.7 eV and 397.4 eV, characteristic of the Auger lines of gallium (Ga LMM), persist in GaN. However, the emergence of an additional peak at 398.1 eV (orange line), exclusive to the post-nitridation spectrum, substantiates the conversion of oxygen to nitrogen, and corroborates the formation of Ga-N bonds. N1s is the allowable range of the Nitrogen binding energy for the Thermo Fisher Scientific XPS instrument. We have performed control experiments by measuring the Auger peaks of Ga, GaN and Ga_2O_3 within the binding energy ranges of Nitrogen to identify and deconvolve Ga LMM Auger peaks. The Ga-LMM has a lower binding energy than that of metal Nitride peaks.

3.2.3 TEM result for Ga_2O_3 and GaN

To gain further insight into the atomic structure of the synthesized Ga_2O_3 and GaN nanosheets, TEM and HRTEM were utilized to further characterize the morphology and assess the crystallographic properties of the Gallium sheets before and after nitridation. In this case, gallium oxide was directly deposited onto a Si_3N_4 TEM grid. **Figure 3-4**(a) shows that no crystalline structure is visible in the TEM measurements of the ultrathin Ga_2O_3, confirming that the latter has an amorphous structure. Afterwards, the Ga_2O_3 deposited on the Si_3N_4 TEM grid was converted to GaN using the above mentioned plasma treatment. Ultrathin nanosheets could be found during TEM imaging, with the sheets being highly translucent, indicating the thin nature of the final GaN sample (**Figure 3-4** (b)) HRTEM confirms the crystalline nature of the synthesized GaN with a lattice spacing of ~0.189 nm, corresponding to the (102) planes of wurtzite GaN.

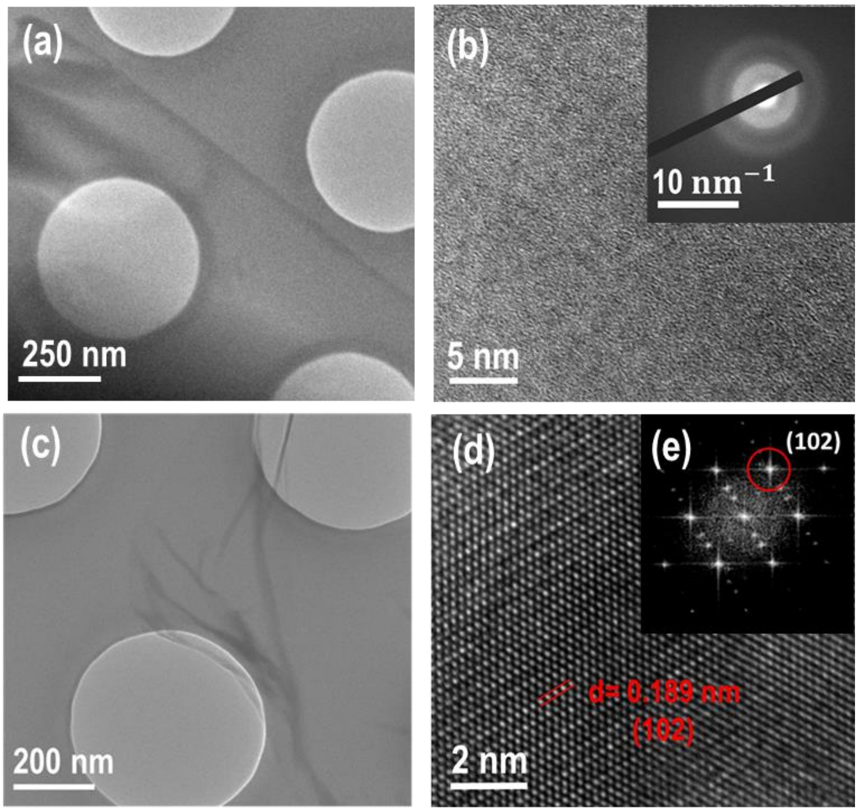

Figure 3-4 Structural characterization of the ultrathin film before and after full nitridation (a) TEM micrograph of the Ga_2O_3 (b) Ga_2O_3 lattice fringe and the corresponding SAED pattern (c) HRTEM micrograph of the GaN (d) The insets represent the lattice fringes (e) FFT pattern demonstrating (102) plane of the GaN sheet

3.2.4 Ellipsometry results for Ga_2O_3 and GaN

The knowledge of the Ga_2O_3 and GaN optical index is essential to properly design gallium-based optoelectronic devices. Although the optical properties of Ga_2O_3 thin films (down to sev. 10’s nm) have been investigated [382]–[385], there remains a lack of experimental measurements of the properties of ultrathin Ga_2O_3 sheets with a few nanometers thickness. Similarly, for GaN, the available data focus on either bulk or thin layers (mentioned in Table3.2) and are not directly applicable to ultrathin (~3nm) GaN sheets [386]–[390]. Therefore, the properties of both materials in their 2D form remains elusive. Spectroscopic ellipsometry (SE) has been used to study bulk optical properties of Ga_2O_3 [391]–[395] and GaN [39], [396]–[400]. Here, we characterized the Ga_2O_3 and GaN ultrathin films with spectroscopic ellipsometer. The substrate used for all the ultra-thin films was SiO_2/ Si with a 3 nm thick silica layer.The refractive indices of Ga_2O_3 and GaN were determined through the fitting of Is and Ic parameters of SE data obtained before or after the full nitridation process with a Tauc-Lorentz dispersion formula (See section 2.3.2.2.4 in Chapter 2:), wherein a 3 nm thick layer of the respective material was placed on a SiO_2/ Si substrate. **Figure 3-5**(a) and (b) displays two sets of data (Is and Ic) plotted against wavelength for Ga_2O_3 and GaN, respectively. Circles represent the fitted data from our model, while solid lines represent the experimental data.In addition, **Table 3-1** enumerates the parameters deduced from our experimental data through the fitting procedure. χ^2 is a statistical measure used to quantify the difference between the observed data and the values expected based on the model used for fitting. In this case, the low χ^2 value suggests that our model provides an excellent fit to the observed data, meaning that the model effectively captures the behavior of the materials. In both materials, the film thickness ascertained through ellipsometric analysis exhibited close agreement with the values obtained via AFM, as depicted in **Figure 3-1**.

Regarding the bandgap, denoted as E_g, for Ga_2O_3 it was found to be 3.8±0.11 eV, which is intermediate between the bandgap of bulk β-Ga_2O_3 (4.8 eV) /γ−Ga_2O_3 (7.0eV)[401] and that of a monolayer (2.9 eV)[402]. Similarly, for GaN, the extracted bandgap was 2.4±0.2 eV, which is lower than the bandgap of bulk GaN (3.4 eV)[403] and closer to a single-layer (2.95 eV)[404] .These findings confirm that the bandgap of the synthesized ultra-thin materials are distinct from both bulk and monolayer forms, which is consistent with our results given the thickness of the materials (3 nm) being greater than that of a monolayer but less than their bulk (for GaN is lower than the monolayer). AOI denotes the Angle of Incidence, which was determined and subsequently fixed at 70 degrees in accordance with the measurements.

Table 3-1 Fit parameters of the dispersion relation as obtained from ellipsometry analysis of the Ga_2O_3 and GaN ultrathin films deposited at SiO_2/Si substrate

Parameter	**Ga_2O_3**	**GaN**
χ^2	0.04	0.07
Thickness (nm)	3.2±0.07	3.2±0.8
E_g (eV)	3.8±0.11	2.4±0.2
AOI °	69.9±0.005	71±0.01

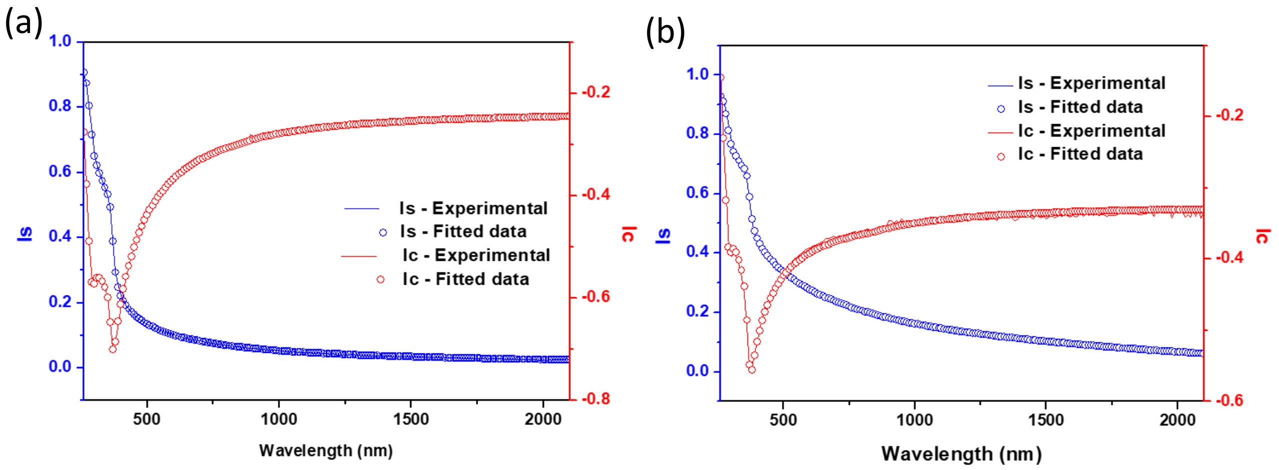

Figure 3-5 Is and Ic as a function of wavelength (a) Ga_2O_3 (b)GaN (The solid lines are experimental data while the circles show the fitted data)

From this fitting procedure, we can extract the optical index of the films, so as to assess the linear optical properties of the Ga_2O_3 and GaN ultra-thin materials and their potential difference. **Figure 3-6**(a) shows the refractive index (n) and extinction coefficient (k) of the Ga_2O_3 material. The resulting refractive index is around 1.89 at 632nm and 1.865 at 980 nm wavelength. Despite the reduced thickness of our films (~3nm), these values are very close to those measured for Ga_2O_3 68nm thick films (n=1.84 at 632 nm) [405], or Ga_2O_3 800nm thick films (n=1.82 at 600 nm) [406]. Similarly, **Figure 3-6** (b) displays the n and k spectra of GaN measured after the full nitridation process. The extracted refractive index is 2.318 at 632 nm and 2.1 at 1200 nm, showing that the nitridation process was effective in turning the oxide films into GaN with very distinct optical properties. Again, this refractive index value is only slightly lower than the values found in the literature for bulk GaN crystals (n = 2.34 at 632nm), metalorganic chemical vapor deposited (MOCVD) GaN layers (n = 2.33 at 632 nm) on sapphire from Ref. [396] and GaN epilayers (n~2.42 at 632 nm) from Ref. [407]. Moreover, the refractive index at 1200 nm is consistent with Ref [408] for GaN films with 532 nm thickness.Moreover, the extinction coefficient, denoted as “k”, an equally important parameter, we observe a remarkable trait in both Ga_2O_3 and GaN at a wavelength of 1550 nm. The extinction coefficient, which is an indicator of the absorption characteristics of the material, is found to be 0 for both materials at this wavelength. This essentially implies a negligible absorption of the incident light, highlighting the high transparency of the materials in this spectral region. This behavior of Ga_2O_3 and GaN at 1550 nm is of essential significance, especially in the context of optical communication technologies, where the 1550 nm wavelength is a standard for fiber optic transmission.

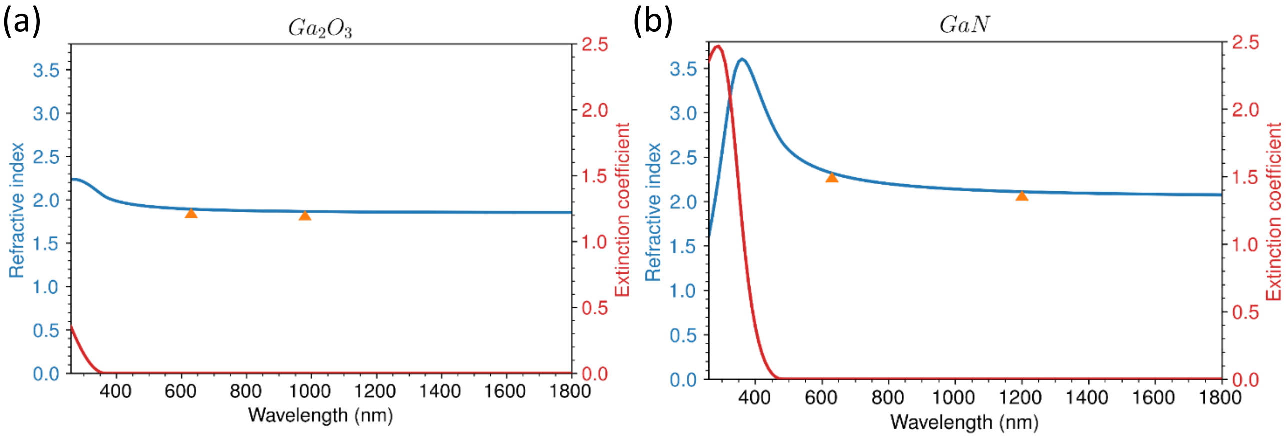

Figure 3-6 Optical properties of Ga_2O_3 and GaN ultra-thin films, extracted from SE in the range 260–1800 nm. (a) shows the refractive index n and extinction coefficient k of Ga_2O_3 as a function of wavelength (triangles shows n=1.89 at 632nm and n=1.865 at 980 nm) (b) shows the refractive index n and extinction coefficient k of GaN as a function of wavelength (triangles shows n=2.318 at 632nm and n=2.1 at 1200nm)

A summary of the comparison of our work and the literature from the measurement of Ga_2O_3 and GaN refractive index (n) at different thicknesses and wavelengths (λ) is reported in **Table 3-2**. Considering that our measured value for 3nm thick films is in the same range as for bulk and thick films, we conclude that the refractive index of these materials remains roughly constant regardless of changes in film thickness down to about 3nm. In addition, by comparing the refractive index of Ga_2O_3 and GaN at the same wavelength, we note that the relatively high index difference (~0.42), featuring a significant ~20% variation, could be highly relevant for adjusting the optical properties of silicon photonic devices on top of which this ultrathin material is deposited.

Table 3-2 Comparison of refractive index measurement for Ga_2O_3 and GaN at different thicknesses

Material	Thickness	N	λ (nm)	Ref
Ga_2O_3	Bulk	1.84-1.88	980	[409]
Ga_2O_3	67.9 nm	1.84	632	[405]
Ga_2O_3	31.9-2468 nm	1.89	295-826	[410]
Ga_2O_3	30 nm	1.87	632	[395]
Ga_2O_3	89 nm	1.85	632	[411]
Ga_2O_3	**3 nm**	**1.89**	**632**	**This work**
GaN	Bulk	2.34	632	[412]
GaN	2.3 µm	2.42	632	[407]
GaN	1.5 µm	2.33	632	[390]
GaN	1.3 µm	2.37	632	[389]
GaN	1.06 µm	2.34	632	[399]
GaN	532 nm	2.1	1200	[408]
GaN	**3 nm**	**2.31**	**632**	**This work**

3.2.5 DFT result for Ga_2O_3 and GaN

In addition, density functional theory (DFT) calculation was used by our collaborator at CNR-NANO Istituto Nanoscienze (Modena-Italy) to study crystallographic and optical indices of GaN and Ga_2O_3.

First principles simulations were carried out to corroborate the optical properties of GaN and Ga_2O_3. The theoretical calculations were performed within the framework of density functional theory (DFT) as implemented in the Quantum Espresso package [413] (see the methods section). In order to get rid the statistical complexity of dealing with amorphous systems, in this work we considered the electronic and optical properties only of Ga_2O_3 crystal in the monoclinic phase. Even though this may appear as a too crude approximation, this choice is justified by the well-known observation [109-110] that the polar nature of the bonds in metal-oxides (with respect, e.g. to the covalent character of Si or Ge) makes the system almost insensitive to structural distortions. As a consequence, the optical properties of most amorphous oxides are very similar to their crystalline counterpart [109-110].

Figure 3-7 shows the bulk unit cells of Ga_2O_3 (panel a), and GaN (panel b) that were considered in the calculations. The optimized lattice parameters for monoclinic β- Ga_2O_3 crystal are a= 12.42 Å, b= 3.08 Å and c= 5.87 Å, b=103.74°, while those for the wurtzite GaN are a=b= 3.22 Å and c= 5.24 Å, in good agreement with previous DFT calculations [414][415].

The density of states (DOS) and band structure of β- Ga_2O_3 and GaN are shown in **Figure 3-7** (c) and (d), respectively. The well-known underestimation of the band gap (Eg) due to the standard DFT functionals has been corrected by including a Hubbard-like potential on each chemical species, within the DFT + U frameworks [416]. Both materials have a direct band gap, namely Eg=2.93 for GaN and Eg=4.89 eV for β- Ga_2O_3, The calculated values are very close to those calculated at HSE level, and in very good agreement with experimental data, confirming the numerical accuracy of the methodology used in our calculations[417]. The projected-DOS plots indicate that in both cases the top of the valence band has mainly a non-metal, i.e. O, N, character, with a small contribution from Ga sp-orbitals. The bottom of conduction band has an almost equal contribution of O (N) and Ga orbitals. The different polarity of the Ga-O and Ga-N bonds is mainly responsible for the different bandgap, and thus of the different optical properties. Further localized states close to the mobility gap might appear in the amorphous structure of Ga_2O_3 [418]. This does not change the overall scenario described below about the optical response of the metal-oxide system.

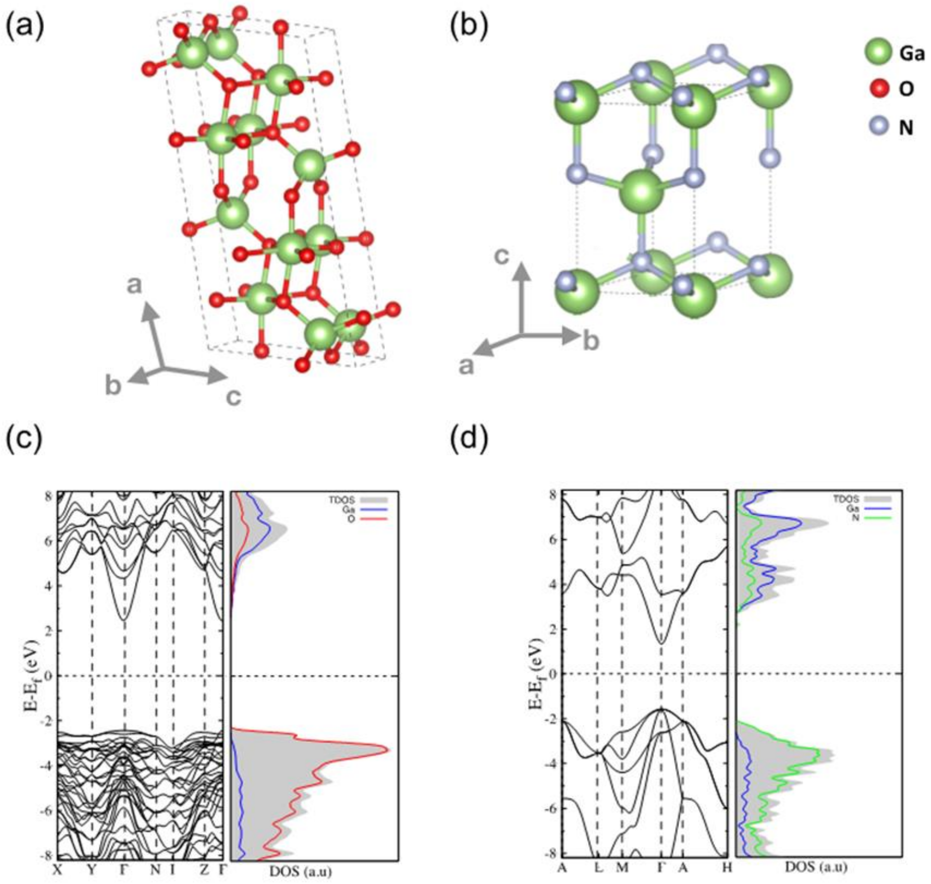

Figure 3-7 Atomic structure of (a) β-Ga_2O_3, and (b) GaN bulk crystals. Bandstructure (left panels), total and atom-projected (right panels) of (c) β-Ga_2O_3, and (d) GaN, respectively. Zero energy reference is set to the Fermi level (Ef) of each system.

The optical properties are evaluated from first principles through a band-to-band single-particle approach based on a generalized Drude−Lorentz formulation of the macroscopic dielectric function $\hat{\varepsilon} = \varepsilon_1 + i\varepsilon_2$. The refractive index (n) and extinction coefficient (k) are straightforwardly obtained from the algebraic transformation of the real (ε_1) and the imaginary (ε_2) part of the dielectric function.

Figure 3-8 shows the refractive indexes and extinction coefficients spectra of Ga_2O_3 (panel a) and GaN (panel b) ultrathin layers obtained from the SE experiments compared with the DFT results about corresponding bulk crystals. The theoretical absorption edge is at λ=253 nm (λ=423 nm) for Ga_2O_3 (GaN), respectively, that corresponds to the valence-to-conduction bandgap. Despite the numerical differences (mostly probably related to the effect of the residual presence of defects and impurities) the agreement between the experimental and DFT optical indices brings two important conclusions: i. the experimental data for GaN well fit the results for crystalline (i.e. ordered) phase. This corroborates the analysis of the structural quality of the ultrathin layer (as observed by TEM, section 3.2.3) and the effectiveness of the nitridation process. The good agreement observed also in the Ga_2O_3 case relies on the well-known observation that for metal-oxides the highly polar character of the bonding makes the systems less sensitive to structural distortion and medium-range order[419] [420]. Thus the optical properties of metal-oxides in the amorphous and crystalline phases are very similar. ii. The experimental data for ultrathin layers well fit the results for extended bulk (i.e. extended) materials. This confirms the observation that ultra-thin films fast recover the bulk/thick film properties, getting rid of strong-localization and or major surface effects.

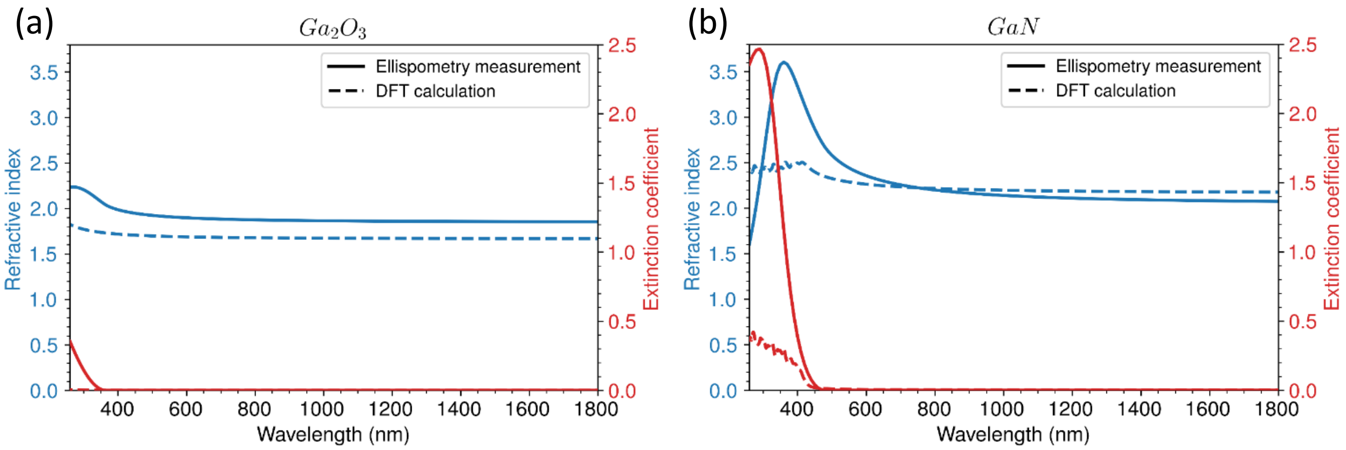

Figure 3-8 Optical properties of Ga_2O_3 and GaN ultrathin films, extracted from DFT in the range 260–1800 nm. (a) Show the refractive index n and extinction coefficient k of Ga_2O_3 as a function of wavelength (b) shows the refractive index n and extinction coefficient k of GaN as a function of wavelength.

3.2.6 Raman measurement

To gain a deeper understanding of the structure of synthesized ultrathin materials, we conducted Raman measurements on deposited gallium on SiO_2/Si substrates both before and after the nitridation process. These measurements were carried out by our collaborator at the CEA-LETI-LTM laboratory in Grenoble, France. The instrument employed for this purpose was LabRAM Soleil_Impact_Renishaw, which is renowned for being an apt tool for studying 2D and ultrathin materials. The experimental conditions under which the measurements were taken are as follows: Filter = Power study (max 500 mW), Laser = 473 nm, Hole = 100 µm, Objective = 100x, Accumulations = 20, and Acquisition Time = 10 seconds.

In **Figure 3-9**, broad bands attributed to the bending and stretching of the Ga-O bond can be observed in the Raman spectrum of γ-Ga_2O_3. This observation confirms the γ-phase of Ga_2O_3 and also strongly supports the notion of γ- Ga_2O_3 having low crystallinity[421] . These findings are in agreement with our TEM results, as depicted in **Figure 3-4**, which show the amorphous structure of Ga_2O_3. Furthermore, recent studies have reported that the γ- Ga_2O_3 phase is not completely crystalline but may exhibit varying degrees of crystallinity. It is regarded as either an amorphous phase or a partially crystalline phase. The crystalline structure of γ- Ga_2O_3 may contain defects, imperfections, or structural disorders that bestow specific properties upon the material[422] .It is imperative to highlight that the crystallinity of γ- Ga_2O_3 can fluctuate depending on the growth conditions or preparation methods employed. In certain instances, regions of crystalline order may emerge, while other portions of the structure may remain more disordered[422].

In **Figure 3-9**, the red spectra represents the Raman measurements for GaN. The detected peak is consistent with GaN peaks reported in the literature [423][424][425]. The observed red shift of 5 cm^{-1} can be attributed to the marginally compressive strain in the sample relative to that of Ga_2O_3/Si. It is also show that the intensity of Raman spectra slightly increases after the growth of GaN films. These results corroborate the transformation of γ- Ga_2O_3 into γ-GaN on Si through nitridation.

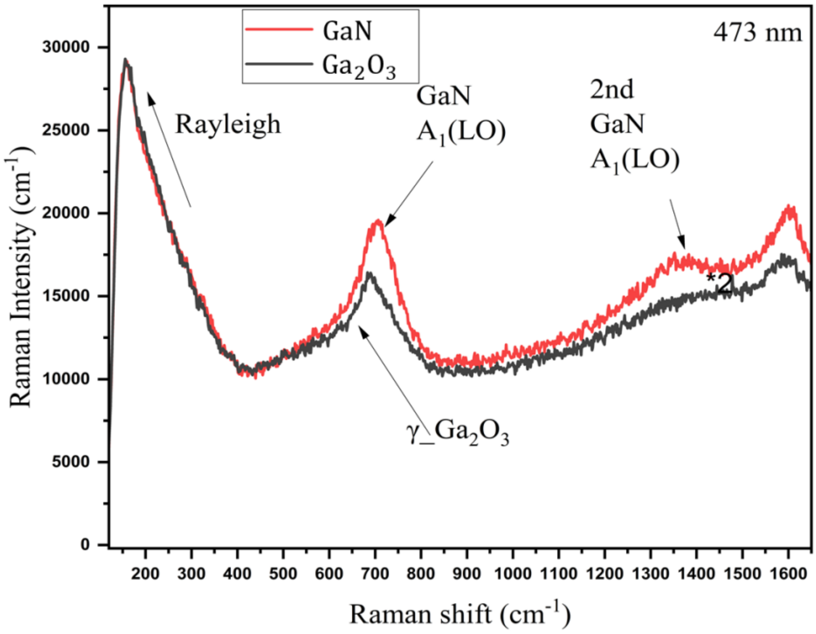

Figure 3-9 Raman spectra of Ga_2O_3 (Black line) and GaN (Red line) on SiO_2/Si (Before and after nitridation)

3.3 Tailoring GaO_xN_y Composition via Plasma assisted nitridation

Although extensive research has been conducted on Ga_2O_3 and GaN, limited information is available on their compounds, specifically GaO_xN_y [376]. Given that Ga_2O_3 and GaN find broad applications in luminescent and power devices, investigating their alloys could offer opportunities to enhance device performance by controlling their composition and crystalline structure. For example, by modifying its optical bandgap, GaO_xN_y may serve as an efficient photo catalyst [426]–[430]. Some experimental studies have reported the conversion of GaN to Ga_2O_3 through oxidation, as well as the transformation of Ga_2O_3 to GaN via nitridation [431][432][433]. Nonetheless, no comprehensive research has been conducted on GaO_xN_y films while progressively altering the O/N composition ratio. In one of the pioneering studies by H. Akazawa, the fabrication of GaO_xN_y thin films was investigated [434]. These films were produced by RF magnetron sputtering on Si (100) substrates at room temperature, using O_2 and N_2 gas flows at different rates. However, the film thickness in Akazawa's work ranged between 300 and 400 nm. In contrast, our research focuses on much thinner films with a thickness of approximately 3 nm, representing a novel approach to the study of GaO_xN_y films and their properties.

In this research, I explore the formation of intermediate levels during the transformation of ultrathin Ga_2O_3 to ultrathin GaN using plasma. Since the presence of oxygen can significantly affect the material's structural, electrical, and optical properties, in this context, during the nitridation process, careful control of the plasma conditions, such as power, pressure, and gas flow, could enable us to tailor the level of oxygen substitution. The ultrathin Ga_2O_3 films are fabricated using the squeeze printing technique of liquid metal chemistry method (explained in Chapter 2 section 2.2.2.1 and 2.2.2). To investigate the intermediate levels and understand how the degree of oxygen substitution in the developed ultrathin material samples could be changed, the nitridation process was conducted under various powers and time durations. Modifying the nitridation time allows us to monitor the gradual transition and identify the various intermediate levels during the transformation process. This approach enables us to determine the optimal conditions for achieving desired intermediate compositions and properties. In addition to varying the time, I also adjusted the PECVD power. By investigating the impact of power on the transformation process, we can better understand the role of plasma energy in driving the reaction kinetics and controlling the formation of intermediate levels. After fabricating the intermediate levels, we will analyze its composition using XPS. Detailed XPS results for these intermediate levels will be presented in the subsequent characterization section, along with the analysis and discussion.

Overall, this comprehensive study of the intermediate levels formed during the transformation of ultrathin layer of Ga_2O_3 to ultrathin layer of GaN using PECVD provides valuable insights into the underlying mechanisms and the influence of process parameters on the resulting material properties. By systematically varying the time and power, we can elucidate the optimal conditions for achieving specific intermediate compositions of these materials for various applications.

3.3.1 XPS result for GaO_xN_y

The presence of residual oxygen can significantly affect the structural, electrical, and optical properties of the material. In this context, during the nitridation process, a carefully control of the plasma conditions, such as power, pressure, and gas flow, enable the tailoring of the amount of the oxygen substitution. In order to explore how the oxygen substitution can be controlled, the nitridation process was conducted under various powers and time duration. First, the plasma was generated for 10 minutes at different powers of 100 W, 150 W and 200 W.

High-resolution spectra were achieved by 50 eV pass energy and 70 number of scans. The typical penetration depth of XPS is ~10 nm of the surface. The liquid metal exfoliated materials thickness is always below this range. In addition, these deposited layers are flat and smooth. The few nm thickness nature of the sheets is always within the interaction volume of the XPS. The sensitivity factor of N 1s, Ga2p and O 1s are 1.8, 21.4 and of 2.93, respectively obtained from Thermo Fisher Advantage Software version 5.9. The software automatically incorporates the correct sensitivity factor during the fitting of the spectra to calculate the atomic ratios. In addition, the spot size of XPS was set to 400 µm covering large lateral area of the sheets and the measurements were repeated on several samples (N=x) resulting in a small measured standard deviation.

In the XPS spectra, the peaks corresponding to gallium, oxygen, and nitrogen were fitted, using Gaussian functions, to estimate the area under each peak, which is proportional to the concentration of the respective element. These raw peak areas were then corrected using element-specific sensitivity factors to account for the different cross-sections for photoelectron emission among the elements. The corrected peak areas were normalized such that the sum of the atomic percentages of all elements equals 100% for each set of conditions. As displayed in **Figure 3-10**(a), XPS results show that by increasing the power, the atomic percentage of oxygen in the sample decreases, while the percentage of nitrogen increases, demonstrating a more effective replacement of oxygen with nitrogen bonds to Gallium. By increasing the power to 200 W, the complete removal of oxygen was achieved. Alternatively, **Figure 3-10** (b) presents the XPS results of 5 samples with different nitridation times varying from 0 to 10 min. During this experiment, power was kept constant at 150 W. Over time, as plasma exposure continues, the Ga_2O_3 film is gradually converted to GaN. This evidence is proved by the decrease in the oxygen percentage to gallium bond from 57.2% to 2.5% and an increase in the rate of nitrogen bonds to gallium from 0% to 46.5%.This demonstrates that the control of either the power and/or time duration of the plasma assisted nitridation process allows us to reliably obtain intermediate compositions of GaO_xN_y films. This provides us with an additional degree of freedom to change the optical properties of the ultra-thin film deposited on top of optical devices.

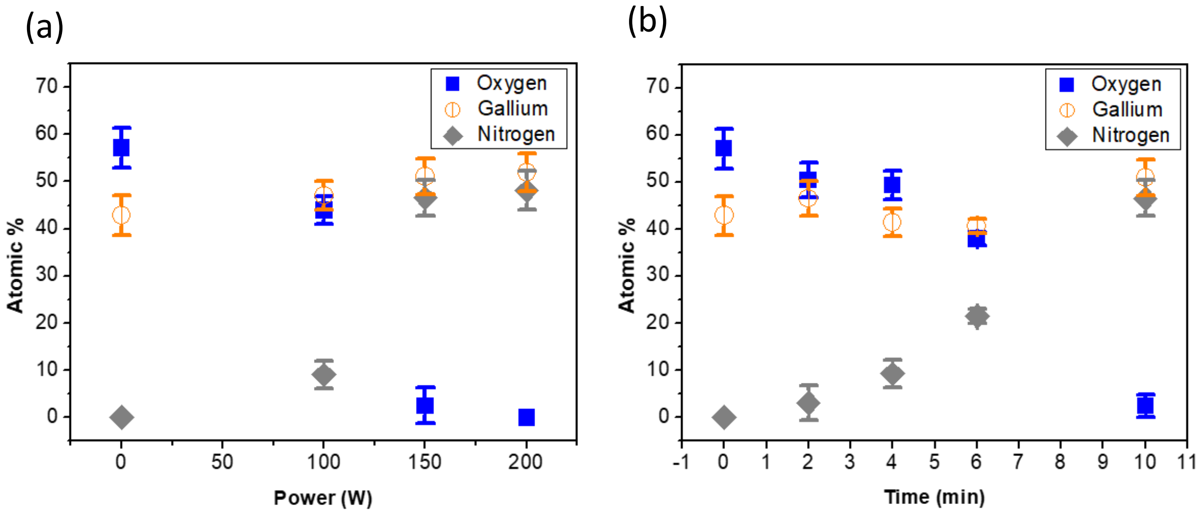

Figure 3-10 (a) XPS data for Ga_2O_3/ SiO_2/ Si samples that have undergone a plasma nitridation reaction with a varying power (constant time=10 min) or (b) a variable plasma duration (constant power=150 W)

3.3.2 Ellipsometry result for GaO_xN_y

In order to measure the effective index of the intermediate GaO_xN_y layers, ellipsometry spectra were fitted using the effective layer model. This model considers that the layer on top of the SiO_2/ Si consists of a composite (mixed) GaN/ Ga_2O_3 layer, with each material following the Tauc–Lorentz dispersion formula extracted from the previous measurements (i.e. for the GaN and Ga_2O_3 layer, see section 3.2.4 above). For these intermediate GaO_xN_y compounds, only the percentage ratio of GaN to Ga_2O_3 in the mixed layer is used to fit the data, while the thickness (3nm) and the corresponding dispersion relation for either the GaN to Ga_2O_3 layer were kept fixed, in accordance with the AFM results of **Figure 3-1**. After fitting the data with this model, we were able to extract the percentage of GaN for each intermediate level, as well as the χ^2 values (see **Table 3-3**). We selected two intermediate levels as examples to demonstrate a strong correlation between the measured data and the fitted data. This result corroborates our hypothesis that the intermediate level comprises a mixture of Ga_2O_3 and GaN. **Figure 3-11**(a) and (b) illustrates Is and Ic as functions of wavelength, with a time setting of 2 minutes and a power setting of 100W, respectively.

Table 3-3 Fit parameters of the dispersion relation as obtained from ellipsometry analysis of the intermediate levels synthesized at different time and power (Time = 2 , 4 , 6 min and Power= 50 , 100 and 150 W

Parameter	**T= 2 min**	**T=4 min**	**T=6 min**	**P=50 W**	**P=100 W**	**P=150 W**
χ^2	0.1	0.53	0.39	0.54	0.86	0.25
GaN%	9.82 ±2.29	36.06±4.21	72.71±2.11	50.56±2.50	76.22±1.85	89.73±2.89

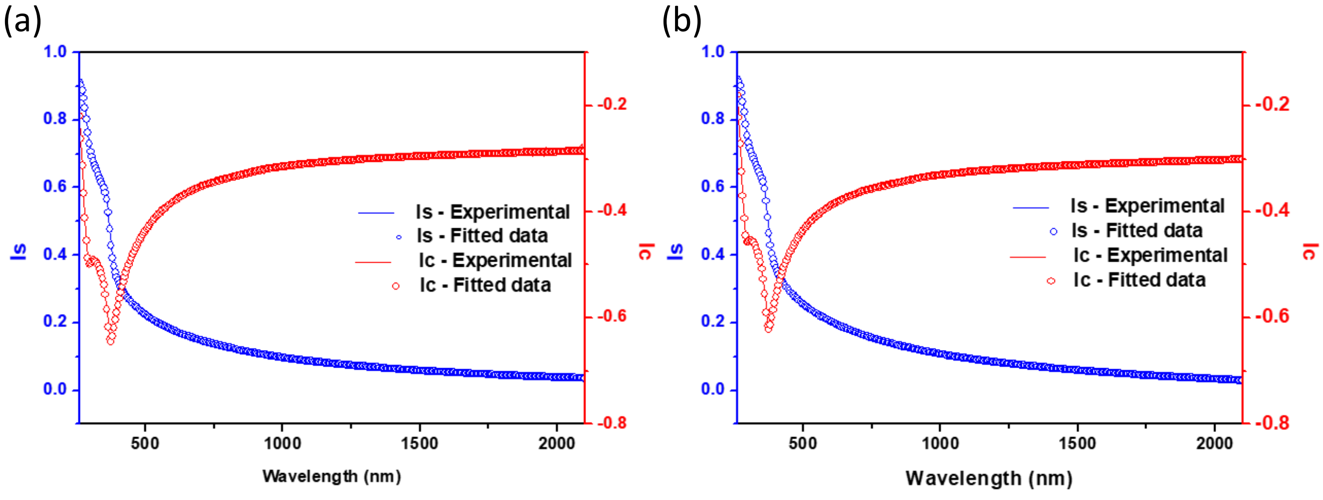

Figure 3-11 Is and Ic as a function of wavelength for intermediate levels (a)Time =2 min (b)Power=100 W (The solid lines are experimental data while the circles show the fitted data) parameters

According to this model, we extract the effective refractive index, extinction coefficient of the GaO_xN_y layer in the modeled composite layer.

Figure 3-12 (a) and (b) show the measurement of the effective index of intermediate GaO_xN_y compound. Panel a (panel b) presents the evolution of n and k as the plasma power (treatment duration) is increased. The evident variations observed on these curves strongly depends on the degree of nitridation of the oxide film. These results indicate that the optical properties of the ultra-thin GaO_xN_y film can be reliably adjusted by the plasma parameters in a controlled manner, as would be useful for photonic device applications.

Figure 3-12 (c) and (d) represent the increase of refractive index as a function of power and time, respectively, at 1550 nm wavelength adopted during the plasma nitridation treatment, respectively. Additionally,

Figure 3-12 (c) and (d) illustrate the increase in the percentage of GaN with increasing power and time (data obtained from Table 3-1).These data show a consistent increase of the percentage of GaN versus Ga_2O_3 in the modeled composite layer as a function of growth parameters, in agreement with the XPS measurements in **Figure 3-10**.

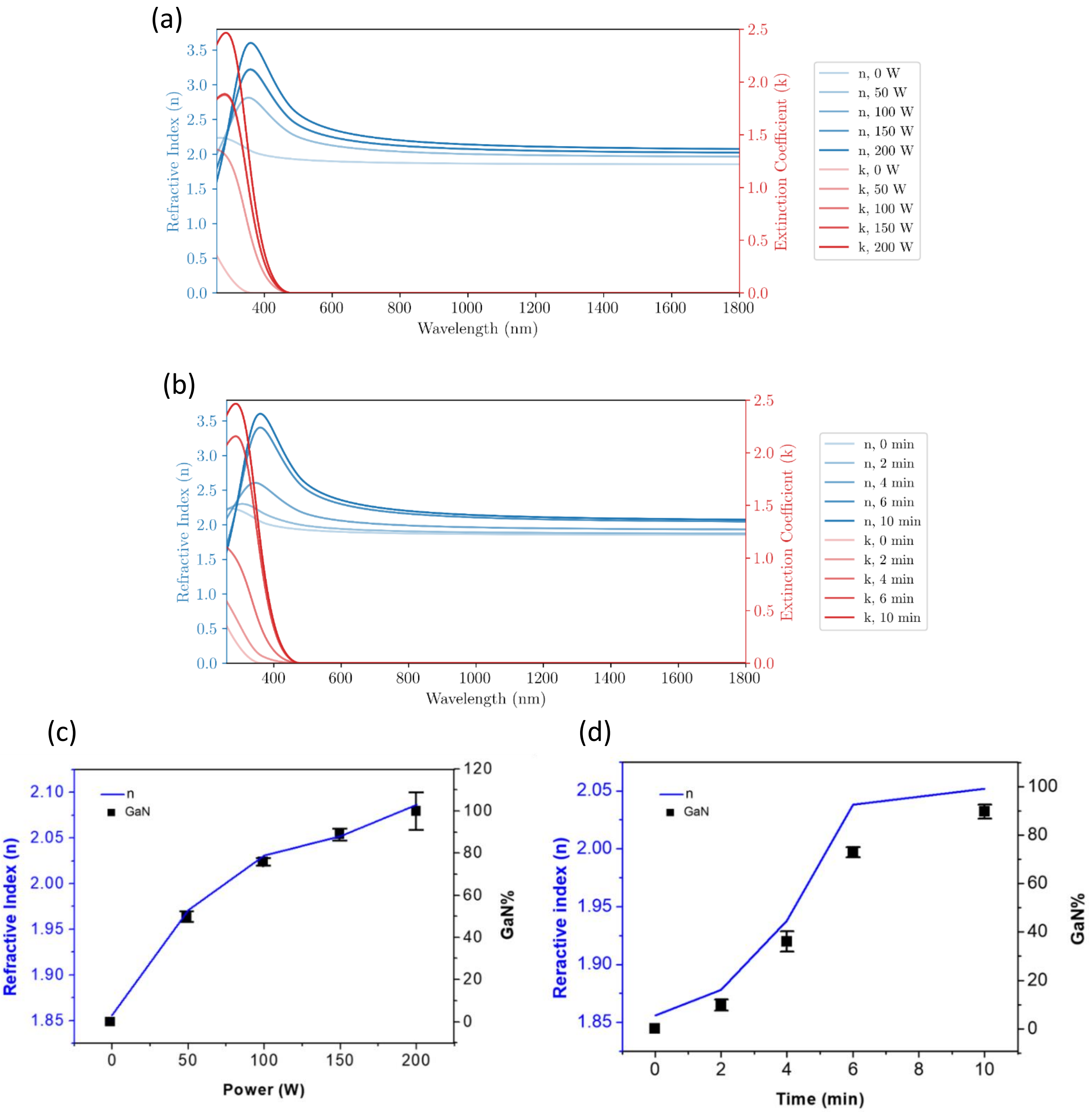

Figure 3-12 a) and (b) Optical properties of intermediate ultrathin films, extracted from SE in the range 260–2100 nm. (a) Shows the vary of refractive index n and extinction coefficient k of GaO_xN_y as a function of wavelength by increasing power (b) shows the vary of refractive index n and extinction coefficient k of GaO_xN_y as a function of wavelength over the time. (c) Shows increase in GaN percentage and refractive index at 1550 nm extracted from ellipsometry as a function of power (Constant time=10 min) (d) Shows increase in GaN percentage and refractive index, extracted from ellipsometry as a function of time (Constant power=150 W)

3.4 Conclusion

In conclusion, we have successfully synthesized ultra-thin layer of Ga_2O_3, which are amorphous and approximately 3 nm thick. This was confirmed through the use of AFM and TEM. Additionally, we observed the wurtzite crystalline structure of GaN using TEM. We further validated the effectiveness of the nitridation process by employing XPS and Raman spectroscopy.

Our ellipsometry measurements provided crucial insights by revealing the unique refractive indices of Ga_2O_3 and GaN. We compared the refractive index of the ultra-thin layers with data on bulk and thick materials from existing literature. Interestingly, the refractive index of these ultra-thin sheets of Ga_2O_3 and GaN does not vary significantly with thickness, at least down to the 3 nm thickness that we explored. Furthermore, we determined the bandgap of the ultra-thin Ga_2O_3 and GaN through an ellipsometry fitting model. The bandgap that we obtained is smaller than that of bulk materials but larger than that of a single layer, as reported in the literature. We also found that the optical properties measured through ellipsometry are in agreement with DFT calculations. It is worth mentioning that these DFT calculations were carried out for bulk Ga_2O_3 and GaN. Hence, our results indicate that the material we synthesized belongs to a category of ultra-thin materials, as it possesses distinct properties compared to traditional 2D materials considering their bandgap and DFT calculation.

Considering that Ga_2O_3 and GaN are widely used in luminescent and power devices, characterization of their alloys could enable the development of materials with tailored properties and provide opportunities to improve device performance if the composition and crystal structures can be properly controlled. Our work demonstrates that the plasma-assisted nitridation process allows us to fine-tune the composition of GaO_xN_y ultra-thin layers. This results in optical properties that are intermediate between Ga_2O_3 and GaN. We characterized the composition and optical properties of the GaO_xN_y ultra-thin films using XPS and ellipsometry measurements. The measurement of the effective index of the GaO_xN_y ultra-thin film across the visible and near-IR range shows that a significant and controlled 20% variation of the ultra-thin film refractive index can be achieved by tuning the composition. In the next chapter, we will explore how we can integrate these ultrathin layer on the device and how this refractive index variation impacts when this material is coated on top of a SiN waveguide. This knowledge can be leveraged to adjust the properties of optical devices based on these materials. Additionally, this research offers a strategy for integrating 2D materials into hybrid photonic chips, which allows for the local modification or enhancement of an otherwise passive optical circuit.

Chapter 4: Integrated Optics

The primary aim of this chapter is to integrate the 2D materials, synthesized and explored in previous chapters, onto photonic devices. To assess the viability and potential of this approach, we will utilize a test structure, specifically a SiN based integrated photonic Mach-Zehnder Interferometer (MZI). This choice will allow us not only to verify the technological feasibility of hybrid integration but also to extract the effective index and loss of the hybrid waveguide, when coated with 2D materials. In this chapter I discuss the technological development underpinning this integration and present measurements of SiN MZI incorporating 2D GaN and Ga_2O_3 materials. This last chapter of my research studies, which is focused on 'hybrid integration', demands a controlled way of patterning the 2D materials. Indeed, the ultimate goal would be to use passive photonic circuits (and not only MZI that are here exploited as test structures) that can be locally functionalized with 2D materials patches exhibiting specific (linear or nonlinear) properties. As a path towards this, patterning techniques dedicated to 2D materials are needed, and will be discussed in the technological section of this chapter.

4.1 Introduction

In this final chapter, I focus on integrating 2D Ga_2O_3 and GaN materials into MZI as a key step towards realizing hybrid integrated photonics with these 2D materials. Building on the previous chapters, where I showed an effective approach to synthesize 2D materials with interesting optical properties, this last one shows a pathway towards their integration onto chip-based photonic devices, to locally enhance the photonic device performance and potentially achieve new functionalities.

As mentioned in Chapter 1, Section 1.5.2 integrating 2D materials into photonic devices, such as waveguides, has attracted significant attention in recent years due to the unique properties of these materials. These include a high refractive index contrast, tunable optical properties, and inherent light emission capabilities or high absorption. These properties, coupled with the possibility to engineer the device geometry can enable strong light-matter interactions with the 2D materials. Numerous research groups have reported promising results in integrating 2D materials such as graphene, transition metal dichalcogenides, and black phosphorus into various photonic devices, leading to optical modulators, switches, and sensors with improved performance [47], [435]–[437]. As a first step towards demonstrating the potential of these hybrid structures in device applications, MZIs can serve as an effective test structure for the integration and characterization of the 2D materials.

In this chapter, MZI are used as a platform for studying GaN and Ga_2O_3 2D materials. Researchers have shown that by incorporating 2D materials into the waveguides or junctions of MZIs, device architectures can be developed. For example, recent studies have demonstrated the use of ultrathin gallium sulfide (Ga_2S_3) [438], few-layer indium selenide (InSe) [439] and monolayer WS_2 [440] in MZIs to create ultrafast optical switches, enhance sensitivity of sensors, and develop low-loss phase modulators. These demonstrations hold great potential for optical communication, sensing, and signal processing, paving the way to faster, more energy-efficient, and compact optoelectronic systems fully integrated on photonic chips. However, integrating wide bandgap Ga_2O_3 and GaN into photonic devices, particularly MZIs, remains relatively unexplored, presenting an opportunity to expand the scope of hybrid integrated photonics. In line with the recent progress relying on 2D materials integrated into MZIs, I explore here the impact of Ga_2O_3 and GaN onto the optical and spectral response of MZIs. According to the characterization results of chapter 3, both ultra-thin Ga_2O_3 and GaN layers possess favorable material characteristics such as a wide bandgap, making them promising candidates not only for use in optical devices but also, potentially, for nonlinear optics.

On the other hand, although the design of the underlying photonic devices could be further optimized to enhance the typically low light-matter interaction with these ultra-thin materials, integrating them into photonic devices already represents a significant technological challenge. Developing new fabrication techniques for these 2D materials, wherein integration and synthesis could be seamlessly achieved and independently of the host photonic device platform, would greatly facilitate the development of hybrid 2D material optoelectronics devices. Fortunately, the squeeze printing of liquid metal introduced in Chapter 2-3 offers a promising solution for direct deposition on devices, potentially addressing this technological challenge. To ensure the 2D materials cover only certain locations of the photonic chip, a controlled way of patterning is necessary. Therefore, I detail here the use of the photolithography and lift-off steps to pattern the 2D materials. The resulting devices provide us with a suitable platform for experimentally probing the linear properties of Ga_2O_3 and GaN after their integration on photonic chips. I present experimental measurements of MZI locally coated/ uncoated with 2D materials. I extract the effective index of the hybrid mode coated with the 2D material and show the impact of the nitridation process on the device response. Our present investigation is also supported by numerical simulations of the hybrid mode associated with the SiN waveguide coated with the GaN or Ga_2O_3 2D materials, respectively. These preliminary measurements allow us to validate our technological process and evaluate the impact of the 2D materials onto hybrid waveguides in simple structures. Furthermore, they lay the foundation for future investigations, involving e.g. nonlinear measurements on GaN, which are not discussed in this chapter.

4.2 Integration of 2D material onto photonic chip-based devices

Before we delve into the next sections, it is crucial to emphasize that our investigation focuses on the interaction of 2D materials with unclad SiN waveguides. These waveguides serve as a mature platform for passive photonic circuits at 1.55μm. The interaction between light and the 2D material that is coated on top of the waveguide is mediated by the evanescent field of the guided mode which extends outside the waveguide core. We first explore numerically how the guided mode of these structures is affected by the additional ultra-thin layer of Ga_2O_3 and GaN. It is important to note that this waveguide design has not been optimized for increasing the interaction of light with the 2D material. We use here simulations to evaluate this interaction by quantifying the energy overlap of the guided mode with the 2D material.

Lastly, I present in the second part of this section the SiN-based Mach-Zehnder interferometer fabricated by ST-microelectronics and that is used as the test device to measure the optical properties of the 2D materials. I received the help of Prof. Regis OROBTCHOUK for the optical characterization of these devices at INL as well as the data analysis that is presented towards the end of this chapter.

4.2.1 Numerical mode simulations of 2D material hybrid photonic waveguides

4.2.1.1 Optical device geometry

The first device geometry selected for probing our 2D material is a SiN waveguide fabricated at ST Microelectronics [441]. The substrate consists of a 750 µm thick Si layer covered by a 2 µm layer of SiO_2. A 600 nm layer of SiN is deposited on top of the SiO_2 layer using PECVD. The material's characteristics, such as dispersion and absorption, were measured using ellipsometry. The SiN waveguides were fabricated using deep-UV photolithography and inductively coupled plasma reactive ion etching. The chip layout contains different basic optical test devices, including MZIs (see section 4.3). The final technological steps involve SiO_2 deposition using PECVD and chemical mechanical polishing of the surface to provide a planar photonic device surface suitable for 2D material integration. The cross sections of the waveguides under test are shown in **Figure 4-1** (a) and (b), without and with the 2D material integrated on top of the waveguide. The bare devices of **Figure 4-1**(a) are used to evaluate the optical properties of the SiN waveguide, while the configuration of **Figure 4-1**(b) allows us to probe the optical properties of the 2D materials under study.

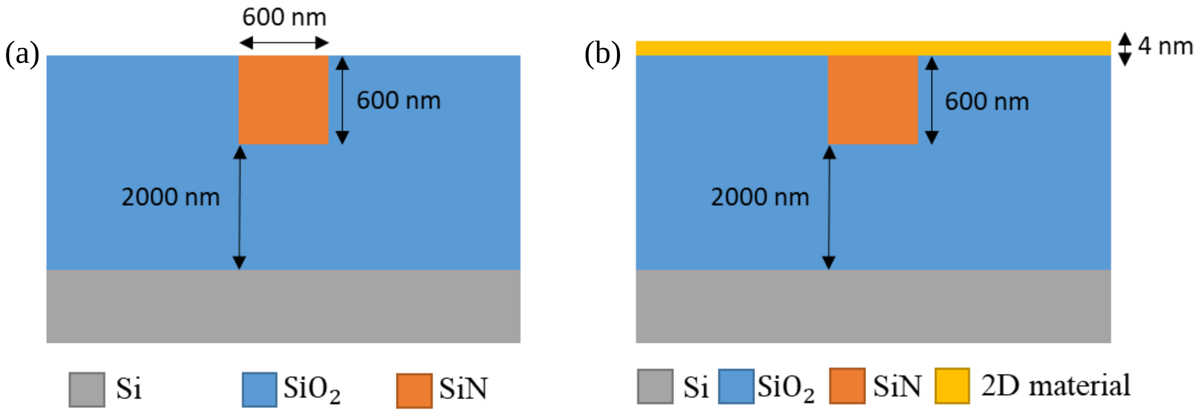

Figure 4-1 (a) Illustration of the cross section of SiN strip waveguide and (b) cross section of strip SiN waveguide loaded with 2D materials under studies.

4.2.1.2Material refractive indices

For the numerical simulations, we considered the optical indices of Ga_2O_3 and GaN that were determined by ellipsometry (see section 3.2.4 of Chapter 3). All measured refractive indices were fitted to a Cauchy law from 1.2µm to 1.7µm in order to avoid discontinuities arising from sampling. The Cauchy expression is the following:

$$n = N_0 + \frac{N_1}{\lambda^2} + \frac{N_2}{\lambda^4} + \frac{N_3}{\lambda^6} + \frac{N_4}{\lambda^8}$$

where n is the refractive index, λ the wavelength (in µm) and N_0, N_1 (in μm^2), N_2 (in μm^4), … are the Cauchy coefficients of the material determined through least squares fitting. **Figure 4-2** (a), (b) and (c), show the result of Cauchy fits applied to ellipsometric data for SiN, Ga_2O_3 and GaN, respectively.

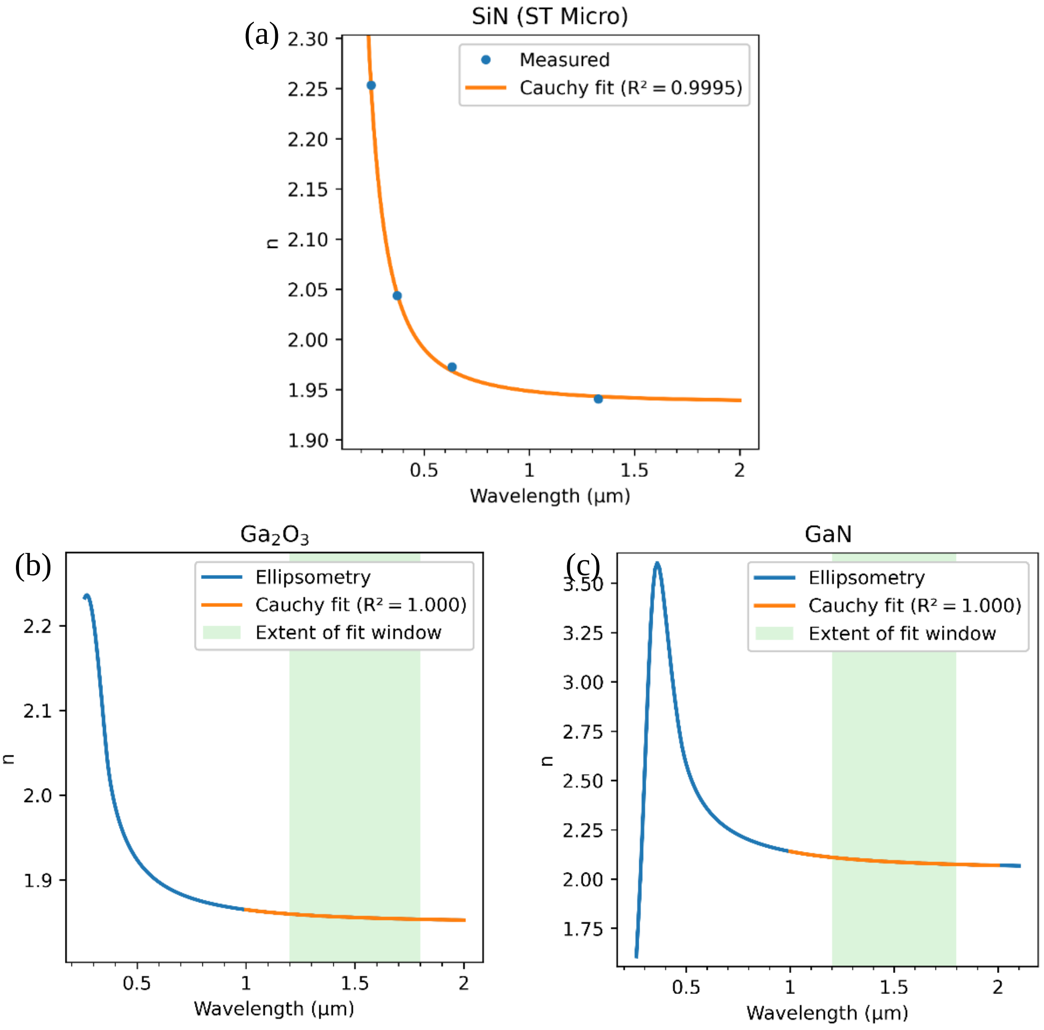

Figure 4-2 Evolution of refractive indices versus wavelength (λ) used for the determination of Cauchy coefficients for the materials composing the device: (a) PECVD SiN (b) Ga_2O_3 (c) GaN

4.2.1.3 Eigenmode calculations of the SiN waveguides with and without 2D materials

The optical modes supported by the waveguides at $\lambda = 1.55\mu m$ are shown in **Figure 4-3**, corresponding to the SiN waveguide, as well as the SiN waveguide overlaid with ultrathin (4 nm) layers of Ga_2O_3 and GaN. I used Lumerical MODE to find the modes and their corresponding propagation constants from 1.2μm to 1.7μm. We considered the optical indices of Ga_2O_3 and GaN measured by ellipsometry and fitted to a Cauchy law, as explained in the previous section.

The calculations show that for all three configurations, the waveguide is capable of supporting a single mode in both transverse electric (quasi-TE) and transverse magnetic (quasi-TM) polarizations from 1.2µm to 1.7µm. Their effective indices range from about 1.66 at 1.2µm to 1.51 at 1.7µm for the quasi-TE polarization and about 1.65 at 1.2µm to 1.48 at 1.7µm for the quasi-TM polarization, as reported in **Figure 4-3**. The difference between both polarizations owe to the difference between the horizontal and vertical index profiles of the cross-section, which makes it so that in TM polarization, a higher fraction of the field travels through air rather than SiO_2.

The effective indices of the coated waveguides are very close (within 0.2%) to the effective index of the bare waveguide, as shown in **Figure 4-4**. This similarity in effective indices, as well as the large resemblance between the mode profiles of the bare and coated waveguides, as can be qualitatively inferred from **Figure 4-5**, indicate that light in the near infrared can efficiently couple between bare waveguides and waveguide with 2D material, with negligible scattering and reflection losses, even in the absence of coupling structures.

Subsequently, the data is fitted using a third order polynomial to provide an analytical description of $n_{eff}(\lambda)$ used in later stages of the work:

$$n_{eff}(\lambda) = a_1 + a_2\lambda + a_3\lambda^2 + a_4\lambda^3 \qquad (1)$$

Where n_{eff} is the effective index, λ is wavelength expressed in µm and a_1, a_2, a_3, a_4 are the polynomial coefficients.

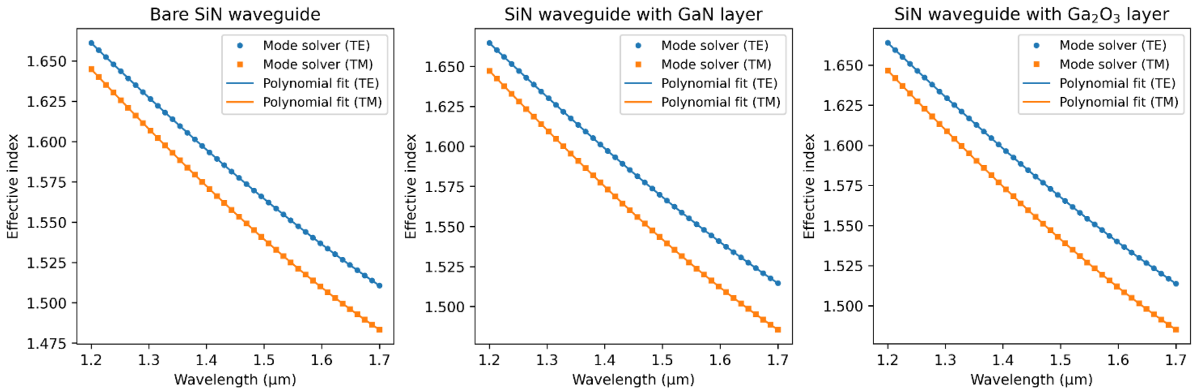

Figure 4-3 Effective indices of the three structures considered: bare SiN waveguide, GaN and Ga_2O_3 coated SiN waveguide. Individual markers denote mode calculations and continuous lines of the same colour the corresponding polynomial fit.

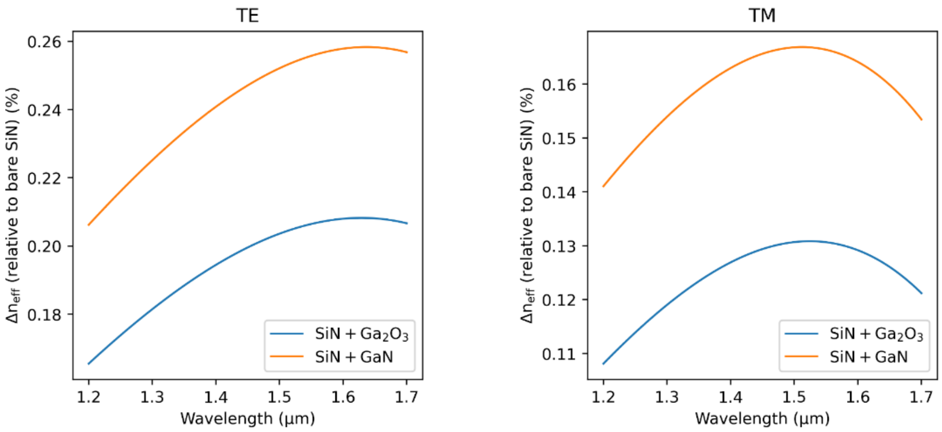

Figure 4-4 Relative change in the effective index of the waveguide after it is coated with 2D material, in both polarization conditions.

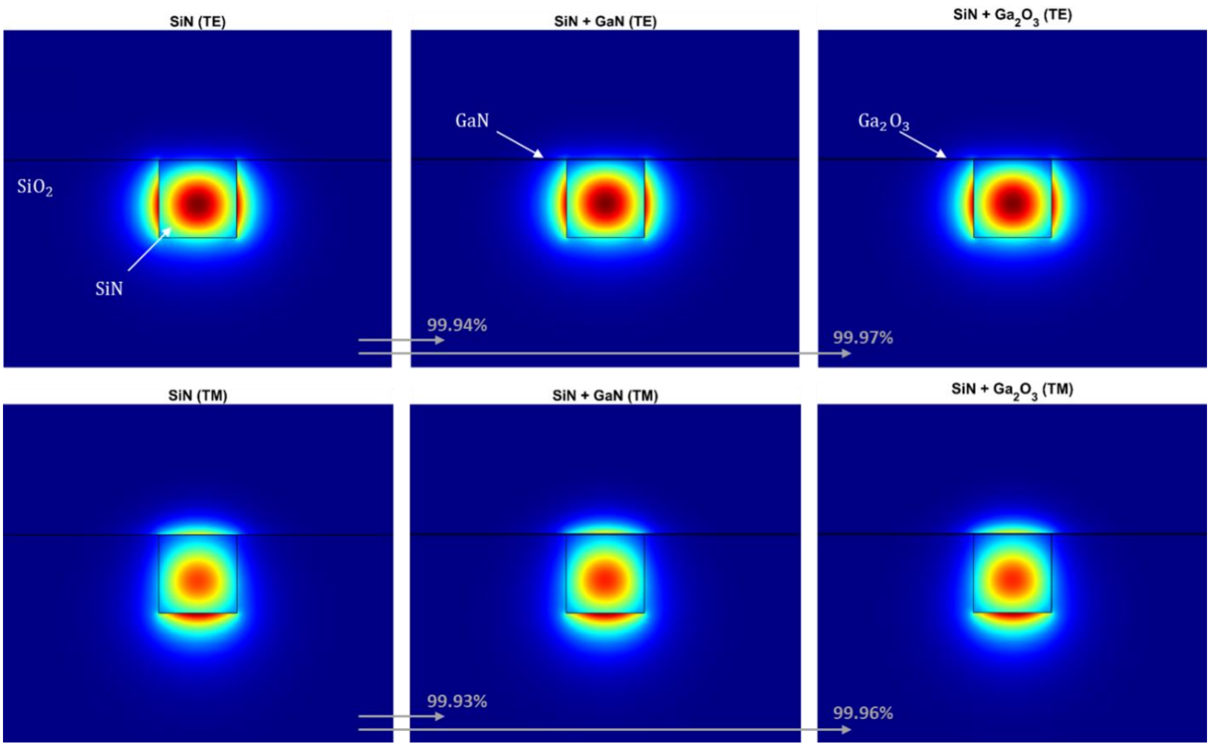

Figure 4-5 Electric field intensity $|E|^2$ of the TE and TM modes supported by the three cross-sections under consideration at 1.55μm. Grey arrows and percentage values denote the calculated power-coupling between bare and 2D-material coated sections.

From the numerical mode simulations of the hybrid photonic waveguides coated with 2D materials, we can also compute the fraction of the electric field intensity $|E|^2$ propagating through the 2D material layer by integrating its value over the 2D material cross-section, and dividing that value by the total intensity.

This fraction is a critical quantity, as it gives an estimate of the interaction between the propagating mode and the 2D material, thereby offering insights into how the mode's properties might be altered due to the presence of the 2D layer, as well as the intensity needed in the waveguide to start observing non-linear behavior.

We have calculated these fractions using Lumerical MODE’s built-in functionality for both Ga_2O_3 and GaN and for both TE and TM polarizations. Our results, presented in the **Table 4-1,** indicate that, in all cases, only a small portion of the electric field ($\approx 0.18\%$) effectively travels through the material. These values are also consistent with the low impact of the 2D materials on the effective index of the waveguide ($\Delta n_{eff} \approx 0.2\%$) as was plotted on **Figure 4-4**. We note that the overlap is very similar in both polarizations, except for a slight improvement in the case of GaN in TE polarization over TM polarization. This lack of preferential polarization for interacting with the 2D material is not a surprising result considering the square cross-section of the waveguide.

Table 4-1 Overlap percentages of electric field intensity for waveguide with Ga_2O_3 and GaN in both TE and TM modes, calculated in terms of power and electric field intensity at 1.55µm

Mode	Material	Fraction of electric field intensity in 2D material (%)
TE	Ga_2O_3	0.184
	GaN	0.186
TM	Ga_2O_3	0.185
	GaN	0.177

This low interaction sets a limit to the changes that could be detected from measurements on those chips later in the chapter. Globally, these results are not surprising as the waveguide geometry has not been optimized yet for these applications, and because the thickness of the 2D material is very small. Nevertheless, the light-2D material interaction should still enable the experimental investigation of the properties of 2D materials coated on photonic devices.

In future works, the overlap with the guided mode could be substantially enhanced by making use of thinner waveguide cross-sections or anti-resonant slot waveguides[442] , opening up another avenue for the control and optimization of the resulting hybrid device.

4.2.2 Mach-Zehnder Interferometers (MZI)

The Mach–Zehnder Interferomete, initially developed by Ludwig Mach and Ludwig Zehnder, involves two beam splitters that can split two beams of light and recombine them into one output. It is a simple device that demonstrates the appearance of interference patterns when the two beams experience different optical lengths, illustrating the wave nature of light.

In integrated photonics, the MZI structure consists of an input waveguide and an output waveguide, as well as two straight waveguides that function as the sensing arm and the reference arm, respectively. In this work, we considered an asymmetric MZI, where the two arms of the MZI have different optical lengths, due to a change in either arm length or optical properties of the waveguide, leading to distinct propagation characteristics for the light traveling through each arm. The MZI structure involves a beam splitter and a beam combiner, which are realized using a Multi-Mode Interference device (MMI). In operation, the monochromatic and polarized light from the laser source is coupled into the input waveguide and split equally at the beam splitter. Then the two guided modes respectively propagate along the sensing arm and the reference arm and recombine at the beam combiner. Some optical path difference between the two arms leads to oscillation in the transmission spectrum due to either constructive or destructive interference. In our study, additional changes in the optical path is induced by the deposition of 2D material (Ga_2O_3 and GaN) on the sensing arm of the MZI, which has a 100 µm length. The waveguide cross-section is the same as presented in section 4.2.1.1. A certain spectrally dependent interference pattern is observed when the sensing waveguide is free of any 2D material. The deposition of a 2D material alters the effective refractive index of the sensing arm, leading to a different interference pattern. This change provides information about the deposited material. As we will detail later, we fit the observed patterns to a model and compare it to theoretical values based on the refractive index of the 2D material and the MZI dimensions. Locally covering the sensing arm by 2D materials implies the patterning development presented in the section 4.3.2 of this chapter.

Figure 4-6 illustrates the process where light of amplitude A is injected into the input waveguide and subsequently divided between the two arms of the asymmetric MZI through the MMI device. Once we've deposited the material on the sensing arm, we need to consider potential imperfections of the asymmetric MZI, such as imperfections of the MMIs and a difference in optical losses in the two arms of the asymmetric MZI. In order to account for these factors, we model the device's response using the following formula:

$$P(\lambda) = P_{in}(\lambda) \cdot \cos^2\left(\frac{2\pi}{\lambda} n_{eff}^{SiN} L_2 + \frac{\pi}{\lambda}\left(n_{eff}^{MUT} - n_{eff}^{SiN}\right) L_{MUT}\right) + P_{offset}(\lambda) \qquad (4-1)$$

Where λ is the wavelength, n_{eff} is the effective index of the mode, and P_{in} and P_{offset} are used to cover effects stemming from the emission spectrum of the source, the photodetector's response, and MZI imperfections.

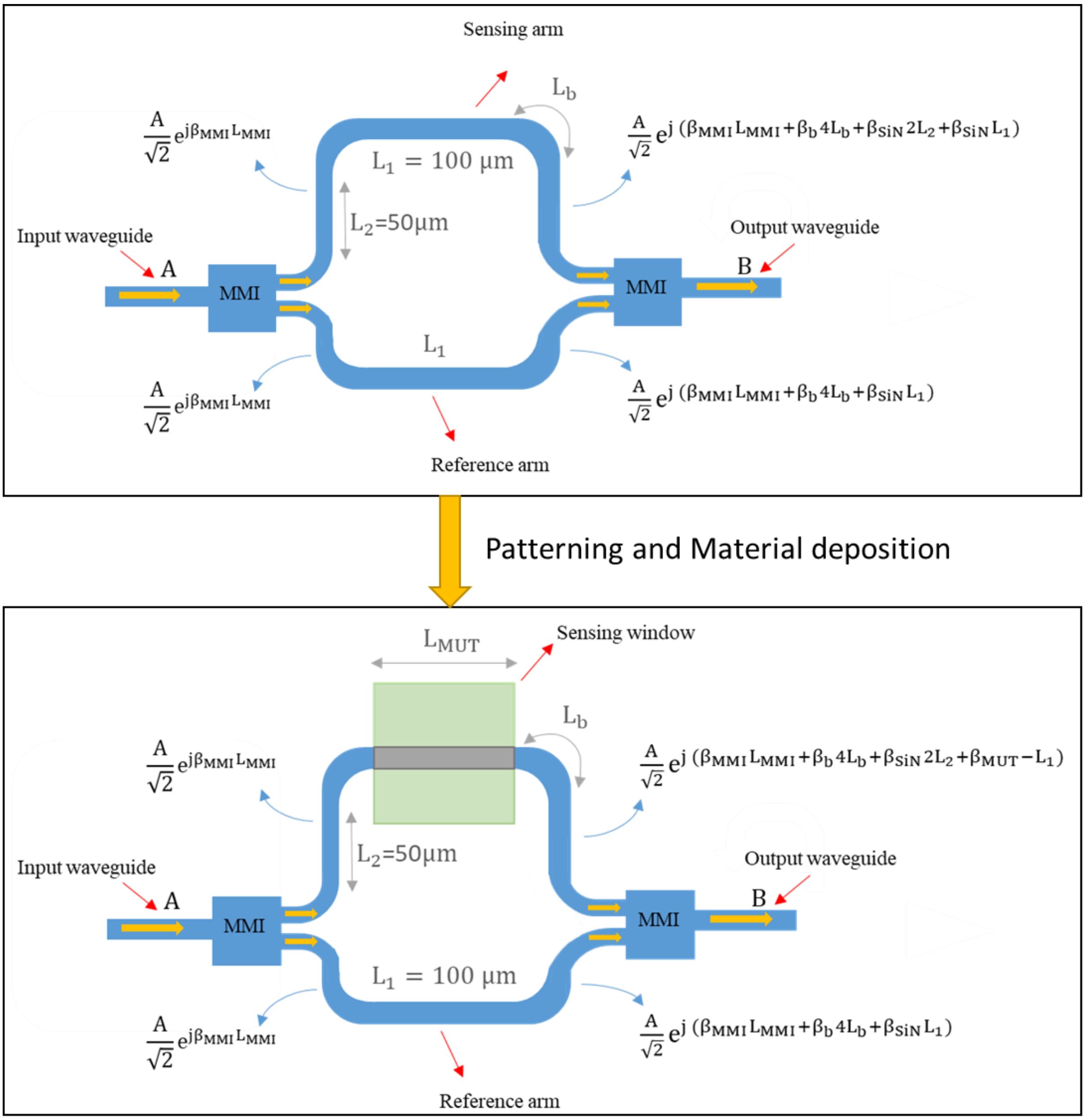

Figure 4-6 Schematics of a Mach-Zehnder interferometer. The input intensity A is split in the two arms of the interferometer. The arms are asymmetric so when the signals recombine in the output MMI they interfere. The interference is quantified by analyzing the output intensity B. (a) MZI before patterning the sensing arm (b) MZI with material deposited in sensing window on the sensing arm. (b = bend, MUT = Material under Study)

4.3 Technological development for selective transfer of Ga-based 2D materials

In our study, we aim to explore the potential of Ga-based 2D materials in integrated photonics. The selective transfer of these materials onto photonic devices, like in the MZI test structure described in the previous section, is needed for this. From a broader perspective, **Figure 4-7**(a) [267] depicts an illustrative schematic of an integrated photonic circuit featuring various active optoelectronic devices that could be locally functionalized by the presence of 2D material patches. By judiciously incorporating our Ga-based 2D materials into specific parts of such a circuit, we could envision to optimize its overall functionality. The MZI (**Figure 4-7** (b)) used for our experiments serves here as a testbed to validate our technological developments. Notably, with patterning the substrate we want to control where the 2D material is deposited on the waveguides. Nonetheless, several issues may arise. One concern is that metal residues from the deposition process could negatively affect the optical properties of the device, resulting in increased absorption of light and reduced transmission. These issues are related to the use of these liquid based 2D materials in general, and addressing them is a necessary step for their successful incorporation into devices**.** By patterning the substrate with a mask through photolithography prior to the integration of the 2D materials, the latter can be confined to specific substrate areas, avoiding deposition in unwanted areas and minimizing the impact of metal residues. The details of this process and our findings will be discussed in the subsequent sections.

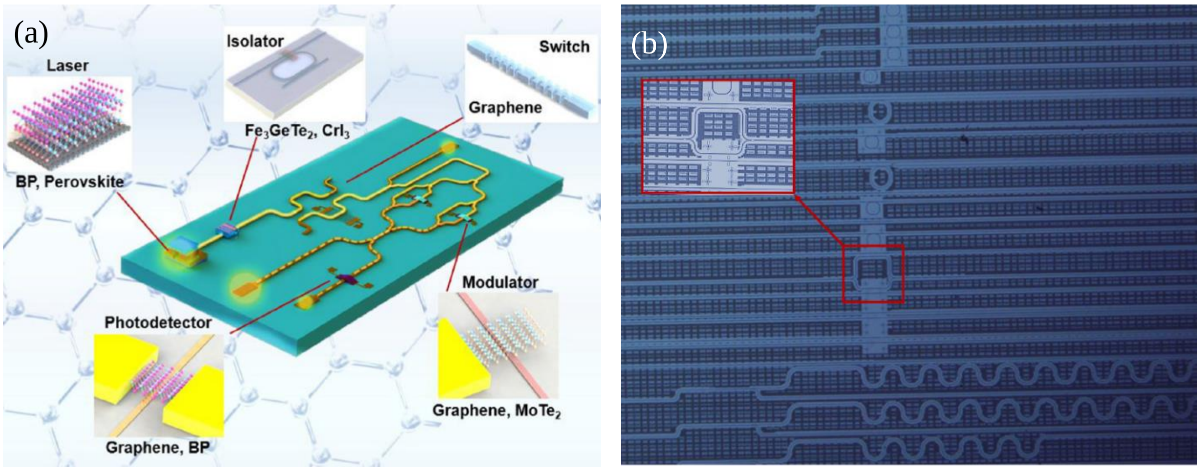

Figure 4-7 (a) A basic schematic of an integrated photonic circuit with active optoelectronic devices including a light source, isolator, switch, modulator, photodetector [267] (b) MZI on a wafer alongside a series of other photonic devices.

4.3.1 Substrate patterning for selective transfer of 2D materials

Selective transfer of 2D materials onto a patterned substrate is needed to constrain their location where intended for optimal device performance, and to avoid any unwanted interaction between neighbouring components, which can adversely impact the device's functionality. I developed here this selective transfer process by making use of photolithography patterned substrates. This approach should also enable the integration of multiple 2D materials with different properties within a single device.

Photolithography is a process originating from the words "Photo," "Lithos," and "Graphy," meaning "Light," "Stone," and "Write," respectively. It is well-known in integrated circuit fabrication, imprinting patterns on wafers to create various devices. Photolithography process includes an illuminator, a photomask, an optical system, and the photoresist applied on the wafer. These fundamental components are assembled as depicted in **Figure 4-8**(a), which also illustrates the operating principle. The process involves applying a photosensitive polymer or photoresist to a wafer; the resist undergoes a change in its chemical composition upon UV light exposure. As a result, the pattern is stored as a latent bulk image within the resist. When immersed in a developer solution, the exposed resist areas either remain or dissolve, depending on their polarity. Once the lithography process is complete, an approximate replica of the mask pattern is left on the wafer surface.

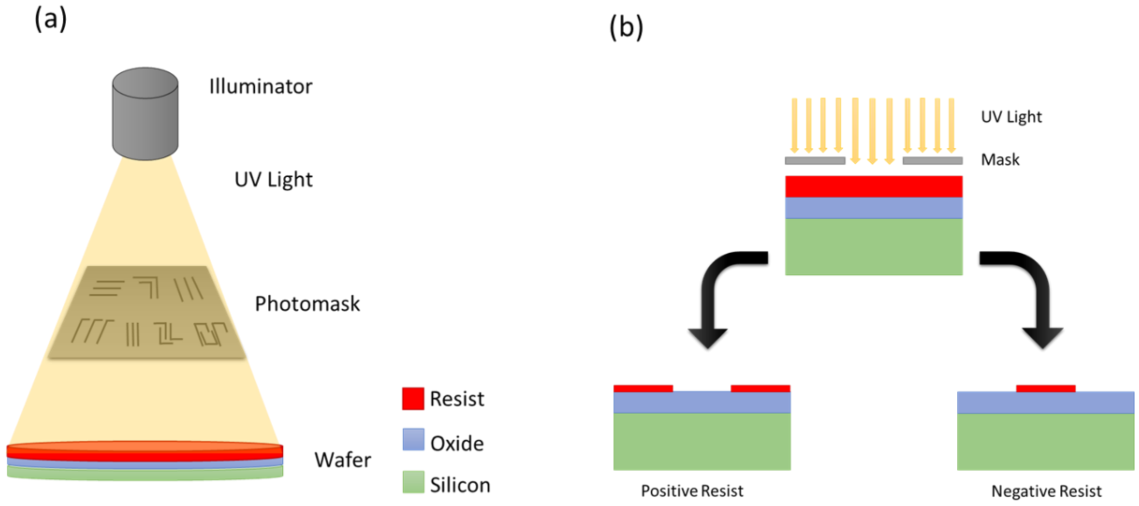

Figure 4-8 (a) Schematic of main components of photolithography machine (b) Schematic of Positive and Negative photolithography

There are two types of photoresists: positive and negative (**Figure 4-8** (b)). In positive photoresists, exposure to UV light makes resist material soluble and susceptible to the subsequent development process, preserving the unexposed resist on the wafer surface. On the other hand, in negative photoresists, exposure to UV light maintains the resist material's resistance to the developer solution, preserving the exposed resist on the wafer surface.

We first tested the integration of our 2D materials using a Si/SiO_2 substrate (Si with 200nm SiO_2) that was patterned using photolithography and etching techniques. The three main steps of our photolithography process involve (1) photoresist coating, (2) UV light exposure through a hard mask and (3) the resist development.

1. ***Photoresist coating*****:** For the first step, we must prepare the surface condition to accept the photoresist by providing a clean surface. Next, we coat the wafer with a chemical that boosts the adhesion of the photoresist to the wafer's surface. It starts with applying a primer to create a hydrophobic surface. Consequently, the sample is placed on a vacuum chuck of a spin coater. The positive photoresist process was employed, with AZ5214 photoresist applied to the substrate surface (**Figure 4-9**(a)). The sample was subsequently subjected to spin coating for 30 seconds at a speed of 5500 rpm and an acceleration of 4000 rpm/s, resulting in a photoresist layer with a thickness of approximately 1.2-1.3µm. Following this, the sample underwent a soft bake on a hot plate for 90 seconds at 110°C to remove the residual solvents of the photoresist. After the soft bake, the wafer is cooled to room temperature.

2. ***UV light exposure through a hard mask*****:** These steps are followed by alignment, one of the most critical steps in the entire microsystems fabrication process. I used MJB4 Mask Aligner shown in **Figure 4-9** (b). The MJB4 Mask Aligner allows contact exposures of different types (vacuum, hard, soft contact) and exposures at short distances. The achievable alignment accuracy of X, Y, and Theta is below 1 µm. The MJB4 is equipped with 400 nm exposure optics and lamps that allow a resolution of< 1 µm in vacuum contact. The wafer coated with resist is exposed to UV light through the chromium mask (**Figure 4-9** (c)); hence only those areas not protected by the mask undergo a chemical reaction. At this stage, the substrate was exposed to UV light for 8 seconds, enabling the mask pattern to transfer onto the sample's surface.

3. ***Resist development:*** Finally, the patterned substrate was immersed in AZ726 MIF developer for 25 seconds to complete the photolithography process (**Figure 4-10**(a)).

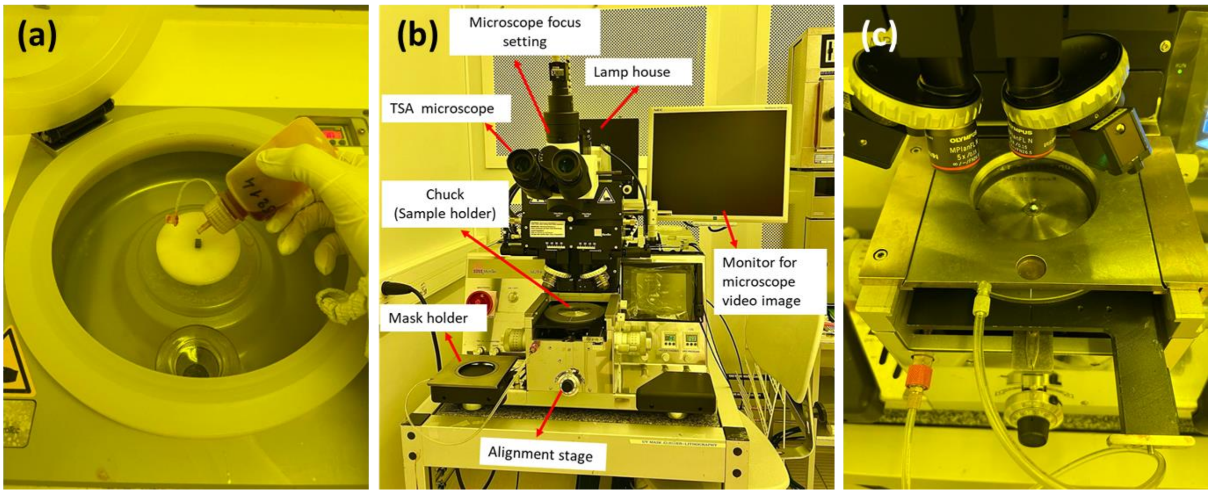

Figure 4-9 (a) Covering the device with Photoresist on Spin coater (b)SUSS MicroTec MJB4 Mask Aligner (c) Device under UV exposure

After the photolithography process, the Si layer was etched using Inductively Coupled Plasma (ICP) to achieve the final patterned substrate, depicted in **Figure 4-10** (b). Then, we proceeded with the procedure specific to the integration of 2D materials onto the patterned substrates. A liquid droplet of gallium was positioned on the sample and compressed using a second wafer, as described in detail in Chapter 2, Section 2.2.1and 2.2.2. The outcome of this procedure is illustrated in **Figure 4-10** (c).

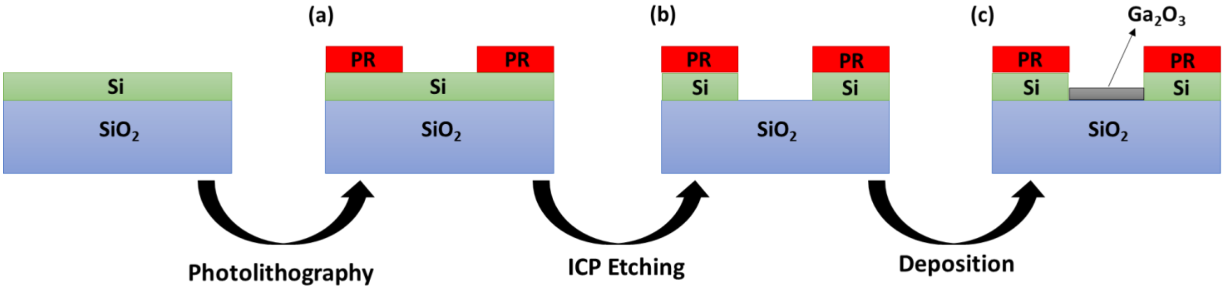

Figure 4-10 Substrate patterning and deposition (a) Photolithography , positive photoresist on Si/SiO$_2$ substrate (PR=Photoresist) (b) Si layer etched by ICP etching (c) liquid droplet of Ga$_2$O$_3$ deposited and squeezed on SiO$_2$ substrate.

Figure 4-11(a) presents Scanning Electron Microscope (SEM) images of the patterned substrate, processed as explained earlier. The pattern, depicted in dark gray, is SiO$_2$, created after etching Si shown in light gray, which is covered by photoresist. As evident in **Figure 4-11**(b), post the gallium deposition, the material deposited solely on areas not covered by photoresist (SiO_2), leaving the rest of the sample unscathed by gallium. It is important to note that the photoresist applied during the patterning process was not removed after the ICP etching of the substrate. This remaining photoresist played a protective role, preventing gallium deposition on the covered areas. By comparing **Figure 4-11** (a) and (b), which display the patterned substrate before and after the deposition of Ga_2O_3 respectively, it is clear that Ga_2O_3 was selectively transferred to the parts of the sample devoid of photoresist. Both images were captured using the Back Scattered Emission (BSE) mode of SEM.

In conclusion, this method enables control over the transfer of 2D materials onto the substrate, potentially resulting in selective deposition onto a photonic device, which will be further discussed in the following sections.

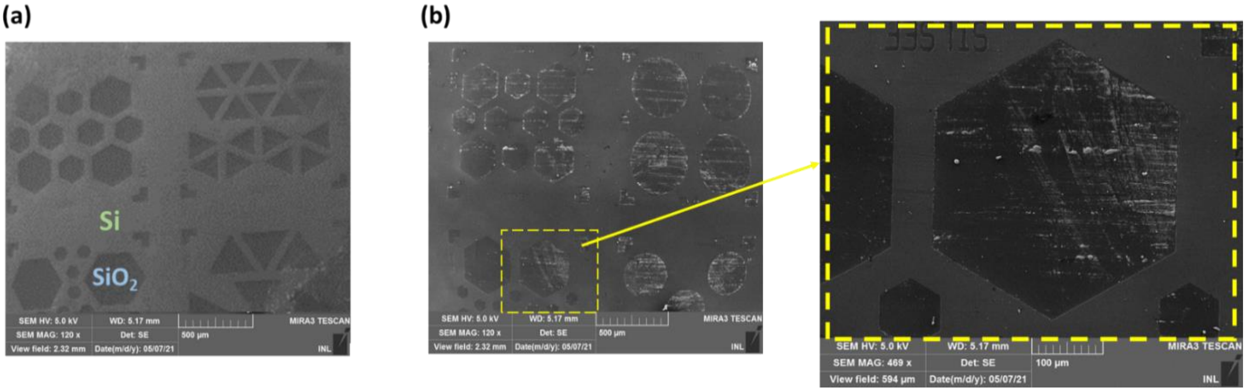

Figure 4-11(a) BSE image of patterned substrate before deposition (b) BSE image of patterned substrate after deposition

4.3.2 Patterning MZI for selective deposition of 2D materials

Building on the approach described in the previous section, opening a window on top of the sensing arm of a MZI for selectively coating this area with the 2D material, can be achieved using photolithography. The size and shape of the sensing window can be controlled by adjusting the exposure time and mask design. The mask and the substrate should be aligned to ensure that the patterned window is located in the desired areas. For creating the sensing window, I leveraged an Image Reversal procedure. This approach slightly deviates from the technique we used for patterning the Si/SiO_2 substrate (as detailed in section 4.3.1), specifically in terms of exposure and baking steps. First, the sample was coated with AZ5214 photoresist and spun at 5500 rpm with an acceleration of 4000 for 30 seconds .The coated sample was then soft-baked on a hot plate at 110°C for 90 seconds, followed by a first exposure of 3 second. After the first exposure, the sample underwent a second bake at 110°C for 60 seconds. Subsequently, a second flood exposure was performed for 25 seconds. Finally, the sample was immersed in AZ 726 MIF developer for 30 seconds. The resulting pattern created a sensing window on the sensing arm of the MZI, allowing for the deposition of 2D material into the sensing arm. **Figure 4-12** shows the MZI before (a) and after (b) the sensing window was opened using photolithography.

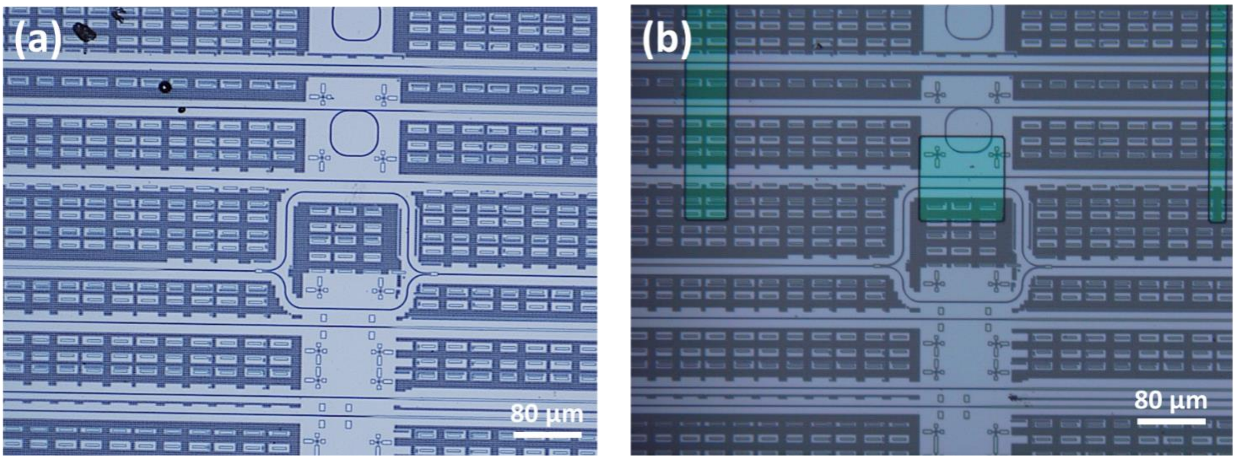

Figure 4-12 (a) Optical image of an MZI before opening window on sensing arm with photolithography (b) Optical image of MZI after opening window on sensing arm with photolithography.

4.3.3 Direct transfer of 2D material on MZI

According to the results of Section 4.3.1, the transfer of Ga_2O_3 occurred solely on the substrate area not covered by photoresist, i.e. within the window on top of the sensing arm of the MZI. The squeeze printing technique, detailed in Section 2.2.1 of Chapter 2, was utilized to deposit an ultrathin layer of Ga_2O_3. The sample was preheated to 40°C on a hot plate, and a liquid droplet of gallium was placed onto the sample and squeezed with the second wafer. After removal of the second wafer, an ultrathin layer of Ga_2O_3 was selectively transferred onto the sensing window. To eliminate the remaining liquid metal micro-droplets, the sample was immersed in hot ethanol (78°C), followed by a solvent-assisted mechanical cleaning protocol using polyurethane foam swab. This process removed both metal residue and the photoresist covering the remaining sample. Hence, thanks to the ethanol wash, the sample was thoroughly cleaned from any photoresist. **Figure 4-13** (a) and (b) depict the sensing window before and after the de position of Ga_2O_3. **Figure 4-13** (b) shows the deposited material before removing the metal residue with the ethanol bath. At this stage, the photoresist was removed by wiping with a Q-tip drenched in ethanol (see the absence of contrast at the edge of the window).

Thereby illustrating the capability of this approach to enable the precise deposition of Ga_2O_3 onto the sensing window of the MZI. To eventually convert the deposited Ga_2O_3 to GaN, a nitridation process was employed following the procedure described in detail in Section 2.2.2 of Chapter 2. (**Figure 4-13** (c) and (d)). Structural characterization will be used next to assess the presence of the 2D material in the sensing arm and its nature.

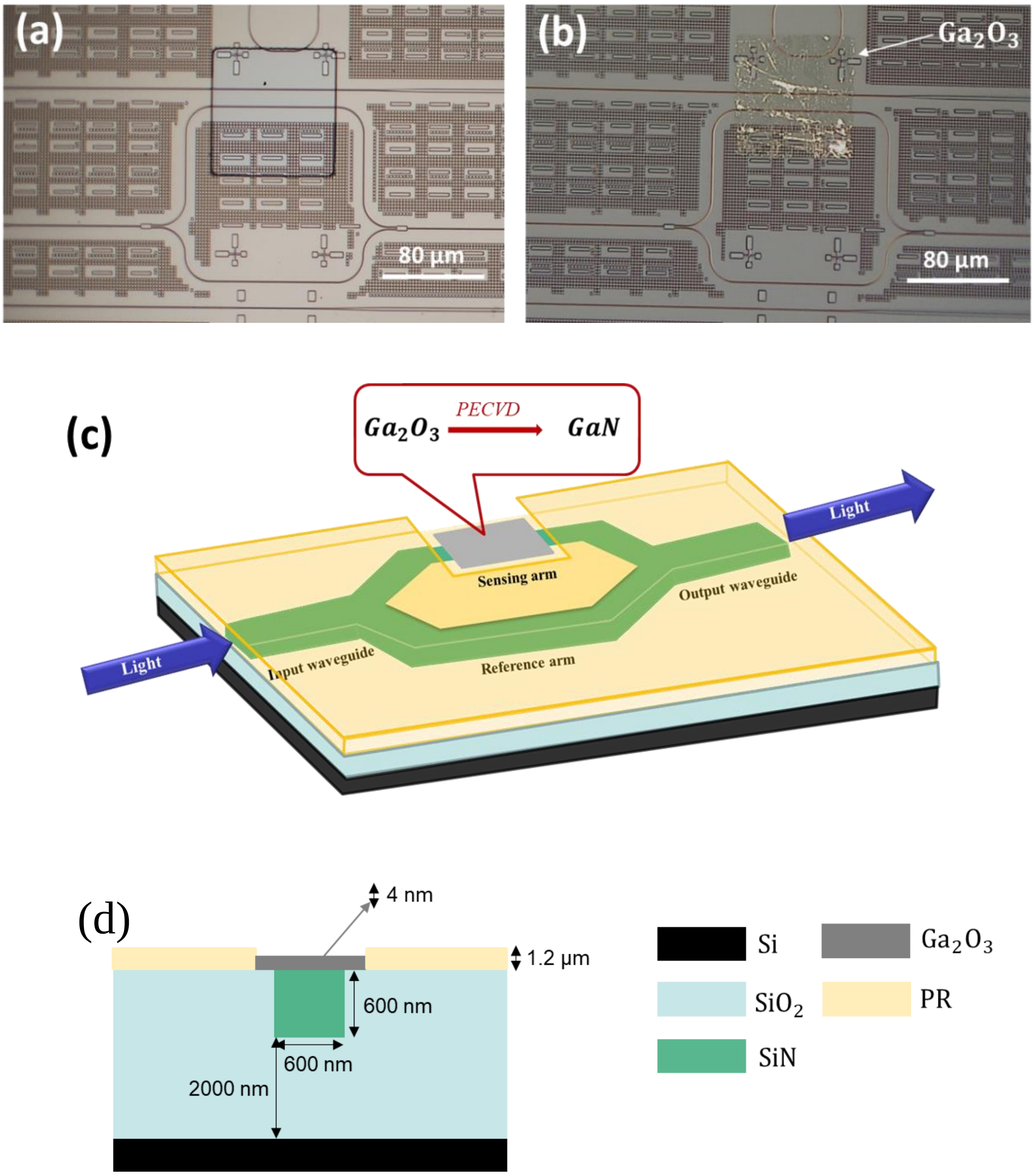

Figure 4-13 Optical image of MZI before deposition of Ga_2O_3 on sensing arm (a) Optical image of MZI before deposition of Ga_2O_3 on sensing arm (b) Optical image of MZI after deposition of Ga_2O_3 on sensing arm (c) schematic of MZI with opened window on sensing arm with deposited material (d) The cross- section of MZI at sensing arm with deposited GaN (PR= Photo Resisit)

4.4 Characterization of 2D materials integrated on chip-based SiN devices

Two primary characterization methods employed at this stage are AFM and XPS, which confirm the presence and assess the intrinsic properties of the deposited material on the sensing arm.

4.4.1 AFM measurements of the 2D material on the MZI

As discussed in Section 2.3.1.1 of Chapter 2, AFM has been utilized as the initial characterization technique following each deposition. The rationale for employing AFM in our study was twofold: first, to verify the deposition on the targeted area, which is not possible through optical microscopy. Moreover, due to the fabrication method of the planarized MZI, SEM is incapable of providing relevant information. Consequently, AFM serves as the first characterization technique for detecting the deposition area. Second, AFM enables the measurement of deposited material thickness by calculating the difference between the MZI's surface and the top of the deposited material, which is vital for transmission measurement (to be discussed in the subsequent section). Thus, with the assistance of AFM, we confirmed the area, uniformity, and thickness of the deposited 2D material directly on the sensing arm of the MZI.

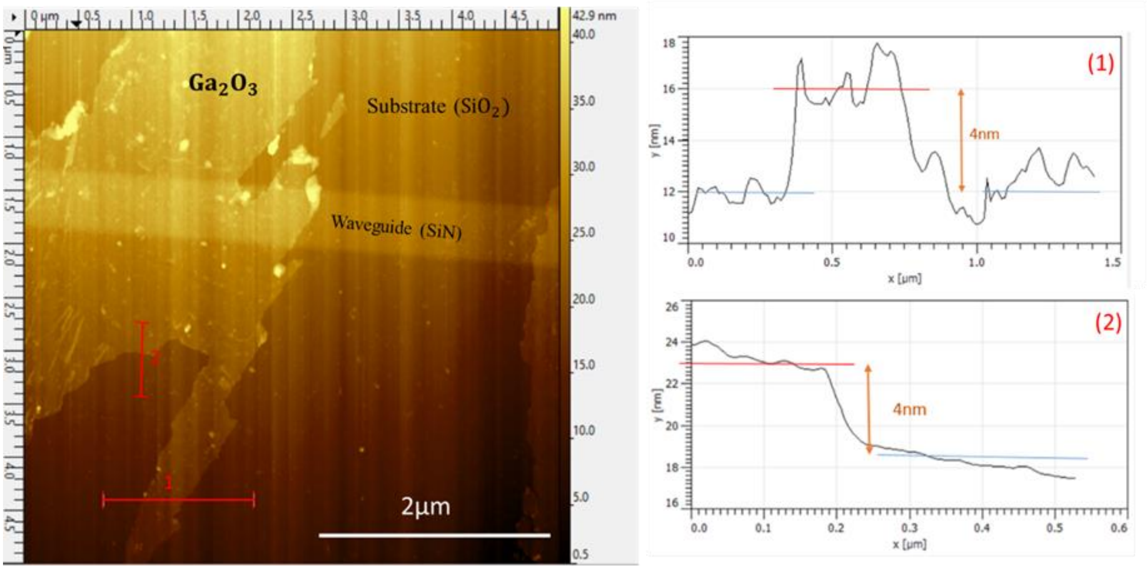

Figure 4-14 Deposited 4 nm thick Ga_2O_3 on SiN waveguide (sensing arm). Cross section number 1 and 2 show demonstrate the homogeneity of the deposited layer.

Figure 4-14 shows the detection of an ultrathin layer (~4nm thick) of Ga_2O_3 as obtained by the squeezed printing method on the sensing arm patterned by photolithography. The AFM image only presents a localized view of the sensing arm. While the 2D material is obvious in this region, it does not appear to cover the entire intended window of 100µm across the sensing arm. Therefore, future work needs to focus on refining the deposition method to ensure that the 2D material can fully cover the sensing arm, which is crucial for optimal device performance.

4.4.2 XPS analysis of the 2D material deposited on the MZI

The MZI with the deposited material was characterized by XPS before and after the nitridation process to confirm the replacement of oxygen by nitrogen. As illustrated in Section 3.2.2 of Chapter 3:, the comparison of the O1s peak for Ga_2O_3 and GaN reveals the extent of nitridation. **Figure 4-15**(a) displays a double peak for O1s: the peak at approximately 520.6 eV can be attributed to the O-Ga-O bonds in gallium oxide, while the O1s peak at a binding energy of around 532.1 eV can be assigned to the Si-O bonding originating from the SiO_2 substrate layer beneath. In contrast, following the nitridation process, only a single O1s peak is detected in **Figure 4-15**(b), centered at approximately 532.1 eV. The disappearance of the shorter energy peak thus verifies the effectiveness of the nitridation process in fully converting Ga_2O_3 into GaN.

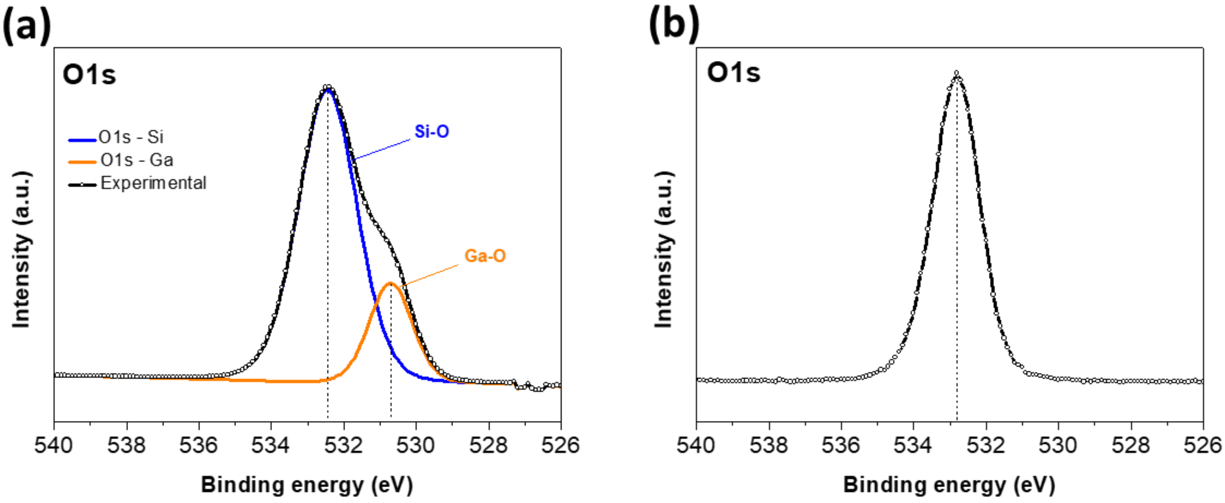

Figure 4-15 (a) O1s peak of Ga_2O_3 on MZI (Before nitridation) (b) O1s peak of GaN (After nitridation)

4.4.3 Optical Characterization of the MZI device selectively coated with 2D Ga_2O_3 and GaN

Optical characterization of 2D materials is essential for studying their unique properties and identifying their potential for applications. Optical characterization becomes even more critical in the context of 2D materials deposited on devices like waveguides. The optical properties of the 2D material can affect the propagation of light through the waveguide and vice versa. By characterizing the optical properties of the 2D material deposited on the device, we can gain insights into the device's performance and identify ways to optimize it**.**

4.4.3.1 MZI transmission measurements

We probed our MZI structure in transmission using the optical setup shown in **Figure 4-16**. For these optical measurements, I utilized the test-bed available at INL, under the guidance of Regis Orobtchouk. The components of the optical setup, as detailed in the schematic of **Figure 4-16**(a) and (b), include a source, isolator, polarizing filter, input and output lensed fiber, and spectrometer.

The first block of the characterization setup is the source: the center wavelength is in the infrared, in particular around 1.31 µm because of the low losses of the SiN waveguides. Two sources corresponded to this requirement: an SLD source from 1.2 µm to 1.4 µm, (nominal average output power of 14.56 mW) from THORlabs and another from 1.2 µm to 1.7 µm from BestSLED (5 LEDs with nominal average output power 30 mW). The output of both sources is oriented in transverse electric (TE) polarization. After the source, an isolator was placed to avoid back reflection that might damage or influence the source output. A polarization converter and filter was put after the isolator in order to ensure only TE/TM polarization to pass. All the photonic fibers used are polarization maintaining. The ellipticity and the polarization state were verified with a THORlab polarimeter PAX1000IR2/M from 900 to 1700nm. A maximum of transmission is noted when the polarizing filter was set to 0° corresponding to the TE polarization (90° corresponding to the TM) polarization. The ellipticity was below 1°, indicating linearly polarized light. There are mainly two methods to transfer light from a fiber to a chip: grating coupling and butt coupling [443].

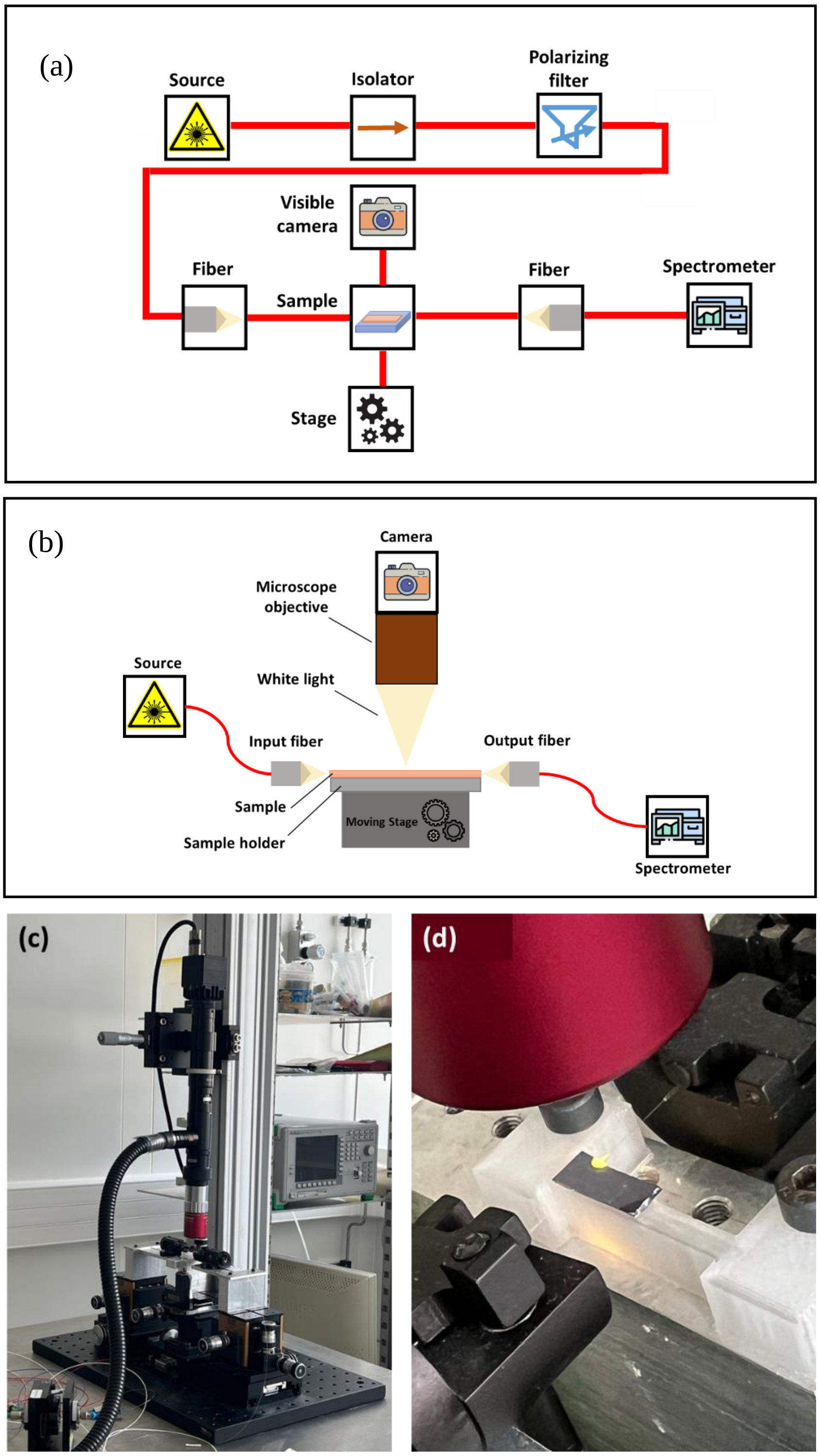

Figure 4-16 (a) schematic of the optical set up from the source to the spectrometer (b) sketch of the cross section of the stage, (c) picture of the setup (d) Picture of MZI sample on the setup.

We have used a Butt coupling method in our measurement to launch the broadband light signal between 1.2 to 1.7 µm into our chip. For this, two lensed fibers with a 1.2 µm mode field spot diameter are brought in the close surrounding of the waveguide end-facets (input and output). Butt coupling has less constraints in terms of polarization and bandwidth compared to grating coupling, thus making this method better suited to test devices. Above the chip, a white light source (Fiber-Lite DC-950) and a camera ranging from the visible to the infrared (WiDy SenS 640V-ST from NIT) enable the visualization of the chip and the fibers. **Figure 4-17** shows the input and the output top view of the butt coupling injection and collection.

The power collected is transferred to the spectrometer, model Agilent 86140B. The scan time is set according to the number of points (10001) and the resolution. For long scans the scan time is 65 sec. A measurement is taken 10 times and then averaged to reduce the high frequency noise of the signal (changing the RMS noise from 40pW to 10pW). The average is done 10 times as a tradeoff between the measurement time and the improvement of the signal quality.

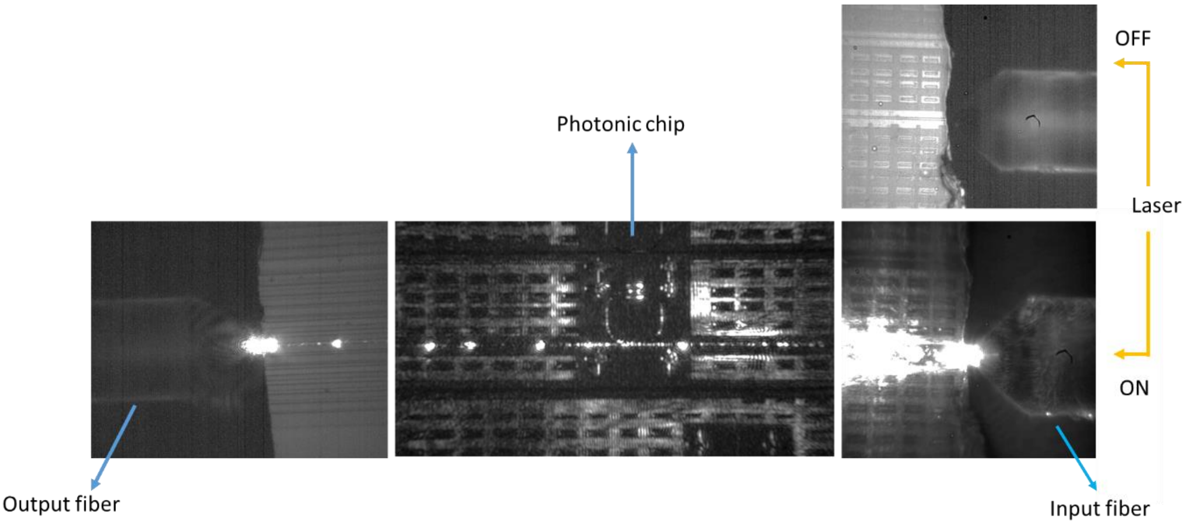

Figure 4-17 Top view of the chip while injecting and collecting light by the butt coupling method for the input waveguide (left side) and output waveguide (right side). The image right side on top shows an input waveguide while laser is off.

Figure 4-18 shows the response of the MZI before any deposition, after deposition and after nitridation for both polarizations. Qualitatively, the slight changes in the fringe patterns of the three devices, evidenced in **Figure 4-19**, confirms that there is a measureable impact from depositing the 2D material when present on the sensing arm, as will be confirmed through numerical analysis of those results.

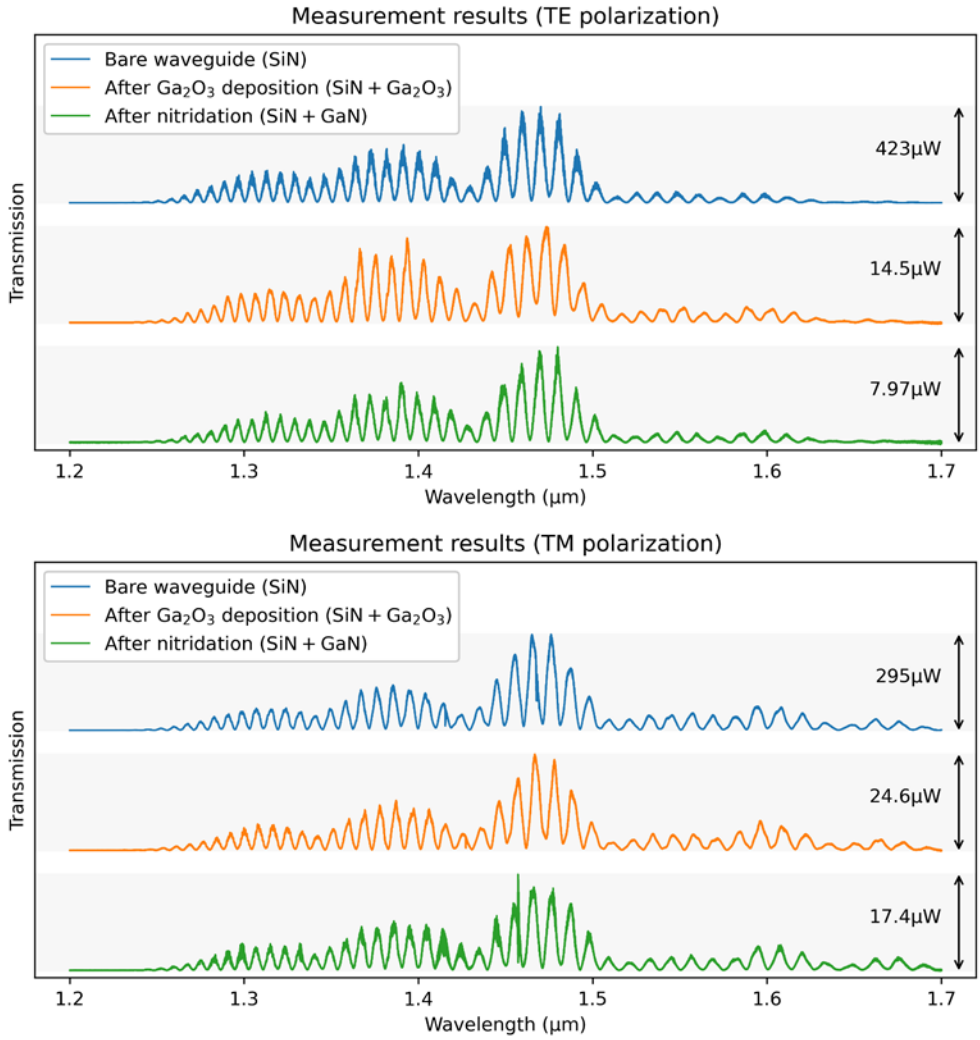

Figure 4-18 Measured response of the MZI at all three steps of the experiment, for both polarizations. Maximum transmission power is shown on the right for each response.

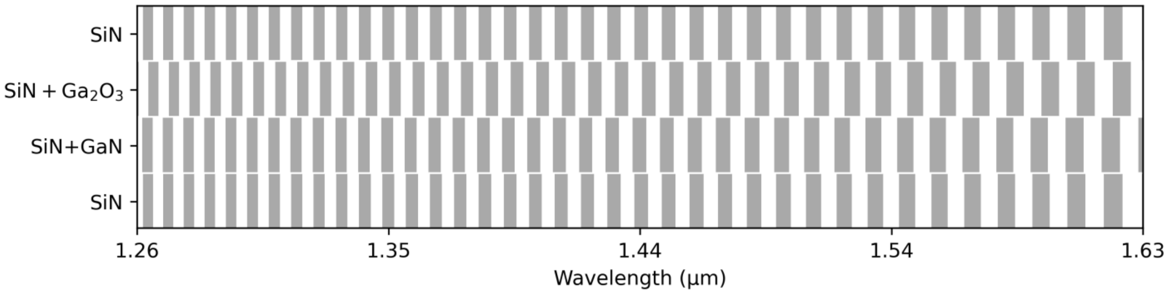

Figure 4-19 Qualitative analysis of the interference pattern of the MZI transmission: each line shows the sign of the cosine component of the transmission (grey: positive; white: negative). The differences in patterns alignment and phase shows that each fabrication step had an impact on the transmission of the device. The last «SiN» line is there to help visual comparison and does not constitute a separate experiment.

While transmission decreases after deposition of 2D material, the fringe pattern remains mostly unaffected, indicating that loss has increased globally and not only on the sensing arm. Indeed, if one arm of the MZI had higher loss than the other, then the output light would never be fully cancelled out through interference, and we would observe a non-zero offset of the output.For all devices, the lower envelope of the signal, drafted by the minima of transmissions, is close to zero, indicating that there is a good balance of losses between both arms. We can note a small anomaly Ga_2O_3 between 1.45µm and 1.5µm, where measurements in both TE and TM show that losses are perceptibly different between MZI arms at these wavelengths specifically. To a lesser degree, we make a similar comment about the measured transmission of the bare waveguide.While this oddity will have to be investigated in future works, we can conclude that the deposition of the 2D material on the sensing arm did not introduce significant losses, and that the expected fringe pattern can be seen in the output.

4.4.3.2 Data analysis of the MZI transmission measurements

Using the transmission model described in 4.2.2 (equation 4-1), we use the measured interference pattern to solve for the effective indices of the waveguide (with and without 2D material) and the characteristic lengths $\mathrm{L_2}$ and $\mathrm{L_{MUT}}$ of the MZI sensing arm. Details of the methods are described in Appendix.

Figure 4-20 (a) and (b) shows the fitted waveform obtained for the SiN waveguide in both TE and TM polarizations. We can see that in TE polarization the fit is slightly offset from the measured transmission below 1.3 μ m and above 1.6 μ m, while in TM polarization it faithfully reproduces the measured transmission.

Figure 4-20 (c) and (d) shows the fitted waveform obtained for the SiN waveguide coated with Ga_2O_3 and GaN in TM polarization. In the case of SiN+Ga_2O_3 the fit does match the measured transmission rather faithfully, but the fitted transmission for SiN+GaN shows some noticeable deviation compared to the measurements at shorter wavelengths.

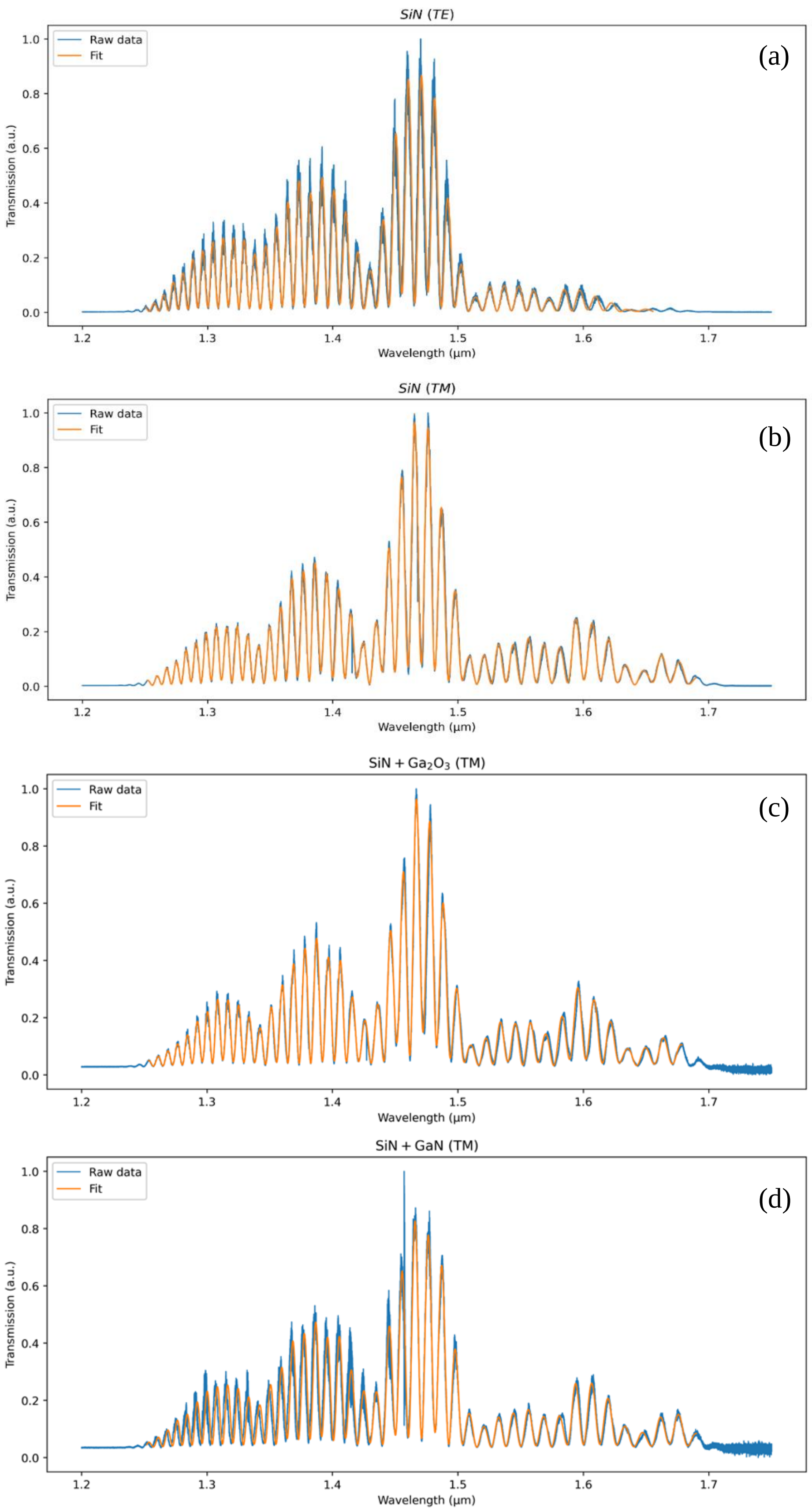

Figure 4-20 Result of the fit for the bare SiN waveguide in (a) TE and (b)TM polarizations**.**

Results of fitting TM measurements for the SiN waveguide coated with (c) Ga_2O_3 and (d) GaN

Finally, **Figure 4-21** shows, for each configuration and polarization, the theoretical value of n_{eff} (based on design parameters) and the experimental value of n_{eff} that was calculated by fitting the measurements to the transmission model. For the bare waveguide experiment, the width of the waveguide was also considered as a fitting parameter within the fabrication tolerances of ST's technological platform. Numerical results of the fit are presented in **Table 4-2**, offering a more comprehensive understanding of the waveguide properties under different conditions and the result of fitting the characteristic lengths of the MZI.

Table 4-2 Nominal and experimental values of polynomial coefficients for fitted values: n_{eff}, L_2 and L_{MUT} for both TE and TM like polarization.

	TE Polarization		TM Polarization	
	Nominal	Experimental	Nominal	Experimental
a1SiN	2.0444	2.0431	1.9617	1.9617
a2SiN	- 0.2022	-0.2077	0.0197	0.0200
a3SiN	- 0.1741	-0.1718	- 0.3790	-0.3796
a4SiN	0.0638	0.0560	0.1187	0.1194
L2 (µm)	50	49.999	50	50.046
a1 Ga2O3	2.0447	2.0445	1.9621	1.9820
a2 Ga2O3	- 0.2026	-0.2018	0.0178	0.0177
a3 Ga2O3	- 0.1692	-0.1724	- 0.3731	-0.3725
a4 Ga2O3	0.0617	0.0525	0.1163	0.1168
LMUT (µm)	100	63.126	100	63.364
a1GaN	2.0437	2.0431	1.9622	1.9622
a2 GaN	- 0.2011	-0.1982	0.0175	0.0202
a3 GaN	- 0.1709	-0.1700	- 0.3737	-0.3735
a4 GaN	0.0622	0.0607	0.1167	0.1161
LMUT (µm)	100	59.788	100	63.180

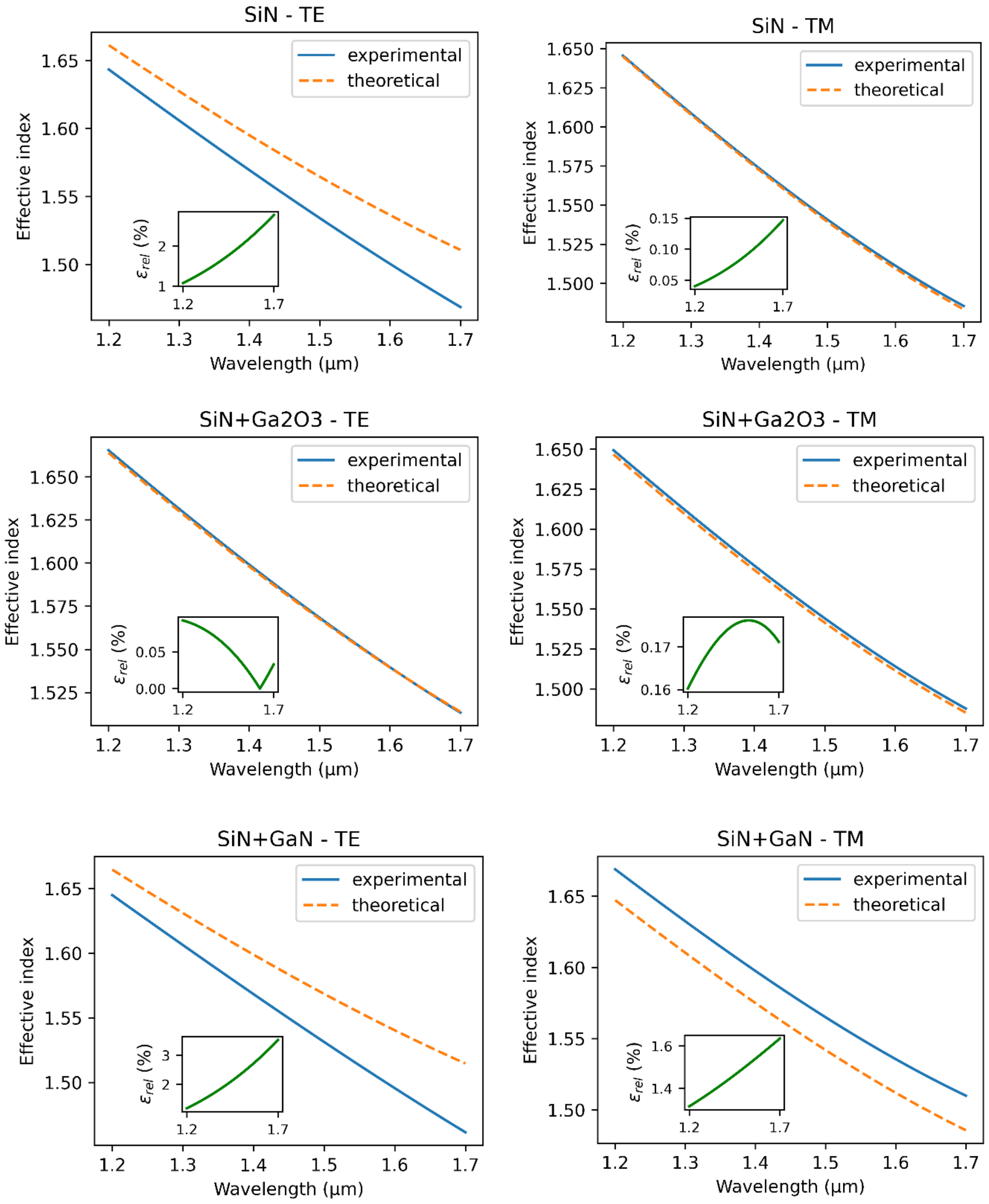

Figure 4-21 Results of fitting the effective index using measured transmission data of (a,b) bare SiN waveguide (c,d) ultrathin Ga_2O_3 layer deposited on SiN waveguide and (e,f) ultrathin GaN layer deposited on SiN waveguide; Theoretical denotes the nominal indices and experimental the results of the fit; insets show the relative error between nominal and fitted values.

A key observation from these results is the relatively high deviation between nominal and experimental values for SiN (TE) and SiN+GaN (both TE and TM), as evidenced by the inset graphs. In particular, the experimental findings for the GaN coated waveguide are unexpected, as $\mathrm{n_{eff}}$ is supposed to increase after the addition of GaN to the structure. Microscope observations provided visual confirmation that the GaN material was still present on the sensing arm of the device.

These observations suggest that either another aspect of the device impacts its behavior in a way that breaks the assumed model or the mode calculations, such as the temperature variations between experiments, or that we were not able to fit the model properly.

In the case of the SiN (TE) data, because we were able to closely match the expected transmission for SiN (TM) and SiN+Ga_2O_3 in both polarizations, we can assume that we could likely reach a good fit if the algorithm is adjusted.

In the case of the SiN+GaN data, there is unfortunately not enough data to conclude with certainty on whether the discrepancy comes from the fitting procedure or from wrong assumptions. Additional experiments and analyses are needed to reach a more conclusive answer.

However, in general, all measurements can be matched fairly well by the model using coefficients relatively close to the theoretical values. This would have been very unlikely if our initial assumptions and the model were incorrect. Additionally, the fact that the behavior of the circuit changes after nitridation confirms that there is an impact from turning the Ga_2O_3 into GaN.

Finally, the fitting procedure allows us to approximate the length of the Ga_2O_3 and GaN layers deposited on the sensing arm of the MZI. While the nominal length of the sensing window MZI arm is $\mathrm{L_1} = 100\ \mu\mathrm{m}$, the results indicates that the effective length of the 2D material is approximately $\mathrm{L_{MUT}} = 63\ \mu\mathrm{m}$ instead. This discrepancy could be attributed to multiple factors. A plausible explanation could be the variance in material thickness across the length of the sensing section. In our fitting process, we considered a uniform thickness of 4 nm. It is therefore likely that the difference between the effective MUT length and its theoretical value encompasses the variation of 2D material thickness along the waveguide as well as potential absence from some parts of the sensing arm.

Therefore, the fitted L_{MUT} can be thought of as the equivalent length of the MUT covered section if it had indeed been 4 nm thick over the whole sensing section arm.

To improve the certainty of future experiments, the waveguide geometry should be optimized in order to maximize the interaction with the 2D material, as discussed in section 4.2.1.3, which will likely simplify fitting the results and increase the accuracy in the extracted values.

4.5 Conclusion

In Chapter 4, we navigate through the essential process of integrating 2D Ga_2O_3 and GaN materials into the MZI device, a crucial component of our exploration in hybrid integrated photonics. The successful application of photolithography, as detailed in this chapter, proves an effective means for controlling the deposition area of the 2D materials onto the final device.

Our flexible methodology was put to test in patterning the SiN MZI waveguide, our chosen photonic device, displaying its broad applicability. The practicality of our direct transfer technique for synthesized 2D materials, particularly the squeeze printing method using liquid metal, was underscored, affirming its compatibility with the central project goal of integrating 2D materials onto devices without complications.

Valuable insights were gleaned from the characterization of integrated 2D materials, utilizing characterization techniques such as AFM, XPS, and Optical Characterization. These insights provide a clearer path towards refining the integration process and enhancing the performance of the integrated devices. The successful integration of a 2D material onto the device, as highlighted in this section, promises potential advancements in nonlinear measurements. While the ultra-thin nature of the Ga_2O_3 and GaN layers results in minimal variations observable in the linear regime, these findings remain critical for future studies.

Our evaluations confirm the operational functionality of the device post-deposition and post-nitridation processes, signifying the successful incorporation of the 2D material. Furthermore, the integration of the MZI yields valuable insights into the device's performance. This chapter, therefore, not only fulfills the objectives set out initially but also lays some foundation for further explorations in the domain of nonlinear optical properties of the integrated 2D material.

Conclusions and future perspectives

In the sphere of materials science, especially nanomaterials, two-dimensional (2D) materials hold tremendous potential. These unique materials, with their intriguing properties such as high refractive index contrast, tunability of optical properties, and inherent light emission capabilities, are well-suited for an array of applications. They can be utilized in areas ranging from photonic devices, such as waveguides and sensors, to energy storage and conversion. However, challenges persist, mainly concerning their synthesis and incorporation into functional devices. These obstacles have limited their widespread usage across various industries.

Given these challenges, the work documented in this PhD thesis is both relevant and influential. It paves new paths for large-scale production and seamless integration of 2D materials onto photonic integrated circuits. Consequently, our research objectives were:

- Identifying a suitable 2D material exhibit non-linear optical properties, thereby complementing silicon photonic technology for near-IR applications (lambda~1,55µm).

- Developing a suitable method for the synthesis of the chosen 2D material. This method facilitating the straightforward integration of the material directly onto waveguide.

- Characterizing our synthesized ultra-thin materials, to probe both their structural and optical properties and to clarify how the fabrication process influences these properties.

- Successfully incorporating the synthesized material onto the final device to evaluate the impact of the material's optical properties onto passive photonic devices.

We began our work by researching the state-of-the-art properties of the large family of 2D materials to find one with nonlinear optical properties. Among all candidates, we selected Gallium Nitride (GaN), known for its strong nonlinearity in its bulk form. GaN became our targeted material, bearing in mind that material's properties can vary between its bulk and ultrathin forms, and the properties can change based on thickness. While GaN is widely studied today, there is a lack of research on its linear and nonlinear properties in the 2D dimension (less than 5 nm), especially at the near-infrared range that we target. Therefore, our research filled this gap.

We demonstrated the synthesis of ultrathin layers of GaN using a fabrication technique known as Liquid Metal Chemistry has been recently developed at RMIT University. This technique consists of two main steps: squeeze printing of liquid droplets of gallium followed by a plasma nitridation process. We elaborated on the first step of our technique, showing that by squeezing a gallium droplet at room temperature onto any substrate with low surface roughness, we could easily synthesize an ultrathin layer of Ga_2O_3. We then demonstrated that with the aid of plasma, we could efficiently convert Ga_2O_3 to GaN. This two-step method allowed us to study the structural and optical properties of both Ga_2O_3 and the GaN we initially targeted. Our fabrication method proved its utility, cost-effectiveness, and time-saving potential. Moreover, this technique enables the synthesis of materials that cannot be achieved using traditional methods such as mechanical exfoliation, for instance, GaN, due to its wurtzite structure. Consequently, we believe this fabrication technique could be a pathway to synthesize other 2D materials using the Liquid Metal Chemistry method rather than traditional techniques.

Furthermore, we employed various characterization techniques to confirm the fabrication of ultrathin layers, gain information about the chemical composition and structure of our synthesized material, and compare the differences before and after the nitridation process. We studied the nature of this transformation. Thanks to Atomic Force Microscopy (AFM), we showed that our ultrathin layer, was relatively homogeneous, with a thickness of around 3 nm. Moreover, optical microscopy confirmed that our ultrathin layer extends to several millimeters in lateral size.

In the process of converting oxide sheets to nitride sheets, we optimized various plasma parameters of the nitridation treatment. Notably, we showed that time and power parameters played a pivotal role in this transformation and could be reliably used to control the composition of the final layer. We could thus monitor the gradual transition from Ga_2O_3 to GaN by manipulating these two parameters. This allowed us to create intermediate GaO_xN_y compounds, which have not been widely studied, and we characterized their properties.

We used X-ray Photoelectron Spectroscopy (XPS) to reveal the bonding configuration and chemical composition of the deposited oxide layer as well as every stage of the transformation to nitride. Moreover, by extracting the atomic percentage of XPS for each GaN_xO_y intermediate level, we observed how control over time and power led to different levels, each possessing a unique chemical composition. With the aid of XPS, we also examined in detail the change in the different spectra peaks, especially the O1s peak after nitridation, which confirmed a complete transformation to nitride at optimized parameters (time: 10 minutes and power: 200 W). Thanks to Raman measurements conducted by our collaborators at CEA, this transformation was confirmed as well.

To investigate the crystalline structure of our fabricated material, we conducted Transmission Electron Microscopy (TEM) on the oxide and nitride ultrathin layers. We found that our Ga_2O_3 possessed an amorphous structure, which transformed into a crystalline structure when it was converted into nitride. The nitride had a lattice spacing of approximately 0.189 nm, corresponding to the (102) planes, a characteristic of the wurtzite crystalline structure of GaN. This result added another layer of confirmation to the XPS and Raman findings concerning the transformation of oxide to nitride.

On the other hand, as two-dimensional Ga_2O_3 and GaN have not been widely used in applications, their optical properties remain largely unknown and might differ from that of their bulk counterparts. In general, gallium compounds hold promise for photonic applications due to their wide bandgap. One of our first steps, was to measure the optical indices of these ultrathin layers of Ga_2O_3 and GaN using ellipsometry. The obtained refractive index for 3 nm Ga_2O_3 and GaN was similar to the refractive index value of their bulk counterparts found in the literature. From this, we concluded that the refractive index for Ga_2O_3 and GaN is independent of their thickness (down to 3nm). In our work, while we have been able to achieve a minimum thickness of 2.5 nm, it is important to note that we have not yet been able to achieve the synthesis of monolayer material. Interestingly, the difference in refractive index between Ga_2O_3 and GaN ($\Delta n= 0.23$ at 1550 nm) confirmed an effective nitridation process, and shows a pathway to control the optical properties of the 2D layer to be integrated onto photonic devices. By extending our dispersion measurement to each intermediate level, we clearly observed the evolution of n (refractive index) and k (extinction coefficient) as the plasma power or time duration increased. The variations seen in these curves were strongly dependent on the degree of nitridation of the oxide film. These results indicate that the optical properties of the ultra-thin GaO_xN_y film can be reliably adjusted by the plasma parameters in a controlled manner, useful for photonic device applications. Therefore, these results offer a pathway to the integration of 2D materials with adjustable optical properties onto silicon photonic devices.

Furthermore, with ellipsometry, we were able to determine the ratio of GaN in the modeled composite layer. The result showed an increase in the fitted percentage of GaN in the modeled layer as a function of the plasma parameters, which is consistent with the XPS measurements. This reaffirms the effectiveness of the plasma treatment to transform the oxide layer into GaN in a gradual and controlled manner.

Density Functional Theory (DFT) calculations, performed by our collaborators at CNR-NANO institution, were used to study the optical properties of Ga_2O_3 and GaN and compare with our experimental results. It is important to note that due to the difficulty of applying DFT to amorphous material, Ga_2O_3 was considered as crystalline in this case. The final results showed compatibility between the refractive index calculations afforded by DFT for both Ga_2O_3 and GaN and the values extracted from ellipsometry. The extracted bandgap values confirm that the bandgaps of the synthesized ultra-thin materials are lower than those of their bulk forms and higher than those of their monolayer forms. This observation is consistent with our results, given that the material's thickness is intermediate, falling between that of a monolayer and a bulk structure .

In the final chapter of this manuscript, we focused on the integration of ultra-thin materials on a photonic integrated circuit manufactured by ST microelectronics. We chose an unclad SiN waveguide of a MZI as a test structure device. Our fabrication technique offered us the advantage of directly transferring the 2D material onto the device. Moreover, thanks to the second step of our fabrication process, nitridation by plasma, we could transition from oxide to nitride on the device with a high degree of precision, and study the impact on the device transmission.

To ensure accurate deposition on the MZI's sensing arm, we developed a technique based on photolithography to pattern the substrate with photoresist. We found that photoresist acted as a repellant for the deposited 2D materials and could be used for constraining its coating to specific areas of the chip. We developed this process further to localize the 2D material on one arm of an SiN MZI structure. Transmission measurements were performed and compared for the structure without 2D material, or selectively coated with Ga_2O_3 and GaN, and slightly distinct responses were obtained. The extinction coefficients obtained for Ga_2O_3 and GaN are both 0 at the wavelength of 1550 nm. This indicates a nearly non-existent absorption of incident light, underlining the impressive transparency of these materials within this spectral region. This characteristic behavior of Ga_2O_3 and GaN at 1550 nm is of paramount importance.The successful integration of a 2D material onto the device was also confirmed by AFM and XPS. Even if the effect on the effective index was relatively low on these non-optimized structures where the light-matter interaction with the 2D material was reduced to 0.2%, this shows some promise for further applications of these hybrid passive photonic circuits locally functionalized with 2D materials.

In addition, all the results extracted from our various characterization methods in chapters 3 and 4 can be useful for further study on the potential applications of Ga_2O_3 and GaN. This work also represents the first step in studying the potential of the intermediate level (GaO_xN_y). The knowledge gleaned can be utilized to adjust the properties of optical devices based on these materials. Furthermore, this research provides a strategy for integrating 2D materials into hybrid photonic chips, thereby enabling the local modification or enhancement of an otherwise passive optical circuit.

Last but not least, due to time constraints during the three-and-a-half years of this PhD program, the exploration of GaN's nonlinear properties remains incomplete. Nonetheless, I firmly believe that the extensive efforts and groundwork established throughout this research have effectively paved the way for subsequent projects. Future studies can now concentrate more proficiently on unraveling the nonlinearity of these materials. The scientific insights and technological advancements accomplished in this work provide a foundation for the next phase of exploration into the fascinating realm of 2D materials and their nonlinear properties. Consequently, our journey toward unlocking the full potential of these materials for various applications continues unabated.

Looking ahead, this work opens up multiple promising avenues for exploration and development.

- *Technological Prospects:* There is potential to refine and expand this innovative method towards a more reliable and controlled synthesis/transfer approach. This would involve addressing challenges such as the residual metal from the process and enhancing reproducibility. Furthermore, the adoption of sophisticated tools such as nano-imprint equipment could potentially optimize the fabrication process.

- *Material Prospects:* Our approach could also be extended to synthesize other materials, such as InN. By employing multiple steps of this process, it might be feasible to create 2D heterostructures combining GaN and Ga_2O_3, thus expanding the range of potential materials with unique properties.

- *Device Prospects:* The device's performance could be significantly improved by optimizing its geometry, specifically the waveguide cross-section, to augment the light-matter interaction with the 2D material. Other strategies to enhance this interaction could include the use of slot waveguides or optical cavities. These modifications could allow for greater control and increased efficiency in light manipulation, paving the way for a new generation of photonic devices.

In conclusion, our work provides a strong foundation for future research in the field of 2D materials and their incorporation into photonic devices.

Bibliography

[1] "Cisco Annual Internet Report - Cisco Annual Internet Report (2018–2023) White Paper - Cisco." [Online]. Available: https://www.cisco.com/c/en/us/solutions/collateral/executive-perspectives/annual-internet-report/white-paper-c11-741490.html. [Accessed: 15-Jul-2023].

[2] P. J. Winzer and D. T. Neilson, "From Scaling Disparities to Integrated Parallelism: A Decathlon for a Decade," *J. Light. Technol.*, vol. 35, no. 5, pp. 1099–1115, 2017, doi: 10.1109/JLT.2017.2662082.

[3] D. Thomson *et al.*, "Roadmap on silicon photonics," *J. Opt. (United Kingdom)*, vol. 18, no. 7, 2016, doi: 10.1088/2040-8978/18/7/073003.

[4] B. Jalali and S. Fathpour, "Silicon photonics," *J. Light. Technol.*, vol. 24, no. 12, pp. 4600–4615, 2006, doi: 10.1109/JLT.2006.885782.

[5] "Programmable photonic chip lights up quantum computing – Physics World." [Online]. Available: https://physicsworld.com/a/programmable-photonic-chip-lights-up-quantum-computing/. [Accessed: 14-Jul-2023].

[6] "Nonlinear photonics | Nonlinear Nanophotonics (NLNP)." [Online]. Available: https://davidmarpaung.com/nonlinear-nanophotonics/. [Accessed: 15-Jul-2023].

[7] T. E. Kazior, "Beyond Cmos: Heterogeneous integration of III-V devices, RF MEMS and other dissimilar materials/devices with Si CMOS to create intelligent microsystems," *Philos. Trans. R. Soc. A Math. Phys. Eng. Sci.*, vol. 372, no. 2012, 2014, doi: 10.1098/rsta.2013.0105.

[8] T. Komljenovic, D. Huang, P. Pintus, M. A. Tran, M. L. Davenport, and J. E. Bowers, "Photonic Integrated Circuits Using Heterogeneous Integration on Silicon," *Proc. IEEE*, vol. 106, no. 12, pp. 2246–2257, 2018, doi: 10.1109/JPROC.2018.2864668.

[9] L. Chang, Y. Li, N. Volet, L. Wang, J. Peters, and J. E. Bowers, "Thin film wavelength converters for photonic integrated circuits," *Optica*, vol. 3, no. 5, p. 531, 2016, doi: 10.1364/optica.3.000531.

[10] A. Zavabeti *et al.*, "A liquid metal reaction environment for the room-temperature synthesis of atomically thin metal oxides," *Science (80-.).*, vol. 358, no. 6361, pp. 332–335, 2017, doi: 10.1126/science.aao4249.

[11] T. Daeneke *et al.*, "Liquid metals: Fundamentals and applications in chemistry," *Chem. Soc. Rev.*, vol. 47, no. 11, pp. 4073–4111, 2018, doi: 10.1039/c7cs00043j.

[12] N. Syed *et al.*, "Large Area Ultrathin InN and Tin Doped InN Nanosheets Featuring 2D Electron Gases," *ACS Nano*, vol. 16, no. 4, pp. 5476–5486, 2022, doi: 10.1021/acsnano.1c09636.

[13] E. MILLER, "Integrated Optics : An Introduction," *BELL Syst. Tech. J.*, vol. 48, no. 7, pp. 2059–2069, 1969, doi: https://doi.org/10.1002/j.1538-7305.1969.tb01165.x.

[14] P. K. Tien, "Light Waves in Thin Films and Integrated Optics," *Appl. Opt.*, vol. 10, no. 11, p. 2395, 1971, doi: 10.1364/ao.10.002395.

[15] P. K. Tien, S. Riva-Sanseverino, R. J. Martin, and G. Smolinsky, "Two-layered construction of integrated optical circuits and formation of thin-film prisms, lenses, and reflectors," *Appl. Phys. Lett.*, vol. 24, no. 11, pp. 547–549, 1974, doi: 10.1063/1.1655048.

[16] S. E. Miller, "A Survey of Integrated Optics," *IEEE J. Quantum Electron.*, vol. 8, no. 2, pp. 199–205, 1972, doi: 10.1109/JQE.1972.1076910.

[17] S. E. Miller, T. Li, and E. A. J. Marcatili, “Part I : The Transmission Medium It : Devices and Systems Considerations I : The Transmission Medium,” vol. 61, no. 12, pp. 1703–1704, 1973.

[18] P. K. Tien, “Integrated optics and new wave phenomena in optical waveguides,” *Rev. Mod. Phys.*, vol. 49, no. 2, pp. 361–420, 1977, doi: 10.1103/RevModPhys.49.361.

[19] H. Kogelnik, “An Introduction to Integrated optics,” *IEEE Trans. Microw. Theory Tech. 23.1*, no. 1, pp. 2–16, 1975, doi: https://doi.org/10.1109/TMTT.1975.1128500.

[20] R. G. Hunsperger, *Integrated optics*, vol. 24, no. 6. Springer Science & Business Media, 2009.

[21] J. H. Gosling *et al.*, “Universal mobility characteristics of graphene originating from charge scattering by ionised impurities,” *Commun. Phys.*, vol. 4, no. 1, 2021, doi: 10.1038/s42005-021-00518-2.

[22] S. Manzeli, A. Allain, A. Ghadimi, and A. Kis, “Piezoresistivity and Strain-induced Band Gap Tuning in Atomically Thin MoS2,” *Nano Lett.*, vol. 15, no. 8, pp. 5330–5335, 2015, doi: 10.1021/acs.nanolett.5b01689.

[23] X. Li *et al.*, “High-speed black phosphorus field-effect transistors approaching ballistic limit,” *Sci. Adv.*, vol. 5, no. 6, pp. 1–6, 2019, doi: 10.1126/sciadv.aau3194.

[24] X. Gan *et al.*, “Chip-integrated ultrafast graphene photodetector with high responsivity,” *Nat. Photonics*, vol. 7, no. 11, pp. 883–887, 2013, doi: 10.1038/nphoton.2013.253.

[25] F. Withers *et al.*, “Light-emitting diodes by band-structure engineering in van der Waals heterostructures,” *Nat. Mater.*, vol. 14, no. 3, pp. 301–306, 2015, doi: 10.1038/nmat4205.

[26] G. R. Bhimanapati *et al.*, “Recent Advances in Two-Dimensional Materials beyond Graphene,” *ACS Nano*, vol. 9, no. 12, pp. 11509–11539, 2015, doi: 10.1021/acsnano.5b05556.

[27] M. Chhowalla, H. S. Shin, G. Eda, L. J. Li, K. P. Loh, and H. Zhang, “The chemistry of two-dimensional layered transition metal dichalcogenide nanosheets,” *Nat. Chem.*, vol. 5, no. 4, pp. 263–275, 2013, doi: 10.1038/nchem.1589.

[28] Q. H. Wang, K. Kalantar-Zadeh, A. Kis, J. N. Coleman, and M. S. Strano, “Electronics and optoelectronics of two-dimensional transition metal dichalcogenides,” *Nat. Nanotechnol.*, vol. 7, no. 11, pp. 699–712, 2012, doi: 10.1038/nnano.2012.193.

[29] T. Daeneke *et al.*, “Liquid metals: Fundamentals and applications in chemistry,” *Chem. Soc. Rev.*, vol. 47, no. 11, pp. 4073–4111, 2018, doi: 10.1039/c7cs00043j.

[30] B. J. Carey *et al.*, “Wafer-scale two-dimensional semiconductors from printed oxide skin of liquid metals,” *Nat. Commun.*, vol. 8, pp. 1–10, 2017, doi: 10.1038/ncomms14482.

[31] K. S. Novoselov, A. Mishchenko, A. Carvalho, and A. H. Castro Neto, “2D materials and van der Waals heterostructures,” *Science (80-.).*, vol. 353, no. 6298, pp. 1–25, 2016, doi: https://doi.org/10.1126/science.aac9439.

[32] N. Mounet *et al.*, “Two-dimensional materials from high-throughput computational exfoliation of experimentally known compounds,” *Nat. Nanotechnol.*, vol. 13, no. 3, pp. 246–252, 2018, doi: 10.1038/s41565-017-0035-5.

[33] S. Das, M. Kim, J. W. Lee, and W. Choi, “Synthesis, properties, and applications of 2-D materials: A comprehensive review,” *Crit. Rev. Solid State Mater. Sci.*, vol. 39, no. 4, pp. 231–252, 2014, doi: 10.1080/10408436.2013.836075.

[34] K. S. Novoselov, “Electric Field Effect in Atomically Thin Carbon Films,” *Science (80-.).*, vol. 306, no. 5696, pp. 341–342, 2004, doi: 10.1126/science.os-2.57.341-a.

[35] P. Miró, M. Audiffred, and T. Heine, “An atlas of two-dimensional materials,” *Chem. Soc. Rev.*, vol. 43, no. 18, pp. 6537–6554, 2014, doi: 10.1039/c4cs00102h.

[36] D. Akinwande *et al.*, “A review on mechanics and mechanical properties of 2D materials—Graphene and beyond,” *Extrem. Mech. Lett.*, vol. 13, pp. 42–77, 2017, doi: 10.1016/j.eml.2017.01.008.

[37] S. Z. Butler *et al.*, “Progress, challenges, and opportunities in two-dimensional materials beyond graphene,” *ACS Nano*, vol. 7, no. 4, pp. 2898–2926, 2013, doi: 10.1021/nn400280c.

[38] P. Sun, “Recent Developments in Graphene-Based Membranes: Structure, Mass-Transport Mechanism and Potential Applications.” Advanced Materials, 2016, doi: https://doi.org/10.1002/adma.201502595.

[39] T. J. Kim, J. S. Byun, Y. D. Kim, Y. C. Chang, and H. J. Kim, “Optical properties of GaN by using ellipsometry and a band calculation,” *J. Korean Phys. Soc.*, vol. 53, no. 3, pp. 1575–1579, 2008, doi: 10.3938/jkps.53.1575.

[40] Y. Wei and R. Yang, “Nanomechanics of graphene,” *Natl. Sci. Rev.*, vol. 6, no. 2, pp. 324–348, 2019, doi: 10.1093/nsr/nwy067.

[41] M. D. Stoller, S. Park, Y. Zhu, J. An, and R. S. Ruoff, “Graphene-Based Ultracapacitors,” *Nano Lett.*, pp. 6–10, 2008, doi: https://doi.org/10.1021/nl802558y.

[42] W. Xu *et al.*, “Reversible MoS2 Origami with Spatially Resolved and Reconfigurable Photosensitivity,” *Nano Lett.*, vol. 19, no. 11, pp. 7941–7949, 2019, doi: 10.1021/acs.nanolett.9b03107.

[43] C. Lee *et al.*, “Measurement of the Elastic Properties and Intrinsic Strength of Monolayer Graphene,” *Science (80-.).*, vol. 321, no. 5887, pp. 385–388, 2016, doi: https://doi.org/10.1126/science.1157996.

[44] Q. Weng, G. Li, X. Feng, K. Nielsch, D. Golberg, and O. G. Schmidt, “Electronic and Optical Properties of 2D Materials Constructed from Light Atoms,” *Adv. Mater.*, vol. 30, no. 46, 2018, doi: 10.1002/adma.201801600.

[45] A. Splendiani *et al.*, “Emerging photoluminescence in monolayer MoS2,” *Nano Lett.*, vol. 10, no. 4, pp. 1271–1275, 2010, doi: 10.1021/nl903868w.

[46] D. Deng, K. S. Novoselov, Q. Fu, N. Zheng, Z. Tian, and X. Bao, “Catalysis with two-dimensional materials and their heterostructures,” *Nat. Nanotechnol.*, vol. 11, no. 3, pp. 218–230, 2016, doi: 10.1038/nnano.2015.340.

[47] Fengnian Xia, “Two-Dimensional Material Nanophotonics,” *Nat. p*, vol. 8, no. 12, pp. 899–907, 2014, doi: https://doi.org/10.48550/arXiv.1410.3882.

[48] F. Xia, H. Wang, D. Xiao, M. Dubey, and A. Ramasubramaniam, “Two - Dimensional Material Nanophotonics,” *Nat. Photonics*, vol. 8, no. 12, pp. 899–907, 2014, doi: https://doi.org/10.48550/arXiv.1410.3882.

[49] Z. Cui, M. Wang, N. Lyu, S. Zhang, and Y. Ding, “Superlattices and Microstructures Electronic , magnetism and optical properties of transition metals adsorbed puckered arsenene,” *Superlattices Microstruct.*, vol. 152, no. October 2020, p. 106852, 2021, doi: 10.1016/j.spmi.2021.106852.

[50] M. Sun, “Unique Omnidirectional Negative Poisson ’ s Ratio in δ - Phase Carbon Monochalcogenides,” 2021, doi: 10.1021/acs.jpcc.0c11555.

[51] M. Sun, “Structure Prototype Outperforming MXenes in Stability and Performance in Metal-Ion Batteries: A High Throughput Study.” Advanced energy materials, 2021.

[52] Z. Cui, Y. Luo, J. Yu, and Y. Xu, “Physica E : Low-dimensional Systems and Nanostructures Tuning the electronic properties of MoSi 2 N 4 by molecular doping : A first principles investigation,” *Phys. E Low-dimensional Syst. Nanostructures*, vol. 134, no. June, p. 114873, 2021, doi: 10.1016/j.physe.2021.114873.

[53] B. Radisavljevic, A. Radenovic, J. Brivio, V. Giacometti, and A. Kis, “Single-layer MoS2 transistors,” *Nat. Nanotechnol.*, vol. 6, no. 3, pp. 147–150, 2011, doi: 10.1038/nnano.2010.279.

[54] M. Chhowalla, Z. Liu, and H. Zhang, “Two-dimensional transition metal dichalcogenide (TMD) nanosheets,” *Chem. Soc. Rev.*, vol. 44, no. 9, pp. 2584–2586, 2015, doi: 10.1039/c5cs90037a.

[55] J. A. Wilson and A. D. Yoffe, “The transition metal dichalcogenides discussion and interpretation of the observed optical, electrical and structural properties,” *Adv. Phys.*, vol. 18, no. 73, pp. 193–335, 1969, doi: 10.1080/00018736900101307.

[56] M. Osada and T. Sasaki, “Exfoliated oxide nanosheets: New solution to nanoelectronics,” *J. Mater. Chem.*, vol. 19, no. 17, pp. 2503–2511, 2009, doi: 10.1039/b820160a.

[57] R. Ma and T. Sasaki, “Nanosheets of oxides and hydroxides: Ultimate 2D charge-bearing functional crystallites,” *Adv. Mater.*, vol. 22, no. 45, pp. 5082–5104, 2010, doi: 10.1002/adma.201001722.

[58] P. Nalawade, B. Aware, V. J. Kadam, and R. S. Hirlekar, “Layered double hydroxides: A review,” *J. Sci. Ind. Res. (India).*, vol. 68, no. 4, pp. 267–272, 2009.

[59] V. Grasso, *Electronic structure and electronic transitions in layered materials.*, vol. 13, no. 1. 1959.

[60] D. Li, X. Duan, Q. Qin, H. Fan, and W. Zheng, “Ionic liquid-assisted synthesis of mesoporous α-Ga2O 3 hierarchical structures with enhanced photocatalytic activity,” *J. Mater. Chem. A*, vol. 1, no. 40, pp. 12417–12421, 2013, doi: 10.1039/c3ta12619f.

[61] S. Gao, “A Single-Source Approach to Bi 2 S 3 and Sb 2 S 3 Nanorods via a Hydrothermal Treatment 2004,” *Growth (Lakeland)*, vol. 4, no. 3, p. 513, 2004.

[62] K. Shavanova *et al.*, “Application of 2D non-graphene materials and 2D oxide nanostructures for biosensing technology,” *Sensors (Switzerland)*, vol. 16, no. 2, 2016, doi: 10.3390/s16020223.

[63] R. Mas-Ballesté, C. Gómez-Navarro, J. Gómez-Herrero, and F. Zamora, “2D materials: To graphene and beyond,” *Nanoscale*, vol. 3, no. 1, pp. 20–30, 2011, doi: 10.1039/c0nr00323a.

[64] H. Li, J. Wu, Z. Yin, and H. Zhang, “Preparation and applications of mechanically exfoliated single-layer and multilayer MoS2 and WSe2 nanosheets,” *Acc. Chem. Res.*, vol. 47, no. 4, pp. 1067–1075, 2014, doi: 10.1021/ar4002312.

[65] A. J. Mannix, B. Kiraly, M. C. Hersam, and N. P. Guisinger, “Synthesis and chemistry of elemental 2D materials,” *Nat. Rev. Chem.*, vol. 1, pp. 1–15, 2017, doi: 10.1038/s41570-016-0014.

[66] H. Wu *et al.*, “Biocompatible inorganic fullerene-like molybdenum disulfide nanoparticles produced by pulsed laser ablation in water,” *ACS Nano*, vol. 5, no. 2, pp. 1276–1281, 2011, doi: 10.1021/nn102941b.

[67] V. Nicolosi, M. Chhowalla, M. G. Kanatzidis, M. S. Strano, and J. N. Coleman, “Liquid exfoliation of layered materials,” *Science (80-.).*, vol. 340, no. 6139, pp. 72–75, 2013, doi: 10.1126/science.1226419.

[68] J. N. Coleman *et al.*, “Two-Dimensional Nanosheets Produced by Liquid Exfoliation of Layered Materials,” *Science (80-.).*, vol. 331, no. February, pp. 568–571, 2011, doi: https://doi.org/10.1126/science.1194975.

[69] A. Nano *et al.*, “Synthesis and Transfer of Large-Area Monolayer WS2 Crystals: Moving Toward the Recyclable Use of Sapphire Substrates,” *ACS Nano*, vol. 9, pp. 6178–6187, 2015, doi: https://doi.org/10.1021/acsnano.5b01480.

[70] C. Altavilla, M. Sarno, and P. Ciambelli, “A novel wet chemistry approach for the synthesis of hybrid 2D free-floating single or multilayer nanosheets of MS2@oleylamine (M=Mo, W),” *Chem. Mater.*, vol. 23, no. 17, pp. 3879–3885, 2011, doi: 10.1021/cm200837g.

[71] L. K. Tan, B. Liu, J. H. Teng, S. Guo, H. Y. Low, and K. P. Loh, “Atomic layer deposition of a MoS2 film,” *Nanoscale*, vol. 6, no. 18, pp. 10584–10588, 2014, doi: 10.1039/c4nr02451f.

[72] K. K. Liu *et al.*, “Growth of large-area and highly crystalline MoS 2 thin layers on insulating substrates,” *Nano Lett.*, vol. 12, no. 3, pp. 1538–1544, 2012, doi: 10.1021/nl2043612.

[73] C. Tan and H. Zhang, “Wet-chemical synthesis and applications of non-layer structured two-dimensional nanomaterials,” *Nat. Commun.*, vol. 6, 2015, doi: 10.1038/ncomms8873.

[74] E. R. Balasooriya, C. D. Jayasinghe, U. A. Jayawardena, R. W. D. Ruwanthika, R. M. De Silva, and P. V. Udagama, “Honey Mediated Green Synthesis of Nanoparticles: New Era of Safe Nanotechnology,” *J. Nanomater.*, vol. 2017, 2017, doi: 10.1155/2017/5919836.

[75] L. Tapasztó, G. Dobrik, P. Lambin, and L. P. Biró, “Tailoring the atomic structure of graphene nanoribbons by scanning tunnelling microscope lithography,” *Nat. Nanotechnol.*, vol. 3, no. 7, pp. 397–401, 2008, doi: 10.1038/nnano.2008.149.

[76] S. Barcikowski, F. Devesa, and K. Moldenhauer, “Impact and structure of literature on nanoparticle generation by laser ablation in liquids,” *J. Nanoparticle Res.*, vol. 11, no. 8, pp. 1883–1893, 2009, doi: 10.1007/s11051-009-9765-0.

[77] J. Bell, Z. Chen, and A. Olofinjana, “Synthesis of amorphous carbon nitride using reactive ion beam sputtering deposition with grazing bombardment,” *Diam. Relat. Mater.*, vol. 10, no. 12, pp. 2184–2189, 2001, doi: 10.1016/S0925-9635(01)00505-2.

[78] T. Nissinen, T. Ikonen, M. Lama, J. Riikonen, and V. P. Lehto, “Improved production efficiency of mesoporous silicon nanoparticles by pulsed electrochemical etching,” *Powder Technol.*, vol. 288, pp. 360–365, 2016, doi: 10.1016/j.powtec.2015.11.015.

[79] M. Kumar and Y. Ando, “Chemical vapor deposition of carbon nanotubes: A review on growth mechanism and mass production,” *J. Nanosci. Nanotechnol.*, vol. 10, no. 6, pp. 3739–3758, 2010, doi: 10.1166/jnn.2010.2939.

[80] G. Yi, Z. Wu, and M. Sayer, “Preparation of Pb(Zr,Ti)O3 thin films by sol gel processing: Electrical, optical, and electro-optic properties,” *J. Appl. Phys.*, vol. 64, no. 5, pp. 2717–2724, 1988, doi: 10.1063/1.341613.

[81] A. Y. Li, I. A. Kinloch, A. H. Windle, Y. Li, A. Kinloch, and A. H. Windle, “Direct Spinning of Carbon Nanotube Fibers from Chemical Vapor Deposition Synthesis,” *Science (80-.).*, vol. 304, no. 5668, pp. 276–278, 2004, doi: https://doi.org/10.1126/science.1094982.

[82] L. Mädler, H. K. Kammler, R. Mueller, and S. E. Pratsinis, “Controlled synthesis of nanostructured particles by flame spray pyrolysis,” *J. Aerosol Sci.*, vol. 33, no. 2, pp. 369–389, 2002, doi: 10.1016/S0021-8502(01)00159-8.

[83] F. Lacour, O. Guillois, X. Portier, H. Perez, N. Herlin, and C. Reynaud, “Laser pyrolysis synthesis and characterization of luminescent silicon nanocrystals,” *Phys. E Low-Dimensional Syst. Nanostructures*, vol. 38, no. 1–2, pp. 11–15, 2007, doi: 10.1016/j.physe.2006.12.051.

[84] M. Darbandi, R. Thomann, and T. Nann, “Single quantum dots in silica spheres by microemulsion synthesis,” *Chem. Mater.*, vol. 17, no. 23, pp. 5720–5725, 2005, doi: 10.1021/cm051467h.

[85] V. Georgakilas *et al.*, “Noncovalent Functionalization of Graphene and Graphene Oxide for Energy Materials, Biosensing, Catalytic, and Biomedical Applications,” *Chem. Rev.*, vol. 116, no. 9, pp. 5464–5519, 2016, doi: 10.1021/acs.chemrev.5b00620.

[86] K. Girija, “Organic additives assisted synthesis of mesoporous β -Ga 2 O 3 nanostructures for photocatalytic dye degradation,” *Semicond. Sci. Technol.*, vol. 035015, 2013, doi: 10.1088/0268-1242/28/3/035015.

[87] M. Muruganandham *et al.*, "Controlled Fabrication of α -GaOOH and α -Ga 2 O 3 Self-Assembly and Its Superior Photocatalytic Activity," *Phys. Chem. Chem. Phys.*, pp. 44–53, 2012, doi: https://doi.org/10.1021/jp205348p.

[88] H. Qian, P. Gunawan, Y. Zhang, G. Lin, J. Zheng, and R. Xu, "Template-Free Synthesis of Highly Uniform r -GaOOH Spindles and & DESIGN 2008," 2008.

[89] V. Heine, "Crystal structure of gallium metal," *J. Phys. C Solid State Phys.*, vol. 1, no. 1, pp. 222–231, 1968, doi: 10.1088/0022-3719/1/1/325.

[90] C. Janowitz *et al.*, "Experimental electronic structure of In2O3 and Ga2O3," *New J. Phys.*, vol. 13, 2011, doi: 10.1088/1367-2630/13/8/085014.

[91] R. Roy, V. G. Hill, and E. F. Osborn, "Polymorphism of Ga2O3 and the system Ga2O3—H2O," *J. Am. Chem. Soc.*, vol. 74, no. 3, pp. 719–722, 1952, doi: https://doi.org/10.1021/ja01123a039.

[92] L. Li, W. Wei, and M. Behrens, "Synthesis and characterization of α-, β-, and γ-Ga 2o 3 prepared from aqueous solutions by controlled precipitation," *Solid State Sci.*, vol. 14, no. 7, pp. 971–981, 2012, doi: 10.1016/j.solidstatesciences.2012.04.037.

[93] D. K. Sarfo, R. R. Taylor, and A. P. O. Mullane, "Investigating Liquid Metal Galinstan as a High Current Carrier and Its Interaction with Collector Electrodes," *ACS Appl. Electron. Mater.*, vol. 2, pp. 2921–2928, 2020, doi: 10.1021/acsaelm.0c00551.

[94] B. R. Tak, S. Kumar, A. K. Kapoor, D. Wang, and X. Li, "Recent advances in the growth of gallium oxide thin films employing various growth techniques — a review," *J. Phys. D. Appl. Phys.*, vol. 54, no. 45, 2021, doi: 10.1088/1361-6463/ac1af2.

[95] M. Kim and S. Seo, "Flexible pressure and touch sensor with liquid metal droplet based on gallium alloys," *Mol. Cryst. Liq. Cryst.*, vol. 685, no. 1, pp. 40–46, 2019, doi: 10.1080/15421406.2019.1645459.

[96] M. Mas-torrent, "Resistive Switching Observation in a Gallium-Based Liquid Metal/ Graphene Junction´," *ACS Azppl. Electron. Mater.*, vol. 2, pp. 3093–3099, 2020, doi: 10.1021/acsaelm.0c00296.

[97] Y.-G. Park, "Liquid Metal-Based Soft Electronics for Wearable Healthcare." Park, Young-Geun, et al. "Liquid metal-based soft electronics for wearable healthcare." Advanced Healthcare Materials 10.17, p. 2002280, 2021, doi: https://doi.org/10.1002/adhm.202002280.

[98] M. Karbalaei, F. Verpoort, and S. Zhuiykov, "Plasma-enhanced elemental enrichment of liquid metal interfaces : Towards realization of GaS nanodomains in two-dimensional Ga 2 O 3," *Appl. Mater. Today*, vol. 27, p. 101461, 2022, doi: 10.1016/j.apmt.2022.101461.

[99] Y. Hou, J. Zhang, Z. Ding, and L. Wu, "Synthesis , characterization and photocatalytic activity of β -Ga 2 O 3 nanostructures," *Powder Technol.*, vol. 203, no. 3, pp. 440–446, 2010, doi: 10.1016/j.powtec.2010.06.004.

[100] J. Zhang, Z. Liu, C. Lin, and J. Lin, "A simple method to synthesize b -Ga 2 O 3 nanorods and their photoluminescence properties," *Cryst. GROWTH &DESIGN*, vol. 280, pp. 99–106, 2005, doi: 10.1016/j.jcrysgro.2005.02.060.

[101] S. Fujihara, Y. Shibata, and E. Hosono, "Chemical Deposition of Rodlike GaOOH and β-Ga[sub 2]O[sub 3] Films Using Simple Aqueous Solutions," *J. Electrochem. Soc.*, vol. 152, no. 11, p. C764, 2005, doi: 10.1149/1.2060627.

[102] Y. Quan, D. Fang, X. Zhang, S. Liu, and K. Huang, "Synthesis and characterization of gallium oxide nanowires via a hydrothermal method," *Mater. Chem. Phys.*, vol. 121, no. 1–2, pp. 142–146, 2010, doi: 10.1016/j.matchemphys.2010.01.009.

[103] C. R. Patra, Y. Mastai, and A. Gedanken, "Microwave-assisted synthesis of submicrometer GaO(OH) and

Ga 2O3 rods," *J. Nanoparticle Res.*, vol. 6, no. 5, pp. 509–518, 2004, doi: 10.1007/s11051-004-2715-y.

[104] X. Liu, G. Qiu, Y. Zhao, N. Zhang, and R. Yi, "Gallium oxide nanorods by the conversion of gallium oxide hydroxide nanorods," *J. Alloys Compd.*, vol. 439, no. 1–2, pp. 275–278, 2007, doi: 10.1016/j.jallcom.2006.08.062.

[105] D. Li, "Ionic liquid-assisted synthesis of mesoporous a-Ga2O3 hierarchical structures with enhanced photocatalytic activity," *J. Mater. Chem. A*, vol. 1, no. 06, pp. 12417–12421, 2013, doi: 10.1039/c3ta12619f.

[106] M. Razeghi and A. Rogalski, "Semiconductor ultraviolet detectors," *J. Appl. Phys.*, vol. 79, no. 10, pp. 7433–7473, 1996, doi: 10.1063/1.362677.

[107] J. Simon *et al.*, "Polarization-Induced Zener Tunnel Junctions in Wide-Band-Gap Heterostructures," vol. 026801, no. July, pp. 1–4, 2009, doi: 10.1103/PhysRevLett.103.026801.

[108] S. Kako, C. Santori, K. Hoshino, and S. G. Otzinger, "ARTICLES A gallium nitride single-photon source," vol. 5, no. November, pp. 887–892, 2006, doi: 10.1038/nmat1763.

[109] M. S. Miao, Q. Yan, C. G. Van De Walle, W. K. Lou, L. L. Li, and K. Chang, "Polarization-Driven Topological Insulator Transition in a GaN = InN = GaN Quantum Well," vol. 186803, no. NOVEMBER, pp. 1–5, 2012, doi: 10.1103/PhysRevLett.109.186803.

[110] F.A.Ponce, "Nitride-based semiconductors for blue and green light-emitting devices." Nature, pp. 351–359, 1997, doi: 10.1038/386351a0.

[111] L. Tong, "Anisotropic carrier mobility in buckled two-dimensional GaN Lijia," 2017, doi: 10.1039/C7CP04117A.

[112] A. Khoa, A. Lu, T. Yayama, T. Morishita, and M. J. S. Spencer, "Uncovering New Buckled Structures of Bilayer GaN: A First- Principles Study," 2019, doi: 10.1021/acs.jpcc.8b09973.

[113] A. D. Bykhovski, V. V. Kaminski, M. S. Shur, Q. C. Chen, and M. A. Khan, "Pyroelectricity in gallium nitride thin films," *Appl. Phys. Lett.*, vol. 69, no. 21, pp. 3254–3256, 1996, doi: 10.1063/1.118027.

[114] R. Agrawal and H. D. Espinosa, "Giant Piezoelectric Size Effects in Zinc Oxide and Gallium Nitride Nanowires. A First Principles Investigation," *Nano Lett.*, vol. 11, no. 2, pp. 786–790, 2011, doi: 10.1021/nl104004d.

[115] L. Li, "Thermal Non-Oxidative Aromatization of Light Alkanes Catalyzed by Gallium Nitride." Wiley: New York, NY, USA, pp. 14330–14333, 2014, doi: 10.1002/ange.201408754.

[116] H. Jeong *et al.*, "Carrier localization in In-rich InGaN/GaN multiple quantum wells for green light-emitting diodes," *Sci. Rep.*, vol. 5, pp. 1–7, 2015, doi: 10.1038/srep09373.

[117] Y. Huang, X. Duan, Y. Cui, and C. M. Lieber, "Gallium Nitride Nanowire Nanodevices," *Nano Lett.*, vol. 2, no. 2, pp. 101–104, 2002, doi: 10.1021/nl015667d.

[118] F. A. Ponce and D. P. Bour, "Nitride-based semiconductors for blue and green light-emitting devices," *Nature*, vol. 386, no. 6623, pp. 351–359, 1997, doi: 10.1038/386351a0.

[119] T. Hashimoto, F. Wu, J. S. Speck, and S. Nakamura, "A GaN bulk crystal with improved structural quality grown by the ammonothermal method," vol. 6, no. August, pp. 4–7, 2007, doi: 10.1038/nmat1955.

[120] F. Qian, Y. Li, S. Gradec, and C. M. Lieber, "Gallium Nitride-Based Nanowire Radial Heterostructures for Nanophotonics," pp. 20–24, 2004, doi: 10.1021/nl0487774.

[121] H. Matsubara, "GaN Photonic-Crystal Surface-Emitting Laser at Blue-Violet Wavelengths," *Science (80-.).*, vol. 319, no. January, pp. 445–447, 2008, doi: https://doi.org/10.1126/science.1150413.

[122] T. Katona, “Ultraviolet light-emitting diodes based on group three nitrides,” *Nat. Photonics*, vol. 2, pp. 77–84, 2008, doi: 10.1038/nphoton.2007.293.

[123] V. D. Murugesan, “Master thesis Quantum well photoluminescence under the influence of externally applied electric field Submitted by : Vignesh Devaki Murugesan,” no. November, 2018, doi: 10.13140/RG.2.2.24270.92488.

[124] T. Kuykendall, P. Pauzauskie, S. Lee, Y. Zhang, J. Goldberger, and P. Yang, “Metalorganic chemical vapor deposition route to GaN nanowires with triangular cross sections,” *Nano Lett.*, vol. 3, no. 8, pp. 1063–1066, 2003, doi: 10.1021/nl034422t.

[125] X. Chen, “High-Quality Ultra-Fine GaN Nanowires Synthesized Via Chemical Vapor Deposition,” *Adv. Mater.*, vol. 15, pp. 419–421, 2003, doi: https://doi.org/10.1002/adma.200390097.

[126] J. Goldberger *et al.*, “Single-crystal gallium nitride nanotubes,” *Nature*, vol. 422, no. 6932, pp. 599–602, 2003, doi: 10.1038/nature01551.

[127] A. Usui, “Thick GaN epitaxial growth with low dislocation density by hydride vapor phase epitaxy,” *JAPANESE J. Appl. Phys. PART 2 Lett.*, pp. 899–902, 1997.

[128] T. Sasaki and T. Matsuoka, “Substrate-polarity dependence of metal-organic vapor-phase epitaxy-grown GaN on SiC,” *J. Appl. Phys.*, vol. 64, no. 9, pp. 4531–4535, 1988, doi: 10.1063/1.341281.

[129] M. G. Kibria, “Atomic-Scale Origin of Long-Term Stability and High Performance of p -GaN Nanowire Arrays for Photocatalytic Overall Pure Water Splitting.” Advanced Materials, pp. 8388–8397, 2016, doi: 10.1002/adma.201602274.

[130] C. Chen, S. Sun, M. M. C. Chou, and K. Xie, “In situ inward epitaxial growth of bulk macroporous single crystals,” *Nat. Commun.*, vol. 8, no. 1, pp. 1–8, 2017, doi: 10.1038/s41467-017-02197-6.

[131] Z. Y. Al Balushi *et al.*, “Two-dimensional gallium nitride realized via graphene encapsulation,” *Nat. Mater.*, vol. 15, no. 11, pp. 1166–1171, 2016, doi: 10.1038/nmat4742.

[132] P. E. Q. L. Iu, “Recent advances in liquid metal photonics : technologies and applications [Invited],” *Opt. Mater. Express*, vol. 13, no. 3, pp. 699–727, 2023, doi: https://doi.org/10.1364/OME.484236.

[133] R. A. Bernhoft, “Mercury toxicity and treatment: A review of the literature,” *J. Environ. Public Health*, vol. 2012, 2012, doi: 10.1155/2012/460508.

[134] S. Zhu *et al.*, “Ultrastretchable fibers with metallic conductivity using a liquid metal alloy core,” *Adv. Funct. Mater.*, vol. 23, no. 18, pp. 2308–2314, 2013, doi: 10.1002/adfm.201202405.

[135] R. C. Chiechi, E. A. Weiss, M. D. Dickey, and G. M. Whitesides, “Eutectic gallium-indium (EGaIn): A moldable liquid metal for electrical characterization of self-assembled monolayers,” *Angew. Chemie - Int. Ed.*, vol. 47, no. 1, pp. 142–144, 2008, doi: 10.1002/anie.200703642.

[136] G. J. Hayes, J. H. So, A. Qusba, M. D. Dickey, and G. Lazzi, “Flexible liquid metal alloy (EGaIn) microstrip patch antenna,” *IEEE Trans. Antennas Propag.*, vol. 60, no. 5, pp. 2151–2156, 2012, doi: 10.1109/TAP.2012.2189698.

[137] M. D. Dickey, “Stretchable and Soft Electronics using Liquid Metals,” *Adv. Mater.*, vol. 29, no. 27, pp. 1–19, 2017, doi: 10.1002/adma.201606425.

[138] Y. Zhang, “Corrected Values for Boiling Points and Enthalpies of Vaporization of Elements in Handbooks Corrected Values for Boiling Points and Enthalpies of Vaporization of Elements,” no. October, 2017.

[139] O. Züger and U. Dürig, “Atomic structure of the α-Ga(001) surface investigated by scanning tunneling microscopy: Direct evidence for the existence of Ga2 molecules in solid gallium,” *Phys. Rev. B*, vol. 46, no. 11, pp. 7319–7321, 1992, doi: 10.1103/PhysRevB.46.7319.

[140] A. F. Chrimes, K. J. Berean, A. Mitchell, G. Rosengarten, and K. Kalantar-Zadeh, “Controlled Electrochemical Deformation of Liquid-Phase Gallium,” *ACS Appl. Mater. Interfaces*, vol. 8, no. 6, pp. 3833–3839, 2016, doi: 10.1021/acsami.5b10625.

[141] M. D. Dickey, “Emerging applications of liquid metals featuring surface oxides,” *ACS Appl. Mater. Interfaces*, vol. 6, no. 21, pp. 18369–18379, 2014, doi: 10.1021/am5043017.

[142] D. Kim *et al.*, “Recovery of nonwetting characteristics by surface modification of gallium-based liquid metal droplets using hydrochloric acid vapor,” *ACS Appl. Mater. Interfaces*, vol. 5, no. 1, pp. 179–185, 2013, doi: 10.1021/am302357t.

[143] K. E. Spells, “The determination of the viscosity of liquid gallium over an extended nrange of temperature,” *Proc. Phys. Soc.*, vol. 48, no. 2, pp. 299–311, 1936, doi: 10.1088/0959-5309/48/2/308.

[144] N. F. Mott and P. R. S. L. A, “The resistance of liquid metals,” *Proc. R. Soc. London. Ser. A, Contain. Pap. a Math. Phys. Character*, vol. 146, no. 857, pp. 465–472, 1934, doi: 10.1098/rspa.1934.0166.

[145] M. D. Dickey, “Eutectic Gallium-Indium (EGaIn): A Liquid Metal Alloy for the Formation of Stable Structures in Microchannels at Room Temperature.” Advanced functional materials, pp. 1097–1104, 2008, doi: 10.1002/adfm.200701216.

[146] K. Zuraiqi *et al.*, “Liquid Metals in Catalysis for Energy Applications,” *Joule*, vol. 4, no. 11, pp. 2290–2321, 2020, doi: 10.1016/j.joule.2020.10.012.

[147] G. A. De Wijs, G. Pastore, A. Selloni, and W. Van Der Lugt, “Electron-ion correlation in liquid metals from first principles: Liquid Mg and liquid Bi,” *Phys. Rev. Lett.*, vol. 75, no. 24, pp. 4480–4483, 1995, doi: 10.1103/PhysRevLett.75.4480.

[148] M. J. Regan and P. S. Pershan, “X-ray reflectivity studies of liquid metal and alloy surfaces,” *Phys. Rev. B*, vol. 55, no. 23, pp. 874–884, 1997, doi: https://doi.org/10.1103/PhysRevB.55.15874.

[149] S. P. Yatsenko, “Dissolution rates and solubility of some metals in liquid gallium and aluminum,” 2008, doi: 10.1088/1742-6596/98/6/062032.

[150] R.A.Oriani, “The Surface Tension of Liquid Metals and the Excess Binding Energy of Surface Atoms,” *J. Chem. Phys.*, vol. 575, no. December 2004, p. 389, 2018, doi: https://doi.org/10.1063/1.1747704.

[151] M. A. R. K. Keeney and J. Heicklen, “Surface tension and the heat of vaporization: A simple empirical correlation,” *J. Inorg. Nucl. Chem.*, vol. 41, no. I, pp. 1755–1758, 1979, doi: https://doi.org/10.1016/0022-1902(79)80118-9.

[152] Y. Ding, M. Zeng, and L. Fu, “Surface Chemistry of Gallium-Based Liquid Metals,” *Matter*, vol. 3, no. 5, pp. 1477–1506, 2020, doi: 10.1016/j.matt.2020.08.012.

[153] Y. Cui *et al.*, “Metallic Bond-Enabled Wetting Behavior at the Liquid Ga / CuGa 2 Interfaces,” 2018, doi: 10.1021/acsami.8b00009.

[154] A. Zavabeti *et al.*, “Ionic imbalance induced self-propulsion of liquid metals,” no. May, 2016, doi: 10.1038/ncomms12402.

[155] M. Korenko, “Measurement of Interfacial Tension in Liquid - Liquid High-Temperature Systems,” *J. Chem. Eng. Data*, vol. 55, pp. 4561–4573, 2010, doi: https://doi.org/10.1021/je1004752.

[156] M. Song, K. E. Daniels, A. Kiani, S. Rashid-nadimi, and M. D. Dickey, “Interfacial Tension Modulation of Liquid Metal via Electrochemical Oxidation,” vol. 2100024, 2021, doi: 10.1002/aisy.202100024.

[157] S. Handschuh-wang, T. Gan, T. Wang, F. J. Stadler, and X. Zhou, “Surface Tension of the Oxide Skin of Gallium-Based Liquid Metals,” 2021, doi: 10.1021/acs.langmuir.1c00966.

[158] A. Martin, C. Du, B. Chang, and M. Thuo, “Complexity and Opportunities in Liquid Metal Surface Oxides †,” 2020, doi: 10.1021/acs.chemmater.0c02047.

[159] E. Dimasi *et al.*, “Pairing Interactions and Gibbs Adsorption at the Liquid Bi-In Surface : A Resonant X-Ray Reflectivity Study,” 2001, doi: 10.1103/PhysRevLett.86.1538.

[160] M. F. Dumke, “Sputtering of the gallium-indium eutectic alloy in the liquid phase,” *Surf. Scienece*, vol. 124, pp. 407–422, 1983, doi: https://doi.org/10.1016/0039-6028(83)90800-2.

[161] A. Goff *et al.*, “An exploration into two-dimensional metal oxides, and other 2D materials, synthesisedvialiquid metal printing and transfer techniques,” *Dalt. Trans.*, vol. 50, no. 22, pp. 7513–7526, 2021, doi: 10.1039/d0dt04364h.

[162] A. Gupta, T. Sakthivel, and S. Seal, “Recent development in 2D materials beyond graphene,” *J. Prog. Mater. Sci.*, vol. 73, pp. 44–126, 2015, doi: 10.1016/j.pmatsci.2015.02.002.

[163] N. Cabrera, “Theory of the oxidation of metals,” 1949.

[164] P. Aukarasereenont *et al.*, “Liquid metals: An ideal platform for the synthesis of two-dimensional materials,” *Chem. Soc. Rev.*, vol. 51, no. 4, pp. 1253–1276, 2022, doi: 10.1039/d1cs01166a.

[165] Z. J. Farrell and C. Tabor, “Control of Gallium Oxide Growth on Liquid Metal Eutectic Gallium/ Indium Nanoparticles via Thiolation,” 2018, doi: 10.1021/acs.langmuir.7b03384.

[166] D. Wang, X. Wang, and W. Rao, “Precise Regulation of Ga-Based Liquid Metal Oxidation,” 2021, doi: 10.1021/accountsmr.1c00173.

[167] Q. Zhang, Y. Zheng, and J. Liu, “Direct writing of electronics based on alloy and metal (DREAM) ink : A newly emerging area and its impact on energy , environment and health sciences,” vol. 6, no. 4, pp. 311–340, 2012, doi: 10.1007/s11708-012-0214-x.

[168] A. J. (viaf)110810322 Downs, *Chemistry of aluminium, gallium, indium, and thallium*, 1st ed. London : Blackie academic and professional, 1993.

[169] M. J. Regan *et al.*, “X-ray study of the oxidation of liquid-gallium surfaces,” vol. 55, no. 16, pp. 786–790, 1997, doi: https://doi.org/10.1103/PhysRevB.55.10786.

[170] F. Scharmann *et al.*, “Viscosity effect on GaInSn studied by XPS,” *Surf. INTERFACE Anal.*, vol. 36, pp. 981–985, 2004, doi: 10.1002/sia.1817.

[171] A. Plech, “In situ x-ray reflectivity study of the oxidation kinetics of liquid gallium and the liquid alloy Ga0.93Hg0.07,” *J. Phys. Condens. Matter*, vol. 10, no. 5, p. 971, 1998, doi: 10.1088/0953-8984/10/5/007.

[172] J. M. Chabala, “Oxide-growth kinetics and fractal-like patterning across liquid gallium surfaces,” *Phys. Rev. B*, vol. 46, no. 18, 1992, doi: https://doi.org/10.1103/PhysRevB.46.11346.

[173] T. Liu, P. Sen, C. C. J. Kim, and A. C. A. Measurements, “Characterization of Nontoxic Liquid-Metal Alloy Galinstan for Applications in Microdevices,” *J. MICROELECTROMECHANICAL Syst.*, vol. 21, no. 2, pp. 443–450, 2012, doi: 10.1109/JMEMS.2011.2174421.

[174] C. Ladd, J. So, J. Muth, and M. D. Dickey, “3D Printing of Free Standing Liquid Metal Microstructures,” pp. 1–5, 2013, doi: 10.1002/adma.201301400.

[175] Khashayar Khoshmanesh 1, “Liquid metal enabled microfluidics,” *R. Soc. Chem.*, pp. 974–993, 2017, doi: 10.1039/C7LC00046D.

[176] S. Zhao, J. Zhang, and L. Fu, “Liquid Metals : A Novel Possibility of Fabricating 2D Metal Oxides,” *Adv. Mater.*, vol. 2005544, pp. 1–14, 2021, doi: 10.1002/adma.202005544.

[177] B. M. Murphy, S. Festersen, and O. M. Magnussen, “The Atomic scale structure of liquid metal-electrolyte interfaces,” *Nanoscale*, vol. 8, no. 29, pp. 13859–13866, 2016, doi: 10.1039/c6nr01571a.

[178] N. Syed *et al.*, “Wafer-Sized Ultrathin Gallium and Indium Nitride Nanosheets through the Ammonolysis of Liquid Metal Derived Oxides,” *J. Am. Chem. Soc.*, vol. 141, no. 1, pp. 104–108, 2019, doi: 10.1021/jacs.8b11483.

[179] R. S. Datta *et al.*, “Flexible two-dimensional indium tin oxide fabricated using a liquid metal printing technique,” *Nat. Electron.*, vol. 3, no. 1, pp. 51–58, 2020, doi: 10.1038/s41928-019-0353-8.

[180] R. Lin, W. Zheng, D. Zhang, Y. Li, and F. Huang, “Brushed Crystallized Ultrathin Oxides: Recrystallization and Deep-Ultraviolet Imaging Application,” *ACS Appl. Electron. Mater.*, vol. 1, no. 10, pp. 2166–2173, 2019, doi: 10.1021/acsaelm.9b00536.

[181] X. Zhang, J. Li, Z. Ma, J. Zhang, B. Leng, and B. Liu, “Design and Integration of a Layered MoS2/GaN van der Waals Heterostructure for Wide Spectral Detection and Enhanced Photoresponse,” *ACS Appl. Mater. Interfaces*, vol. 12, no. 42, pp. 47721–47728, 2020, doi: 10.1021/acsami.0c11021.

[182] J. Li *et al.*, “Template Approach to Large-Area Non-layered Ga-Group Two-Dimensional Crystals from Printed Skin of Liquid Gallium,” *Chem. Mater.*, vol. 33, no. 12, pp. 4568–4577, 2021, doi: 10.1021/acs.chemmater.1c00999.

[183] Q. Li, J. Lin, T. Y. Liu, X. Y. Zhu, W. H. Yao, and J. Liu, “Gas-mediated liquid metal printing toward large-scale 2D semiconductors and ultraviolet photodetector,” *npj 2D Mater. Appl.*, vol. 5, no. 1, 2021, doi: 10.1038/s41699-021-00219-y.

[184] A. Zavabeti *et al.*, “High-mobility p-type semiconducting two-dimensional β-TeO2,” *Nat. Electron.*, vol. 4, no. 4, pp. 277–283, 2021, doi: 10.1038/s41928-021-00561-5.

[185] N. Syed *et al.*, “Sonication-Assisted Synthesis of Gallium Oxide Suspensions Featuring Trap State Absorption: Test of Photochemistry,” *Adv. Funct. Mater.*, vol. 27, no. 43, pp. 1–10, 2017, doi: 10.1002/adfm.201702295.

[186] J. Crawford, A. Cowman, and A. P. O’Mullane, “Synthesis of 2D cobalt oxide nanosheets using a room temperature liquid metal,” *RSC Adv.*, vol. 10, no. 49, pp. 29181–29186, 2020, doi: 10.1039/d0ra06010k.

[187] T. Alkathiri *et al.*, “Atomically thin TiO2nanosheets synthesized using liquid metal chemistry,” *Chem. Commun.*, vol. 56, no. 36, pp. 4914–4917, 2020, doi: 10.1039/d0cc01456g.

[188] M. B. Ghasemian *et al.*, “Self-Limiting Galvanic Growth of MnO2 Monolayers on a Liquid Metal—Applied to Photocatalysis,” *Adv. Funct. Mater.*, vol. 29, no. 36, pp. 1–12, 2019, doi: 10.1002/adfm.201901649.

[189] Y. Wang, “Self-Deposition of 2D Molybdenum Sulfides on Liquid Metals.” Advanced functional materials, p. 2005866, 2021, doi: 10.1002/adfm.202005866.

[190] J. You, M. D. Hossain, and Z. Luo, “Synthesis of 2D transition metal dichalcogenides by chemical vapor deposition with controlled layer number and morphology,” *Nano Converg.*, vol. 5, no. 1, 2018, doi: 10.1186/s40580-018-0158-x.

[191] Y. Huang *et al.*, “Universal mechanical exfoliation of large-area 2D crystals,” *Nat. Commun.*, vol. 11, no. 1, 2020, doi: 10.1038/s41467-020-16266-w.

[192] H. Khan *et al.*, “Liquid metal-based synthesis of high performance monolayer SnS piezoelectric nanogenerators,” *Nat. Commun.*, vol. 11, no. 1, pp. 1–8, 2020, doi: 10.1038/s41467-020-17296-0.

[193] N. Syed *et al.*, “Printing two-dimensional gallium phosphate out of liquid metal,” *Nat. Commun.*, vol. 9, no. 1, 2018, doi: 10.1038/s41467-018-06124-1.

[194] A. Jannat *et al.*, “Ordered-vacancy-enabled indium sulphide printed in wafer-scale with enhanced electron mobility,” *Mater. Horizons*, vol. 7, no. 3, pp. 827–834, 2020, doi: 10.1039/c9mh01365b.

[195] M. M. Y. A. Alsaif *et al.*, “Atomically Thin Ga2S3 from Skin of Liquid Metals for Electrical, Optical, and Sensing Applications,” *ACS Appl. Nano Mater.*, vol. 2, no. 7, pp. 4665–4672, 2019, doi: 10.1021/acsanm.9b01133.

[196] M. M. Y. A. Alsaif *et al.*, “2D SnO/In 2 O 3 van der Waals Heterostructure Photodetector Based on Printed Oxide Skin of Liquid Metals,” *Adv. Mater. Interfaces*, vol. 6, no. 7, pp. 1–8, 2019, doi: 10.1002/admi.201900007.

[197] S. A. Idrus-Saidi *et al.*, “Liquid Metal-Based Route for Synthesizing and Tuning Gas-Sensing Elements,” *ACS Sensors*, vol. 5, no. 4, pp. 1177–1189, 2020, doi: 10.1021/acssensors.0c00233.

[198] M. Wurdack *et al.*, “Ultrathin Ga2O3 Glass: A Large-Scale Passivation and Protection Material for Monolayer WS2,” *Adv. Mater.*, vol. 33, no. 3, pp. 1–6, 2021, doi: 10.1002/adma.202005732.

[199] C. Lee, H. Yan, L. E. Brus, T. F. Heinz, J. Hone, and S. Ryu, “Anomalous lattice vibrations of single- and few-layer MoS2,” *ACS Nano*, vol. 4, no. 5, pp. 2695–2700, 2010, doi: 10.1021/nn1003937.

[200] C. H. Huang, H. Chang, T. Y. Yang, Y. C. Wang, Y. L. Chueh, and K. Nomura, “Artificial Synapse Based on a 2D-SnO2Memtransistor with Dynamically Tunable Analog Switching for Neuromorphic Computing,” *ACS Appl. Mater. Interfaces*, vol. 13, no. 44, pp. 52822–52832, 2021, doi: 10.1021/acsami.1c18329.

[201] T. Yuan *et al.*, “Two-Dimensional Amorphous SnOx from Liquid Metal: Mass Production, Phase Transfer, and Electrocatalytic CO2 Reduction toward Formic Acid,” *Nano Lett.*, vol. 20, no. 4, pp. 2916–2922, 2020, doi: 10.1021/acs.nanolett.0c00844.

[202] K. Khan *et al.*, “Recent developments in emerging two- dimensional materials and their applications,” pp. 387–440, 2020, doi: 10.1039/c9tc04187g.

[203] H. J. Um, G. D. Kong, and H. J. Yoon, “Thermally Controlled Phase Transition of Low-Melting Electrode for Wetting-Based Spontaneous Top Contact in Molecular Tunnel Junction,” *ACS Appl. Mater. Interfaces*, vol. 10, no. 40, pp. 34758–34764, 2018, doi: 10.1021/acsami.8b12312.

[204] S. E. Byeon, M. Kim, and H. J. Yoon, “Maskless Arbitrary Writing of Molecular Tunnel Junctions,” *ACS Appl. Mater. Interfaces*, vol. 9, no. 46, pp. 40556–40563, 2017, doi: 10.1021/acsami.7b14347.

[205] L. Cademartiri *et al.*, “Electrical Resistance of AgTS−S(CH2)n−1CH3//Ga2O3/EGaIn Tunneling Junctions,” *J. Phys. Chem. C*, vol. 116, pp. 10848–60, 2012, doi: 10.1021/jp212501.

[206] Y. Lin, C. Cooper, M. Wang, J. J. Adams, J. Genzer, and M. D. Dickey, “Handwritten, Soft Circuit Boards and Antennas Using Liquid Metal Nanoparticles,” *Small*, vol. 11, no. 48, pp. 6397–6403, 2015, doi: 10.1002/smll.201502692.

[207] E. Douvogianni *et al.*, “Soft Nondamaging Contacts Formed from Eutectic Ga-In for the Accurate Determination of Dielectric Constants of Organic Materials,” *Chem. Mater.*, vol. 30, no. 16, pp. 5527–5533, 2018, doi: 10.1021/acs.chemmater.8b02212.

[208] L. Ren *et al.*, “Nanodroplets for Stretchable Superconducting Circuits,” *Adv. Funct. Mater.*, vol. 26, no. 44, pp. 8111–8118, 2016, doi: 10.1002/adfm.201603427.

[209] M. R. Khan, C. Trlica, J. H. So, M. Valeri, and M. D. Dickey, “Influence of water on the interfacial behavior of gallium liquid metal alloys,” *ACS Appl. Mater. Interfaces*, vol. 6, no. 24, pp. 22467–22473, 2014, doi: 10.1021/am506496u.

[210] S. Y. Tang *et al.*, “Liquid metal enabled pump,” *Proc. Natl. Acad. Sci. U. S. A.*, vol. 111, no. 9, pp. 3304–3309, 2014, doi: 10.1073/pnas.1319878111.

[211] T. H. Hsu, S. Manakasettharn, J. A. Taylor, and T. Krupenkin, “Bubbler: A Novel Ultra-High Power Density Energy Harvesting Method Based on Reverse Electrowetting,” *Sci. Rep.*, vol. 5, pp. 1–13, 2015, doi: 10.1038/srep16537.

[212] R. S. Datta *et al.*, “Flexible two-dimensional indium tin oxide fabricated using a liquid metal printing technique,” *Nat. Electron.*, vol. 3, no. 1, pp. 51–58, 2020, doi: 10.1038/s41928-019-0353-8.

[213] N. Syed *et al.*, “Wafer-Sized Ultrathin Gallium and Indium Nitride Nanosheets through the Ammonolysis of Liquid Metal Derived Oxides,” *J. Am. Chem. Soc.*, vol. 141, no. 1, pp. 104–108, 2019, doi: 10.1021/jacs.8b11483.

[214] Y. Chen *et al.*, “Growth of 2D GaN Single Crystals on Liquid Metals,” *J. Am. Chem. Soc.*, pp. 16392–16395, 2018, doi: 10.1021/jacs.8b08351.

[215] K. A. Messalea *et al.*, “Bi2O3 monolayers from elemental liquid bismuth,” *Nanoscale*, vol. 10, no. 33, pp. 15615–15623, 2018, doi: 10.1039/c8nr03788d.

[216] Z. Zhou, B. Yin, and J. Michel, “On-chip light sources for silicon photonics,” *Light Sci. Appl.*, vol. 4, no. 11, pp. 1–13, 2015, doi: 10.1038/lsa.2015.131.

[217] S. Matsuo and T. Kakitsuka, “Low-operating-energy directly modulated lasers for short-distance optical interconnects,” *Adv. Opt. Photonics*, vol. 10, no. 3, p. 567, 2018, doi: 10.1364/aop.10.000567.

[218] C. Xiang *et al.*, “ Narrow-linewidth III-V/Si/Si 3 N 4 laser using multilayer heterogeneous integration ,” *Optica*, vol. 7, no. 1, p. 20, 2020, doi: 10.1364/optica.384026.

[219] B. Wohlfeil, G. Rademacher, C. Stamatiadis, K. Voigt, L. Zimmermann, and K. Petermann, “A Two-Dimensional Fiber Grating Coupler on SOI for Mode Division Multiplexing,” *IEEE Photonics Technol. Lett.*, vol. 28, no. 11, pp. 1241–1244, 2016, doi: 10.1109/LPT.2016.2514712.

[220] R. G. H. Van Uden *et al.*, “Ultra-high-density spatial division multiplexing with a few-mode multicore fibre,” *Nat. Photonics*, vol. 8, no. 11, pp. 865–870, 2014, doi: 10.1038/nphoton.2014.243.

[221] R. Soref, “The past, present, and future of silicon photonics,” *IEEE J. Sel. Top. Quantum Electron.*, vol. 12, no. 6, pp. 1678–1687, 2006, doi: 10.1109/JSTQE.2006.883151.

[222] J. Hu *et al.*, “Si-CMOS-compatible lift-off fabrication of low-loss planar chalcogenide waveguides,” *Opt. Express*, vol. 15, no. 19, p. 11798, 2007, doi: 10.1364/oe.15.011798.

[223] C. Sun, Y. Yu, G. Chen, and X. Zhang, “Ultra-compact bent multimode silicon waveguide with ultralow inter-mode crosstalk,” *Opt. Lett.*, vol. 42, no. 15, p. 3004, 2017, doi: 10.1364/ol.42.003004.

[224] H. Tang, L. Zhou, J. Xie, L. Lu, and J. Chen, “Electromagnetically Induced Transparency in a Silicon Self-Coupled Optical Waveguide,” *J. Light. Technol.*, vol. 36, no. 11, pp. 2188–2195, 2018, doi: 10.1109/JLT.2018.2804889.

[225] D. Dai, “Advanced Passive Silicon Photonic Devices With Asymmetric Waveguide Structures,” *Proc. IEEE*, vol. 106, no. 12, pp. 2117–2143, 2018, doi: 10.1109/JPROC.2018.2822787.

[226] J. H. Han, F. Boeuf, J. Fujikata, S. Takahashi, S. Takagi, and M. Takenaka, “Efficient low-loss InGaAsP/Si hybrid MOS optical modulator,” *Nat. Photonics*, vol. 11, no. 8, pp. 486–490, 2017, doi: 10.1038/nphoton.2017.122.

[227] T. Hiraki *et al.*, “Heterogeneously integrated III-V/Si MOS capacitor Mach-Zehnder modulator,” *Nat. Photonics*, vol. 11, no. 8, pp. 482–485, 2017, doi: 10.1038/nphoton.2017.120.

[228] G. Zhou, L. Zhou, L. Lu, Y. Guo, and J. Chen, “Phase-Coded Microwave Signal Generation Based on a Segmented Silicon Mach-Zehnder Modulator,” *IEEE J. Sel. Top. Quantum Electron.*, vol. 26, no. 2, pp. 1–8, 2020, doi: 10.1109/JSTQE.2019.2926198.

[229] D. Li, K. Jiang, X. Sun, and C. Guo, “AlGaN photonics: recent advances in materials and ultraviolet devices,” *Adv. Opt. Photonics*, vol. 10, no. 1, p. 43, 2018, doi: 10.1364/aop.10.000043.

[230] J. Cui and Z. Zhou, “High-performance Ge-on-Si photodetector with optimized DBR location,” *Opt. Lett.*, vol. 42, no. 24, p. 5141, 2017, doi: 10.1364/ol.42.005141.

[231] Y. Gao *et al.*, “Photon-trapping microstructures enable high-speed high-efficiency silicon photodiodes,” *Nat. Photonics*, vol. 11, no. 5, pp. 301–308, 2017, doi: 10.1038/nphoton.2017.37.

[232] D. Dai, “Monolithically integrated 64-channel silicon hybrid demultiplexer enabling simultaneous wavelength- and mode-division-multiplexing Daoxin,” *Laser Photonics Rev.*, vol. 9, no. 3, pp. 339–344, 2015, doi: 10.1002/lpor.201400446.

[233] L. Feng *et al.*, “Nonreciprocal light propagation in a silicon photonic circuit,” *Science (80-.).*, vol. 333, no. 6043, pp. 729–733, 2011, doi: 10.1126/science.1206038.

[234] M. J. R. Heck *et al.*, “Hybrid Silicon Photonic Integrated Circuit Technology,” *IEEE J. Sel. Top. Quantum Electron.*, vol. 19, no. 4, pp. 6100117–6100117, 2012, doi: https://doi.org/10.1109/JSTQE.2012.2235413.

[235] H. Fukuda, K. Yamada, T. Tsuchizawa, T. Watanabe, H. Shinojima, and S. Itabashi, “Silicon photonic circuit with polarization diversity,” *Opt. Express*, vol. 16, no. 7, p. 4872, 2008, doi: 10.1364/oe.16.004872.

[236] M. Liu *et al.*, “A graphene-based broadband optical modulator,” *Nature*, vol. 474, no. 7349, pp. 64–67, 2011, doi: 10.1038/nature10067.

[237] L. Ye, K. Sui, Y. Zhang, and Q. H. Liu, “Broadband optical waveguide modulators based on strongly coupled hybrid graphene and metal nanoribbons for near-infrared applications,” *Nanoscale*, vol. 11, no. 7, pp. 3154–3163, 2019, doi: 10.1039/c8nr09157a.

[238] L. Jia, “Fabrication Technologies for the On-Chip Integration of 2D Materials,” *Small Methods*, vol. 6, no. 3, p. 2102435, 2022, doi: 10.1002/smtd.202101435.

[239] L. Jia *et al.*, “Fabrication Technologies for the On-Chip Integration of 2D Materials,” *Small Methods*, vol. 6, no. 3, 2022, doi: 10.1002/smtd.202101435.

[240] A. Castellanos-Gomez *et al.*, “Deterministic transfer of two-dimensional materials by all-dry viscoelastic stamping,” *2D Mater.*, vol. 1, no. 1, 2014, doi: 10.1088/2053-1583/1/1/011002.

[241] S. Fan, “Transfer assembly for two-dimensional van der Waals Heterostructures,” *2D Mater.*, vol. 7, no. 2, p. 022005, 2022, doi: 10.1088/2053-1583/ab7629.

[242] H. Li, J. Wu, X. Huang, Z. Yin, J. Liu, and H. Zhang, “A universal, rapid method for clean transfer of nanostructures onto various substrates,” *ACS Nano*, vol. 8, no. 7, pp. 6563–6570, 2014, doi: 10.1021/nn501779y.

[243] S. J. Cartamil-Bueno, M. Cavalieri, R. Wang, S. Houri, S. Hofmann, and H. S. J. van der Zant, “Mechanical characterization and cleaning of CVD single-layer h-BN resonators,” *npj 2D Mater. Appl.*, vol. 1, no. 1, pp. 1–6, 2017, doi: 10.1038/s41699-017-0020-8.

[244] V. Shautsova *et al.*, “Direct Laser Patterning and Phase Transformation of 2D PdSe2 Films for On-Demand Device Fabrication,” *ACS Nano*, vol. 13, no. 12, pp. 14162–14171, 2019, doi: 10.1021/acsnano.9b06892.

[245] T. Tan, X. Jiang, C. Wang, B. Yao, and H. Zhang, “2D Material Optoelectronics for Information Functional Device Applications: Status and Challenges,” *Adv. Sci.*, vol. 7, no. 11, 2020, doi: 10.1002/advs.202000058.

[246] C. (John) Zhang *et al.*, “Additive-free MXene inks and direct printing of micro-supercapacitors,” *Nat. Commun.*, vol. 10, no. 1, pp. 1–9, 2019, doi: 10.1038/s41467-019-09398-1.

[247] D. McManus *et al.*, “Water-based and biocompatible 2D crystal inks for all-inkjet-printed heterostructures,” *Nat. Nanotechnol.*, vol. 12, no. 4, pp. 343–350, 2017, doi: 10.1038/nnano.2016.281.

[248] G. Hu *et al.*, “Black phosphorus ink formulation for inkjet printing of optoelectronics and photonics,” *Nat. Commun.*, vol. 8, no. 1, 2017, doi: 10.1038/s41467-017-00358-1.

[249] Y. Yang *et al.*, “Graphene-Based Multilayered Metamaterials with Phototunable Architecture for on-Chip Photonic Devices,” *ACS Photonics*, vol. 6, no. 4, pp. 1033–1040, 2019, doi: 10.1021/acsphotonics.9b00060.

[250] D. Xiong, Y. Shi, and H. Y. Yang, “Rational design of MXene-based films for energy storage: Progress, prospects,” *Mater. Today*, vol. 46, no. June, pp. 183–211, 2021, doi: 10.1016/j.mattod.2020.12.004.

[251] M. Prechtl *et al.*, “Hybrid Devices by Selective and Conformal Deposition of PtSe2 at Low Temperatures,” *Adv. Funct. Mater.*, vol. 31, no. 46, 2021, doi: 10.1002/adfm.202103936.

[252] Z. Zhang, “Direct Growth of Multi-Layer Graphene on Quartz Glass for High-Performance Broadband Neutral Density Filter Applications,” *Adv. Opt. Mater.*, vol. 8, p. 2000166 (1, 2020, doi: 10.1002/adom.202000166.

[253] L. Li *et al.*, “Integrated flexible chalcogenide glass photonic devices,” *Nat. Photonics*, vol. 8, no. 8, pp. 643–649, 2014, doi: 10.1038/nphoton.2014.138.

[254] J. Hu, L. Li, H. Lin, P. Zhang, W. Zhou, and Z. Ma, “Flexible integrated photonics: where materials, mechanics and optics meet [Invited],” *Opt. Mater. Express*, vol. 3, no. 9, p. 1313, 2013, doi: 10.1364/ome.3.001313.

[255] L. Li *et al.*, “Monolithically integrated stretchable photonics,” *Light Sci. Appl.*, vol. 7, no. 2, p. 17138, 2018, doi: 10.1038/lsa.2017.138.

[256] H. Lin *et al.*, “Demonstration of high-Q mid-infrared chalcogenide glass-on-silicon resonators,” *Opt. Lett.*, vol. 38, no. 9, p. 1470, 2013, doi: 10.1364/ol.38.001470.

[257] M. Beck *et al.*, “Continuous wave operation of a mid-infrared semiconductor laser at room temperature,” *Science (80-.).*, vol. 295, no. 5553, pp. 301–305, 2002, doi: 10.1126/science.1066408.

[258] M. Tonouchi, “Cutting-edge terahertz technology,” *Nat. Photonics*, vol. 1, no. 2, pp. 97–105, 2007, doi: 10.1038/nphoton.2007.3.

[259] B. Sensale-Rodriguez *et al.*, “Broadband graphene terahertz modulators enabled by intraband transitions,” *Nat. Commun.*, vol. 3, 2012, doi: 10.1038/ncomms1787.

[260] R. Ko¨hler, “Terahertz semiconductor- heterostructure laser,” *Nature*, vol. 417, p. 6885, 2002, doi: 10.1038/417156a.

[261] L. M. Duan, M. D. Lukin, J. I. Cirac, and P. Zoller, “Long-distance quantum communication with atomic ensembles and linear optics,” *Nature*, vol. 414, no. 6862, pp. 413–418, 2001.

[262] J. Pan, D. Bouwmeester, and M. Daniell, “Experimental test of quantum nonlocality in three-photon Greenberger±Horne±Zeilinger entanglement,” *Nature*, vol. 9, no. 1, pp. 515–519, 2000, doi: 10.1038/35000514.

[263] X. Lu *et al.*, “Chip-integrated visible–telecom entangled photon pair source for quantum communication,” *Nat. Phys.*, vol. 15, no. 4, pp. 373–381, 2019, doi: 10.1038/s41567-018-0394-3.

[264] J. Yao, “Microwave photonics,” *J. Light. Technol.*, vol. 27, no. 3, pp. 314–335, 2009, doi: 10.1109/JLT.2008.2009551.

[265] S. A. Diddams *et al.*, “Direct link between microwave and optical frequencies with a 300 THz

femtosecond laser comb," *Phys. Rev. Lett.*, vol. 84, no. 22, pp. 5102–5105, 2000, doi: 10.1103/PhysRevLett.84.5102.

[266] J. Capmany and D. Novak, "Microwave photonics combines two worlds," *Nat. Photonics*, vol. 1, no. 6, pp. 319–330, 2007, doi: 10.1038/nphoton.2007.89.

[267] J. Wu, "Two-Dimensional Materials for Integrated Photonics Recent Advances and Future Challenges." .

[268] C. H. Liu, Y. C. Chang, T. B. Norris, and Z. Zhong, "Graphene photodetectors with ultra-broadband and high responsivity at room temperature," *Nat. Nanotechnol.*, vol. 9, no. 4, pp. 273–278, 2014, doi: 10.1038/nnano.2014.31.

[269] J. Guo *et al.*, "High-performance silicon−graphene hybrid plasmonic waveguide photodetectors beyond 1.55 μm," *Light Sci. Appl.*, vol. 9, no. 1, 2020, doi: 10.1038/s41377-020-0263-6.

[270] J. Klein *et al.*, "Electric-field switchable second-harmonic generation in bilayer MoS2 by inversion symmetry breaking," *Nano Lett.*, vol. 17, no. 1, pp. 392–398, 2017, doi: 10.1021/acs.nanolett.6b04344.

[271] Y. Qu, "Enhanced Four-Wave Mixing in Silicon Nitride Waveguides Integrated with 2D Layered.pdf," *Adv. Opt. Mater.*, vol. 8, p. 2001048, 2020, doi: 10.1002/adom.202001048.

[272] Y. Zhang *et al.*, "Enhanced Self-Phase Modulation in Silicon Nitride Waveguides Integrated With 2D Graphene Oxide Films," vol. 29, no. 1, 2023.

[273] X. Zong *et al.*, "Black phosphorus-based van der Waals heterostructures for mid-infrared light-emission applications," *Light Sci. Appl.*, vol. 9, no. 1, 2020, doi: 10.1038/s41377-020-00356-x.

[274] C. Qiu, Y. Yang, C. Li, Y. Wang, K. Wu, and J. Chen, "All-optical control of light on a graphene-on-silicon nitride chip using thermo-optic effect," *Sci. Rep.*, vol. 7, no. 1, pp. 1–7, 2017, doi: 10.1038/s41598-017-16989-9.

[275] S. B. Desai *et al.*, "MoS 2 transistors with 1-nanometer gate lengths," *Science (80-.).*, vol. 354, no. 6308, pp. 99–103, 2016.

[276] A. Phatak, Z. Cheng, C. Qin, and K. Goda, "Design of electro-optic modulators based on graphene-on-silicon slot waveguides," *Opt. Lett.*, vol. 41, no. 11, p. 2501, 2016, doi: 10.1364/ol.41.002501.

[277] Y. Liu *et al.*, "Ultra-sensitive and plasmon-tunable graphene photodetectors for micro-spectrometry," *Nanoscale*, vol. 10, no. 42. pp. 20013–20019, 2018, doi: 10.1039/c8nr04996c.

[278] X. Yu *et al.*, "Atomically thin noble metal dichalcogenide: A broadband mid-infrared semiconductor," *Nat. Commun.*, vol. 9, no. 1, pp. 1–9, 2018, doi: 10.1038/s41467-018-03935-0.

[279] Y. Xu, Z. Shi, X. Shi, K. Zhang, and H. Zhang, "Recent progress in black phosphorus and black-phosphorus-analogue materials: Properties, synthesis and applications," *Nanoscale*, vol. 11, no. 31, pp. 14491–14527, 2019, doi: 10.1039/c9nr04348a.

[280] Z. Chu, J. Liu, Z. Guo, and H. Zhang, "2 μm passively Q-switched laser based on black phosphorus," *Opt. Mater. Express*, vol. 6, no. 7, p. 2374, 2016, doi: 10.1364/ome.6.002374.

[281] H. Lin *et al.*, "Mid-infrared integrated photonics on silicon: A perspective," *Nanophotonics*, vol. 7, no. 2, pp. 393–420, 2017, doi: 10.1515/nanoph-2017-0085.

[282] Z. Qin, G. Xie, C. Zhao, S. Wen, P. Yuan, and L. Qian, "Mid-infrared mode-locked pulse generation with multilayer black phosphorus as saturable absorber," *Opt. Lett.*, vol. 41, no. 1, p. 56, 2016, doi: 10.1364/ol.41.000056.

[283] Y. Zhang *et al.*, "Infrared photodetector based on 2D monoclinic gold phosphide nanosheets yielded from

one-step chemical vapor transport deposition," *Appl. Phys. Lett.*, vol. 120, no. 13, 2022, doi: 10.1063/5.0086166.

[284] B. Yao *et al.*, "Broadband gate-tunable terahertz plasmons in graphene heterostructures," *Nat. Photonics*, vol. 12, no. 1, pp. 22–28, 2018, doi: 10.1038/s41566-017-0054-7.

[285] Z. Yao *et al.*, "Interfacial THz generation from graphene/Si mixed-dimensional van der Waals heterostructure," *Nanoscale*, vol. 11, no. 35, pp. 16614–16620, 2019, doi: 10.1039/c9nr03570b.

[286] B. Sensale-Rodriguez *et al.*, "Broadband graphene terahertz modulators enabled by intraband transitions," *Nat. Commun.*, vol. 3, pp. 780–787, 2012, doi: 10.1038/ncomms1787.

[287] V. Kilic, M. A. Foster, and J. B. Khurgin, "THz field detection in graphene using deep neural networks," *Appl. Phys. Lett.*, vol. 115, no. 16, 2019, doi: 10.1063/1.5120022.

[288] C. Palacios-Berraquero *et al.*, "Large-scale quantum-emitter arrays in atomically thin semiconductors," *Nat. Commun.*, vol. 8, no. May, pp. 1–6, 2017, doi: 10.1038/ncomms15093.

[289] H. Yu, G. Bin Liu, J. Tang, X. Xu, and W. Yao, "Moiré excitons: From programmable quantum emitter arrays to spin-orbit–coupled artificial lattices," *Sci. Adv.*, vol. 3, no. 11, pp. 1–8, 2017, doi: 10.1126/sciadv.1701696.

[290] A. Tartakovskii, "Excitons in 2D heterostructures," *Nat. Rev. Phys.*, vol. 2, no. 1, pp. 8–9, 2020, doi: 10.1038/s42254-019-0136-1.

[291] B. Yao *et al.*, "Gate-tunable frequency combs in graphene-nitride microresonators," *Nature*, vol. 558, no. 7710, pp. 410–414, 2018, doi: 10.1038/s41586-018-0216-x.

[292] K. F. Mak, L. Ju, F. Wang, and T. F. Heinz, "Optical spectroscopy of graphene: From the far infrared to the ultraviolet," *Solid State Commun.*, vol. 152, no. 15, pp. 1341–1349, 2012, doi: 10.1016/j.ssc.2012.04.064.

[293] B. Peng, P. K. Ang, and K. P. Loh, "Two-dimensional dichalcogenides for light-harvesting applications," *Nano Today*, vol. 10, no. 2, pp. 128–137, 2015, doi: 10.1016/j.nantod.2015.01.007.

[294] S. V. Morozov *et al.*, "Giant intrinsic carrier mobilities in graphene and its bilayer," *Phys. Rev. Lett.*, vol. 100, no. 1, pp. 11–14, 2008, doi: 10.1103/PhysRevLett.100.016602.

[295] K. S. Novoselov, "Electric Field Effect in Atomically Thin Carbon Films," *Sci. Am.*, vol. 75, no. 1933supp, pp. 34–34, 1913, doi: 10.1038/scientificamerican01181913-34supp.

[296] L. Tao, H. Li, M. Sun, D. Xie, X. Li, and J. Bin Xu, "Enhanced photoresponse in interfacial gated graphene phototransistor with ultrathin Al2O3 Dielectric," *IEEE Electron Device Lett.*, vol. 39, no. 7, pp. 987–990, 2018, doi: 10.1109/LED.2018.2843804.

[297] Y. Cao *et al.*, "Correlated insulator behaviour at half-filling in magic-angle graphene superlattices," *Nature*, vol. 556, no. 7699, pp. 80–84, 2018, doi: 10.1038/nature26154.

[298] Y. Cao *et al.*, "Unconventional superconductivity in magic-angle graphene superlattices," *Nature*, vol. 556, no. 7699, pp. 43–50, 2018, doi: 10.1038/nature26160.

[299] T. Jiang, K. Yin, X. Zheng, H. Yu, and X.-A. Cheng, "Black phosphorus as a new broadband saturable absorber for infrared passively Q-switched fiber lasers," vol. 24, no. 23, pp. 411–415, 2015.

[300] Jilin Zheng, "Few-Layer Phosphorene-Decorated Microfiber for All-Optical Thresholding and Optical Modulation Jilin," *Adv. Opt. Mater.*, vol. 5, p. 1700026, 2017, doi: 10.1002/adom.201700026.

[301] N. Vermeulen *et al.*, "Graphene's nonlinear-optical physics revealed through exponentially growing self-phase modulation," *Nat. Commun.*, vol. 9, no. 1, 2018, doi: 10.1038/s41467-018-05081-z.

[302] R. Miao *et al.*, “ Ultrafast nonlinear absorption enhancement of monolayer MoS 2 with plasmonic Au nanoantennas ,” *Opt. Lett.*, vol. 44, no. 13, p. 3198, 2019, doi: 10.1364/ol.44.003198.

[303] J. Guo *et al.*, “Two-dimensional tellurium-polymer membrane for ultrafast photonics,” *Nanoscale*, vol. 11, no. 13, pp. 6235–6242, 2019, doi: 10.1039/C9NR00736A.

[304] S. Valdueza-Felip, L. Monteagudo-Lerma, J. Mangeney, M. Gonzalez-Herraez, F. H. Julien, and F. B. Naranjo, “Nonlinear absorption at optical telecommunication wavelengths of InN films deposited by RF sputtering,” *IEEE Photonics Technol. Lett.*, vol. 24, no. 22, pp. 1998–2000, 2012, doi: 10.1109/LPT.2012.2217484.

[305] Y. Zhang, L. Tao, D. Yi, J. Bin Xu, and H. K. Tsang, “Enhanced thermo-optic nonlinearities in a MoS2-on-silicon microring resonator,” *Appl. Phys. Express*, vol. 13, no. 2, pp. 2–6, 2020, doi: 10.7567/1882-0786/ab626c.

[306] K. L. Seyler *et al.*, “Electrical control of second-harmonic generation in a WSe2 monolayer transistor,” *Nat. Nanotechnol.*, vol. 10, no. 5, pp. 407–411, 2015, doi: 10.1038/nnano.2015.73.

[307] F. Liu *et al.*, “Disassembling 2D van der Waals crystals into macroscopic monolayers and reassembling into artificial lattices,” *Science (80-.).*, vol. 367, no. 6480, pp. 903–906, 2020, doi: 10.1126/science.aba1416.

[308] W. T. Hsu *et al.*, “Second harmonic generation from artificially stacked transition metal dichalcogenide twisted bilayers,” *ACS Nano*, vol. 8, no. 3, pp. 2951–2958, 2014, doi: 10.1021/nn500228r.

[309] T. Jiang *et al.*, “Gate-tunable third-order nonlinear optical response of massless Dirac fermions in graphene,” *Nat. Photonics*, vol. 12, no. 7, pp. 430–436, 2018, doi: 10.1038/s41566-018-0175-7.

[310] Z. Xie *et al.*, “Revealing of the ultrafast third-order nonlinear optical response and enabled photonic application in two-dimensional tin sulfide,” *Photonics Res.*, vol. 7, no. 5, p. 494, 2019, doi: 10.1364/prj.7.000494.

[311] X. Wen, “Nonlinear optics of two-dimensional transition metal dichalcogenides,” *InfoMat*, pp. 317–337, 2019, doi: 10.1002/inf2.12024.

[312] A. Majumdar, C. M. Dodson, T. K. Fryett, A. Zhan, S. Buckley, and D. Gerace, “Hybrid 2D Material Nanophotonics: A Scalable Platform for Low-Power Nonlinear and Quantum Optics,” *ACS Photonics*, vol. 2, no. 8, pp. 1160–1166, 2015, doi: 10.1021/acsphotonics.5b00214.

[313] P. Demongodin *et al.*, “Ultrafast saturable absorption dynamics in hybrid graphene/Si3N4 waveguides,” *APL Photonics*, vol. 4, no. 7, 2019, doi: 10.1063/1.5094523.

[314] P. Demongodin *et al.*, “Pulsed Four-Wave Mixing at Telecom Wavelengths in Si3N4 Waveguides Locally Covered by Graphene,” *Nanomaterials*, vol. 13, no. 3, pp. 14–16, 2023, doi: 10.3390/nano13030451.

[315] X. Miao *et al.*, “Optimizing nonlinear optical visibility of two-dimensional materials,” *ACS Appl. Mater. Interfaces*, vol. 9, no. 39, pp. 34448–34455, 2017, doi: 10.1021/acsami.7b09807.

[316] J. W. You, S. R. Bongu, Q. Bao, and N. C. Panoiu, “Nonlinear optical properties and applications of 2D materials: Theoretical and experimental aspects,” *Nanophotonics*, vol. 8, no. 1, pp. 63–97, 2018, doi: 10.1515/nanoph-2018-0106.

[317] Y. Zheng *et al.*, “Integrated Gallium Nitride Nonlinear Photonics,” *Laser Photonics Rev.*, vol. 16, no. 1, pp. 1–6, 2022, doi: 10.1002/lpor.202100071.

[318] C. Xiong *et al.*, “Integrated GaN photonic circuits on silicon (100) for second harmonic generation,” *Opt. InfoBase Conf. Pap.*, vol. 19, no. 11, pp. 736–738, 2011, doi: 10.1364/iprsn.2011.iwe3.

[319] Erik Stassen, “High-confinement gallium nitride-on-sapphire waveguides for integrated nonlinear

photonics." Optics letters 44.5, pp. 1064–1067, 2019.

[320] D. Munk *et al.*, "Four-wave mixing and nonlinear parameter measurement in a gallium-nitride ridge waveguide," *Opt. Mater. Express*, vol. 8, no. 1, p. 66, 2018, doi: 10.1364/ome.8.000066.

[321] V. Brasch *et al.*, "Photonic chip based optical frequency comb using soliton induced cherenkov radiation," *Opt. InfoBase Conf. Pap.*, vol. 4811, no. December, pp. 1–8, 2014, doi: 10.1126/science.aad4811.

[322] X. Ji *et al.*, "Ultra-low-loss on-chip resonators with sub-milliwatt parametric oscillation threshold," *Optica*, vol. 4, no. 6, p. 619, 2017, doi: 10.1364/optica.4.000619.

[323] Z. Gong *et al.*, "High-fidelity cavity soliton generation in crystalline AlN micro-ring resonators," *Opt. Lett.*, vol. 43, no. 18, p. 4366, 2018, doi: 10.1364/ol.43.004366.

[324] X. Liu *et al.*, "Integrated High- Q Crystalline AlN Microresonators for Broadband Kerr and Raman Frequency Combs," *ACS Photonics*, vol. 5, no. 5, pp. 1943–1950, 2018, doi: 10.1021/acsphotonics.7b01254.

[325] M. I. A. N. Z. Hang and C. H. W. Ang, "Monolithic ultra-high- Q lithium niobate microring resonator," *Optica*, vol. 4, no. 12, pp. 1536–1537, 2017, doi: https://doi.org/10.1364/OPTICA.4.001536 Lithium.

[326] Y. H. E. Ang *et al.*, "Self-starting bi-chromatic LiNbO3 microcomb soliton microcomb," *Optica*, vol. 6, no. 9, p. 1138, 2019, doi: 10.1364/OPTICA.6.001138.

[327] J. Miragliotta, D. K. Wickenden, T. J. Kistenmacher, and W. A. Bryden, "Linear- and nonlinear-optical properties of GaN thin films," *J. Opt. Soc. Am. B*, vol. 10, no. 8, p. 1447, 1993, doi: 10.1364/josab.10.001447.

[328] E. Fazio *et al.*, "Measurement of pure Kerr nonlinearity in GaN thin films at 800 nm by means of eclipsing Z-scan experiments," *J. Opt. A Pure Appl. Opt.*, vol. 9, no. 2, pp. 13–14, 2007, doi: 10.1088/1464-4258/9/2/L01.

[329] U. Dharanipathy *et al.*, "Near-infrared characterization of gallium nitride photonic-crystal waveguides and cavities," *Opt. Lett.*, vol. 37, no. 22, p. 4588, 2012, doi: 10.1364/ol.37.004588.

[330] A. Stolz *et al.*, "Optical waveguide loss minimized into gallium nitride based structures grown by metal organic vapor phase epitaxy," *Appl. Phys. Lett.*, vol. 98, no. 16, pp. 1–4, 2011, doi: 10.1063/1.3582055.

[331] O. Westreich, M. Katz, Y. Paltiel, O. Ternyak, and N. Sicron, "Low propagation loss in GaN/AlGaN-based ridge waveguides," *Phys. Status Solidi Appl. Mater. Sci.*, vol. 212, no. 5, pp. 1043–1048, 2015, doi: 10.1002/pssa.201431663.

[332] H. Chen *et al.*, "Low loss GaN waveguides at the visible spectral wavelengths for integrated photonics applications," *Opt. Express*, vol. 25, no. 25, p. 31758, 2017, doi: 10.1364/oe.25.031758.

[333] A. W. Bruch, C. Xiong, B. Leung, M. Poot, J. Han, and H. X. Tang, "Broadband nanophotonic waveguides and resonators based on epitaxial GaN thin films," *Appl. Phys. Lett.*, vol. 107, no. 14, 2015, doi: 10.1063/1.4933093.

[334] K. Vyas *et al.*, "Group III-V semiconductors as promising nonlinear integrated photonic platforms," *Adv. Phys. X*, vol. 7, no. 1, 2022, doi: 10.1080/23746149.2022.2097020.

[335] H. Y. Zhang, X. H. He, Y. H. Shih, M. Schurman, Z. C. Feng, and R. A. Stall, "Study of nonlinear optical effects in GaN:Mg epitaxial film," *Appl. Phys. Lett.*, vol. 69, no. 20, pp. 2953–2955, 1996, doi: 10.1063/1.117741.

[336] C. K. Sun *et al.*, "Two-photon absorption study of GaN," *Appl. Phys. Lett.*, vol. 76, no. 4, pp. 439–441, 2000, doi: 10.1063/1.125780.

[337] H. Chen *et al.*, “Characterizations of nonlinear optical properties on GaN crystals in polar, nonpolar, and semipolar orientations,” *Appl. Phys. Lett.*, vol. 110, no. 18, pp. 1–5, 2017, doi: 10.1063/1.4983026.

[338] R. Binions, C. J. Carmalt, I. P. Parkin, K. F. E. Pratt, and G. A. Shaw, “Gallium Oxide Thin Films from the Atmospheric Pressure Chemical Vapor Deposition Reaction of Gallium Trichloride and Methanol,” *Chem. Mater.*, vol. 16, no. 23, pp. 2489–2493, 2004, doi: 10.1021/cm035195z.

[339] G. Park, W. Choi, J. Kim, Y. C. Choi, Y. H. Lee, and C. Lim, “Structural investigation of gallium oxide (-Ga O) nanowires grown by arc-discharge,” *Cryst. GROWTH &DESIGN*, vol. 220, pp. 494–500, 2000, doi: https://doi.org/10.1016/S0022-0248(00)00609-6.

[340] J. Q. Hu, Q. Li, X. M. Meng, C. S. Lee, and S. T. Lee, “Synthesis of -Ga 2 O 3 Nanowires by Laser Ablation,” *J. Phys. Chem. B*, vol. 106, no. 37, pp. 9536–9539, 2002, doi: 10.1021/jp020734t.

[341] G. Sinha, K. Adhikary, and S. Chaudhuri, “Effect of annealing temperature on structural transformation of gallium based nanocrystalline oxide thin films and their optical properties,” *Opt. Mater. (Amst).*, vol. 29, pp. 718–722, 2007, doi: 10.1016/j.optmat.2005.12.002.

[342] S. Music, S. Popovic, and M. Ristic, “Application of sol – gel method in the synthesis of gallium (III) - oxide,” *Mater. Lett.*, vol. 59, pp. 1227–1233, 2005, doi: 10.1016/j.matlet.2004.11.055.

[343] B. Geng, L. Zhang, G. Meng, T. Xie, X. Peng, and Y. Lin, “Large-scale synthesis and photoluminescence of single-crystalline b -Ga 2 O 3 nanobelts,” *Cryst. GROWTH &DESIGN*, vol. 259, pp. 291–295, 2003, doi: 10.1016/j.jcrysgro.2003.07.005.

[344] X. H. Wang *et al.*, “Control performance of a single-chip white light emitting diode by adjusting strain in InGaN underlying layer,” *Appl. Phys. Lett.*, vol. 94, no. 11, pp. 2007–2010, 2009, doi: 10.1063/1.3103559.

[345] S. Strite, “GaN, AlN, and InN: A review,” *J. Vac. Sci. Technol. B Microelectron. Nanom. Struct.*, vol. 10, no. 4, p. 1237, 1992, doi: 10.1116/1.585897.

[346] A. Avramescu *et al.*, “InGaN laser diodes with 50 mW output power emitting at 515 nm,” *Appl. Phys. Lett.*, vol. 95, no. 7, 2009, doi: 10.1063/1.3206739.

[347] M.Asif Khan, “Ultraviolet Sensors Based on Insulating,” *Appl. Phys. Lett.*, vol. 2917, no. August, pp. 3–6, 1998, doi: https://doi.org/10.1063/1.106819.

[348] C. J. Neufeld, N. G. Toledo, S. C. Cruz, M. Iza, S. P. DenBaars, and U. K. Mishra, “High quantum efficiency InGaN/GaN solar cells with 2.95 eV band gap,” *Appl. Phys. Lett.*, vol. 93, no. 14, pp. 91–94, 2008, doi: 10.1063/1.2988894.

[349] N. Sanders, D. Bayerl, G. Shi, K. A. Mengle, and E. Kioupakis, “Electronic and Optical Properties of Two-Dimensional GaN from First-Principles,” *Nano Lett.*, vol. 17, no. 12, pp. 7345–7349, 2017, doi: 10.1021/acs.nanolett.7b03003.

[350] M. A. Moram and M. E. Vickers, “X-ray diffraction of III-nitrides,” *Reports Prog. Phys.*, vol. 72, no. 3, 2009, doi: 10.1088/0034-4885/72/3/036502.

[351] M. Wurdack *et al.*, “Ultrathin Ga2O3 Glass: A Large-Scale Passivation and Protection Material for Monolayer WS2,” *Adv. Mater.*, vol. 33, no. 3, 2021, doi: 10.1002/adma.202005732.

[352] J. Ganji, A. Kosarian, and H. Kaabi, “Mathematical Evaluation of a-Si : H Film Formation in rf-PECVD Systems,” *Silicon*, vol. 12, pp. 723–734, 2020, doi: 10.1007/s12633-019-00167-9.

[353] J. H. Van Helden, P. J. Van Den Oever, W. M. M. Kessels, M. C. M. Van De Sanden, D. C. Schram, and R. Engeln, “Production mechanisms of NH and NH2 radicals in N 2-H2 plasmas,” *J. Phys. Chem. A*, vol. 111, no. 45, pp. 11460–11472, 2007, doi: 10.1021/jp0727650.

[354] B. S. Truscott, M. W. Kelly, K. J. Potter, M. N. R. Ashfold, and Y. A. Mankelevich, “Microwave plasma-

Activated chemical vapor deposition of nitrogen-Doped diamond. II: CH4/N2/H2 plasmas," *J. Phys. Chem. A*, vol. 120, no. 43, pp. 8537–8549, 2016, doi: 10.1021/acs.jpca.6b09009.

[355] F. Ohnesorge and G. Binnig, "True Atomic Resolution by Atomic Force Microscopy Through Repulsive and Attractive Forces P," vol. 260, no. 5113, pp. 1451–1456, 1993.

[356] B. D. Forbes, L. Houben, J. Mayer, R. E. Dunin-borkowski, and L. J. Allen, "Ultramicroscopy Elemental mapping in achromatic atomic-resolution energy- fi ltered transmission electron microscopy," *Ultramicroscopy*, vol. 147, pp. 98–105, 2014, doi: 10.1016/j.ultramic.2014.07.002.

[357] J. Meurig, P. A. Midgley, C. Ducati, and R. K. Leary, "Progress in Natural Science : Materials International Nanoscale electron tomography and atomic scale high-resolution electron microscopy of nanoparticles and nanoclusters : A short survey," *Prog. Nat. Sci. Mater. Int.*, vol. 23, no. 3, pp. 222–234, 2013, doi: 10.1016/j.pnsc.2013.04.003.

[358] J. S. Chen *et al.*, "Shape-Controlled Synthesis of Cobalt-based Their Comparative Lithium-Storage Properties," vol. 2, no. 12, 2010, doi: 10.1021/am100787w.

[359] L. Ã. Houben, A. Thust, and K. Urban, "Atomic-precision determination of the reconstruction of a 90 tilt boundary in YBa 2 Cu 3 O 7 À d by aberration corrected HRTEM," vol. 106, pp. 200–214, 2006, doi: 10.1016/j.ultramic.2005.07.009.

[360] "PELCO Holey Silicon Nitride Support Films for TEM." [Online]. Available: https://www.tedpella.com/grids_html/silicon-nitride-holey.aspx. [Accessed: 15-Jul-2023].

[361] R. Al-gaashani, A. Najjar, Y. Zakaria, S. Mansour, and M. A. Atieh, "XPS and structural studies of high quality graphene oxide and reduced graphene oxide prepared by di ff erent chemical oxidation methods," *Ceram. Int.*, vol. 45, no. 11, pp. 14439–14448, 2019, doi: 10.1016/j.ceramint.2019.04.165.

[362] A. Siokou, F. Ravani, S. Karakalos, O. Frank, M. Kalbac, and C. Galiotis, "Applied Surface Science Surface refinement and electronic properties of graphene layers grown on copper substrate : An XPS , UPS and EELS study," *Appl. Surf. Sci.*, vol. 257, no. 23, pp. 9785–9790, 2011, doi: 10.1016/j.apsusc.2011.06.017.

[363] Jin Young Oh, "Chemically exfoliateed transition metaal dichalcogenide nanosheets-based wearable thermoeelectric generators," *R. Soc. Chem.*, 2015, doi: 10.1039/C5EE03813H.

[364] X. Chia, "Electrocatalysis of layered Group 5 metallic transition metal dichalcogenides (MX2 , M = V, Nb,and Ta; X = S, Se, and Te)," 2016, doi: 10.1039/C6TA05110C.

[365] M. T. Edmonds *et al.*, "Creating a Stable Oxide at the Surface of Black Phosphorus," *Appl. Mater. interfaces*, vol. 7, p. 14557−14562, 2015, doi: 10.1021/acsami.5b01297.

[366] Y. Liu and M. Chen, "Chemical functionalization of 2D black phosphorus," no. September 2020, pp. 231–251, 2021, doi: 10.1002/inf2.12171.

[367] A. Mahmoodinezhad *et al.*, "Low-temperature growth of gallium oxide thin films by plasma-enhanced atomic layer deposition," *J. Vac. Sci. Technol. A*, vol. 38, no. 2, p. 022404, 2020, doi: 10.1116/1.5134800.

[368] S. J. Yoo and Q. H. Park, "Spectroscopic ellipsometry for low-dimensional materials and heterostructures," *Nanophotonics*, vol. 11, no. 12, pp. 2811–2825, 2022, doi: 10.1515/nanoph-2022-0039.

[369] S. Funke *et al.*, "Spectroscopic imaging ellipsometry for automated search of flakes of mono- and n-layers of 2D-materials," *Appl. Surf. Sci.*, vol. 421, pp. 435–439, 2017, doi: 10.1016/j.apsusc.2016.10.158.

[370] M. Losurdo, *Ellipsometry at the Nanoscale*. 2013.

[371] H. Fujiwara, *Spectroscopic Ellipsometry*. Wiley: New York, NY, USA, 2007.

[372] P. Nestler and C. A. Helm, “Determination of refractive index and layer thickness of nm-thin films via ellipsometry,” *Opt. Express*, vol. 25, no. 22, p. 27077, 2017, doi: 10.1364/oe.25.027077.

[373] J.Tauc, “Optical Properties and Electronic Structure of Amorphous Germanium,” *J. Appl. Spectrosc.*, vol. 83, no. 4, pp. 567–572, 2016, doi: 10.1007/s10812-016-0329-7.

[374] G. E. Jellison and F. A. Modine, “Parameterization of the optical functions of amorphous materials in the interband region,” *Appl. Phys. Lett.*, vol. 69, no. 3, pp. 371–373, 1996, doi: 10.1063/1.118064.

[375] G. E. Jellison and F. A. Modine, “Erratum: Parameterization of the optical functions of amorphous materials in the interband region [Appl. Phys. Lett. (1996) 69 (371) (10.1063/1.118064)),” *Appl. Phys. Lett.*, vol. 69, no. 14, p. 2137, 1996, doi: 10.1063/1.118155.

[376] M. Martin *et al.*, “Thermodynamics, structure and kinetics in the system Ga-O-N,” *Prog. Solid State Chem.*, vol. 37, no. 2–3, pp. 132–152, 2009, doi: 10.1016/j.progsolidstchem.2009.11.005.

[377] G. Schön, “Auger and direct electron spectra in X-ray photoelectron studies of zinc, zinc oxide, gallium and gallium oxide,” *J. Electron Spectros. Relat. Phenomena*, vol. 2, pp. 75–86, 1973.

[378] N. Elkashef, R. S. Srinivasa, S. Major, S. C. Sabharwal, and K. P. Muthe, “Sputter deposition of gallium nitride films using a GaAs target,” *Thin Solid Films*, vol. 333, no. 1–2, pp. 9–12, 1998, doi: 10.1016/S0040-6090(98)00550-1.

[379] M. Grodzicki, J. G. Rousset, P. Ciechanowicz, E. Piskorska-Hommel, and D. Hommel, “XPS studies on the role of arsenic incorporated into GaN,” *Vacuum*, vol. 167, no. May, pp. 73–76, 2019, doi: 10.1016/j.vacuum.2019.05.043.

[380] M. Grodzicki, “Properties of Thin Film-Covered GaN(0001) Surfaces,” *Mater. Proc.*, no. August, p. 30, 2020, doi: 10.3390/ciwc2020-06833.

[381] Shubhendra Kumar Jain, “Atomically Thin Gallium Nitride for High-Performance Photodetection,” *Adv. Opt. Mater.*, p. 2300438, 2023, doi: 10.1002/adom.202300438.

[382] Z. Liu, T. Yamazaki, Y. Shen, T. Kikuta, N. Nakatani, and Y. Li, “O2 and CO sensing of Ga2O3 multiple nanowire gas sensors,” *Sensors Actuators, B Chem.*, vol. 129, no. 2, pp. 666–670, 2008, doi: 10.1016/j.snb.2007.09.055.

[383] J. T. Yan and C. T. Lee, “Improved detection sensitivity of Pt/β-Ga2O3/GaN hydrogen sensor diode,” *Sensors Actuators, B Chem.*, vol. 143, no. 1, pp. 192–197, 2009, doi: 10.1016/j.snb.2009.08.040.

[384] M. F. Al-Kuhaili, S. M. A. Durrani, and E. E. Khawaja, “Optical properties of gallium oxide films deposited by electron-beam evaporation,” *Appl. Phys. Lett.*, vol. 83, no. 22, pp. 4533–4535, 2003, doi: 10.1063/1.1630845.

[385] P. Marie, X. Portier, and J. Cardin, “Growth and characterization of gallium oxide thin films by radiofrequency magnetron sputtering,” *Phys. Status Solidi Appl. Mater. Sci.*, vol. 205, no. 8, pp. 1943–1946, 2008, doi: 10.1002/pssa.200778856.

[386] M. E. Lin, B. N. Sverdlov, S. Strite, H. Morkoc, and A. E. Drakin, “Refractive indices of wurtzite and zincblende GaN,” *Electron. Lett.*, vol. 29, no. 20, pp. 1759–1760, 1993, doi: 10.1049/el:19931172.

[387] H. Amano, N. Watanabe, N. Koide, and I. Akasaki, “Room-Temperature Low-Threshold Surface-Stimulated Emission by Optical Pumping From Al0.1Ga0.9N/Gan Double Heterostructure,” *Jpn. J. Appl. Phys.*, vol. 32, no. 7, pp. L1000–L1002, 1993, doi: 10.1143/JJAP.32.L1000.

[388] G. Yu *et al.*, “Polarized reflectance spectroscopy and spectroscopic ellipsometry determination of the optical anisotropy of gallium nitride on sapphire,” *Japanese J. Appl. Physics, Part 2 Lett.*, vol. 36, no. 8 PART A, 1997, doi: 10.1143/jjap.36.l1029.

[389] T. Kawashima, H. Yoshikawa, S. Adachi, S. Fuke, and K. Ohtsuka, “Optical properties of hexagonal GaN,” *J. Appl. Phys.*, vol. 82, no. 7, pp. 3528–3535, 1997, doi: 10.1063/1.365671.

[390] G. Yu *et al.*, “Optical properties of AlxGa1-xN/GaN heterostructures on sapphire by spectroscopic ellipsometry,” *Appl. Phys. Lett.*, vol. 72, no. 18, pp. 2202–2204, 1998, doi: 10.1063/1.121322.

[391] T. Onuma, “Spectroscopic ellipsometry studies on β-Ga2O3 films and single crystal,” *Jpn. J. Appl. Phys.*, vol. 55, pp. 0–5, 2016, doi: 10.7567/JJAP.55.1202B2.

[392] M. Rebien, “Optical properties of gallium oxide thin films,” *Appl. Phys. Lett.*, vol. 250, no. May 2002, pp. 10–13, 2016, doi: 10.1063/1.1491613.

[393] A. Segura, L. Artús, R. Cuscó, R. Goldhahn, and M. Feneberg, “Band gap of corundumlike α-Ga2 O3 determined by absorption and ellipsometry,” *Phys. Rev. Mater.*, vol. 1, no. 2, pp. 1–6, 2017, doi: 10.1103/PhysRevMaterials.1.024604.

[394] A. You, M. A. Y. Be, and I. In, “Ga 2 O 3 films for electronic and optoelectronic applications,” *J. Appl. Phys.*, vol. 686, no. August 1994, p. 77, 2020, doi: https://doi.org/10.1063/1.359055.

[395] J. W. Roberts *et al.*, “Low temperature growth and optical properties of α -Ga 2 O 3 deposited on sapphire by plasma enhanced atomic layer deposition,” *J. Cryst. Growth*, vol. 528, no. September, p. 125254, 2019, doi: 10.1016/j.jcrysgro.2019.125254.

[396] A. R. A. Zauner, “Spectroscopic Ellipsometry on GaN: Comparison Between Hetero-epitaxial Layers and Bulk Crystals,” *Mater. Res.*, vol. 2, no. January 1998, pp. 1–10, 1999, doi: 10.1557/S1092578300000892.

[397] E. S. Hellman, “Internet Journal Nitride Semiconductor Research,” *Mater. Res.*, vol. 2, no. January 1998, pp. 1–10, 1999, doi: https://doi.org/10.1557/S1092578300000892.

[398] P. Boher, “Spectroscopic ellipsometry applied to the characterization of Gan and AlGaN/GaN hetero-structures,” *Proceedings-Electrochemical Soc. Electrochem. Soc.*, pp. 258–264, 2003.

[399] T. Yang, S. Goto, M. Kawata, K. Uchida, A. Niwa, and J. Gotoh, “Optical properties of GaN thin films on sapphire substrates characterized by variable-angle spectroscopic ellipsometry,” *Japanese J. Appl. Physics, Part 2 Lett.*, vol. 37, no. 10 PART A, 1998, doi: 10.1143/jjap.37.l1105.

[400] A. Biswas, D. Bhattacharyya, N. K. Sahoo, B. S. Yadav, and S. S. Major, “Spectroscopic ellipsometry studies of GaN films deposited by reactive rf sputtering of GaAs target,” *J. Alloys Compd.*, vol. 083541, no. January 2008, pp. 0–10, 2008, doi: 10.1063/1.2903443.

[401] L. K. Ping, D. D. Berhanuddin, A. K. Mondal, P. S. Menon, and M. A. Mohamed, “Properties and perspectives of ultrawide bandgap Ga2O3 in optoelectronic applications,” *Chinese J. Phys.*, vol. 73, no. July, pp. 195–212, 2021, doi: 10.1016/j.cjph.2021.06.015.

[402] L. Shao, X. Duan, Y. Li, F. Zeng, H. Ye, and P. Ding, “Two-dimensional Ga2O2 monolayer with tunable band gap and high hole mobility,” *Phys. Chem. Chem. Phys.*, vol. 23, no. 1, pp. 666–673, 2021, doi: 10.1039/d0cp05171c.

[403] B. Daudin *et al.*, “How to grow cubic GaN with low hexagonal phase content on (001) SiC by molecular beam epitaxy,” *J. Appl. Phys.*, vol. 84, no. 4, pp. 2295–2300, 1998, doi: 10.1063/1.368296.

[404] N. Sanders, D. Bayerl, G. Shi, K. A. Mengle, and E. Kioupakis, “Electronic and Optical Properties of Two-Dimensional GaN from First-Principles,” *Nano Lett.*, vol. 17, no. 12, pp. 7345–7349, 2017, doi: 10.1021/acs.nanolett.7b03003.

[405] F. K. Shan, G. X. Liu, W. J. Lee, G. H. Lee, I. S. Kim, and B. C. Shin, “Structural, electrical, and optical properties of transparent gallium oxide thin films grown by plasma-enhanced atomic layer deposition,” *J. Appl. Phys.*, vol. 98, no. 2, 2005, doi: 10.1063/1.1980535.

[406] O. M. Bordun, I. Y. Kukharskyy, B. O. Bordun, and V. B. Lushchanets, “Dispersion of Refractive Index of β-Ga2O3 Thin Films,” *J. Appl. Spectrosc.*, vol. 81, no. 5, pp. 771–775, 2014, doi: 10.1007/s10812-014-0004-9.

[407] P. Boher, S. Bourtault, J. P. Piel, G. And, A. / Gan, and H.-S. P. Boher, “SPECTROSCOPIC ELLIPSOMETRY APPLIED TO THE CHARACTERIZATION OF GaN AND AlGaN/GaN HETERO-STRUCTURES,” *Researchgate.Net*, no. April, 2003.

[408] A. Biswas, D. Bhattacharyya, N. K. Sahoo, B. S. Yadav, S. S. Major, and R. S. Srinivasa, “Spectroscopic ellipsometry studies of GaN films deposited by reactive rf sputtering of GaAs target,” *J. Appl. Phys.*, vol. 103, no. 8, 2008, doi: 10.1063/1.2903443.

[409] M. Passlack *et al.*, “Ga2O3 films for electronic and optoelectronic applications,” *J. Appl. Phys.*, vol. 77, no. 2, pp. 686–693, 1995, doi: 10.1063/1.359055.

[410] M. Rebien, W. Henrion, M. Hong, J. P. Mannaerts, and M. Fleischer, “Optical properties of gallium oxide thin films,” *Appl. Phys. Lett.*, vol. 81, no. 2, pp. 250–252, 2002, doi: 10.1063/1.1491613.

[411] A. Ortiz, J. C. Alonso, E. Andrade, and C. Urbiola, “Structural and Optical Characteristics of Gallium Oxide Thin Films Deposited by Ultrasonic Spray Pyrolysis,” *J. Electrochem. Soc.*, vol. 148, no. 2, p. F26, 2001, doi: 10.1149/1.1342183.

[412] A. R. A. Zauner, M. A. C. Devillers, P. R. Hageman, P. K. Larsen, and S. Porowski, “Spectroscopic Ellipsometry on GaN: Comparison Between Hetero-epitaxial Layers and Bulk Crystals,” *Mater. Res.*, vol. 3, no. January 1998, p. e17, Jun. 1998, doi: 10.1557/S1092578300000892.

[413] S. Scandolo, P. G. I, C. C. Iv, S. D. G. I, and A. P. Vi, “First-principles codes for computational crystallography in the Quantum-ESPRESSO package,” *Zeitschrift für Krist. Mater.*, vol. 220, pp. 574–579, 2005, doi: https://doi.org/10.1524/zkri.220.5.574.65062.

[414] S. Poncé, “Structural , electronic , elastic , power , and transport properties of β -Ga 2 O 3 from first principles,” *Phys. Rev. Res.*, vol. 033102, no. 2, p. 033102, 2020, doi: 10.1103/PhysRevResearch.2.033102.

[415] H. Qin, “Mechanical, Thermodynamic and Electronic Properties of Wurtzite and Zinc-Blende GaN Crystals,” *Materials (Basel).*, vol. 10, no. 1419, pp. 1–15, 2017, doi: 10.3390/ma10121419.

[416] L. A. Agapito, S. Curtarolo, and M. B. Nardelli, “Reformulation of DFT þ U as a Pseudohybrid Hubbard Density Functional for Accelerated Materials Discovery,” vol. 011006, pp. 1–16, 2015, doi: 10.1103/PhysRevX.5.011006.

[417] Q. Yan *et al.*, “Effects of strain on the band structure of group-III nitrides,” *Am. Phys. Soc.*, vol. 125118, pp. 1–11, 2014, doi: 10.1103/PhysRevB.90.125118.

[418] D. Mora-Fonz, “Modeling of Intrinsic Electron and Hole Trapping in Crystalline and Amorphous ZnO,” *Adv. Electron. Mater.*, vol. 6, p. 1900760, 2020, doi: 10.1002/aelm.201900760.

[419] B. S. Zou, V. V Volkov, and Z. L. Wang, “Optical Properties of Amorphous ZnO , CdO , and PbO Nanoclusters in Solution,” *Chem. Mater.*, no. 7, pp. 3037–3043, 1999, doi: 10.1021/cm9810990.

[420] J. Robertson, “Disorder and instability processes in amorphous conducting oxides,” *Phys. status solidi*, vol. 1032, no. 6, pp. 1026–1032, 2008, doi: 10.1002/pssb.200743458.

[421] M. Jędrzejczyk *et al.*, “Wide band gap Ga2O3 as efficient UV-C photocatalyst for gas-phase degradation applications,” *Environ. Sci. Pollut. Res.*, vol. 24, no. 34, pp. 26792–26805, 2017, doi: 10.1007/s11356-017-0253-2.

[422] Laura E. Ratclif, “Tackling Disorder in -Ga2O3.pdf,” *Adv. Mater.*, vol. 34, p. 2204217, 2022, doi: 10.1002/adma.202204217.

[423] A. Cros, R. Mata, K. Hestroffer, and B. Daudin, “Ultraviolet Raman spectroscopy of GaN/AlN core-shell nanowires: Core, shell, and interface modes,” *Appl. Phys. Lett.*, vol. 102, no. 14, 2013, doi: 10.1063/1.4801779.

[424] I. S. Roqan and M. M. Muhammed, “ (- 201) β-Gallium oxide substrate for high quality GaN materials ,” *Oxide-based Mater. Devices VI*, vol. 9364, p. 93641K, 2015, doi: 10.1117/12.2076475.

[425] M. H. Asghar, F. Placido, and S. Naseem, “P HYSICAL J OURNAL Characterization of reactively evaporated TiO 2 thin films as high,” *Eur. Phys. JournalApplied Phys.*, vol. 184, no. 3, pp. 177–184, 2006, doi: 10.1051/epjap.

[426] N. Iqbal, I. Khan, Z. H. Yamani, and A. Qurashi, “Sonochemical Assisted Solvothermal Synthesis of Gallium Oxynitride Nanosheets and their Solar-Driven Photoelectrochemical Water-Splitting Applications,” *Sci. Rep.*, vol. 6, no. August, pp. 1–11, 2016, doi: 10.1038/srep32319.

[427] C. Hu and H. Teng, “Gallium Oxynitride Photocatalysts Synthesized from Ga (OH) 3 for Water Splitting under Visible Light Irradiation,” *J. Phys. Chem. C*, no. 3, pp. 20100–20106, 2010, doi: https://doi.org/10.1021/jp1070083.

[428] H. A. N. Dharmagunawardhane *et al.*, “Photocatalytic hydrogen evolution using nanocrystalline gallium oxynitride spinel,” *J. Mater. Chem. A*, vol. 2, no. 45, pp. 19247–19252, 2014, doi: 10.1039/c4ta03676j.

[429] G. R. Berdiyorov, A. Qurashi, and G. Eshonqulov, “E ff ect of Surface Symmetry on the Dissociative Adsorption of Water on Gallium Oxynitride,” pp. 3–7, 2017, doi: 10.1021/acs.jpcc.7b03968.

[430] Y. Asakura, Y. Inaguma, K. Ueda, Y. Masubuchi, and S. Yin, “Synthesis of gallium oxynitride nanoparticles through hydrothermal reaction in the presence of acetylene black and their photocatalytic NO: X decomposition,” *Nanoscale*, vol. 10, no. 4, pp. 1837–1844, 2018, doi: 10.1039/c7nr07502b.

[431] N. M. Ghazali, K. Yasui, and A. M. Hashim, “Synthesis of gallium nitride nanostructures by nitridation of electrochemically deposited gallium oxide on silicon substrate,” pp. 1–8, 2014.

[432] C. J. Szwejkowski, “Size effects in the thermal conductivity of gallium oxide (,” *J. Appl. Phys.*, no. February, p. 117, 2020, doi: https://doi.org/10.1063/1.4913601.

[433] G. Karaoglan-Bebek, “Optical studies of the effect of oxidation on GaN □,” *J. Vac. Sci. Technol. A*, vol. 011213, p. 32, 2014, doi: http://dx.doi.org/10.1116/1.4858467.

[434] H. Akazawa, “Crystallization of gallium oxynitride thin films,” *J. Solid State Chem.*, vol. 282, no. October 2019, p. 121066, 2020, doi: 10.1016/j.jssc.2019.121066.

[435] C. Coletti *et al.*, “Wafer-scale integration of graphene-based photonic devices,” *ACS Nano*, vol. 15, no. 2, pp. 3171–3187, 2021, doi: 10.1021/acsnano.0c09758.

[436] Z. Sun, A. Martinez, and F. Wang, “Optical modulators with 2D layered materials,” *Nat. Photonics*, vol. 10, no. 4, pp. 227–238, 2016, doi: 10.1038/nphoton.2016.15.

[437] V. Sorianello *et al.*, “Graphene-silicon phase modulators with gigahertz bandwidth,” *Nat. Photonics*, vol. 12, no. 1, pp. 40–44, 2018, doi: 10.1038/s41566-017-0071-6.

[438] K. Xu *et al.*, “A high-performance visible-light-driven all-optical switch enabled by ultra-thin gallium sulfide,” *J. Mater. Chem. C*, vol. 9, no. 9, pp. 3115–3121, 2021, doi: 10.1039/d0tc05676f.

[439] R. Wang *et al.*, “A few-layer InSe-based sensitivity-enhanced photothermal fiber sensor,” *J. Mater. Chem. C*, vol. 8, no. 1, pp. 132–138, 2019, doi: 10.1039/c9tc05818d.

[440] I. Datta *et al.*, “Low-loss composite photonic platform based on 2D semiconductor monolayers,” *Nat. Photonics*, vol. 14, no. 4, pp. 256–262, 2020, doi: 10.1038/s41566-020-0590-4.

[441] A. Taute *et al.*, “Emerging Low-Loss Phase Change Material Enabling Non-Volatile Phase Modulation To cite this version : HAL Id : hal-03834997 Emerging Low-Loss Phase Change Material Enabling Non-Volatile Phase Modulation,” 2022.

[442] R. Orobtchouk *et al.*, “Slot ARROW Waveguide : A New Platform for Optical Sensing To cite this version : HAL Id : hal-03517859 Slot ARROW Waveguide : A New Platform for Optical Sensing,” 2022.

[443] T.Tamir, *Integrated Optics*, vol. 27, no. 11. 1975.

[444] W. Ogieglo, H. Wormeester, M. Wessling, and N. E. Benes, *Spectroscopic ellipsometry analysis of a thin film composite membrane consisting of polysulfone on a porous α-alumina support*, vol. 4, no. 2. 2012.

Appendix

Derivation of the theoretical MZI transmission

Light of amplitude A is injected in the input waveguide and split equally in the 2 arms of the asymmetric Mach Zehnder through the MMI. After the MMI, the field in each branch is thus equal to:

$$\frac{A}{\sqrt{2}} e^{j\Delta\varphi_{MMI}} = \frac{A}{\sqrt{2}} e^{j\beta_{MMI}L_{MMI}} \qquad (1)$$

The phase shift at the end of the reference arm is given by:

$$\Delta\varphi_{ref} = \beta_{MMI}L_{MMI} + \beta_b 4L_b + \beta_s L_1 \qquad (2)$$

While thus the phase shift at the end of the sensing arm is given by:

$$\Delta\varphi_{sensing} = \beta_{MMI}L_{MMI} + \beta_b 4L_b + \beta_s 2L_2 + \beta_{MUT}L_{MUT} \quad (3)$$

Where “b”, “s” and “MUT” represent respectively the bend, straight and Material-Under-Test configurations. The MZI dimensions are as follows

- $L1 = 100\ \mu m$
- $L2 = 50\ \mu m$
- $Lb = \pi * \frac{20\mu m}{2} \approx 31.4\ \mu m$

Hence the field amplitude at the B point after recombining the fields from the reference arm $E_{ref} = \frac{A}{\sqrt{2}} e^{j\Delta\varphi_R}$ and the sensing arm $E_{sensing} = \frac{A}{\sqrt{2}} e^{j\Delta\varphi_{sensing}}$ can be expressed as:

$$
\begin{aligned}
E_B &= \frac{e^{j\Delta\varphi_{MMI}}}{\sqrt{2}}\left(E_{ref} + E_{sensing}\right) \\
&= \frac{A}{2}\left(e^{j\,(2\beta_{MMI}L_{MMI}+4\beta_b L_b+\beta_s L_1)} + e^{j\,(2\beta_{MMI}L_{MMI}+4\beta_b L_b+2\beta_s L_2+\beta_{MUT}L_1)}\right) \qquad (4)
\end{aligned}
$$

Before deposition of material on the sensing arm the phase shift from formula (3) changes to:

$$\Delta\varphi_{sensing} = \beta_{MMI}L_{MMI} + 4\beta_b L_b + 2\beta_s L_2 \qquad (5)$$

After some algebraic manipulations and applying Euler's equation, from equation (5) we obtain formula (6) for the output amplitude and (7) for the output power considering that $\beta = \frac{2\pi n_{eff}}{\lambda}$:

$$E(\lambda) = A\cos\left(\frac{2\pi n_{eff}L_2}{\lambda}\right) \qquad (6)$$

$$P(\lambda) \propto E(\lambda)^2 = A^2\cos^2\left(\frac{2\pi n_{eff}L_2}{\lambda}\right) \qquad (7)$$

In order to consider imperfections of the MMI, difference of propagation losses in the 2 arms of the devices, the transmission formula used to extract the refractive indices of the waveguides modes is given by:

$$P(\lambda) = P_{in}(\lambda)\cdot\cos^2\left(\frac{2\pi\cdot n_{eff}}{\lambda}L_2\right) + P_{offset}(\lambda) \qquad (8)$$

Where λ is the wavelength, n_{eff} is the effective refractive index of the mode. Where refractive index is approximated by a 3rd order polynomial.

After deposition of material on the sensing arm, the transmission formula (formula 8) used to extract the refractive indices of the waveguides modes, becomes:

$$P(\lambda) = P_{in}(\lambda)\cdot\cos^2\left(\frac{2\pi n_{eff}}{\lambda}L_2 + \frac{\pi}{\lambda}\left(n_{eff}^{MUT} - n_{eff}^{SiN}\right)L_{MUT}\right) + P_{offset}(\lambda) \qquad (9)$$

Equation (7) and (9) reveal that the real component of n_{eff} influences only the oscillatory element of the output power. The $P_{in}(\lambda)$ term is introduced to account for variation of the light amplitude due to several factors: the power intensity of the light source used in conjunction with λ, the coupling and uncoupling factors between the lensed beams and the device, and the propagation losses incurred across different segments of the device. The $P_{offset}(\lambda)$term is introduced to account for a potential difference in the amplitude of the fields $\mathrm{E_{ref}}$ and $\mathrm{E_{sensing}}$ recombining at the output of the MZI, as well as background light.

Methodology for $\mathbf{n_{eff}}$ extraction from MZI

The fitting procedure we employed for extracting the effective index of the waveguides and length of deposited material, detailed below, was developed by Regis Orobtchouk.

The experimental response of the device includes the source emission spectrum, the photodetector response, coupling and uncoupling efficiency between the lensed fibers and the device, as well as background noise (Figure A1(a)).

To extract the individual contribution of the MZI from the total response, the measured power is first filtered and normalized by its envelope (Figure A1 (b), (c) and (d)). The resulting normalized transmission $\mathrm{T}(\lambda)$ is then assimilated to the $\cos^2(x)$ term of equation (8). Using the $\arccos$ function, the normalized transmission can be converted to an angle between $[0, \pi]$ (Figure A1 (e)). Under the consideration that β_{SiN} and $\beta_{\mathrm{MUT}} - \beta_{\mathrm{SiN}}$ are both monotonously decreasing functions of lambda according to MODE calculations, the angle can be rearranged into the interval $[0, 2\pi]$ by reversing the polarity of increasing sections. The resulting angle is then unwrapped to retrieve the continuous angle of the signal $\theta^{\mathrm{exp}}(\lambda)$ (Figure A1 (f)). Finally, the extracted angle is used as the target of an optimization problem solved using the Levenberg–Marquardt algorithm (Figure A1 (g)).

For example, in the absence of 2D material on the sensing arm, the expected angle is:

$$\theta^{\mathrm{th}}(\lambda) = \beta_{\mathrm{SiN}}^{\mathrm{th}}(\lambda) \cdot \Delta\mathrm{L}^{\mathrm{th}}$$

Therefore, we parametrize the fit with $\beta_{\mathrm{SiN}}^{\mathrm{exp}}(\lambda)$, $\Delta\mathrm{L}^{\mathrm{exp}}$ and solve the system of equations:

$$\begin{cases} \theta^{\mathrm{exp}}(\lambda) = \beta_{\mathrm{SiN}}^{\mathrm{exp}}(\lambda) \cdot \Delta\mathrm{L}^{\mathrm{exp}} + \mathrm{k} \cdot 2\pi \\ \beta_{\mathrm{SiN}}^{\mathrm{exp}}(\lambda) = \beta_{\mathrm{SiN}}^{\mathrm{th}}(\lambda) \\ \Delta\mathrm{L}^{\mathrm{exp}} = \Delta\mathrm{L}^{\mathrm{th}} \\ \mathrm{k} \in \mathbb{N} \end{cases}$$

The resulting $\beta_{\mathrm{SiN}}^{\mathrm{exp}}(\lambda)$ and $\Delta\mathrm{L}^{\mathrm{exp}}$ can be used to reconstruct the original signal, and compared to theoretical values.

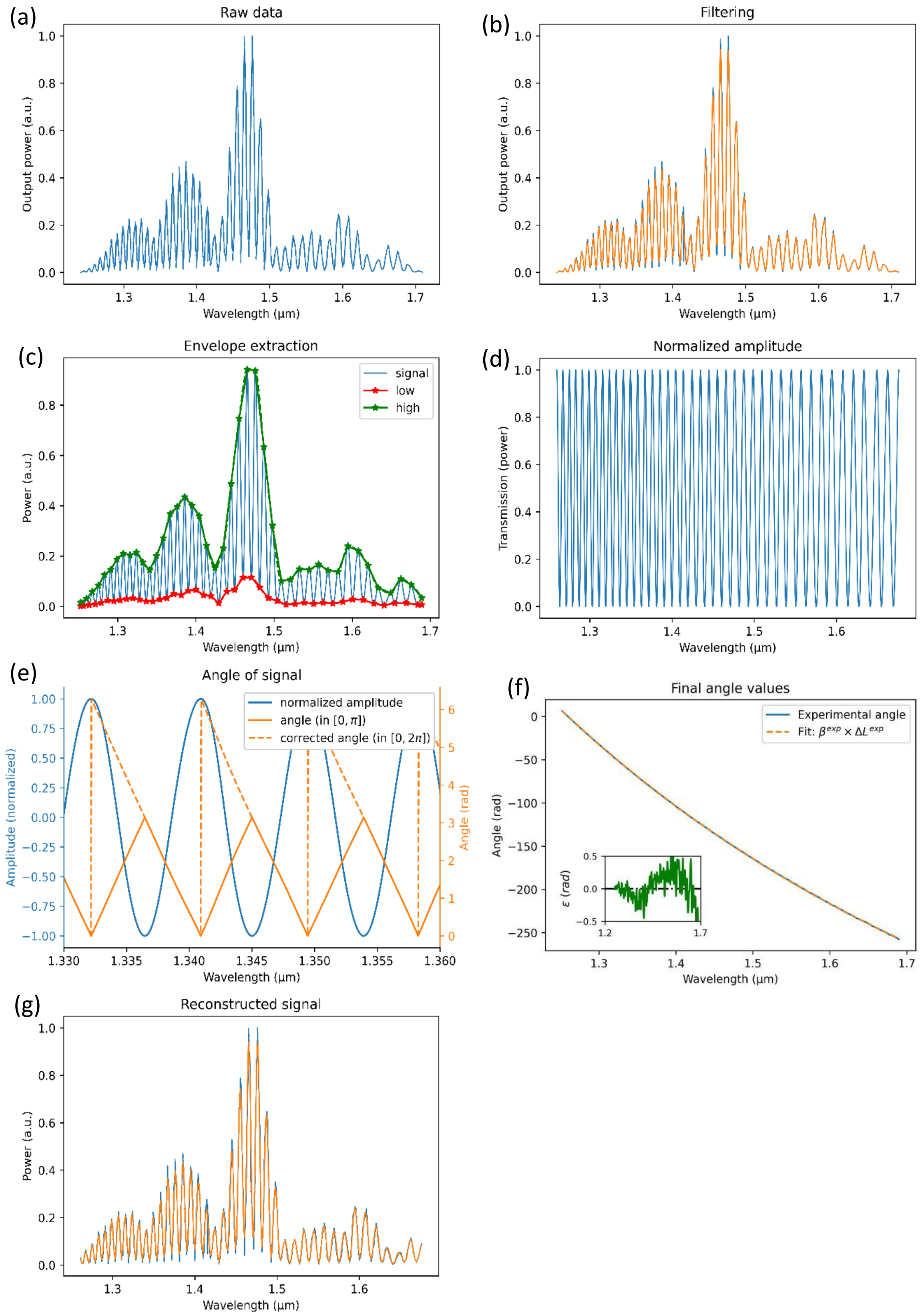

Figure A1. Steps in extracting and optimizing the device's experimental response.

Résumé de la thèse en français

Étude des couches composées de gallium ultra-minces fabriquées par chimie des métaux liquides pour la photonique intégrée hybride

Introduction

À l'ère du numérique, la demande en connectivité internet croît à un rythme sans précédent [1]. Alors que de plus en plus d'appareils sont connectés et que les applications à forte densité de données telles que le streaming multimédia, les services déportés (« cloud ») et l'Internet des Objets (IdO) gagnent en importance, les systèmes de communication traditionnels peinent à répondre aux exigences toujours croissantes, notamment en matière de bande passante [2]. Les émetteurs-récepteurs optiques classiques, bien qu'efficaces, sont souvent encombrants, coûteux et énergivores, ce qui limite leur mise en œuvre à grande échelle. Il est impératif de rechercher des technologies innovantes capables de répondre à la demande de transmission de données à haut débit tout en surmontant les limites des solutions traditionnelles. Au cours des deux dernières décennies, le paysage de la technologie photonique a subi une transformation spectaculaire, la photonique sur silicium s'imposant comme une plateforme technologique de plus en plus mature et versatile. En intégrant divers composants optiques sur un substrat de silicium, elle permet de réaliser des circuits photoniques tout en exploitant les avantages des processus de fabrication bien établis du silicium. La photonique sur silicium, grâce à sa capacité à transférer des données à des vitesses très élevées, à son efficacité énergétique et à son potentiel évolutif, s’est imposé comme technologie efficace et compacte pour les télécommunications, les centres de données et les systèmes de détection [3][4]. Aujourd'hui, il est possible d'intégrer sur une seule et même puce de multiples fonctions optiques, comme des modulateurs électro-optiques, des photodétecteurs SiGe et des guides d'ondes en silicium à faible perte (figure 1).

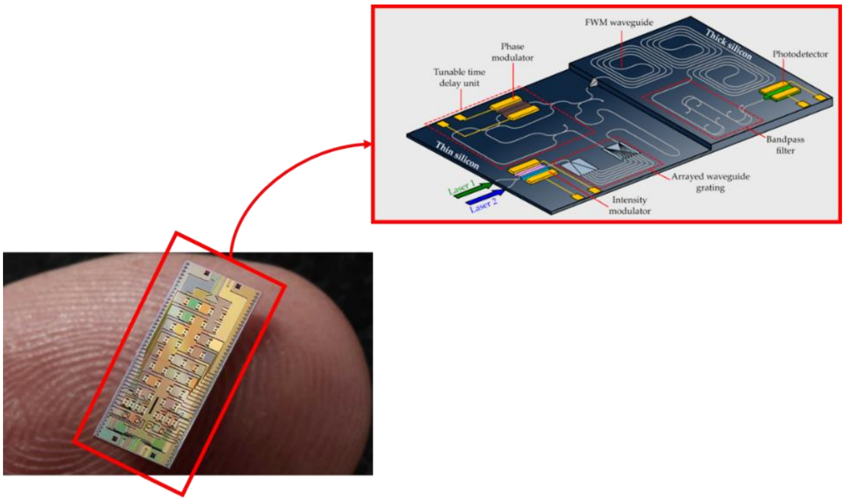

Figure 1. Représentation schématique d'un circuit intégré photonique au silicium [5][6].

Toutefois, le silicium présente des limites intrinsèques en ce qui concerne l'émission de lumière ou les fonctions non linéaires, qui rendent nécessaire le recours à des matériaux complémentaires.

L'émission de lumière permet la transmission de données à grande vitesse, la détection optique et l'imagerie grâce à la génération et au contrôle efficaces de la lumière. Elle joue un rôle essentiel dans des technologies telles que les lasers, les sources lumineuses et la communication optique, offrant une communication plus rapide et plus sûre que les systèmes électroniques traditionnels.

Les fonctions non linéaires, quant à elles, offrent des capacités avancées de traitement des signaux, telles que la conversion des fréquences et des longueurs d'onde, l'amplification des signaux et la commutation tout-optique. Ces fonctionnalités pourraient être utiles pour des tâches telles que la modulation de signaux, la régénération et le traitement optique complexe dans les télécommunications, l'informatique optique et le traitement des signaux, ainsi que la détection d’espèces chimiques par spectroscopie. Les progrès réalisés dans le domaine des dispositifs non linéaires offrent un potentiel intéressant pour le traitement de l'information. Bien qu'il soit encore tôt, leur capacité à manipuler les signaux lumineux offre une alternative prometteuse aux routeurs électroniques volumineux et plus consommateurs couramment employés pour les télécommunications. Alors que les flux de données sur internet continuent de croître à un rythme sans précédent, il devient de plus en plus urgent d'explorer et de développer des technologies innovantes. Les dispositifs non linéaires et entièrement optiques ne remplaceront peut-être pas complètement les routeurs optoélectroniques, mais ils sont prêts à jouer un rôle important et complémentaire dans cette évolution technologique.

L'intégration hétérogène de matériaux III-V sur le silicium a ouvert une voie pour surmonter ces limitations, permettant, par exemple, la réalisation de DEL ou de dispositifs laser efficaces [7][8]. Parallèlement, de nombreux nouveaux matériaux sont à l’étude pour leurs propriétés non linéaires dans le but de les intégrer à la plate-forme photonique sur silicium mature [9]. La réponse optique non linéaire des matériaux a permis la réalisation de dispositifs entièrement optiques tels que des commutateurs et des amplificateurs, capables de contrôler des signaux lumineux avec d'autres signaux lumineux. Les mécanismes optiques offrent plusieurs avantages par rapport à leurs homologues optoélectroniques, notamment des vitesses potentiellement plus élevées. En outre, ils permettent des fonctions innovantes telles que la conversion de longueur d'onde, la génération de peignes de fréquence et la création d'impulsions supercontinuum.

Cependant, malgré le fort potentiel d'application de l'optique non linéaire pour le traitement tout optique de l'information, aucun matériau non linéaire candidat n'a clairement émergé pour compléter la photonique du silicium. Les semi-conducteurs à large bande interdite ont été étudiés, mais leur intégration avec la photonique du silicium n'est pas simple. Malgré quelques avancées importantes sur les matériaux en verre, tels que Si3N4 et SiO2, ces derniers souffrent d'une non-linéarité relativement faible, ce qui entrave la réalisation de dispositifs compacts. C'est pourquoi les scientifiques continuent de rechercher des matériaux présentant de fortes non-linéarités et qui pourraient être facilement intégrés à la photonique du silicium. Idéalement, un tel matériau doit posséder un coefficient non linéaire élevé, une large fenêtre de transparence et être compatible avec les plates-formes photoniques au silicium.

Les matériaux bidimensionnels (2D) apparaissent en candidats prometteurs dans la quête du matériau non linéaire idéal. Depuis l'isolation révolutionnaire, en 2004, du graphène, une monocouche d’atomes de carbone, les chercheurs ont exploré et isolé avec succès une variété d'autres matériaux sous leur forme 2D. Ces matériaux 2D, compatibles avec les dispositifs photoniques planaires grâce à des techniques de post-traitement, apportent de nouvelles propriétés qui peuvent potentiellement compléter la photonique du silicium. Depuis lors, de nombreux matériaux 2D ont été explorés et présentent des propriétés électroniques, optiques et mécaniques uniques. C'est pourquoi nos recherches ont commencé par l'identification de nouveaux matériaux 2D susceptibles de compléter la photonique au silicium pour des applications à une longueur d'onde d'environ 1,55um. Parmi les candidats, l'oxyde de gallium (Ga_2O_3) et le nitrure de gallium (GaN) ont fait l'objet d'une attention particulière en raison de leurs propriétés optoélectroniques impressionnantes et de leurs applications prometteuses en électronique, photonique et biodétection. Cependant, il convient de noter que les recherches existantes se concentrent principalement sur les propriétés de Ga_2O_3 et de GaN dans la masse ou en couches épaisses, ce qui laisse une lacune importante en ce qui concerne leur comportement dans les dimensions 2D ou ultrafines. Reconnaissant cette lacune, notre recherche vise à y remédier en menant une analyse approfondie des propriétés du Ga_2O_3 et du GaN ultraminces. Grâce à cette étude, nous souhaitons mettre en lumière les propriétés uniques de ces matériaux dans le domaine de la 2D, ouvrant ainsi la voie à leurs applications potentielles dans cette dimension.

Mon doctorat s'est concentré sur ces matériaux intrigants, englobant leur synthèse, leur caractérisation et leur intégration éventuelle dans des dispositifs photoniques. Mon projet de recherche doctorale s'est articulé autour de trois axes principaux, qui ont guidé mon travail vers des résultats significatifs :

- la synthèse de Ga_2O_3 et de GaN ultraminces grâce à une méthode inventive connue sous le nom de chimie des métaux liquides
- la caractérisation structurelle et optique de ces matériaux ultraminces à base de Ga
- l'intégration de ces matériaux dans des dispositifs photoniques.

Ce projet s’inscrit dans une collaboration internationale entre l'Ecole Centrale de Lyon (ECL) et le Royal Melbourne Institute of Technology (RMIT) sous l'égide de l'Union Européenne et du programme Marie Curie. Les recherches menées dans le cadre de ce projet se sont déroulées dans deux laboratoires de pointe :

(i) l'Institut des nanotechnologies de Lyon (INL) et la plateforme de nanotechnologie NANOLYON

(ii) le RMIT Micro Nano Research Facility (MNRF) et l'assistance du RMIT Microscopy and Microanalysis Facility (RMMF).

Dans le cadre de notre collaboration avec le CNR-NANO Istituto Nanoscienze à Modène, en Italie, Arrigo Calzolari et Amine Slassi nous ont apporté une aide substantielle en effectuant les calculs intégraux de la théorie de la fonctionnelle de la densité (DFT), essentiels à cette recherche. Ali Zavabeti et Chung Nguyen de l'université RMIT ont effectué avec compétence les mesures TEM et XPS nécessaires à notre recherche. Pour enrichir encore notre recherche, Jules Galipaud nous a apporté son soutien technique en facilitant notre utilisation de l'équipement XPS du laboratoire LTDS de l'École centrale de Lyon. Notre travail a été complété par Bernard Pelissier et Badreddine Smiri du LTM-CNRS de Grenoble, qui ont effectué les mesures Raman. Par la suite, nous avons choisi un guide d'onde SiN comme première géométrie de dispositif pour sonder notre matériau 2D, qui a été fabriqué à STMicroelectronics. Pour les mesures optiques, nous avons utilisé l'installation optique disponible à l'INL, guidés par l'expertise de Regis Orobtchouk.

Cette thèse est divisée en quatre parties. Dans le chapitre 1, intitulé "État de l'art", nous donnons un aperçu complet de la littérature de recherche relative aux matériaux 2D, en mettant particulièrement l'accent sur Ga_2O_3 et GaN, ainsi qu'un aperçu de la façon dont les matériaux 2D ont été utilisés et combinés avec l'optique intégrée jusqu'à présent. Ce chapitre explore les travaux en cours pour trouver une méthode abordable, évolutive et efficace de produire du Ga_2O_3 et du GaN de haute qualité. En outre, nous recherchons une technique qui permette d'intégrer facilement ces matériaux dans des dispositifs photoniques. Nous avons également discuté de la structure et des caractéristiques du métal liquide en tant que méthode de synthèse de ces matériaux. Cette discussion souligne l'importance de trouver de nouvelles techniques pour surmonter les obstacles actuels qui nous empêchent d'exploiter pleinement le potentiel des matériaux 2D et leur intégration dans des dispositifs photoniques.

Le chapitre 2 approfondit notre exploration en abordant une question centrale : la fabrication de couches ultraminces sur de grandes surfaces. Nous présentons ici une approche inventive sous la forme de la chimie des métaux liquides développée récemment au RMIT [10][11] et qui repose sur un processus en deux étapes : la première étape utilise la méthode de la "chimie des métaux liquides" (LMC), qui s'est avérée efficace pour synthétiser des oxydes ultraminces à grande échelle, la seconde étape implique une réaction de nitruration améliorée par un plasma à micro-ondes [12]. Cette méthode a donné des résultats encourageants dans la synthèse évolutive de couches extrêmement fines de Ga_2O_3 et de GaN. Ensuite, le chapitre détaille les diverses méthodes de caractérisation utilisées pour étudier la topographie, la spectroscopie et les caractéristiques optiques des couches ultra-minces de Ga_2O_3 et de GaN synthétisées. L'étude utilise des outils de pointe tels que la microscopie à force atomique (AFM), la microscopie électronique à transmission (TEM), la spectroscopie photoélectronique à rayons X (XPS) et l'ellipsométrie spectroscopique (SE) pour étudier en détail les propriétés structurelles et optiques de ces matériaux.

Le chapitre 3 présente les résultats expérimentaux des couches ultra-minces à base de Ga synthétisées par la méthode développée au chapitre 2. Il porte également notre attention sur un élément central de notre recherche - l'exploration des composés d'oxy-nitrure de gallium (GaO_xN_y). Ces composés intrigants représentent un stade intermédiaire entre le Ga_2O_3 et le GaN. La compréhension de ces composés intermédiaires est essentielle car elle éclaire le processus de transformation de Ga_2O_3 en GaN. En outre, ce chapitre présente les résultats des méthodes de caractérisation introduites au chapitre 2. Il propose un examen approfondi des attributs structurels et optiques de ces composés intermédiaires, de Ga_2O_3 et de GaN. Pour ce faire, nous avons combiné des méthodes de caractérisation sophistiquées et des calculs de théorie de la fonctionnelle de la densité (DFT).

Dans le dernier chapitre, nous nous concentrons sur les applications pratiques. Plus précisément, nous développons une approche pour intégrer les matériaux 2D Ga_2O_3 et GaN dans des dispositifs photoniques. Nous exploitons ici des interféromètres de Mach-Zehnder (MZI) et un modelage sélectif pour étudier les propriétés optiques des guides d'ondes hybrides SiN recouverts de composés ultraminces à base de Ga. Cette étape est cruciale, car elle ouvre la voie à la réalisation d’un photonique hybride intégré avec ces matériaux 2D. Nous examinons en détail le processus d'intégration, les difficultés rencontrées et les moyens de les surmonter. Le chapitre présente comment l'intégration de couches ultraminces de Ga_2O_3 et de GaN dans la MZI peut améliorer notre compréhension de ces matériaux. Nous avons effectué des mesures linéaires précises sur les MZI afin de caractériser en détail les propriétés de Ga_2O_3 et de GaN. Le choix initial de ces matériaux était motivé par notre objectif de développer des matériaux 2D non linéaires pour les dispositifs à base de puces. Cependant, il est important de reconnaître que dans cette phase de notre recherche, nous nous sommes concentrés sur leurs propriétés linéaires et que nous n'avons pas encore étudié leurs caractéristiques non linéaires. Néanmoins, cette étude souligne le potentiel significatif de ces matériaux 2D pour faire progresser le domaine de la photonique intégrée et ouvre la voie à d'autres études sur leurs propriétés non linéaires.

Dans l'ensemble, cette recherche fournit une vue d'ensemble complète du Ga_2O_3 et du GaN ultra-minces, en emmenant le lecteur de leurs propriétés de base et de leurs applications potentielles à leur synthèse, leur caractérisation et leur intégration dans des dispositifs photoniques. En abordant les défis actuels et en proposant des solutions innovantes, cet ouvrage apporte une contribution significative et originale à la recherche mondiale en cours sur les matériaux 2D. L'intérêt pour ces matériaux ne cessant de croître, les connaissances générées par cette étude auront des implications dans les domaines de la science des matériaux, de la nanotechnologie et de la photonique.

Conclusions et perspectives futures

Dans le domaine de la science des matériaux, et plus particulièrement des nanomatériaux, les matériaux bidimensionnels (2D) présentent un énorme potentiel. Ces matériaux uniques, avec leurs propriétés intrigantes telles que le contraste élevé de l'indice de réfraction, l'accordabilité des propriétés optiques et les capacités inhérentes d'émission de lumière, sont bien adaptés à toute une série d'applications. Ils peuvent être utilisés dans des domaines allant des dispositifs photoniques, tels que les guides d'ondes et les capteurs, au stockage et à la conversion de l'énergie. Cependant, des défis persistent, principalement en ce qui concerne leur synthèse et leur incorporation dans des dispositifs fonctionnels. Ces obstacles ont limité leur utilisation à grande échelle dans diverses industries.

Compte tenu de ces défis, le travail documenté dans cette thèse de doctorat est à la fois pertinent et influent. Il ouvre de nouvelles voies pour la production à grande échelle et l'intégration transparente des matériaux 2D dans les circuits intégrés photoniques. Par conséquent, nos objectifs de recherche étaient les suivants :

- Identifier un matériau 2D approprié présentant des propriétés optiques non linéaires, complétant ainsi la technologie photonique du silicium pour les applications dans le proche infrarouge (lambda ~ 1,55um).

- Développer une méthode appropriée pour la synthèse du matériau 2D choisi. Cette méthode facilite l'intégration directe du matériau sur le guide d'ondes.

- Caractérisation des matériaux ultra-minces synthétisés, afin de sonder leurs propriétés structur et optiques et de clarifier l'influence du processus de fabrication sur ces propriétés.

- Incorporer avec succès le matériau synthétisé dans le dispositif final afin d'évaluer l'impact des propriétés optiques du matériau sur les dispositifs photoniques passifs.

Nous avons commencé notre travail en recherchant les propriétés de pointe de la grande famille des matériaux 2D afin d'en trouver un qui possède des propriétés optiques non linéaires. Parmi tous les candidats, nous avons sélectionné le nitrure de gallium (GaN), connu pour sa forte non-linéarité dans sa forme massive. Le GaN est devenu notre matériau cible, en gardant à l'esprit que les propriétés du matériau peuvent varier entre sa forme massive et sa forme ultramince, et que les propriétés peuvent changer en fonction de l'épaisseur. Bien que le GaN soit largement étudié aujourd'hui, il y a un manque de recherche sur ses propriétés linéaires et non linéaires dans la dimension 2D (moins de 5 nm), en particulier dans la gamme de l'infrarouge proche que nous ciblons. Notre recherche a donc comblé cette lacune.

Nous avons démontré la synthèse de couches ultraminces de GaN en utilisant une technique de fabrication connue sous le nom de Liquid Metal Chemistry, récemment développée à l'université RMIT. Cette technique se compose de deux étapes principales : l'impression par pression de gouttelettes liquides de gallium suivie d'un processus de nitruration au plasma. Nous avons développé la première étape de notre technique, en montrant qu'en pressant une gouttelette de gallium à température ambiante sur n'importe quel substrat à faible rugosité de surface, nous pouvions facilement synthétiser une couche ultramince de Ga_2O_3. Nous avons ensuite démontré qu'à l'aide d'un plasma, nous pouvions convertir efficacement Ga_2O_3 en GaN. Cette méthode en deux étapes nous a permis d'étudier les propriétés structur et optiques du Ga_2O_3 et du GaN que nous avions initialement ciblés. Notre méthode de fabrication a prouvé son utilité, sa rentabilité et son potentiel de gain de temps. De plus, cette technique permet de synthétiser des matériaux qui ne peuvent être obtenus par des méthodes traditionnelles telles que l'exfoliation mécanique, par exemple le GaN, en raison de sa structure wurtzite. Par conséquent, nous pensons que cette technique de fabrication pourrait permettre de synthétiser d'autres matériaux 2D en utilisant la méthode de la chimie des métaux liquides plutôt que les techniques traditionnelles.

En outre, nous avons utilisé diverses techniques de caractérisation pour confirmer la fabrication de couches ultraminces, obtenir des informations sur la composition chimique et la structure de notre matériau synthétisé et comparer les différences avant et après le processus de nitruration. Nous avons étudié la nature de cette transformation. Grâce à la microscopie à force atomique (AFM), nous avons montré que notre couche ultramince était relativement homogène, avec une épaisseur moyenne d'environ 3 nm. De plus, la microscopie optique a confirmé que notre couche ultramince s'étendait sur plusieurs millimètres de côté.

Dans le processus de conversion des couches d'oxyde en couches de nitrure, nous avons optimisé divers paramètres plasma du traitement de nitruration. Nous avons notamment montré que les paramètres de temps et de puissance jouaient un rôle central dans cette transformation et pouvaient être utilisés de manière fiable pour contrôler la composition de la couche finale. Nous avons ainsi pu suivre la transition progressive de Ga_2O_3 à GaN en manipulant ces deux paramètres. Cela nous a permis de créer des composés intermédiaires GaO_xN_y, qui n'ont pas encore été largement étudiés, et nous avons caractérisé leurs propriétés.

Nous avons utilisé la spectroscopie photoélectronique à rayons X (XPS) pour révéler la configuration de liaison et la composition chimique de la couche d'oxyde déposée ainsi que chaque étape de la transformation en nitrure. De plus, en extrayant le pourcentage atomique de XPS pour chaque niveau intermédiaire de GaN_xO_y, nous avons observé comment le contrôle du temps et de la puissance a conduit à différents niveaux, chacun possédant une composition chimique unique. A l'aide du XPS, nous avons également examiné en détail le changement des différents pics spectraux, en particulier le pic O1s après nitruration, qui a confirmé une transformation complète en nitrure à des paramètres optimisés (temps : 10 minutes et puissance : 200 W). Grâce aux mesures Raman effectuées par nos collaborateurs au CEA, cette transformation a également été confirmée.

Pour étudier la structure cristalline du matériau fabriqué, nous avons effectué une microscopie électronique à transmission (TEM) sur les couches ultraminces d'oxyde et de nitrure. Nous avons constaté que notre Ga_2O_3 possédait une structure amorphe, qui s'est transformée en structure cristalline lorsqu'il a été converti en nitrure. Le nitrure avait un espacement de réseau d'environ 0,189 nm, correspondant aux plans (102), une caractéristique de la structure cristalline wurtzite de GaN. Ce résultat a apporté une confirmation supplémentaire aux résultats XPS et Raman concernant la transformation de l'oxyde en nitrure.

D'autre part, comme les Ga_2O_3 et GaN bidimensionnels n'ont pas été largement utilisés dans des applications photoniques, leurs propriétés optiques restent largement inconnues et pourraient différer de celles de leurs homologues sous forme plus épaisse. En général, les composés de gallium sont prometteurs pour les applications photoniques en raison de leur large bande interdite. L'une de nos premières étapes a consisté à mesurer les indices optiques de ces couches ultraminces de Ga_2O_3 et de GaN à l'aide de l'ellipsométrie. L'indice de réfraction obtenu pour 3 nm de Ga_2O_3 et de GaN était similaire à la valeur de l'indice de réfraction de leurs homologues sous forme massique trouvée dans la littérature. Nous en avons conclu que l'indice de réfraction de Ga_2O_3 et GaN est indépendant de leur épaisseur (jusqu'à 3 nm). Dans notre travail, bien que nous ayons réussi à atteindre une épaisseur minimale de 2,5 nm, il est important de noter que nous n'avons pas réussi à synthétiser un matériau monocouche. Il est intéressant de noter que la différence d'indice de réfraction entre Ga_2O_3 et GaN ($\Delta n = 0,23$ à 1550 nm) confirme l'efficacité du processus de nitruration et montre une voie pour contrôler les propriétés optiques de la couche 2D à intégrer dans des dispositifs photoniques. En étendant notre mesure de dispersion à chaque niveau intermédiaire, nous avons clairement observé l'évolution de n (indice de réfraction) et de k (coefficient d'extinction) en fonction de l'augmentation de la puissance du plasma ou de la durée. Les variations observées dans ces courbes dépendent fortement du degré de nitruration du film d'oxyde. Ces résultats indiquent que les propriétés optiques du film ultra-mince de GaO_xN_y peuvent être ajustées de manière fiable et contrôlée par les paramètres du plasma, ce qui est utile pour les applications de dispositifs photoniques. Ces résultats ouvrent donc la voie à l'intégration de matériaux 2D aux propriétés optiques ajustables dans des dispositifs photoniques en silicium.

En outre, grâce à l'ellipsométrie, nous avons pu déterminer la proportion de GaN dans la couche composite modélisée. Le résultat a montré une augmentation du pourcentage ajusté de GaN dans la couche modélisée en fonction des paramètres du plasma, ce qui est cohérent avec les mesures XPS. Ceci réaffirme l'efficacité du traitement plasma pour transformer la couche d'oxyde en GaN de manière graduelle et contrôlée.

Les calculs de la théorie de la fonctionnelle de la densité (DFT), effectués par nos collaborateurs de l'institution CNR-NANO, ont été utilisés pour étudier les propriétés optiques de Ga_2O_3 et de GaN et les comparer à nos résultats expérimentaux. Il est important de noter qu'en raison de la difficulté d'appliquer la DFT à un matériau amorphe, Ga_2O_3 a été considéré comme cristallin dans ce cas. Les résultats finaux ont montré une compatibilité entre les calculs de l'indice de réfraction fournis par la DFT pour Ga_2O_3 et GaN et les valeurs extraites de l'ellipsométrie. Les valeurs de bande interdite extraites confirment que les bandes interdites des matériaux ultra-minces synthétisés sont inférieures à celles de leurs formes massiques et supérieures à celles de leurs formes monocouches. Cette observation est cohérente avec nos résultats, étant donné que l'épaisseur du matériau est intermédiaire, se situant entre celle d'une monocouche et d’une couche épaisse.

Dans le dernier chapitre de ce manuscrit, nous nous sommes concentrés sur l'intégration de matériaux ultra-minces sur un circuit intégré photonique fabriqué par ST microelectronics. Nous avons utilisé un guide d'onde en nitrure de silicium (SiN) conduisant la lumière au sein d'un interféromètre Mach-Zehnder (MZI) comme dispositif de structure de test. Notre technique de fabrication nous a permis de transférer directement le matériau 2D sur le dispositif de manière sélective. De plus, grâce à la deuxième étape de notre processus de fabrication, la nitruration par plasma, nous avons pu passer de l'oxyde au nitrure sur le dispositif avec un haut degré de fiabilité, et étudier l'impact sur la transmission du dispositif.

Pour garantir un dépôt précis sur le bras de détection du MZI, nous avons mis au point une technique basée sur la photolithographie pour protéger le substrat à l'aide d'une résine photosensible. Nous avons constaté que la résine photosensible agissait comme un répulsif pour les matériaux 2D déposés et qu'elle pouvait être utilisée pour contraindre le revêtement à des zones spécifiques de la puce. Nous avons développé ce processus pour localiser le matériau 2D sur un bras d'une structure MZI SiN9. Des mesures de transmission ont été effectuées et comparées pour la structure sans matériau 2D, ou recouverte sélectivement de Ga_2O_3 et de GaN, et des réponses légèrement distinctes ont été obtenues. Les coefficients d'extinction obtenus pour Ga_2O_3 et GaN sont tous deux de 0 à la longueur d'onde de 1550 nm. Cela indique une absorption quasi inexistante de la lumière incidente, soulignant la transparence de ces matériaux dans cette région spectrale. Ce comportement caractéristique de Ga_2O_3 et GaN à 1550 nm est d'une importance capitale. L'intégration réussie d'un matériau 2D sur le dispositif a également été confirmée par AFM et XPS. Même si l'effet sur l'indice effectif était relativement faible sur ces structures non optimisées où l'interaction lumière-matière avec le matériau 2D était réduite à 0,2 %, cela laisse entrevoir des applications futures pour ces circuits photoniques hybrides passifs fonctionnalisés localement avec des matériaux 2D.

De plus, tous les résultats extraits de nos différentes méthodes de caractérisation dans les chapitres 3 et 4 peuvent être utiles pour une étude plus approfondie des applications potentielles de Ga_2O_3 et GaN. Ce travail représente également la première étape dans l'étude du potentiel du niveau intermédiaire (GaO_xN_y). Les connaissances acquises peuvent être utilisées pour ajuster les propriétés des dispositifs optiques basés sur ces matériaux. En outre, cette recherche fournit une stratégie d'intégration des matériaux 2D dans les puces photoniques hybrides, permettant ainsi la modification ou l'amélioration locale d'un circuit optique par ailleurs passif.

Enfin, en raison de contraintes de temps au cours des trois ans et demi de ce programme de doctorat, l'exploration des propriétés non linéaires du GaN reste incomplète. Néanmoins, je suis fermement convaincue que les efforts considérables et le travail de fond réalisés tout au long de cette recherche ont effectivement ouvert la voie à des projets ultérieurs. Les études futures peuvent désormais se concentrer plus efficacement sur l'élucidation de la non-linéarité de ces matériaux. Les connaissances scientifiques et les avancées technologiques réalisées dans le cadre de ce travail constituent une base pour la prochaine phase d'exploration du domaine fascinant des matériaux 2D et de leurs propriétés non linéaires. Par conséquent, notre voyage vers l'exploitation du plein potentiel de ces matériaux pour diverses applications se poursuit sans relâche.

Pour l'avenir, ces travaux ouvrent de multiples voies prometteuses pour l'exploration et le développement.

- *Perspectives technologiques* : Il est possible d'affiner et d'étendre cette méthode innovante vers une approche de synthèse/transfert plus fiable et contrôlée. Cela impliquerait de relever des défis tels que l'élimination métal résiduel du processus et d'améliorer la reproductibilité. En outre, l'adoption d'outils sophistiqués tels qu'un équipement de nano-impression pourrait potentiellement optimiser le processus de fabrication.
- *Perspectives matériaux* : Notre approche pourrait également être étendue à la synthèse d'autres matériaux, tels que l'InN. En employant plusieurs étapes de ce processus, il pourrait être possible de créer des hétérostructures 2D combinant GaN et Ga_2O_3, élargissant ainsi la gamme de matériaux potentiels aux propriétés uniques.
- *Perspectives du dispositif* : Les performances du dispositif pourraient être considérablement améliorées en optimisant sa géométrie, en particulier la section transversale du guide d'ondes, afin d'augmenter l'interaction lumière-matière avec le matériau 2D. D'autres stratégies visant à améliorer cette interaction pourraient inclure l'utilisation de guides d'ondes à fentes ou de cavités optiques. Ces modifications pourraient permettre un meilleur contrôle et une plus grande efficacité dans la manipulation de la lumière, ouvrant ainsi la voie à une nouvelle génération de dispositifs photoniques.

En conclusion, notre travail constitue une base solide pour les recherches futures dans le domaine des matériaux 2D et de leur incorporation dans les dispositifs photoniques.

Abstract

Liquid-Metal Fabrication of Ultrathin Ga_2O_3 and GaN for Hybrid Integrated Photonics

2D materials have emerged as promising candidates for enhancing silicon photonics. With their atomically thin structure, high carrier mobility, and strong light-matter interaction, 2D materials offer the potential for efficient light emission, modulation, and sensing in silicon photonics. Their compatibility with silicon processing techniques and ability to integrate into existing silicon photonic platforms make them attractive for achieving compact, high-performance, and energy-efficient photonic devices.In this context, we introduced ultrathin Ga_2O_3 and GaN synthesized using the liquid metal chemistry technique. Our approach primarily exploits the LMC technique, which allows for easier integration of 2D materials onto photonic devices compared to traditional top-down and bottom-up methods. Our fabrication process involves a two-step procedure: liquid metal-based printing of Ga_2O_3, followed by plasma-enhanced nitridation reaction. This two-step process enables control over the composition of the resulting nm-thick GaO_xN_y layer and the eventual achievement of stoichiometric GaN. The structural properties and elemental composition of these 2D materials are characterized using AFM, TEM, XPS, and Raman spectroscopy.Our fabrication process grants access to a range of GaO_xN_y compounds with distinct optical properties, which can be tailored between those of Ga_2O_3 and GaN, as demonstrated by ellipsometry measurements and comparison with DFT simulations. Additionally, we successfully demonstrated the integration of these materials into a MZI and performed linear measurements before and after nitridation. Our findings expand the knowledge of ultra-thin gallium compounds, which have been poorly studied, and represent an essential step toward integrating such 2D materials into photonic chips. This work offers new opportunities to improve the performance of hybrid optoelectronic devices.

Keywords: 2D materials, Liquid metal chemistry, Gallium Nitride, Refractive index, MZI, GaO_xN_y

Résumé

Investigation of ultra-thin Gallium compound layers fabricated by liquid metal chemistry for hybrid integrated photonics

Les matériaux 2D sont apparus comme des candidats prometteurs pour l'amélioration de la photonique du silicium. Avec leur structure atomiquement fine, leur mobilité élevée des porteurs et leur forte interaction lumière-matière, les matériaux 2D offrent la possibilité d'une émission, d'une modulation et d'une détection efficaces de la lumière dans la photonique du silicium. Leur compatibilité avec les techniques de traitement du silicium et leur capacité à s'intégrer dans les plates-formes photoniques au silicium existantes les rendent attrayants pour la réalisation de dispositifs photoniques compacts, à haute performance et à faible consommation d'énergie. Notre approche exploite principalement la technique LMC, qui permet une intégration plus facile des matériaux 2D sur les dispositifs photoniques par rapport aux méthodes traditionnelles descendantes et ascendantes. Notre processus de fabrication comporte deux étapes : l'impression de Ga_2O_3 à base de métal liquide, suivie d'une réaction de nitruration améliorée par plasma. Ce processus en deux étapes permet de contrôler la composition de la couche de GaO_xN_y de quelques millimètres d'épaisseur qui en résulte et d'obtenir finalement du GaN stœchiométrique. Les propriétés structurelles et la composition élémentaire de ces matériaux 2D sont caractérisées par AFM, TEM, XPS et spectroscopie Raman. Notre processus de fabrication donne accès à une gamme de composés GaO_xN_y avec des propriétés optiques distinctes, qui peuvent être adaptées entre celles de Ga_2O_3 et GaN, comme le démontrent les mesures ellipsométriques et la comparaison avec les simulations DFT. En outre, nous avons démontré avec succès l'intégration de ces matériaux dans un MZI et effectué des mesures linéaires avant et après nitruration. Nos résultats élargissent les connaissances sur les composés ultraminces de gallium, qui ont été peu étudiés, et représentent une étape essentielle vers l'intégration de ces matériaux 2D dans les puces photoniques. Ce travail offre de nouvelles possibilités d'améliorer les performances des dispositifs optoélectroniques hybrides.

Mots-clés : Matériaux 2D, chimie des métaux liquides, nitrure de gallium, indice de réfraction, MZI, GaO_xN_y